MOLECULAR DYNAMICS SIMULATION OF WATER AND AQUEOUS SOLUTIONS

Igor Shvab

Dissertation
submitted in fulfillment of requirements for the degree of
Doctor of Philosophy

Centre for Molecular Simulation
Faculty of Information and Communication Technologies
Swinburne University of Technology

February 2014

Abstract

The objectives of this work is to use molecular dynamic simulation to systematically investigate all basic properties of water and aqueous solutions of neon, argon, krypton, xenon and methane in the liquid phase.

The structural properties of pure water at densities 1, 0.8, and 0.6 g/cm^3, and aqueous nonpolar solute mixtures at constant density 1g/cm^3 have been investigated in the canonical NVT ensemble over the temperature range 278 - 750 K. We have used and compared several water models, namely the *ab initio* MCYna model and rigid SPC/E and SPC/Fw models to study hydrogen-bond network and shell structure of bulk water. Structure of aqueous solutions has been investigated with the help of combined MCYna + LJ and SPC/E + LJ potentials. For aqueous solutions water-water interaction were obtained from the MCYna and SPC/E water models, whereas water-solute and solute-solute interactions were calculated with the help of the Lennard-Jones potential. Simulations show that SPC/E, SPC/Fw, and to a lesser degree MCYna models underestimate water structure and the level of hydrogen bonding in the high temperature region. The presence of nonpolar solutes in small concentrations appears to have local strengthening effect on water structure, while at higher concentrations solute particles clearly prevent water molecules from forming hydrogen bonds.

Polarization properties of water and aqueous nonpolar solute mixtures have been thoroughly investigated using MCYna + LJ potential model. The dielectric constant and dipole moment of pure water and aqueous solutions have been found. The dielectric constant of bulk water given by *ab initio* polarizable MCYna model is in good agreement with experimental data. Introduction of nonpolar solutes decreases polarization properties of water. The dielectric constant and average dipole moment of the mentioned mixtures are decreasing with temperature and solute concentration.

A novel technique of statistical averages has been applied to study all thermodynamic properties of water and water-methane mixtures in the liquid phase. Namely, thermal pressure coefficient, isothermal and adiabatic compressibilities, thermal expansion coefficient, isochoric and isobaric heat capacities, Joule-Thompson coefficient, and speed of sound of water and water-methane mixtures. Results obtained by using nonpolarizable SPC/E and TIP4P/2005 water models show qualitative agreement with experimental

data at temperatures up to 400 K. Comparison of the present results with results obtained from polarizable MCYna model indicate superiority of the polarizable potential over nonpolarizable SPC/E and TIP4P/2005 potentials. In case of water-methane mixtures, simulated results show that methane decreases heat capacities and compressibilities, and increases expansion coefficient and speed of sound comparing to pure water.

Finally, transport properties of aqueous solutions of neon, argon, krypton, xenon and methane have been also calculated in the liquid phase. The presence of nonpolar solutes like methane or noble gases decreases diffusion coefficient of water. This decrease is mainly proportional to the solute concentration number. Comparison of diffusion coefficients of noble gases and methane clearly indicate their mass and size dependency. Nonpolar particles with large mass and atomic diameter diffuse in water more slowly than light particles. Velocity autocorrelation functions also indicate specific changes in solvation shell structure caused by solute particles.

Acknowledgements

I would like to acknowledge and thank my supervisors Prof. Richard J. Sadus and Prof. Billy D Todd for their positive direction and continuing support. In particular, I am grateful to my principal supervisor Prof. Richard Sadus for his invaluable encouragement, professionalism and patience to achieve quality. Both of my supervisors gifted me the best attributes of a researcher through their scientific knowledge, professional attitude and fantastic interpersonal skill.

I would like to thank Swinburne University of Technology for financial support through a Swinburne University Postgraduate Research Award scholarship (SUPRA). This work also received computational time from Victorian Partnership for Advanced Computing (VPAC).

Thanks to other academic staff and students in the Centre for Molecular Simulation and SUCCESS department for all encouraging discussions and friendly atmosphere.

Finally, I would like to thank my family whose love continues to encourage me, as it has always done.

Declaration

I hereby declare that this thesis entitled "Molecular Dynamics Simulation of Water and Aqueous Solutions" is my own work. To the best of my knowledge, it contains no materials previously published by other persons except where reference is made in the text of the thesis.

Igor Shvab

February 2014

Publications

1. I. Shvab and R. J. Sadus. Structure and polarization properties of water: Molecular dynamics with a nonadditive intermolecular potential. Physical Review E, **85**, 051509 (2012).

2. I. Shvab and R. J. Sadus. Dielectric and structural properties of aqueous nonpolar solute mixtures. J. Chem. Phys, **137**, 124501 (2012).

3. I. Shvab and R. J. Sadus. Intermolecular potentials and the accurate prediction of the thermodynamic properties of water. J. Chem. Phys, **139**, 194505 (2013).

4. I. Shvab and R. J. Sadus. Thermodynamic properties and diffusion of water + methane binary mixtures. (Submitted to J. Chem. Phys.)

Contents

Abstract i

Acknowledgements iii

Declaration of Authorship iv

Publications v

Notations ix

Physical Constants xii

List of Tables xiii

List of Figures xiv

1 Introduction 1
- 1.1 Aims and Motivations . . . 1
- 1.2 Background and current progress . . . 3
  - 1.2.1 Water structure . . . 3
  - 1.2.2 Polarization properties . . . 5
  - 1.2.3 Thermodynamic properties . . . 6
  - 1.2.4 Transports properties . . . 9
- 1.3 Outline of the thesis . . . 10

2 Molecular Dynamic Simulation 12
- 2.1 Water-water interaction . . . 14
  - 2.1.1 Water molecule . . . 14
  - 2.1.2 Water models, criteria . . . 19
  - 2.1.3 Rigid water models . . . 21
    - 2.1.3.1 SPC . . . 21
    - 2.1.3.2 TIP3P . . . 23
    - 2.1.3.3 SPC/E . . . 23
    - 2.1.3.4 TIP4P/2005 . . . 24

2.1.3.5 MCY (Matsuoka-Clementi-Yoshimine) . . . 25
2.1.3.6 TIP5P . . . 27
2.1.3.7 NvdE . . . 28
2.1.4 Polarizable water models . . . 28
2.1.4.1 SPC/FQ . . . 29
2.1.4.2 TIP4P/FQ . . . 29
2.1.4.3 GCPM (Gaussian charge polarizable model) . . . 30
2.1.4.4 BKd3 (Baranyai-Kiss) . . . 30
2.1.4.5 MCYna (Matsuoka-Clementi-Yoshimine nonadditive) . . . 30
2.1.5 Flexible water models . . . 32
2.1.5.1 SPC/Fw . . . 33
2.1.5.2 TIP4P/2005f . . . 34
2.1.5.3 MCYL (Matsuoka-Clementi-Yoshimine-Lie) . . . 34
2.1.6 *Ab initio* water models . . . 34
2.1.7 Improving water models . . . 39
2.2 Water-solute interaction . . . 41
2.2.1 Methane clathrate . . . 42
2.2.2 Hydrophobic interaction . . . 44
2.2.2.1 Water-Neon . . . 47
2.2.2.2 Water-Argon . . . 47
2.2.2.3 Water-Krypton . . . 48
2.2.2.4 Water-Xenon . . . 49
2.2.2.5 Water-Methane . . . 49
2.3 Simulation details . . . 53
2.3.1 Simulation ensemble . . . 53
2.3.2 Equations of motion . . . 53
2.3.3 Initial lattice configuration . . . 54
2.3.4 Initial random velocity . . . 54
2.3.5 Constant temperature . . . 55
2.3.6 Force calculation . . . 55
2.3.7 Integration of motion . . . 56
2.3.8 Constraint method . . . 57
2.3.9 Periodic boundaries . . . 57
2.3.10 Treatment of long-range and Coulomb interactions . . . 59

3 Calculation of Thermodynamic Properties from Molecular Simulation 63
3.1 Thermodynamic quantities from fluctuation theory . . . 63
3.2 Thermodynamic quantities from statistical mechanics theory . . . 65
3.2.1 Thermal pressure coefficient . . . 67
3.2.2 Compressibilities . . . 67
3.2.3 Thermal expansion coefficient . . . 68
3.2.4 Heat capacities . . . 69
3.2.5 Speed of sound . . . 70
3.2.6 Joule-Thomson coefficient . . . 70
3.3 Calculation of thermodynamic quantities in the NVT ensemble . . . 71

4 Molecular Structure and Hydrogen Bonding in Aqueous Solutions 74

4.1 Simulation details . . . 77
4.2 Molecular structure and hydrogen bonding in bulk water . . . 78
4.2.1 Structural properties along the isochore at 1 g/cm^3. . . . 78
4.2.2 Structural properties along the isochore at 0.8 g/cm^3. . . . 80
4.2.3 Structural properties along the isochore at 0.6 g/cm^3. . . . 81
4.2.4 Shell structure . . . 83
4.3 Molecular structure and hydrogen bonding in aqueous nonpolar solute mixtures . . . 87
4.3.1 Water-solute radial distribution functions . . . 87
4.3.2 Structure of the solvation shells . . . 89
4.3.3 One-phase region . . . 94

5 Polarization Properties of Aqueous Nonpolar Solute Mixtures 97
5.1 Current theories of dielectrics . . . 97
5.2 Polarization properties of bulk water . . . 101
5.2.1 Dielectric constant . . . 102
5.2.2 Dipole moment . . . 105
5.3 Polarization properties of aqueous nonpolar solute mixtures . . . 106
5.3.1 Dielectric constant . . . 107
5.3.2 Comparison of MD and analytical calculations of dielectric constants 110
5.3.3 Dipole moment . . . 112

6 Thermodynamic Properties of Water and Aqueous Nonpolar Solute Mixtures 116
6.1 Thermodynamics of solvation . . . 119
6.2 Reference data for water . . . 124
6.3 Pressure . . . 124
6.4 Thermal pressure coefficient . . . 127
6.5 Isothermal and adiabatic compressibilities . . . 129
6.6 Thermal expansion coefficient . . . 132
6.7 Isochoric and isobaric heat capacities . . . 135
6.8 Speed of sound . . . 140
6.9 Joule-Thomson coefficient . . . 142

7 Transport Properties 145
7.1 Diffusion theories . . . 145
7.1.1 Trajectory analysis . . . 150
7.1.2 Correlation function . . . 151
7.2 Diffusion coefficients of aqueous nonpolar solute mixtures . . . 152
7.3 VACF and the shell structure . . . 159

8 Conclusions and Recommendations 162

Bibliography 168

Notations

Abbreviations

SPC	simple point charge
SPC/E	extended simple point charge
SPC/Fw	flexible simple point charge
SPC/Fd	flexible simple point charge
SPC/FQ	simple point charge with fluctuating charges
TIP3P	transferable intermolecular potential three point
TIP4P	transferable intermolecular potential four point
TIP4P/FQ	transferable intermolecular potential four point with fluctuating charges
TIP4P/2005	transferable intermolecular potential four point 2005
TIP5P	transferable intermolecular potential five point
MCY	Matsuoka-Clementi-Yoshimine water model
MCYL	Matsuoka-Clementi-Yoshimine-Lie flexible water model
MCYna	Matsuoka-Clementi-Yoshimine water model with nonadditive terms
BNS	Ben-Naim and Stillinger model
ST2	Stillinger and Rahman model
PPC	polarizable point charge model
GCPM	Gaussian charge polarizable model
RPOL	Revised polarizable model
LJ	Lennard-Jones
CHARMM	Chemistry at HARvard Macromolecular Mechanics
DL_POLY	Daresbury Laboratory Polyatomic
MD	molecular dynamics
MC	Monte Carlo
AIMD	*Ab initio* molecular dynamics

CPMD	Car-Parrinello molecular dynamics
PIMD	Path integral molecular dynamics
T	temperature
T_c	critical temperature
T_m	melting temperature
TMD	temperature of maximum density
RDF	radial distribution function
EOS	equation of state
Exp.	experiment
Ref.	reference
fcc	face centered cubic
CGM	conjugate gradient method
MPI	message passing interface
PBC	periodic boundary conditions
IAPWS	international association for the properties of water and steam
Δt	simulation step length
t	total simulation time
ρ	density
p	pressure
$\mathbf{P}$	total linear momentum
m	mass of a single atom/molecule
M	total mass of the system
V	volume
N	number of molecules/atoms
U	molar potential energy
K	molar kinetic energy
E	molar internal energy
Π_{mn}	derivatives of partition function with respect to temperature and volume
S	Entropy
G	Gibbs energy
A	Helmholtz energy
H	Enthalpy
ΔS	changes in Entropy upon solvation

ΔG	changes in Gibbs energy upon solvation
ΔA	changes in Helmholtz energy upon solvation
ΔH	changes in Enthalpy upon solvation
α	electronic polarizability
ε_r	dielectric constant
$\boldsymbol{\mu}$	dipole moment
$\mathbf{r}_{ij}$	relative position of particles i and j
r_i	position of the particle i
u_{ij}	potential energy between particles i and j
$\mathbf{v}$	velocity of the particle
$\mathbf{a}$	acceleration of the particle
$\mathbf{f}_{ij}$	force between particles i and j
L	length of the side of simulation box
q_i	charge of atom i or on site i inside of the molecule
l_1	oxygen-hydrogen bond length
l_2	the distance between oxygen and the displaced charge (dummy) site
ϕ	angle between the hydrogen-oxygen bond and the oxygen-dummy line
θ	bond angle between two oxygen-hydrogen bonds
σ	Lennard-Jones length constant
ε	Lennard-Jones energy constant
C_v	isochoric heat capacity
C_p	isobaric heat capacity
ΔC_v	C_v difference between the C_v of pure water and mixture
ΔC_p	C_p difference between the C_p of pure water and mixture
γ_v	thermal pressure coefficient
κ_T	isothermal compressibility
κ_S	adiabatic compressibility
α_p	thermal expansion coefficient
ω_0	speed of sound at zero frequency
μ_{JT}	Joule-Thomson coefficient

Physical Constants

e	elementary positive charge ($1.602176565(35)\times10^{-19}$ C)
k	Boltzmann constant (1.380662×10^{-23} J/K)
R	universal gas constant (8.31441 J mol^{-1} K^{-1})
N_a	Avogadro number (6.022045×10^{23} mol^{-1})
Å	Ångström 10^{-10} m
nm	nano meter (10^{-9} m)
ns	nano second (10^{-9} s)
ps	pico second (10^{-12} s)
fs	femto second (10^{-15} s)
D	Debye (unit of molecular dipole moment) ($\approx 3.33564\times10^{-30}$ C m)
ε_0	vacuum permittivity ($\approx 8.854187817620\times10^{-12}$ C^2 $\text{N}^{-1}\text{m}^{-2}$)

List of Tables

2.1 Intermolecular parameters used in the MCY and MCYna intermolecular potential. Values are in atomic units. 27
2.2 Parameters for some water molecules. Angles θ, φ, distances l_1, l_2, and charges q_1, q_2, and q_3 are shown in Figure 2.5. 38

3.1 Summary of thermodynamic functions in terms of partial derivatives of partition function $\Pi(\beta, V, N)$. 72

4.1 Positions of the first minima of the MCYna RDFs together with n_{oo} values along the 1, 0.8, and 0.6 g/cm^3 isochores. 86
4.2 Lennard-Jones potential parameters used for water-solute and solute-solute pair interactions (Guillot and Guissani, 1993). 87

5.1 Dielectric constants for the MCYna and SPCE models along the 1, 0.8, and 0.6 g/cm^3 isochores. 104

6.1 Comparison with experiment for the thermodynamic properties of several water models at 298K and 0.1 MPa. 123

List of Figures

2.1 Simple representation of water molecule. . . . 15
2.2 Schematic representation of the water dimer. . . . 16
2.3 Schematic representation of the tetrahedral shape of water. . . . 17
2.4 Hydrogen bond network in water. . . . 18
2.5 Schematic representation of water models. . . . 22
2.6 Structure of the MCYna water molecule. . . . 25
2.7 Definition of the MCY water dimer geometry. . . . 26
2.8 Methane clathrate. . . . 43
2.9 Formation of hydrophobic interaction. . . . 45
2.10 Ne-H_2O coordinate system. . . . 47
2.11 Ar-H_2O coordinate system. . . . 48
2.12 CH_4-H_2O coordinate system. . . . 50
2.13 Periodic boundary conditions, minimum image convention and spherical cutoff radius. . . . 58

4.1 Radial distribution function calculation . . . 75
4.2 Temperature dependence of the water RDFs along the 1 g/cm^3 isochore. . 80
4.3 Temperature dependence of the water RDFs along the 0.8 g/cm^3 isochore. 81
4.4 Temperature dependence of the water RDFs along the 0.6 g/cm^3 isochore. 82
4.5 Oxygen-hydrogen coordination numbers at densities 1, 0.8, and 0.6 g/cm^3 84
4.6 Solute-oxygen RDFs for water-solute systems at 298 K. . . . 89
4.7 Comparison of pure water and mixture RDFs. . . . 90
4.8 Argon-oxygen, oxygen-oxygen, and oxygen-hydrogen coordination numbers at different argon mole fractions. . . . 91
4.9 Coordination numbers of different aqueous solutions at 298 K as a function of solute concentration. . . . 93

5.1 Dielectric constant ε_r of bulk water at densities 1, 0.8, and 0.6 g/cm^3. . . 103
5.2 Water dipole moments distribution. . . . 106
5.3 Water dipole moments at densities 1, 0.8, and 0.6 g/cm^3. . . . 107
5.4 Dielectric constants of water-neon, water-argon, and water-methane mixtures . . . 108
5.5 Dielectric constants of aqueous solutions of Ne, Ar, CH_4, Kr, and Xe as functions of solutes concentration. . . . 109
5.6 Comparison of theoretical and simulation dielectric constants. . . . 113
5.7 Temperature dependence of the average dipole moments of water-neon, water-argon, and water-methane mixtures . . . 114
5.8 Dipole moment distributions of water-methane mixture. . . . 115

5.9 Dipole moments of different aqueous solutions as functions of solutes concentration. . . . 115

6.1 Isochores of pure water from SPC/E, TIP4P-2005 and MCYna models. . . . 125
6.2 Isochores of water-methane mixtures. . . . 126
6.3 Thermal pressure coefficient of pure water. . . . 128
6.4 Thermal pressure coefficient of water-methane mixtures. . . . 128
6.5 Isothermal compressibility of pure water. . . . 130
6.6 Adiabatic compressibility of pure water. . . . 130
6.7 Isothermal compressibility of water-methane mixtures. . . . 132
6.8 Adiabatic compressibility of water-methane mixtures. . . . 133
6.9 Thermal expansion coefficient of pure water. . . . 134
6.10 Thermal expansion coefficient of water-methane mixtures. . . . 134
6.11 Isochoric heat capacity of pure water. . . . 136
6.12 Isobaric heat capacity of pure water. . . . 136
6.13 Isochoric heat capacity of water-methane mixtures. . . . 138
6.14 Isobaric heat capacity of water-methane mixtures. . . . 138
6.15 Speed of sound in pure water. . . . 141
6.16 Speed of sound in water-methane mixtures. . . . 141
6.17 Joule-Thomson coefficient of pure water. . . . 143
6.18 Joule-Thomson coefficient of water-methane mixtures. . . . 143

7.1 Diffusion coefficients of water-methane mixtures. . . . 154
7.2 Diffusion coefficients of water-krypton mixtures. . . . 155
7.3 Diffusion coefficients - comparison with theory. . . . 157
7.4 Diffusion coefficients of different nonpolar solutes in aqueous solutions. . . . 158
7.5 The velocity autocorrelation functions for water-methane mixtures. . . . 160
7.6 The velocity autocorrelation functions for water-krypton mixtures. . . . 161

Chapter 1

Introduction

1.1 Aims and Motivations

It is well known (Eisenberg and Kauzman, 1967; Franks, 1972; Ball, 2008) that water exhibits a number of unusual properties such as density maximum and isothermal compressibility minimum at normal conditions, volume contraction under melting conditions, at least 15 crystalline polymorphs, and a high dielectric constant. Water is the most abundant substance in nature and knowledge of its thermodynamic and electrostatic properties is very important to understanding phenomena in fields such as protein crystallization and folding, biological membranes, electrolyte solutions, detergency, and metal extraction. In some cases these properties must be known to the utmost precision, requiring robust experimental techniques, theoretical studies, and molecular simulations.

In practice, water almost always contains some solute components, isotopes, and even living microorganisms. Hence, aqueous solutions are the first most ubiquitous substances on Earth. Aqueous mixtures are of considerable interest in geochemistry and chemical technology (development of undersea deposits of gas hydrates), industrial technology (electric power generation, extraction process, decontamination), and biochemistry (protein folding, micellization). Binary fluid systems of water and inert nonpolar solutes despite being the simplest form of aqueous solutions, are of significant interest in modern chemical and energy industry. Phase equilibria, critical curves, and thermodynamics functions for a wide range of temperatures and pressures have been determined for mixtures containing water plus argon (Wu *et al.*, 1990), xenon (Franck *et al.*, 1974), neon (Japas and Franck, 1985), and methane (Errington *et al.*, 1998), etc. Due to very small solubility of nonpolar solutes in water experimental data on these mixtures are rather scant (Kennan and Pollack, 1990). Similar situation can be found in simulation literature where only very dilute mixtures at ambient conditions are considered. Obviously, due

to the clear lack of attention from the scientific community some properties of aqueous nonpolar solute mixtures remain unknown and other remain controversial. The main aims of this dissertation are:

- To investigate the molecular bond structure of water and aqueous nonpolar solute mixtures over the wide temperature, pressure and solute concentration range. Due to unclear picture of hydrogen bonding in water at high temperatures, we will investigate molecular structure in water normal and reduced densities, and temperature range 278 - 750 K. Changes in water hydrogen-bond network and solvation shell structure caused by nonpolar solutes are still surrounded by controversy. We will investigate temperature and solute concentration dependence of molecular structure of binary aqueous solutions of neon, argon, krypton, xenon, and methane. This choice of nonpolar solutes can allow us to recognize influence of solute mass and atomic diameter on solvation shell structure.

- To investigate the polarization properties of water and aqueous nonpolar solute mixtures. The dielectric constant and especially dipole moments of water at reduced densities and aqueous solutions at subcritical and critical temperatures are not well understood even today. By using molecular dynamic simulations we will calculate dielectric constant and average dipole moment of bulk water at densities 1, 0.8, and 0.6 g/cm^3 and of aqueous solutions at solute concentrations up to 30%. A thorough comparison with experimental data and theroretical predictions will be made.

- To calculate basic thermodynamic properties of water and water-methane mixture, like isochoric and isobaric heat capacities, isothermal and isentropic pressure coefficients, thermal pressure and thermal expansion coefficients, Joule-Thompson coefficient, and the speed of sound at zero frequency. The H_2O-CH_4 binary system has been chosen as a model system to study thermodynamic properties of aqueous nonpolar solutes. As it is commonly accepted, in this study we treat all nonpolar solutes as Lennard-Jones chargless spheres which allows us to study effects of solutes size σ, energy parameter ε, and mass m on structural, thermodynamic, and transport properties of aqueous solutions. We will apply an alternative method of calculating the thermodynamic quantities as an average of the appropriate microscopic dynamical functions over the molecular dynamics ensemble. Comparison of simulation results obtained from nonpolarizable SPC/E and TIP4P/2005 potentials with experimental data will allow us to establish the optimal nonpolarizable water model. Calculation of thermodynamic properties of water-methane mixtures will help us to estimate qualitative and quantitative changes in water upon methane dissolution. To the best of our knowledge, this is the first attempt to calculate

changes in heat capacity, compressibilities, expansion coefficient, Joule-Thomson coefficient, etc. brought by the solvation of nonpolar solute at solute concentration more than 1%.

- To calculate the transport properties of aqueous solutions of methane and noble gases. Our study of aqueous nonpolar solute mixtures would be incomplete without information about dynamics of molecules inside aqueous nonpolar solute mixtures. Thus, we will calculate diffusion coefficients and velocity autocorrelation functions of water and solutions in the temperature range from 278 K till 750 K and solute concentrations up to 15%. This simulation will elucidate specific changes in solvation shells around solute particles and the mobility of water molecules and solute particles at high tempeartures, pressures, and solute concentrations.

1.2 Background and current progress

The review presented in this Section is organized to reflect the aims of the thesis.

1.2.1 Water structure

A survey of the literature in the field of molecular simulation of water and aqueous solutions shows a great variety (at least 46) of different potentials models designed and tuned to best reproduce some selected water properties at narrow range of temperature-pressure-density conditions (Guillot, 2011). Usually these are properties of water and ice at ambient conditions. One of the most successful water models are nonpolarizable rigid SPC (Berendsen *et al.*, 1981), SPC/E (Berendsen *et al.*, 1987), SPC-Fw (Wu *et al.*, 2006), TIP3P and TIP4P (Jorgensen *et al.*, 1983), TIP4P-Ew (Horn *et al.*, 2004), TIP4P/2005 (Abascal and Vega, 2005), TIP5P (Mahoney and Jorgensen, 2000), and polarizable SPC/FQ and TIP4P/FQ (Rick *et al.*, 1994), MCYna (Li *et al.*, 2007), etc. While many water models indeed achieved significant success in reproducing such basic water properties as phase diagram, density behavior, enthalpy of vaporisation, dielectric constant and dipole moment, one has a feeling that these results are limited and lag behind the fast development of modern computers. Indeed, properties of water outside of "safe zone" of ambient conditions and normal density 0.998 g/cm^3 are far from satisfactory, which, probably drives researchers away from doing simulations at high temperature-pressure region. Incomplete results of water simulations at temperatures higher than boiling temperature leads to unclear picture of hydrogen bonding and shell structure at high temperatures and pressures.

Most of the peculiarities of water behavior are ascribed to the hydrogen bond (H-bond) and the ability of water molecules to form three-dimensional networks (Eisenberg and Kauzmann, 1969; Franks, 1972; Chaplin, 2013). The fluid structure of water has been characterized by atomic pair correlation functions: oxygen-oxygen, oxygen-hydrogen, and hydrogen-hydrogen pair correlation functions. At ambient conditions, the first peak of the oxygen-hydrogen radial distribution function (RDF) around 1.8 Å is a manifestation of hydrogen bonding between molecules. Despite some ambiguity in H-bond definition, computer calculations with common empirical intermolecular potentials have successfully reproduced this hydrogen-bonding peak for ambient water (Jorgensen *et al.*, 1987; Shvab and Sadus, 2012a; Kalinichev and Bass, 1994).

To investigate the properties of the hydrogen bonds at extreme conditions, studies have been extended to the supercritical state (Yoshii *et al.*, 1998; Kang *et al.*, 2011; Dyer and Cummings, 2006; Shvab and Sadus 2012a). The region of supercritical temperatures and pressures is where most of the discrepancy between MD data and experiments arises. The *ab initio* calculations of Kang *et al.* (2011) indicate a conservation of 50% of H-bonds above 800 K. Molecular dynamics calculation with the TIP4P (Jorgensen *et al.*, 1983) model indicated that 70% of the hydrogen bonds found at ambient conditions remain at temperatures up to 1130 K. However, neutron diffraction experiments using the isotopic substitution technique (NDIS) of Soper (2000) show that the first peak of the oxygen-hydrogen RDF completely disappears in the supercritical state at 673 K and densities of 0.58 and 0.66 g/cm^3. This suggests that the hydrogen bonding network does not exist at supercritical conditions despite the fact that the hydrogen-bonding energy is well above the thermal energy at 673 K. Tromp *et al.* (1994) suggested that the reason for this discrepancy is due to the deficiency of pairwise additive potentials such as TIP4P. Alternatively, Loffler *et al.* (1994) claimed that the discrepancy arises from the inelasticity correction to the neutron data, which is particularly large for the light water sample. Recent *in situ* x-ray diffraction (XRD) experiments of Ikeda *et al.* (2010) and Weck *et al.* (2009) are in better agreement with the calculated results. However, calculations and experiments still provide a different description of hydrogen bonding in water at elevated temperatures and pressures.

Water is a major component of all aqueous solutions and as a consequence, gaps in understanding water properties is being automatically transferred to mixtures. Due to huge variety of aqueous solutions most of the research efforts have been concentrated on biologically and industrially most important mixtures again at very limited range of conditions. However, continuous progress in chemical and energy industry, development of new resources, makes drastic changes in modern research priorities. Mixtures of water and methane, water and noble gases being largely omitted from research focus previously,

became the main topic of the 21st century energy industry agenda (Kvenvolden, 1995; Vanneste *et al.*, 2001).

Despite the rapidly growing interest in this field simulation results are very scarce and experimental data are far from complete. Binary fluid systems of water and an inert nonpolar second component is another important category of molecular liquids where H-bonding plays crucial role (Ben-Naim, 2006; Chandler, 2005; Pauling, 1961). Phase diagrams of these aqueous solutions have been investigated experimentally (Wu *et al.*, 1990; Franck *et al.*, 1974; Japas and Franck, 1985) and with the help of molecular dynamics (MD) and Monte Carlo (MC) techniques. Recent neutron diffraction studies explored the hydration shell of argon at sub-critical conditions, using distinct isotopes of argon in normal and heavy water (Sullivan *et al.*, 2001; Botti *et al.*, 2003). These data showed structural changes in the hydration shell of the solute, compared to ambient conditions, in agreement with previous MD simulations on mixtures of rare gases and extended simple point charge (SPC/E) water (Guillot and Guissani, 1993; De Grandis *et al.*, 2003). In the presence of a nonpolar solute, reorganization of the water solvent is observed (Guillot and Guissani, 1993; Botti *et al.*, 2003; De Grandis *et al.*, 2003) around the hydrophobic solute molecules. The ordering of water causes a decrease of entropy in competition with the enthalpic term, which favors solvation. The nonpolar molecules in the solution tend to aggregate to reduce the local order of the water molecules. The balance between the entropic and the enthalpic terms determines the phenomenon of hydrophobic hydration (Guillot and Guissani, 1993; Ben-Naim, 1989). The variety of nonpolar solutes and lack of experimental data at high temperatures and solute concentrations leads to different interpretations of the nature of hydrophobic effect, and as a consequence absence of one commonly accepted picture of hydrophobic interaction.

1.2.2 Polarization properties

Arguably, electrostatic interactions are the most important contribution to intermolecular interactions in water. The properties of water are most commonly obtained using fixed-point charge models (Botti *et al.*, 2003; Shvab and Sadus, 2012b). Typical examples are the SPC/E (Berendsen *et al.*, 1987) and TIP4P (Jorgensen *et al.*, 1983) models. The parameters for such potentials are optimized to reproduce the properties of liquid water at ambient conditions, i.e., a temperature of 298 K and a density of 1 g/cm^3. The dipole moment of an isolated water molecule is 1.85 D. However, in condensed phases, the electrostatic field from the other molecules reorganizes the charge distribution. The average total dipole moment of ice Ih from self-consistent induction calculations is 3.09 D (Batista *et al.*, 1998). In the fluid phase, the dipole moment must have intermediate values between those in the gas and the ice. Therefore, it is not sufficient to describe the

properties of water over a wide range of physical states using this kind of fixed-charge potential model. Instead, a realistic model should include the polarization effect of the molecule to describe the intermolecular interaction in the sub- and supercritical states. *Ab initio* quantum mechanical methods are one of the best methods to account for the state dependence of intermolecular interactions (Car and Parrinello, 1985). *Ab initio* approach, unlike empirical methods, are based on density function theory and compute ground-state electronic properties and density of electronic states. A significant advantage of using *ab initio* methods is the ability to study reactions that involve breaking or formation of covalent bonds, which correspond to multiple electronic states. Kang *et al.* (2011) and Dyer and Cummings (2006) reported a first principle study of sub- and supercritical water. These workers calculated the structure factors and polarization distribution in water. However, the method used is computationally expensive and involves a very small number of particles (32 - 64 molecules). We need simpler models to investigate the properties of water over a wide range of thermodynamic states. A natural improvement of the empirical potential models is to explicitly introduce nonadditive many-body interactions such as three-body and polarizable contributions.

Aqueous mixtures are of considerable interest in geochemistry and chemical technology (development of undersea deposits of gas hydrates), industrial technology (electric power generation, extraction process, decontamination), and biochemistry (protein folding, micellization). The influence of nonpolar solutes on the polarization properties of water has significant interest for chemical and energy industry. As was shown by Pascheck (2004) and Dyer *et al.* (2008) polarizability has significant impact on solubility of inert solutes in water. By using different polarizable potentials and modified Lorentz-Berthelot rules these authors achieved improved agreement between experimental solubilities and simulations. Despite the importance of aqueous solutions, the polarization properties of subcritical and critical water in the presence of nonpolar solutes have not been determined experimentally. Polarizable potentials were used in the molecular simulation studies of Cristofori *et al.* (2005) and Dyer *et al.* (2008) and references therein. However, these studies were devoted mainly to the question of the solubility of nonpolar solutes in water at very low concentrations. The data about polarization properties like dielectric constant or dipole moment of aqueous nonpolar solute mixtures in the single liquid phase and at high solute concentration is very scarce.

1.2.3 Thermodynamic properties

Typically only a few properties can be observed directly from a single molecular simulations (Lustig, 2011; Li and Johnson, 1992). A variety of thermodynamic properties show strong bias towards certain statistical ensembles (Lustig, 2011). For example, quantities,

such as the isobaric heat capacity, thermal expansion coefficient, thermodynamic speed of sound, etc. originating from differentiation with respect to temperature at constant pressure are most likely considered to be candidates for the isothermal-isobaric NpT ensemble (p denotes pressure) (Pi *et al.*, (2009); Abascal and Vega, 2005). The canonical NVT ensemble (V denotes volume) is often used to calculate isochoric heat capacity C_v (Lustig. 2011), and Joule-Thomson coefficient μ_{JT} is often calculated (Kioupis and Maginn, (2002) in the isobaric-isenthalpic (NpH) ensemble (H denotes enthalpy). The underlying reason is perhaps that the properties which involve constant pressure p, constant entropy S and constant enthalpy H appear to be foreign to the most popular NVT ensemble. However, for molecular simulation calculations it is both inconvenient and time consuming to switch between different ensembles to obtain the desired structures, fluctuations, and response functions. Therefore, it is necessary to develop special simulation techniques for particular thermodynamic quantities within particular ensembles.

Such techniques have been developed in a series of works by Lustig (1994abc, 1998, 2011, 2012), using unified statistical mechanical approach. Lustig (2011, 2012) showed that, in principle, it is possible to calculate all thermodynamic state variables from key derivatives obtained directly from either molecular dynamics or Monte Carlo simulations from any statistical mechanical ensemble. Such a method was developed first for the extended $NVE\mathbf{P}$ ensemble (Cağin and Ray, 2008), where the total momentum of the system $\mathbf{P}$ and an additional quantity $\mathbf{G}$ which is related to the initial position of the centre of mass are constants of motion. The method was later extended for the systems of rigid polyatomic molecules (Meier and Kabelac, 2006), and recently successfully tested for bulk water (Yigzawe, Sadus, 2013). It is well known, that whatever thermodynamic property can be measured in one statistical mechanical ensemble (Lustig, 2011), can also be measured in any other proper statistical mechanical ensemble, at least in thermodynamic limit (Blundel and Blundel, 2009). This is a direct consequence of the physical equivalence of various forms of the thermodynamic fundamental equation, i.e. entropy $S = S(N, V, A)$, Helmholtz free energy $A = A(N, V, T)$, Gibbs free energy $G = G(N, p, T)$ or others. In other words, for a request for any thermodynamic property from molecular simulation, the underlying statistical mechanical ensemble is irrelevant in principle. Lustig (1994abc, 2010, 2012) showed that, in principle, it is possible to calculate all thermodynamic state variables from key derivatives obtained directly from either molecular dynamics or Monte Carlo simulations from any statistical mechanical ensemble. The method applicable for NVT ensemble is based on the Massieu-Planck system of thermodynamics (Lustig, 2010) and proceeds from the entropy form of the fundamental equation $S(N, V, E)$ and devises different forms, such as the Helmholtz energy $A/T = A(N, V, 1/T)$ and others through successive Legendre transformation (Münster, 1970). As a consequence, any

thermodynamic property can be obtained from some combination of partial derivatives of the function $A(N, V, 1/T)$.

Recently, Yigzawe and Sadus (2013) used Lustig's method for the microcanonical ensemble to predict the thermodynamic properties of water over a wider range of temperatures using the Matsuoka-Clementi-Yoshimine non-additive (MCYna) potential (Li *et al.*, 2007), which combines an ab initio two-body potential with an explicit evaluation of induction forces. Comparison with theory indicated very good agreement with experiment in many cases demonstrating the importance of poloarization on thermodynamic properties. Nonetheless, from a practical perspective it is desirable to used simple intermolecular potentials such as either the SPC/E (Berendsen *et al.*, 1987) or TIP4/2005 (Abascal and Vega, 2005) because they are computationally easy to handle and included in many software packages. The question that was left unanswered by previous work is can such simple intermolecular potentials also provide good predictions of thermodynamic properties?

A review of the literature also shows some fundamental challenges in understanding properties of water and aqueous solutions. As was mentioned above, there is a large number of water models none of which can reproduce all water properties satisfactory. The inclusion of solutes makes the situation even more challenging because each solute interacts in own way with water. Even for the large group of nonpolar solutes like methane, neon, argon, krypton, xenon, etc., all of which interact in similar fashion with water (hydrophobic interaction) there is no general theory or even universally recognized mechanism of hydrophobic interaction (Ben-Naim, 2006; Chandler, 2005).

Phase conditions of binary solutions of water with noble gases and methane were extensively investigated experimentally in the series of works of Franck and coworkers (Wu *et al.*, 1990; Franck *et al.*, 1974; Japas and Franck, 1985; Uematsu *et al.*, 1980; Shmonov *et al.*, 1993). However, our knowledge about thermodynamic properties of the same binary mixtures has seriously lagged behind. Experimental measurements of thermodynamic properties were largely done for aqueous solutions of alcohols and hydrocarbons (Abdulagatov *et al.*, 2005; Kuroki *et al.*, 2001; Kitajima *et al.*, 2003; Fujita *et al.*, 2008). While heat capacity changes in aqueous solutions of methane and noble gases did attract some attention from the simulation community (Sharp and Madan, 1997), information about solvation changes of isothermal compressibility, thermal expansion coefficient, Joule-Thomson coefficient or speed of sound for these substances is virtually nonexistent.

1.2.4 Transports properties

Transport properties of water such as self-diffusion coefficient and viscosity at temperatures up to 498.2 K are well known (Krynicki *et al.*, 1978; Haynes *et al.*, 2013). However, theoretical calculations and simulations of transport properties were of limited success. Theories like hydrodynamic theory (Einstein, 1905), activated state theory (Eyring, 1935), free-volume theory (Batchinsky, 1913), kinetic theory (Chapman and Cowling, 1970), etc. have their own areas of applicability and limitations. Molecular dynamic simulations of water self-diffusion constant were also of varying success. Water models like SPC, SPC/E, TIP3P, TIP4P-Ew, and TIP4P/2005 (Rozmanov and Kusalik, 2012), probably yield the best agreement with experiment at ambient and near ambient conditions. However, at temperatures above the normal boiling temperature almost all molecular simulation results start to underestimate experimental diffusion coefficients (Bourg and Sposito, 2007, 2008; Raabe and Sadus, 2012; Levitt *et al.*, 1997). This underestimation (Levitt *et al.*, 1997) could be partially attributed to incomplete experimental data for water self-diffusion constant. To the best of our knowledge, there is no experimental data on self-diffusion constant at temperatures above 550 K and pressures above 200 MPa. Svischew and Kusalik (1994) performed a comparative simulation study of dynamics in liquid SPC/E water and its isotopes D_2O and T_2O at 25°C. Their simulation results clearly shows smaller diffusion constants of heavy water comparing to light water. Svischew and Kusalik showed that the Y-component of the self-diffusion coefficient $D = (D_x, D_y, D_y)$ is larger than their respective X and Z components by almost a factor of 2. This means, that among the many possible routes for local translational diffusion the out-of-plane diffusive motion of H_20, D_20, and T_20 molecules is preferred (Svischew and Kusalik, 1994). In contrast to this, velocity autocorrelation functions of different isotopes of water are almost identical.

Despite their great importance in low-temperature geochemistry, diffusion coefficients (D) of noble gas isotopes in liquid water have been measured only for the major isotopes of helium, neon, krypton and xenon (Jähne *et al.*, 1987). Data on the diffusion coefficients of minor noble gas isotopes are essentially non-existent and so typically have been estimated by a kinetic-theory model in which D varies as the inverse square root of the isotopic mass (m): $D \propto m^{-0.5}$ (Bourg and Sposito, 2007, 2008). Molecular dynamics simulation studies available in the literature are performed mostly for either very dilute aqueous nonpolar solute mixtures at ambient conditions or for mixtures of water and highly soluble solutes like alcohols (Guevara-Carrion *et al.*, 2011) or ionic substances (Bouazizi and Nasr, 2011; Koneshan *et al.*, 1998).

Numerous experiments and simulations show that the dynamic of water in solutions differ significantly from those of pure water (Guevara-Carrion *et al.*, 2011; Bouazizi and Nasr,

2011; Koneshan *et al.*, 1998). Moreover, velocity autocorrelation functions of nonpolar solutes and ionic components in water differ significantly, which indicates different nature of organization of hydration shells around polar and nonpolar solutes.

1.3 Outline of the thesis

In Chapter 2, the general scheme of modern Molecular Dynamics is shown, and the basic technical aspects of intermolecular interactions calculations are explained. The potential models adopted in this work for the study of water and aqueous nonpolar solute mixtures are described in great detail.

The description of method of statistical averages developed in a series of works of Lustig (1994, 1998, 2011, 2012) for molecular dynamic canonical ensemble is given in Chapter 3. The calculation of the thermodynamics quantities using Lustig's formalism and the classical fluctuation formulas is described.

Chapter 4 will present a systematic picture of structural changes in bulk water and water-neon, -argon, -methane, -krypton, and -xenon mixtures in the temperature interval from 278 K till 750 K at constant density 1 g/cm^3. The evolution of oxygen-hydrogen, oxygen-oxygen and oxygen-solute particle coordinate numbers for both pure water and mixtures will be thoroughly explained. The formation of solvation shells around solute particles, their dependence from the solute particles size is discussed. Solute-oxygen, oxygen-oxygen, and oxygen-hydrogen 1st order coordination numbers as a function of temperature and solute concentration are analyzed.

Chapter 5 will be devoted to study of polarization properties of water at densities 1, 0.8, and 0.6 g/cm^3, and several aqueous nonpolar solute mixtures. Dielectric constant, dipole moment distribution and the average dipole moment of pure water and mixtures are calculated in this chapter. The dependence of dielectric constant and dipole moment from temperature and solute concentration will be shown in great detail.

In Chapter 6 we will calculate basic thermodynamic properties of aqueous nonpolar mixtures, like isochoric and isobaric heat capacities, isothermal and isentropic pressure coefficients, thermal pressure and thermal expansion coefficients, Joule-Thompson coefficient, and the speed of sound. A novel analytical technique of statistical averages obtained from canonical ensemble will be applied here. Important changes in the values of all thermodynamic properties induced by nonpolar solutes will be discussed in detail.

Chapter 7 will present some transport properties of aqueous solutions of Ne, Ar, Kr, Xe, and CH_4, like diffusion coefficients and velocity autocorrelation functions. A thorough

comparison of diffusion coefficients of aqueous nonpolar mixtures at solute concentrations up to 15% with pure water is also shown in this chapter.

Finally, the conclusions and recommendations for future work will be made in Chapter 8.

Chapter 2

Molecular Dynamic Simulation

Molecular simulation is a generic term which encompasses a variety molecular modelling techniques, such as *ab initio*, Monte Carlo (MC), and molecular dynamics (MD) computing methods. Unlike approximate solutions, molecular dynamics was first developed to obtain exact results for statistical mechanical problems (Alder and Wainwright, 1957). Molecular simulation is a powerful computational technique, based on rigorous statistical mechanics principles, which can assist us in determining macroscopic properties of virtually any atomic or molecular system. By using approximate theoretical model of molecular interaction, these properties can be calculated through a appropriate computer program.

The Monte-Carlo (MC) method was the first non-quantum calculation method applied to a system with large number of particles (Frenkel and Smit, 2001). The modern MC method utilizes random motion of molecules, adjusted according to probability distribution principle of statistical mechanics. Specific probability criteria, based on physical considerations, are used to accept or reject the change in the system. By running multiple trial runs on a computer (called simulations), different trial configurations are being generated. After the last simulation run, thermodynamics properties are calculated as ensemble averages. The first application of Monte Carlo method for molecular simulation of liquid was performed by Metropolis *et al.* in 1953 on the MANIAC computer at Los Alamos.

The molecular dynamics (MD) method was introduced by Alder and Wainwright in 1958. Not long after that, driven by of fast development of computer technique, molecular dynamics became the most popular simulation method, especially in material science, biochemistry, and biophysics. In this work we use MD technique to investigate properties of aqueous nonpolar solute mixtures. A working definition of MD simulation is technique by which one generates the atomic trajectories of a system of N particles by numerical

integration of Newton's equation of motion, for a specific interatomic potential, with certain initial and boundary conditions. The general idea behind MD is the ergodicity principle that states that if a system of particles evolve in time literally infinitely, that system will eventually pass through all possible configurations (atomic or molecular states) (Ahmed, 2010). In mathematical terms, an average of over time is equivalent to an average over space of all system's states as it is shown on Eq. (2.1).

$$\langle A \rangle_{time} = \lim_{\tau \to \infty} \frac{1}{\tau} \int_{t=0}^{\tau} A\left(\mathbf{p}^N(t)\mathbf{q}^N(t)\right) dt \approx \frac{1}{N_\tau} \sum_{t=1}^{N_\tau} A\left(\mathbf{p}^N \mathbf{q}^N\right), \tag{2.1}$$

where A is any measurable physical quantity, τ is the simulation time, N_τ is the number of time steps in the simulation, and $A\left(\mathbf{p}^N(t)\mathbf{q}^N(t)\right)$ is the instantaneous value of A at time t when $\mathbf{p}^N$ and $\mathbf{q}^N$ are the generalized coordinates and momenta, respectively. The right-hand side part of the Eq. (2.1) is called ensemble average and is used for practical calculations in molecular dynamic simulations. Almost all properties calculated during the simulation run are obtained as an ensemble or time averages. Ensemble averages are directly related to the calculation of different thermodynamic properties with the help of the so-called fluctuation formulas, and will be described in more details in Chapter 3. The dynamics of the particles is governed by the interparticle instantaneous forces available as the gradient of a potential energy function. The numerical values of position and momenta of all particles can be calculated from either Lagrangian or Hamiltonian classical mechanics formalisms (see the subsection 2.3.2).

The MD technique has acquired significant popularity in the recent decades, due to its simplicity and increased computational resources. A clear physical basis, relatively simple empirical potentials, and high accuracy of MD calculations, are only one of the few advantages over other methods. The most important virtue of MD is the ability to generate system's dynamics and statistics at the same time. Molecular dynamics differs from Monte Carlo mainly in two aspects. First, as the name implies, molecular dynamics is mostly used to obtain the dynamics properties of the system although attempts have been made to develop dynamic Monte Carlo also (Fichthorn and Weinberg, 1991). Second, unlike conventional MC simulations, MD is completely deterministic and chance plays no role. The other important distinction is that MD uses intermolecular forces to evolve the system whereas MC simulation involves primarily the calculation of changes in intermolecular energy. Molecular dynamic technique with Newtonian formalism is used in this work.

2.1 Water-water interaction

Water is the main component of any aqueous solution, therefore, deep knowledge of all aspects of water-water interaction is of paramount importance not only for pure water but for mixtures also. In this Chapter we will discuss the various ways two water molecules can interact (water-water interaction) as well as interaction between water molecule and molecules or atoms of solute (water-solute interaction). As we shall see in the following sections, knowledge of these interactions is essential to our understanding of the properties of liquid water and aqueous solutions. We will start our investigation by examining different models of liquid water and review the progress in the development of water potentials from the SPC model (Berendsen *et al.*, 1981) to the most recent six site model (Nada and Erden, 2003). We will also highlight the strength and weakness of various water models, discuss their ability to predict structural, physical, thermodynamic, and transport properties, and the role of both polarizable and flexible water models. We will pay special attention to the SPC/E (Berendsen *et al.*, 1987), SPC/Fw (Wu *et al.*, 2006), TIP4P/2005 (Abascal and Vega, 2005), and MCYna (Matsuoka *et al.*, 1976; Li *et al.*, 2007) models which are used in this work. A systematic comparison of polarizable MCYna and nonpolarizable SPC/E, SPC/Fw, and TIP4P/2005 water models, and their abilities to predict water properties will be performed. Finally we will point out the weakness of water models and discuss the ways for future improvements.

2.1.1 Water molecule

In order to better understand all possible ways water molecules interact with each other in gaseous, liquid, and solid phases, first we have to familiarize ourselves with the geometry and properties of a single water molecule. Despite the somewhat idealized notation "single water molecule", it can only be considered as an isolated in the gaseous phase due to large average intermolecular distances. In reality water has a structure in which multiple entities are combined via hydrogen bonding. In short, water molecule consists of two hydrogen atoms (H) covalently bonded with the oxygen (O) atom. The electron charge density is shifted towards oxygen atom, thus making hydrogen atoms slightly positive and the oxygen atom negative (Chaplin, 2013). In order to keep water molecule electrically neutral, the charge δ^- located around oxygen atom is chosen to be equal to the sum of two hydrogen atom charges δ^+, but with opposite sign. The average length of the O-H covalent bond in the ground state is $0.9572 \sim 1$ Å, and the average angle ϕ between these covalent bonds is between 104.52 and 113.24°. Water molecules being polar and chemically active always form chemical bonds with other water molecules. The schematic representation of water molecule is given in Figure 2.1.

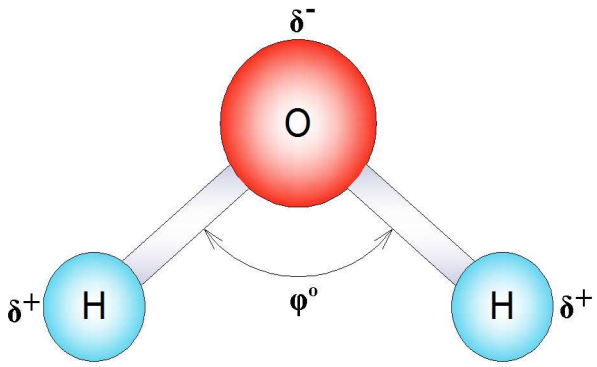

FIGURE 2.1: Simple representation of water molecule.

The structure of water is one of the 125 problems selected by Science magazine to be the most important question confronting researchers now and in the future (Kennedy, Norman, 2005). Guillot in his review from 2002, found 46 distinct computer water models. Such a number of different water models seems embarassing and only substantiates our lack of knowledge about water interaction. Creating a single model of water-water interaction is deemed to be an unfeasible task, which directs research efforts into the narrower areas (water at ambient conditions, ice near 0°C, basic thermodynamic properties at 25°C, etc.) where more success can be achieved. The challenges on the way to a comprehensive molecular theory for water are formidable. Water exhibits a number of unusual properties such as density maximum and isothermal compressibility minimum at normal conditions, volume contraction under melting conditions, at least 15 crystalline polymorphs, and a high dielectric constant. Water is the most abundant substance in nature and knowledge of its thermodynamic and electrostatic properties is very important to understanding phenomena in fields such as protein crystallization and folding, biological membranes, electrolyte solutions, detergency, and metal extraction. In some cases these properties must be known to the utmost precision, requiring robust experimental techniques, theoretical studies, and molecular simulations. The availability of structural data of water from neutron scattering and x-ray diffraction at ambient and supercritical conditions (Soper, 2000; Botti *et al.*, 2003; Ikeda *et al.*, 2010) contributed to the search of a better water model.

In condensed phases water molecules are always connected with other molecules, forming either water clusters via chemical bonds with other molecules, or coordination compounds with inert gases. Figure 2.2 represents the simplest case of two water molecules (water dimer) bonded via so called hydrogen bond (H-bond). A hydrogen bond is the electromagnetic attractive interaction between polar molecules in which hydrogen is bound to a highly electronegative atom such as oxygen. The average ground state distance between hydrogen and oxygen atoms of two H-bonded water molecules depends

from the bond strength, temperature, and pressure. The typical experimentally observed length is 1.97 Å (Legon and Millen, 1987), however, most of water models use a larger length. The angle θ between the covalent O-H bond and the hydrogen O...H bond has range 6 - 20° depending from water model (Chaplin *et al.*, 2013). According to several simulation studies, the strength of the water-water H-bond in the ground state is approximately -10 kJ/mol (Swiatla-Wojcik *et al.*, 2008, Kalinichev and Bass, 1994).

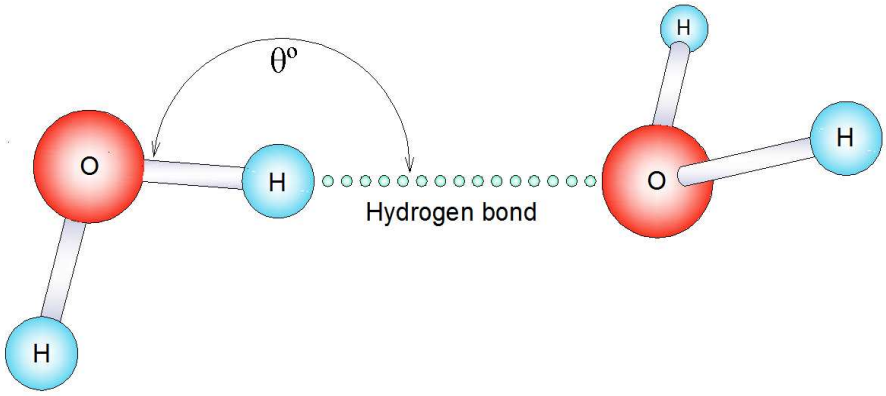

FIGURE 2.2: Schematic representation of the water dimer.

The water dimer is the simplest configuration from many possible water clusters. Many simulation and experimental studies suggest existence of much more complexe spatial water clusters with number of water molecules from 2 to as many as 300 (Chaplin, 2013). However, the most fundamental and property-defining water cluster is water tetrahedron shown on Fig. (2.3). Numerous physical anomalies of water, such as negative temperature dependence of the volume, the large negative entropy of solvation of inert solute, temperature dependence of density near freezing temperature, temperature dependence of isothermal compressibility, high boiling temperature and the large number of phases of ice, have been attributed to its tetrahedral shape (Eisenberg and Kauzmann, 1969). Molecules which have four electron groups around their central atom, such as ammonia (NH_3), methane (CH_4), and water (H_2O) have a tetrahedral shape (shown in Figure 2.3) with a bond angle of about 109.5° (Ben-Naim, 2009). The ammonia molecule has three bond groups and one lone pair, and the water molecules have two bond groups and two lone pairs. In a tetrahedral molecular geometry a central atom is located at the center with four substituents that are located at the corners of a tetrahedron. In a tetrahedral configuration the positively charged end of the molecule is more orientationally constrained than in the negative lone-pair region, allowing both trigonal and tetrahedral local structures and enabling hydrogen bonding. The bond angles are $\cos^{-1}(-1/3) \approx 109.5°$ when all four substituents are the same, as in H_2O

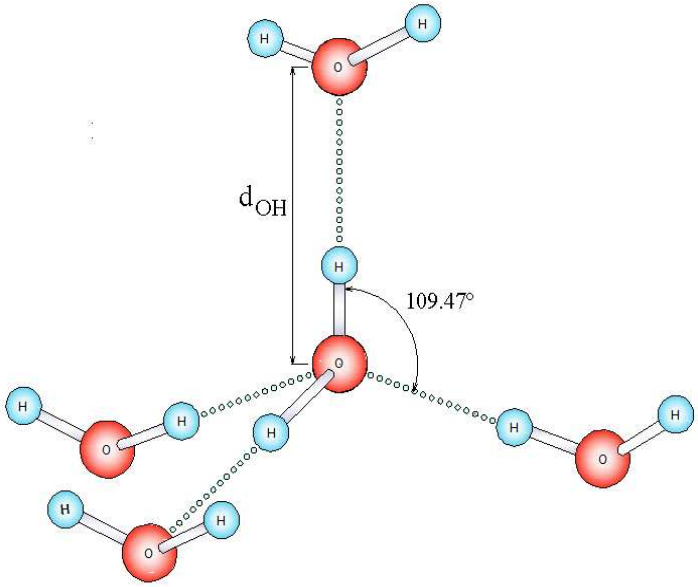

FIGURE 2.3: Schematic representation of the tetrahedral shape of water.

Formation of all these water clusters is possible due to specific charge distribution in water molecule. Water has one slightly negative end around oxygen atom and two slightly positive ends around hydrogen atoms. It can interact with itself and form a highly organized inter-molecular hydrogen-bond network (H-bond network). The positive hydrogen end of one molecule interact favorably with the negative lone pair of another water molecule, which in turn form the same H-bond with other molecule and so on. The result is an extensive network of hydrogen bonds like in the Figure 2.4. The H-bond network is the most extensive at ambient conditions (25°C and 0.1 MPa) when water molecules can form up to four hydrogen bonds. As the temperature and pressure increase, the average number of H-bonds per water molecule decreases (Shvab and Sadus, 2012a; Kalinichev and Bass, 1994).

The intermolecular potential function, which captures the correct and sufficient physical features for the system of interest, is imperative for a successful molecular simulation of water and aqueous solutions (Yigzawe and Sadus, 2013; Vega and Abascal, 2011). The general chemical and geometrical features of water molecule have been known for a long time due to developments in x-ray and neutron diffraction techniques (Eisenberg and Kauzmann, 1969; Soper, 2000). However, due to very complicate quantum-mechanical, potential function of water-water or water-solute interactions in the analytical form is not known. The different behavior of water in solid, liquid, and gaseous phase only contributes to the overall complexity. The key to understanding anomalous properties of water in different phases is to have a model which reflects its true nature, i.e., a model which account for intramolecular degrees of freedom, electric interaction with neighboring molecules, charge redistribution, manibody effects, etc. Inclusion of all the above

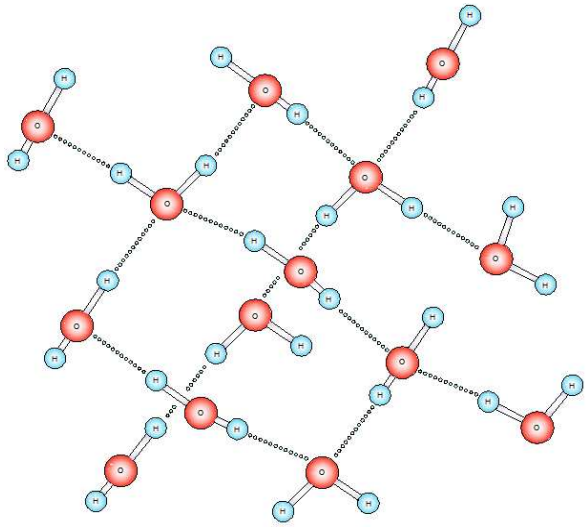

FIGURE 2.4: Hydrogen bond network in water.

mentioned characteristics into a computer model would be analytically unwieldy and computationally expensive. The only viable solution for molecular simulations is to use simplified models of water, models which capture the basic chemical and physical properties of water (Guillot, 2002). Many water models were built since the pioneering Bernall and Fowler model (1933). Models with different number of charged sites, geometries, and potential interactions work well in some areas and fail in other (Vega and Abascal, 2011). The main reason for having all these different models is the inability of a single model to describe all water properties, which are results of either its high degree of H-bonding and strong intermolecular interaction or its tetrahedral shape.

First principle or *ab initio* approach is a very promising tool for better understanding of underlying principles water-water interaction. Based on DFT formalism, *ab initio* models are built taking into account ground-state electronic properties and density of electronic states (Car and Parrinello, 1985; Guillot and Guissani, 2001). Such potentials are very computationally expensive and difficult to modify according to the users needs. All *ab initio* models use limited number of basis sets and the approximation on the theory, which sometimes reflects on the accuracy of the results (Matsuoka *et al.*, 1976; Lie and Clementi, 1986). The complicated picture of water-water interaction (water clusters) is a direct consequence of manybody interaction between water molecules. Therefore, any model expected to predict properties of liquid water correctly must be either non-pairadditive or it must use an effective pair potential that includes nonadditive effects implicitly (Berendsen *et al.* 1987; Vega and Abascal, 2011). As was speculated in many investigations (Yigzawe and Sadus, 2013; Vega and Abascal, 2011), arguably the main reason that pair-additive potentials cannot reproduce condensed-state properties of water is that such potentials neglect the higher-order interactions like polarization,

three- and four-body interactions, and intramolecular degrees of freedom. In water and in other polar liquids there is a considerable average polarization, leading to a cooperative strengthening of intermolecular bonding. Because of this, effective pair potentials were designed to have larger dipole moments than water molecules in vapor have and produce second virial coefficients larger than the experimental ones (Berendsen *et al.*, 1987).

2.1.2 Water models, criteria

Molecular dynamics and Monte Carlo simulations of any molecular system depend critically on the availability of potential models that provide an accurate representation of the system. In case of many body system like water, the model should be computationally economical, physically justifiable, and estimate most of the experimental properties of the real water over the wide range of state points (Guillot and Guissani, 2001; Baranyai and Kiss, 2010; Kisss and Baranyai, 2009). The accuracy of the model can be tested by comparing simulation results with experimental data as the nature of the theoretical model used solely determined the results of a molecular simulation. The discrepancies between accurate experimental measurements and molecular simulation data can be unambiguously caused by the failure of a particular model to present molecular behavior.

The main differences between various water models can be groupped into the following four cases (Yigzawe, 2012).

1. Parametrization values. Different models use different target quantities for parametrization depending on the availability of experimental data and the area of model applicability.

2. The charge distribution and the position of interaction sites. Different water models locate negative charge at different positions with respect to the position of oxygen atom. As a consequence there are three-, four-, five-, and six-site water models.

3. Internal degrees of freedom. While most of the water models do not account for internal degrees of freedom, some models do have flexible geometry, i.e. account for O-H covalent bond stretching and O-H-O angle bending.

4. Non-additive interaction terms. Few water models account for nonadditive interaction like polarization, charge redistribution, three-body and higher order interaction, etc. Inclusion of all these additional interactions significantly increases computational load. Except from this, adequate experimental data on these kind of interactions is still very incomplete.

Comprehensive reviews of water models from the three-site SPC model (Berendsen *et al.*, 1981) to the recent six-site model (Nada *et al.*, 2003) indicate that they are in a very good agreement with experiment at least for the values at which they are parametrized, but there is no one single water model capable of describing its properties in different phases (Vega and Abascal, 2011, Wu *et al.*, 2006). Continuing efforts are being made on improving existing water models and developing new ones. For example, the SPC/E model (Berendsen *et al.*, 1987) using the polarization correction gives improved values for diffusion coefficient and radial distribution function, which emphasizes the need to have a polarization term. Dang (1992), Li *et al.* (2007), Kiss and Baranyai (2013) and many other researchers found that introduction of polarization results in good predictions of radial distribution function (RDF), dielectric constant and dipole moments. Moreover, Svishchev *et al.* (1994) asserted that accounting for polarisation interaction is crucial for the correct estimation of static and dynamic properties of liquid water from supercooled to near-critical conditions. Polarisation intercation is one of the many possible forms of nonadditive interactions.

Three-, four-body and higher order interactions are other important forms of interactions which attract attention of scientific community. Investigations of Li *et al.* (2007) and Ahlstrom *et al.* (1989) show that up to 10% of the total intermolecular interaction energy in a water trimer may arise from three-body interaction. Different studies deviate in estimation of the contribution polarization interaction makes into the total energy of water interaction. For example, Chialvo and Cummings (1996, 1998) showed that the polarization energy contributes from 40 to 57% to the total configuration internal energy of water. A more recent MD simulation of Li *et al.* (2007) indicates the energy contribution from the polarizable term to be approximately 30%. While the importance of polarization ineraction for polar liquids is evident, its role in aqueous solutions of nonpolar solutes is not so clear. Some researchers try to account for electronic polarizability of nonpolar solutes like methane or big nonpolar atoms like xenon or krypton. Dyer *et al.* (2008) and Pascheck (2004a, 2004b) reported that the use of an explicitly polarizable solute improves agreement between experiment and simulation of the solubility of simple nonpolar solutes in water. In nonpolarisable water models the polarization effect is usually ignored completely or, in the best case, incorporated as an effective dipole moment (Rahman and Stillinger, 1971; Stillinger and Rahman, 1972). Using suitably chosen effective moments, the later approach may yield a good approximation to the correct poperties of water in thermodynamic equilibrium.

The main source of differencies of existing water models is the charge distribution around oxygen atom. Based on the charge distribution, upon which some of the water models are named after, all water models can be assigned to three broad groups. Models with fixed geometry or in other words with fixed positions of charged sites are called rigid models.

There are three-, four-, five- and six-site models where each site is occupied by either the charge of hydrogen, oxygen atom and/or the Lennard-Jones interaction site. Apart from the number of charged sites one can also consider internal degrees of freedom and their contribution to total interaction potential. Consequently flexible models make the second group of water models which slightly change their overall geometry depending from surrounding situation. The third large group of water models contains models with variable charges or dipole moments. These are polarizable models with dipole moments induced by the simultaneous electric field of neighboring water molecules or charges which fluctuate also in response to local conditions. In what follows we will describe the potentials, target properties, values used for parametrization, and briefly examine failure and success of selected models from each group.

Schematic representations of three-, four-, five-, and six-site water models are given in the Figure 2.5. θ is the H-O-H bond angle, φ is the angle between the negative charge and hydrogen atom, or between two lone-pairs, l_1 is the O-H covalent bond length, l_2 and l_3 are the distances between lone-pair/dummy charge and oxygen atom center of mass (Chaplin, 2013). q_1 is the positive charge situated on H-atom and q_2 and q_3 are the negative charges prtaining to lone-pair or dummy charge. We will examine different water models which will represent the majority of the models developed so far. Our review will be focusing mainly on results at ambient conditions (25°C and 0.1 MPa). In this study we used several water models in order to crosscheck and compare their results, compare with experimental data, and establish the optimal model suitable for the purposes or this work. The water models employed in this work are: SPC/E (rigid three-site model), SPC/Fw(flexible three-site model), TIP4P/2005 (rigid four-site model), and MCYna (polarizable four-site model).

2.1.3 Rigid water models

Surprisingly, despite the complex nature of water molecule and essentially quantum origin of covalent and hydrogen bonds inside water complexes, most successful water models so far are rigid models. We will consider success and failures of the most prominent rigid models such as TIP3P, SPC, SPC/E, TIP4P/2005, MCY, TIP5P, and NvDe.

2.1.3.1 SPC

The simple point charge (SPC) model is one of the first water models which serves as a progenitor of a whole SPC-family of water models. This three-site model was proposed by Berendsen *et al.* in 1981. The model averages many-body interaction (included in the

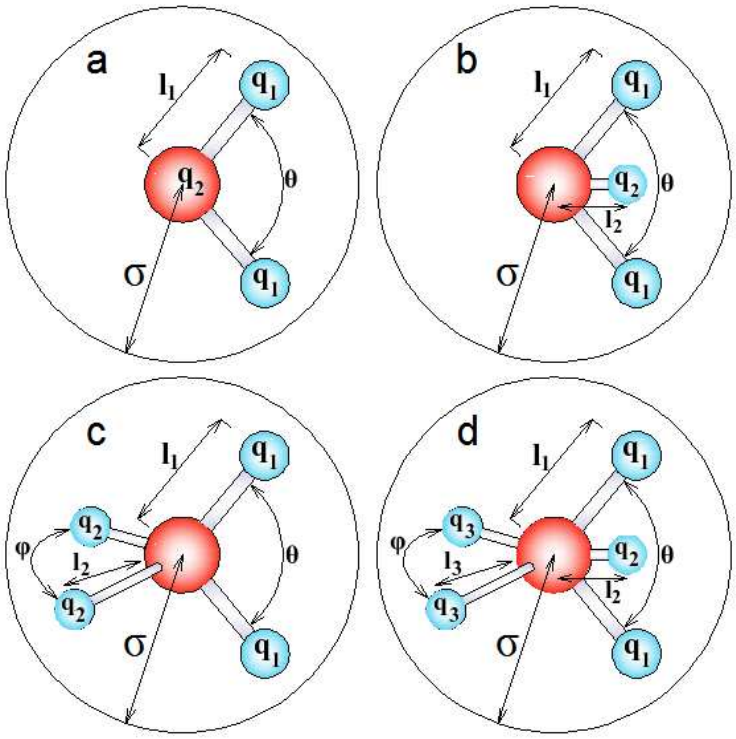

FIGURE 2.5: Schematic representation of water models: a) three-site, b) four-site, c) five-site, and d) six-site water models.

effective potential), is computationally less expensive and easy to incorporate in protein-water potential. The intermolecular potential is a combination of Lennard-Jones term and electrostatic interaction.

$$u = 4\varepsilon \sum_i \sum_{j \neq i} \left[\left(\frac{\sigma}{r_{ij}^{oo}} \right)^{12} - \left(\frac{\sigma}{r_{ij}^{oo}} \right)^{6} \right] + \frac{e^2}{4\pi\varepsilon_0} \sum_i \sum_{j \neq i} \frac{q_i q_j}{r_{ij}}, \tag{2.2}$$

where r_{ij}^{oo} and r_{ij} are the distances between the oxygen sites and charged sites of two molecules respectively, e is the proton charge, ε_0 is the permittivity of vacuum. The intermolecular potential given by Eq. (2.2) is common for many other rigid pair-potentials. The model gives values of enthalpy of vaporisation 44,213 kJ/mol·K (44.0451), isobaric heat capacity 72.264 J/mol·K (75.312), and isothermal compressibility 0.461 1/Gpa (0.458) which are in good agreement with experiment (values in brackets) (Wu *et al.*, 2007). At the same time, dipole moment, viscosity, and temperature of maximum density (TMD) are much smaller than experimental data. Thermal expansion and thermal pressure coefficient are more than 3-times bigger from experimental data. Results of the charge concentration, and the widened O-H bond and H-O-H bond angle is that the bulk density at 25°C and 0.1 MPa is only 0.977 g/cm^3 (Narten and Levy, 1971). The SPC water molecule is able to move faster than it would in "real water" due to the missing

two lone electron pairs. Nevertheless, being one of the first water models, SPC served as a good starting point for the development of the further water models.

2.1.3.2 TIP3P

A transferable intermolecular potential three point (TIP3P) model was proposed by Jorgensen *et al.* in 1983. This three-site model has smaller O-H bond lenght and H-O-H angle than SPC model. The parameters of the model (the Lennard-Jones constants and the charge on the hydrogen atom) were obtained by reproducing the vaporization enthalpy and liquid density of water at ambient conditions. TIP3P gives too high self-diffusion and thermal expansion coefficients, and too small TMD and viscosity compared with experimental values. It also exhibits very low second peak on the O-O radial distribution function. However, as has been reported recently (Mao and Zhang, 2012), TIP3P water model provides a value of isochoric heat capacity at ambient condition with less than 1% error from the experimental value 74.77 kJ/mol·K. This model is still commonly used in biological molecules for its computational effciency. All of the protein, nucleic acid, lipid, carbohydrate, etc., parameters used in the CHARMM force field (Brooks *et al.*, 2009), have been developed with respect to the TIP3P model. Like the SPC model, the TIP3P served as a source for the large TIP-family of water models.

2.1.3.3 SPC/E

The extended simple point charge (SPC/E) model, is possibly the most popular water model. Proposed in 1987 by Berendsen *et al.* as an improvement of the previous SPC model, SPC/E model was, probably the first model to successfully reproduce general features of the water-ice phase diagram and give many water properties in reasonable agreement with experiment. It is rigid three-site model similar to SPC and TIP3P, with oxygen-hydrogen (O-H) distance 1 Å, H-O-H angle 109.47°, σ = 3.166 Å, ε = 0.65 kJ/mol, charge $+0.4238q$ located on H atoms, and charge -0.8427 located on O atom. The intermolecular potential is given by Eq. (2.2).

The failure of the original SPC model to predict correct energy, self-diffusion constant, radial distribution function etc., led to the inclusion of polarization correction and resulting reparametrization of the model constants. The correction term which was missing in older SPC model is given by (Berendsen *et al.*, 1987; Vega *et al.*, 2009)

$$E_{pol} = \frac{1}{2}\sum_i (\boldsymbol{\mu} - \boldsymbol{\mu}^0)^2/\alpha_i, \tag{2.3}$$

where $\boldsymbol{\mu}$ is the dipole moment of the molecule, $\boldsymbol{\mu}^0$ is the dipole moment of the isolated molecule and the α_i is the isotropic scalar polariazability of water molecule. The correction increased the atomic charges on hydrogen and oxygen site i.e., the values used for the charges of hydrogen and oxygen is slightly higher than the one used in SPC and TIP3P. SPC/E reproduces the vaporization enthalpy of real water when a polarization energy correction is included (Berendsen *et al.*, 1987). This model is capable of predicting challenging features such as the critical behavior, pair-correlation and dielectric constant reasonably well (Guillot, 2002). Among the drawbacks SPC/E water model are slightly high self-diffusion coefficient, specific heat capacity (Mao, Zhang, 2012), and too low temperature of maximum density (TMD). The TMD in SPC/E is -38°C (Baez and Clancy, 1994), which is far below the experimental value of +4°C. A detailed review by Vega and Abascal (2011) indicates that SPC/E alongside with the TIP4P/2005 (Abascal and Vega, 2005) are two the most successful rigid water models, based on good agreement of SPC/E predictions for water and ice at ambient and near ambient conditions. However, investigations presented in this work show that SPC/E model largely fails to correctly reproduce experimental thermodynamic properties in the extended temperature-pressure range, namely at critical and supercritical conditions.

Being the first successful water model, SPC/E serves as a benchmark for all MD simulations of water even today. Therefore, the SPC/E water model is one of the main water models used in this work.

2.1.3.4 TIP4P/2005

The TIP4P/2005 potential is arguably the best nonpolarizable and rigid model, capable of describing the different properties of water and ice in the wide pressure range (Abascal and Vega, 2005; Pi *et al.*, 2009). It is a four-site rigid water model derived from the earlier TIP4P model (Jorgensen *et al.*, 1983). TIP4P was reparametrized by Abascal and Vega (2005) with the intention of producing a general and computationally simple water model. The potential function is given by Eq. (2.2), but with different values of parameters σ, ε, and q_i. The TIP4P/2005 model has O-H distance 0.9572 Å, H-O-H angle 104.52°, σ = 3.1589 Å, ε = 0.7749 kJ/mol, and the charge $+0.5564q$ located on H atoms. A significant difference of TIP4P/2005 water model from SPC/E model is a charge of $-1.1128q$ which is not located on O atom but displaced by 0.1546 Å on a bisector between the H atoms. The target properties used for the parametrization of TIP4P/2005 model are temperature of maximum density, phase diagram, melting temperature of hexagonal ice and polarization correction. The model predicts a large number of properties in different phases such as phase diagram (Vega *et al.*, 2008), density and temperature of maximum density at +5°C. The model is also able to provide a good

description of the vapor-liquid equilibria (Vega *et al.*, 2006) and the surface tension (Vega and Miguel, 2007). However, this potential also have a number of shortcomings such as: a low temperature of maximum density (Vega and Abascal, 2005b), low static dielectric constant, dipole moment and self-diffusion constants. In some cases these discrepancies can be expected, as the TIP4P/2005 potential does not include molecular polarizability. This water model will be used in Chapter 6 to calculate thermodynamic properties of liquid water.

2.1.3.5 MCY (Matsuoka-Clementi-Yoshimine)

The MCY is a four-site water model developed by Matsuoka, Clementi and Yoshimine (1976) with the intention of obtaining a quantitative accurate description of pair potential function for two water molecules. The model is based on configuration interaction (CI) method of calculation of potential surface for water dimer. There is no parametrization in this model. The schematic representation of MCY model charge distribution is shown in Figure 2.6.

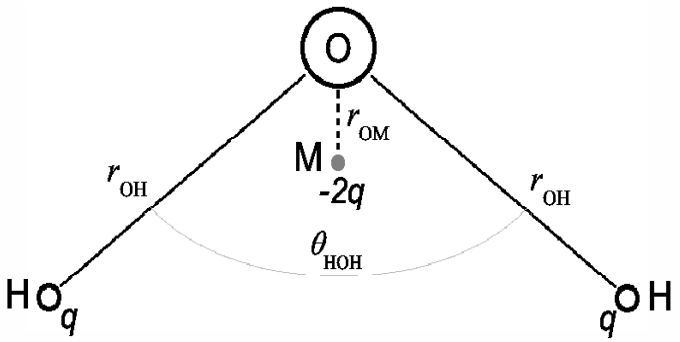

FIGURE 2.6: Structure of the MCYna water molecule.

Points H, O, and M represent the position of the hydrogen, oxygen, and dummy charge sites respectively. The potential used in the MCY water dimer interaction is

$$\begin{aligned} u_2 = {} & q^2 \cdot \left(\frac{1}{r_{13}} + \frac{1}{r_{14}} + \frac{1}{r_{23}} + \frac{1}{r_{24}}\right) + \frac{4q^2}{r_{78}} - 2q^2\left(\frac{1}{r_{18}} + \frac{1}{r_{28}} + \frac{1}{r_{37}} + \frac{1}{r_{47}}\right) + \\ & + a_1 e^{(-b_1 r_{56})} + a_2\left[e^{(-b_2 r_{13})} + e^{(-b_2 r_{14})} + e^{(-b_2 r_{23})} + e^{(-b_2 r_{24})}\right] + \\ & + a_3\left[e^{(-b_3 r_{16})} + e^{(-b_3 r_{26})} + e^{(-b_3 r_{35})} + e^{(-b_3 r_{45})}\right] - \\ & - a_4\left[e^{(-b_4 r_{16})} + e^{(-b_4 r_{26})} + e^{(-b_4 r_{35})} + e^{(-b_4 r_{45})}\right]. \end{aligned} \tag{2.4}$$

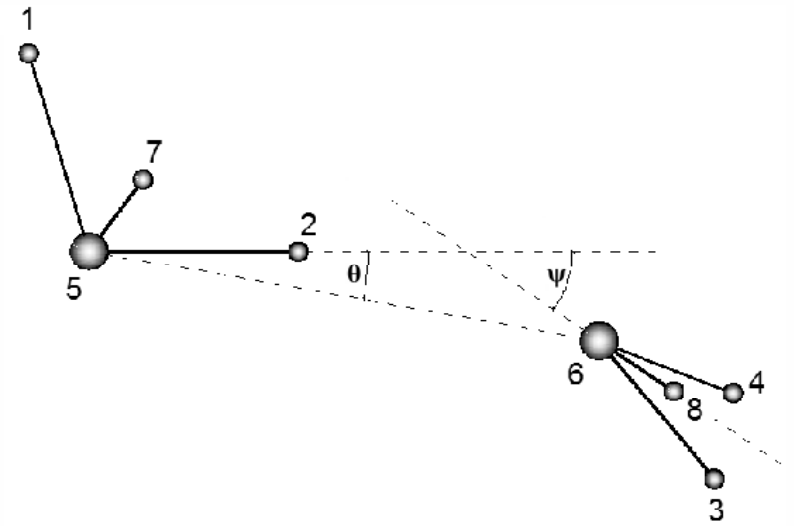

FIGURE 2.7: Definition of the MCY water dimer geometry identifying the intermolecular separations used in the two-body potential Eq. (2.4).

where q is a charge on hydrogen atom, r_{ij} is the distance between two sites i and j, and a_i and b_i are determined from the *ab inito* calculation. The values of a_i and b_i used in MCY model are given in Table 2.1.

The MCY underpredicts the first and second oxygen-oxygen peaks in radial distribution function, the energy and dielectric constant of the liquid is too small, and pressure is too high. Lie and Clementi (1986) argued that MCY potential is too repulsive, which only allow a computation of a small number of configurations that will be used for fitting and conclude that this compact configurations is the main reason for high pressure prediction. Among the good qualities of the MCY model are the correct representation of oxygen-hydrogen and hydrogen-hydrogen radial distribution functions (Shvab and Sadus, 2012), and the isochoric heat capacity 70.8 J/mol·K (O'Shea and Tremain, 1980). The MCY model is important from hystorical perspective also, as it forms the basis for many more advanced potential models which include bond flexibility (Li and Clementi, 1986), three-body and polarisation interaction terms (Li *et al.*, 2007; Niesar *et al.*, 1990).

Different modifications have been proposed to improve the prediction of water properties using MCY model. Wojcik and Clementi (1985) found that the many-body interactions make up as much as 15% of the internal energy and can affect the liquid structure. This is a very big amount of energy to be ignored, suggesting future models should incorporate multibody interaction. Li and Clementi (1986) included intramolecular vibrations to the original MCY water model. The new flexible MCYL model yielded only little improvement over the original model. Niesar *et al.* (1990) added a polarization term. The new polarizable NCC potential is capable of accurately predicting a wide spectrum of static and dynamic properties of liquid water. However, similar to all models of MCY-family,

TABLE 2.1: Intermolecular parameters used in the MCY and MCYna intermolecular potential. Values are in atomic units.

Parameter	Value
a_1	1734.1960
a_2	2.726696
a_3	1.061887
a_4	1.460975
b_1	2.319395
b_2	1.567367
b_3	0.436060
b_4	1.181792
q^2	0.514783
R^{OM}	0.505783
R^{OH}	0.957200
Θ^{HOH}(deg)	104.52
$\alpha\beta$(Å^3)	0.802804*
β(dimensionless)	0.557503*
ν	287.9444*

* - these parameteres are used in the MCYna water model.

the NCC model also gives much smaller first oxygen-oxygen radial distribution peak. It was suggested that accurate dispersion energy term and an extended basis set are needed to improve the structural properties (Niesar *et al.*, 1990). Li *et al.* (2007) moved further and developed potential model similar to NCC but with inclusion of three-body interaction term. The new MCYna model will be discussed in details later.

2.1.3.6 TIP5P

Mahoney and Jorgensen (2000) developed this five-site model with the intention to improve the density over the wide temperature (from -37.5 to 62.5°C) and pressure range (1 to 10000 atm). This model places the negative charge on dummy atoms (labeled q_2 on Figure 2.5d) representing the lone pairs of the oxygen atom, with a tetrahedral-like geometry. A positive charge is placed on each of the hydrogen atom forming H-O-H angle of 104.52°. There is no charge on oxygen, and the interaction between different oxygen atoms is obtained using the Lennard-Jones potential. TIP5P water potential successfully predicted energy the average congfigurational energy -41.3 kJ/mol (-41.5), density at ambient conditions 0.999 g/cm^3 (0.998), and temperature of maximum density 277 K (277)

(experimental values at ambient conditions are given in brackets). However, the five-site scheme of TIP5P water model increases the computational time, and forces tetrahedral arrangement for hydrogen-bonded pairs to be more attractive than for real water. This leads to a very high 1st peak in H-H radial distribution function. TIP5P also gives too high isobaric heat capacity, self-diffusion and thermal expansion coefficients (Mahoney and Jorgensen, 2001).

2.1.3.7 NvdE

A six-site water model (NvdE) was developed by Nada and van der Eerden (2003) for simulating ice and water near the ice melting point. Geometrically this model looks like combination of four and five-site models discussed above. A positive charge is placed on each hydrogen site and a negative charge plus three negative dummy charges, one of which is located on H-O-H bisector and another two from the other side of the H-O-H plane. The distance l_3 of the two negative charges located outside of the H-O-H sector (see Fig. 2.5) is 0.8892 Å, and the rest of the parameters are given in Table 2.2. A point of difference from either the TIP4P or TIP5P models is that the Lennard-Jones interaction acts not only on the oxygen site but also on the hydrogen site. Despite being developed to simulate properties of ice and water nearthe melting point, the actual melting temperature of the NvdE model is in the range 16 - 21°C (Nada and Furukawa, 2005). Apart from being computationally expensive, the six-site model fails to reproduce many properties of liquid water. For example, water density is only 0.989 g/cm^3 (Nada and van der Eerden, 2003), the dipole moment is 1.89 D and the dielectric constant is 33 (Chaplin, 2013). The positive qualities of the given six-site water model include enthalpy of vaporisation 45.283 kJ/mol (44.0451) and thermal expansion coefficient 2.57 $10^{-4}/K$ (2.54). Experimental values are given in brackets.

2.1.4 Polarizable water models

Polarization is a redistribution in space of a charge distribution due to an electric field (Yu and Gunsteren, 2005). Unlike rigid nonpolarizable potentials described above, polarizable potentials dynamically respond to fluctuations in the electric field due to molecular motion. The polarity of a molecule is a measure of the symmetry in the distribution of the charged particles. Molecular polarization may be electronic (caused by the redistribution of electrons), geometric (caused by changes in the bond length and angles) and/or orientational (caused by the rotation of the whole molecule) (Yu and Gunsteren, 2005). Each of these cases requires different mathematical approach. For example, to account for charge density redistribution inside the molecule water molecules with fluctuating

charges were developed (Rick *et al.* 1994; Rick, 2001). Geometric polarization can be partially mimicked by flexible water models, i.e. models which account for intermolecular vibrations (Wu *et al.*, 2006; Raabe and Sadus, 2011; González and Abascal, 2011). Finally, orientational or dipolar polarization can be approximated by introducing permanent or variable dipole moments and their interaction (Niesar *et al.*, 1990; Dang and Chang, 1997; Li *et al.*, 2007).

2.1.4.1 SPC/FQ

The SPC/FQ water model is a three-site model with the charges that fluctuate in response to the environment. The model was developed by Rick *et al.* in 1994 as an extension of the SPC model. The charges are treated as dynamical variables using an extended Lagrangian method in which the charges are given a fictitious mass, velocities, and kinetic energy and then propagated according to Newtonian mechanics along with the atomic degrees of freedom. The model gives accurate predictions for gas-phase and liquid state properties, including radial distribution functions and dipole moment. The dielectric constant at 25°C is 86 (78.5) and average configurational energy is 41.449 kJ/-mol (41.5), where values correspondign experimental values are given in brackets (Rick *et al.*, 1994). However, the self-diffusion coefficient in very low $1.7 \cdot 10^{-5}$ cm^2/s (Rick *et al.*, 1994).

2.1.4.2 TIP4P/FQ

The TIP4P/FQ water model is a four-site model developed by Rick *et al.* in 1994. The model uses the concept of electronegativity equalization. The TIP4P-FQ model uses the geometry of the TIP4P water model and includes Lenard-Jones interactions between oxygen sites and three charge sites. The FQ model has additional interactions between charge sites on the same molecule. The fluctuating charges are found by minimizing the energy subject to a charge neutrality constraint. The model is quite successful in predicting some properties in the liquid and solid (ice Ih) states of water. This model fairly well reproduces water radial-distribution functions, relative prmittivity and dipole moment of liquid water. The temperature of maximum density is +7°C. For ice, the model has a dipole moment of the perfect lattice of 3.05 D, which is in good agreement with a self-consistent induction calculation (Batista *et al.*, 1998). For other solid properties, the TIP4P/FQ model is not as accurate. The density is too high and the heat of sublimation is too large relative to experimental values, which suggests that the potential is too attractive. Similarly to SPC/FQ, the TIP4P/FQ self-diffusion constant of liquid water at 298 K is only 1.93 10^{-5} cm^2/s (Rick, 2011).

2.1.4.3 GCPM (Gaussian charge polarizable model)

The Gaussian charge polarizable model (GCPM) (Chialvo and Cummings, 1998; Paricaud *et al.*, 2005) is a modification of the original SPC potential (Berendsen *et al.*, 1981). To improve the short-range polarization behavior the Gaussian distribution (smeared charge) is used to represent the partial charge on the water molecule centered at the SPC charged sites. This model quite accurately describes the pressure, configuration energy, dipole moment, dielectric constant and self-diffusion coefficient of water at ambient conditions (Chaplin, 2013). However, the temperature of maximum density and the melting temperature are very low (260 K and 255 K respectively), isobaric heat capacity and thermal expansion coefficient are too high (94 kJ/mol·K and $4.2 \cdot 10^{-4}\mathrm{K}^{-1}$ respectively). As was shown by Paricaud *et al.* (2001), with some more parametrization this model is capable of improving most of its predictions over the wider range of state points.

2.1.4.4 BKd3 (Baranyai-Kiss)

The BKd3 is the most recent polarizable water model based on Gaussian charges and developed by Kiss and Baranyai (2013). This model gives very good estimates for ambient liquid properties such as: isothermal compressibility, thermal pressure and expansion coefficients, isobaric heat capacity, TMD and liquid density. At the same time, the model has few drawbacks such as slightly higher self-diffusion constant ($2.43 \cdot 10^{-5}$ cm^2/s) and lower average dipole moment 2.51 D (Kiss and Baranyai, 2013; Baranyai and Kiss, 2013).

2.1.4.5 MCYna (Matsuoka-Clementi-Yoshimine nonadditive)

The MCYna is an extension of the original MCY potential (Matsuoka *et al.*, 1975) that includes nonadditive contributions from three-body interaction and polarization (Li *et al.*, 2007). The intermolecular potential $U(\mathbf{r})$ for water is the sum of two-body additive u_2, nonadditive three-body u_3, and polarizable u_{pol} contributions.

$$U(\mathbf{r}) = \sum_{i<j}^{N} u_2(\mathbf{r}_i, \mathbf{r}_j) + \sum_{i<j<k}^{N} u_3(\mathbf{r}_i, \mathbf{r}_j, \mathbf{r}_k) + u^{pol}. \tag{2.5}$$

The leading two-body term has exactly the same form as in original MCY potential and is given by Eq. (2.4). Nonadditive contributions to intermolecular interactions arise for induction interactions, resulting from molecular polarizability, short-range repulsion, and dispersion interactions. It is well documented (Marcelli and Sadus, 1999; Wang and

Sadus, 2006) that multibody dispersion interactions can be adequately described using the Axilrod-Teller (Axilrod and Teller, 1943) triple dipole term,

$$u_3 = \frac{\nu(1 + 3\cos\theta_i \cos\theta_j \cos\theta_k)}{(r_{ij} r_{ik} r_{jk})^3}, \tag{2.6}$$

where θ_i, θ_j, and θ_k are inside angles of the triangle formed by three atoms denoted by i, j, and k, and r_{ij}, r_{ik}, and r_{jk} are the three side lengths of the triangle. Equation (2.6) is applied exclusively for triplets of oxygen atoms because their positions almost coincide with the center of the mass of the water molecule and the three-body interaction between hydrogen atoms is negligible by comparison. All parameters for the u_2, u_3, and u_{pol} terms are given in Table 2.1. The α and β (dimensionless) values are from (Gray and Gubbins, 1984). Figure 2.7 shows MCY water dimer with explicitly labeled interatomic distances r_{ij}. The parameter ν is the nonadditive coefficient, which can be determined from experiment (Leonard and Barker, 1975). The theoretical background and rationale for using this formula is given elsewhere (Shvab and Sadus, 2012a). The contribution of multibody nonadditive from polarization interactions was obtained from (Coulson and Eisenberg, 1966)

$$u^{pol} = -\frac{1}{2} \sum_{i=1}^{N} \boldsymbol{\mu}_i^{ind} \cdot \mathbf{E}_i^0, \tag{2.7}$$

where $\mathbf{E}_i^0$ is the electrostatic field of surrounding charges, and $\boldsymbol{\mu}_i^{ind}$ is the induced dipole at site i given by

$$\boldsymbol{\mu}_i^{ind} = \alpha\beta \cdot \mathbf{E}_i = \alpha\beta \left[\mathbf{E}_i^0 + \sum_{j=1, j\neq i}^{N} \mathbf{T}_{ij} \boldsymbol{\mu}_j^{ind} \right]. \tag{2.8}$$

In Eq. (2.8), $\alpha\beta$ is the polarizability and $\mathbf{T}_{ij}$ is the dipole tensor given by

$$\mathbf{T}_{ij} = \frac{1}{4\pi\varepsilon_0 r_{ij}^5} [3\mathbf{r}_{ij}\mathbf{r}_{ij}^{'} - \mathbf{r}_{ij}^2]. \tag{2.9}$$

It is important to note that the β from 2.1 is adjustable parameter in the MCYna water model. We use different values of β in order to better predict dipole moments of bulk water at reduced densities. Using a gas phase polarizability coefficient of 1.44 Å from Gray and Gubbins (1984), we obtained a dipole moment that significantly exceeded the 2.95 - 3 D range reported from *ab initio* MD and experiment (Coulson and Eisenberg, 1966). To improve the calculation of the induced dipole, we scaled the polarizability

coefficient by a factor of $\beta = 0.557503$. This means that the actual polarizability term is $\alpha\beta = 0.802804$ Å^3. This resulted in a dipole moment of 2.9 D, with 0.9 D attributed to induction interactions. To the best of our knowledge, there is no reliable experimental data of dipole moment for reduced densities of 0.8 and 0.6 g/cm^3, which are the densities of interest in this work. Therefore, we have chosen values of the polarization constants $\alpha\beta$ for $\rho = 0.8$ and 0.6 g/cm^3 to match with experimental values of dielectric constants. For these cases, the values of β are 0.348441 and 0.250878, respectively.

The MCYna is known for very good representation of dielectric constant and dipole moment of liquid water (Shvab and Sadus, 2012a) and aqueous solutions (Shvab and Sadus, 2012b). Recently, Yigzawe and Sadus (2013) showed that MCYna model gives the values of thermodynamic properties like heat capacities, compressibilities, expansion coefficient and the speed of sound which are in very good agreement with experimental data in the very wide temperature and pressure range. For all these virtues MCYna model is the main water model in this work. In Chapters 4 and 5 MCYna potential is being used extensively to investigate structural and dielectric properties of bulk water and aqueous nonpolar solutions.

2.1.5 Flexible water models

The water molecule as well as any other polyatomic molecule change their geometry and charge distribution according to the environment. However, in present-day biosimulations, the most widely used water models are rigid models with frozen internal degrees of freedom. Despite their great simplicity rigid nonpolarizable models quite well reproduce many properties of water and ice at ambient and nearambient conditions (Vega and Abascal, 2011). Many consider this success to be fortuitous or caused by careful parametrization or self-polarization correction (Berendsen *et al.*, 1987). However, these polarization effects or target properties used for parametrization are highly environment dependent which reduces the applicability of rigid water models. Therefore, it is highly desirable to build computationally efficient water models that work well in those areas where effect of internal degrees of freedom are not negligible. The diffusion constant (or relaxation time) and the dielectric constant constant are extremely sensitive to the equilibrium bond length and equilibrium bond angle respectively (Wu *et al.*, 2006; Raabe and Sadus, 2011, 2012). In most of water models these properties are poorly predicted. The self diffusion constant and dielectric constant are very important since they are directly related to the solvent dynamics and solvent-mediated electrostatic interactions. Raabe and Sadus (2011, 2012) using the DL_POLY (Smith *et al.*, 2012) molecular simulation package, found out that introducing internal vibration (intramolecular degree of freedom) into SPC has an observable effect on vapor-liquid coexistence curve.

Flexible models indeed improve such properties like the diffusion coefficient, dielectric constant, and dipole moment, or at least can partially compensate for polarization effects. However they also have a number of technical and theoretical difficulties. Internal vibrations has reorientation time of 2 ps at ambient conditions (Teixeira *et al.*, 1985), thus, in a computer model we need to use a much smaller time step when integrating the equations of motion. This, obviously, will take a very long time for a picosecond simulation. Also one can argue that internal vibrations are essentially quantum mechanical in nature and cannot be strictly incorporated into a classical molecular dynamics simulation (Teleman *et al.*, 1987). Indeed, most of the flexible water models have much higher heat capacities than their rigid counterparts (Wu *et al.*, 2006).

2.1.5.1 SPC/Fw

Wu *et al.* (2006) developed a flexible SPC model (SPC/Fw) with an intention of having a model with an improved dynamic and electrostatic properties of water without damaging other properties. It is a flexible three-site model derived by optimizing bulk diffusion and dielectric constants to the experimental value via the equilibrium bond length and angle. The bond angle and bond length (is responsible for the improvement of self diffusion constant (Raabe and Sadus, 2011)) are slightly higher than the values used in SPC. The molecular geometry in these models can be defined by three internal degrees of freedom: two O-H bond lengths (r_{OH_1} and r_{OH_2}) and one H-O-H bond angle $\theta_{\angle HOH}$. The general interaction potential can be written as a sum of two parts:

$$\begin{aligned} u_{inter} &= \sum_i \sum_{j \neq i} \left\{ 4\varepsilon \left[\left(\frac{\sigma}{r_{ij}^o} \right)^{12} - \left(\frac{\sigma}{r_{ij}^o} \right)^{6} \right] + \frac{e^2}{4\pi\varepsilon_0} \frac{q_i q_j}{r_{ij}} \right\}, \\ u_{intra} &= \frac{k_b}{2} \left[(r_{OH_1} - r_{OH}^0)^2 + (r_{OH_2} - r_{OH}^0)^2 \right] + \frac{k_a}{2} \left(\theta_{\angle HOH} - \theta_{\angle HOH}^0 \right)^2, \end{aligned} \tag{2.10}$$

with u_{intra} and u_{inter} as the intra and intermolecular interactions, r_{OH}^0 and $\theta_{\angle HOH}^0$ as the equilibrium bond length and angle (in the gas phase), r_{ij} as the distance between atoms i and j, ε_{ij} and σ_{ij} as the Lennard-Jones parameters for atom pair i, j, and q_i as the partial charge on atom i. The intramolecular interaction is represented by simple harmonic potential. The SPC/Fw model indeed gives many values very close to the original SPC/E model (Wu *et al.*, 2006). However, due to better description of the inter and intramolecular interactions, SPC/Fw gives better values of diffusion constant, dipole moment and dielectric constant than SPC/E. One of the few significant deficiencies of this model is a very high isobaric heat capacity of 99.353 kJ/K·mol at 25°. In this work

we use SPC/Fw water model to calculate radial distribution functions and the 1st order oxygen-htdrogen coordination numbers of bulk water.

2.1.5.2 TIP4P/2005f

Gonzalez and Abascal (2011) incorporated intramolecular degrees of freedom to the successful rigid model TIP4P/2005 (Abascal and Vega, 2005) in order to try to improve the predictions for some properties, and to enable the calculation of new ones. The new model incorporates flexibility by means of a Morse potential for the bond stretching and a harmonic term for the angle bending. Simulations show that the model slightly improves the melting point and isothermal compressibility. On the negative side, the results for the dielectric constant and self-diffusion coefficient are far from experiment (Gonzalez and Abascal, 2011). The flexible TIP4P/2005f seems to inherit many good qualities of the original TIP4P/2005 model. Additional investigations are needed to test the performance of the promising TIP4P/2005f water model.

2.1.5.3 MCYL (Matsuoka-Clementi-Yoshimine-Lie)

Lie and Clementi (1989) developed the flexible MCYL water model which is an analytical continuation of the four-site MCY (Matsuoka *et al.*, 1975) configuration interaction potential. MCYL include the intramolecular vibration with an intention of calculating the static and dynamic properties of liquid water. The rigid MCY potential contains a charged site displaced from the O atom. Extending this potential to a flexible model must include a specification of how this displaced site (site M on Fig. 2.6) changes with the deformation of water molecule, it is assumed that M-site to reside on the H-O-H bisector. The MCYL model seems to inherit a lot of features of the original MCY, like low 1st peak of the O-O radial distribution function, high pressure and isochoric heat capacity.

2.1.6 *Ab initio* water models

Most of the water models described so far are semi-empirical potentials with simple functional form, suited to describe water liquid state on molecular level. They are used in MD or MC simulations and have an advantage of allowing the study of time-dependent processes. These models are very expedient tools to investigate macroscopic and collective properties of water such as: energy, heat capacity, compressibility, dielectric constant, dipole moment distribution, and shell structure. Being empirical, these models strongly depend from our experimental knowledge about substance of interest, as they

are developed and tuned to reproduce these experimental data. Some models, like MCY (Matsuoka *et al.*, 1976) and its derivatives (NCC (Niesar *et al.*, 1990), MCYL (Lie and Clementi, 1986), MCYna (Li *et al.*, 2007)) were fitted to reproduce water dimer potential energy surface obtained from the configuration interaction (CI) calculation of the 66 dimer positions. The MCY water model has a simple analytic atom-atom form consisting of a double exponential and of Coulomb terms (see Eq. (2.4)). Despite somewhat low, by modern standarts, number of grid points, potentials from the MCY family describe water structure and energy quite well.

As was already stated, computer simulations of any molecular system strongly depends from available experimental data about the system, especially energy levels and electron structure. Any molecular or atomic system on a nanoscale is essentially a quantum system with strong electron cooperative effects, electron-nuclei interactions, charge transfers and so on. These processes are responsible for bond breaking and forming events, which are essential to describe chemical reactions. A special technique called *ab initio* molecular dynamics (AIMD) has been developed to predict fundamental problems of energy spectra and bond formation (Tuckerman, 2002). This approach starts from the quantum mechanical description of atomic interactions, and makes necessary approximations in order to solve complex many-body equations. Numerous AIMD methods (Fawzi, 2006) are based on such an approximate quantum many-body techniques as Hartri-Fock method (HF), density-functional theory (DFT), and Car-Parinello molecular dynamics (CPMD). In this subsection we will give only brief description of the mentioned first principles methods and then list some recent *ab initio* based water models.

The Hartree-Fock method (Levine, 1991) is one of the simplest wave-function based techniques which forms the foundation for many more elaborate electronic structure methods. The exact many-body wave function is approximated by a single Slater determinant. The minimization of the HF energy is done according to variational principles, which results in HF wavefunction and energy of the system. Several post-Hartree-Fock methods were developed such as configuration interaction (CI), coupled clusters (CC), Møller-Plesset perturbation theory (MP2, MP3, MP4, etc.) (Levine, 1991), quadratic configuration interaction (QCI), quantum chemistry composite methods, etc. (Lipkowitz *et al.*, 2007).

The DFT developed in the works of Hohenberger and Kohn (1964) makes use of Born-Oppenheimer (BO) adiabatic approximation of separate electron and nuclei wave functions. The main challenge of this method is the minimization of a functional of the electron density and consequent choice of exchange correlation functionals which is critical in generating accurate DFT results (Parr and Yang, 1989).

The Car-Parinello (1985) implementation of DFT explicitly introduces the electronic degrees of freedom as fictitious dynamical variables. An extended Lagrangian for the

system leads to a system of coupled equations of motion for both ions and electrons. In this approach the valence electrons wavefunction are usually approximated by a plane wave basis set. A small fictitious mass is assigned to each electron in order to keep them on the electronic ground state, thus yielding accurate ionic forces. A popular and powerful computational chemistry software program has been developed based on Car-Parinello method (CPMD, 1990-2008).

A comprehensive review of the modern *ab initio* water studies is given in the work of Szalewicz *et al.* (2009). Extensive *ab initio* simulations of water has been done since the work of Car and Parinello in 1985. These simulations are mostly concerned with structural properties such as radial distribution functions (RDF), energy levels of dimer, trimer, and higher-order configurations, and dipole moments of individual water molecules. Perhaps, due to large computational load and small number of molecules, macroscopic thermodynamic properties such as heat capacities or compressibilities are reported in rare instances (Shiga and Shinoda, 2005; Vega *et al.*, 2010). Dyer and Cummings (2006) used CPMD to calculate RDF, dielectric constants and dipole moments of liquid water at densities ranging from 0.1 till 1 g/cm^3 and temperatures 300 - 1000 K. Kang *et al.* (2011) performed similar study for elevated densities 1 - 2.2 g/cm^3 and temperatures 300 - 2800 K. Both *ab initio* investigations indicate large number of H-bonds conserved at extreme temperatures. Stern *et al.* (2001) developed POL/TZ and POL/QZ five-site water models, with the parametrization based largely on quantum-chemical calculations. The model gives densities, RDFs, and condensed-phase properties at ambient conditions that are in reasonable accord with experiment. Among the drawbacks are high temperature of maximum density (20°C) and weak hydrogen-bond network at elevated temperatures.

The CC-pol potential (Bukowsky *et al.* 2007, 2008; Cencek *et al.*, 2008) was probably the first *ab initio* potential that accomplished the goal of the description of the wide range of water properties: from spectra of the water dimer to structure and dynamics of liquid water. This potential was developed using symmetry-adapted perturbation theory (SAPT) and lead to a whole new family of SAPT potentials (Cencek *et al.*, 2008). Mas *et al.* (2003) developed new *ab initio* three-body potential based on HF method and SAPT calculations performed at 7533 trimer geometries. This investigation allowed to directly evaluate the effects of nonadditive interactions by comparing these geometries with the ones obtained from pairwise potentials. Application of *ab initio* derived water potentials to the water coexisting properties also yields satisfactory agreement with experiment at ambient conditions (Hernández-Cobos *et al.*, 2005).

In summary, the *ab initio* based water models have proved to be a very powerful tool in investigation of water configurations, quantum effects, and electronic structure. Such

calculations provides invaluable information about potential energy surface of water configurations, which can be used for development of classical empirical water models, or comparison with experiment. Despite the fact that fully satisfactory agreement with experiment has not been achieved yet, particularly with H-bonding and diffusion coefficients, recent results indicate significant improvements in this area (Tkatchenko and Scheffler, 2009).

Table 2.2 summarizes parameters for most of the water models discussed in this chapter.

TABLE 2.2: Parameters for some water molecules. Angles θ, φ, distances l_1, l_2, and charges q_1, q_2, and q_3 are shown in Figure 2.5.

Water model	sites	q_1 (e)	q_2	q_3	l_1 (Å)	l_2	θ (°)	ϕ (°)	σ (Å)	ε (kJ/mol)	Ref.
SPC	3	0.4100	-0.820	-	1.0000	-	109.47	-	3.1660	0.6500	Berendsen *et al.*, (1981)
SPC/E	3	0.4238	-0.8476	-	1.0000	-	109.47	-	3.1660	0.6500	Berendsen et al., (1987)
SPC/Fw	3	0.4170	-0.8340	-	1.0120	-	113.24	-	3.1655	0.6507	Wu *et al.*, (2006)
SPC/FQ	3	fluct.	fluct.	-	1.0000	-	109.47	-	3.1760	1.2313	Rick *et al.* (1994)
TIP3P	3	0.4170	-0.8340	-	0.9527	-	104.52	-	3.1506	0.6368	Jorgensen *et al.* (1983)
TIP4P/2005	4	0.5564	-1.1280	-	0.9572	0.1546	104.52	52.26	3.1589	0.7749	Abascal and Vega (2005)
TIP4P/FQ	4	fluct.	fluct.	-	0.9572	0.1500	104.52	52.26	3.1590	1.1983	Rick *et al.* (1994)
TIP4P/2005f	4	0.5564	-1.1280	-	0.9572	0.1546	104.52	52.26	3.1589	0.7749	González and Abascal (2011)
MCY	4	0.71748	-1.4349	-	0.9572	0.2676	104.52	52.26	-	-	Matsuoka *et al.* (1975)
MCYna	4	0.71740	-1.4348	-	0.9572	0.2677	104.52	52.26	-	-	Li *et al.* (2007)
MCYL	4	0.71740	-1.4348	-	0.9572	0.2677	104.52	52.26	-	-	Li and Clementi (1986)
BKd3	4	fluct.	fluct.	-	0.9750	0.2661	104.52	52.26	-	-	Kiss and Baranyai (2013)
GCPM	4	0.61130	-1.2226	-	0.9572	0.2500	104.52	52.26	3.5140	0.5869	Chialvo and Cummings (1998)
BNS	5	0.19000	-0.19000	-	1.0000	1.0000	109.28	109.28	2.8200	0.3028	Ben-Naim and Stillinger (1972)
ST2	5	0.24357	-0.24357	-	0.9572	0.8000	109.47	109.47	3.1000	0.3169	Stillinger and Rahman (1974)
TIP5P	5	0.2410	-0.2410	-	0.9572	0.7000	104.52	109.47	3.1200	0.6694	Mahoney and Jorgensen (2000)
NveD	6	0.4770	-0.8660	-0.044	0.9800	0.2300	108.00	111.00	3.1150	0.7140	Nada and Erden (2003)

2.1.7 Improving water models

After brief discussion of the main water models, their achievements as well as deficiencies, we can summarize few directions of research where we should focus our attention in order to improve existing water models (Yigzawe, 2012).

- Temperature of maximum density (TMD). Experimental temperature of maximum density for liquid water is +4°C. One may think that this basic property should be the first that all computer models should reproduce. However, as it is clearly shown in an online review by Chaplin (2013), the TMD of the existing water models falls in the range from -90 till +25°C. Polarisable potentials give especially poor values of TMD (Kiss and Baranyai, 2013; Guillot, 2002). Probably only TIP5P (Mahoney and Jorgensen, 2000) and TIP4P/2005 (Abascal and Vega, 2005) water models give reasonable values +5°C and +4°C respectively. Correct description of water density at all temperature is especially important for understanding of the hydrophobic effect (Paschek, 2004).

- Critical parameters. As revealed by Guillot (2002) and Vega and Abascal (2011), most of the nonpolarisable water models give inaccurate values of the critical temperature (T_c) and pressure (p_c). The general trend is that majority of the water models underestimate critical temperature and density. Calculating the thermodynamic quantities near or at the critical point is challenging and at times impossible, which is a result the finite size and cutoff radius of the system. More recent review by Kiss and Baranyai (2013) show some improvement in this area. For example GCPM gives T_c = 642 K, p_c = 24.6 MPa and BK3d gives T_c = 634 K, p_c = 21.4 MPa, which are reasonably close to experimental values 647 K and 22.064 MPa. Apart from these two, most of the water models deviate from the experimental values significantly. Thus, it is important to pay attention to this aspect when developing new water models.

- Phase diagram/liquid-vapor coexistence curve. Few water models were thoroughly tested for the phase diagram or the liquid-vapor coexistence curve. SPC/E (Berendsen *et al.*, 1987) was the first to qualitatively reproduce main features of the ice-liquid-vapor phase diagram of water. Some models like TIP4P/Ice (Abascal *et al.*, 2005) were designed to study ices and amorphous water. TIP4P/2005 is the first model to qualitatively reproduce whole phase diagram and liquid-vapor coexistence curve. Though it seems impossible to get the full phase diagram and liquid-vapor coexistence curve of water with a single model, it will be worth trying to get as many properties as possible from each of the models.

- Polarization properties. Water's ability to dissolve electrolytes plays a crucial role in chemical reaction in cells (Eisenberg and Kauzmann, 1969; Fröohlich, 1958). In order to accurately describe solvation processes we need to have a water model capable of predicting the dielectric constant and dipole moment of water in different phases and densities. Most water models which are used for biosimulation are not able to predict the experimental value of the dielectric constant or dipole moment correctly (Chaplin, 2013). In some cases these discrepancies can be expected, as the potentials do not include molecular polarizability. As was discussed above, there are 2 ways to improve this situation. The first is to account for intermolecular degrees of freedom. For example, recently, Raabe and Sadus (2011) improved the prediction of dielectric constant by using a flexible SPC/Fw water model. The second way is to include polarization explicitly. Success of the polarizable water models like MCYna (Li *et al*, 2007), BKd3 (Kiss and Baranyai, 2013), GCPM (Chialvo and Cummings, 1998), etc. in predicting polarization properties ow water, serves as the best example.

- Non-additive interaction. Most of the water models are effective pair potentials which calculate only interactions between pair of atoms. Many *ab initio* potentials were also developed by calculating energy of water dimers, and more scarcely trimers or higher order clusters. However, it is long been speculated that for some liquids, and at certain conditions three-, four-, and higher-order interactions can not be neglected. Three body interaction has an effect on vapor-liquid (Wang and Sadus, 2006a) and solid-liquid (Wang, Sadus, 2006b) phase behaviour of fluids. Marcelli and Sadus (1999) found that vapor-liquid equilibria are affected substantially by three-body interactions. Three-body and higher order interactions play significant role in monoatomic gases and liquids as well. For instance, incorporation of three-body interaction term results in very good agreement of thermodynamic properties of argon from near critical point to twice the critical density (Leder, 1985). Vega and Abascal (2011) in their extensive review concluded that polarization interaction is arguably the main component necessary for the present water models to make a step forward. Despite the fact that incorporation of additional terms in the potential function has negative implication on computational cost, modern computer technique like graphical processors and different parralelisation techniques make this inclusion absolutely timely and possible.

- Thermodynamic properties. During the last few decades most of the efforts were directed to reproduce the most basic water properties like: temperature of maximum density, melting and critical temperatures, enthalpy of vaporisation, pair-correlation function, internal energy, pressure, vapor-liquid phase properties, etc. Despite slow, reasonable progress has been made in predicting all these properties

in the last decade (Abascal and Vega, 2005). Properties like heat capacities, compressibilities, expansion coefficient, Joule-Thomson coefficient, or speed of sound have been largely left aside by the simulation community (Vega and Aabascal, 2011). It is not surprising that the results in this area are more then modest (Mao and Zhang, 2012). Such a situation happend not least due to certain limitations imposed by different statistical mechanical ensembles on properties which contain pressure and volume derivatives (Lustig, 2004abc, 2010, 2012). However, at this stage in molecular dynamics development it is of vital importance to focus more on industrially relevant properties of molecular liquids like heat capacities, compressibilities, speed of sound, etc. Suitable experimental database have been composed (Wagner, 1995) and new analytical technique applicable for all statistical mechanical ensembles have been developed and already tested for water (Lustig, 2004abc, 2010, 2012; Yigzawe and Sadus, 2013).

2.2 Water-solute interaction

In this work we investigate properties of binary aqueous solutions of nonpolar solutes in the liquid phase, from ambient to critical conditions. We will be focusing on specific group of solutes, mainly gases like methane, neon, argon, krypton and xenon. These are nonpolar, very weakly interacting gases, almost chemically neutral with very small solubility in water. Binary fluid systems of water and an inert nonpolar second component have been extensively investigated experimentally and with the help of molecular dynamics (MD) and Monte Carlo (MC) techniques. Phase equilibria, critical curves, and thermodynamics functions for a wide range of temperatures and pressures have been determined for mixtures containing water plus Ar (Wu *et al.*, 1990), Xe (Franck *et al.*, 1974), Ne (Japas and Franck, 1985), and CH_4 (Errington *et al.*, 1998), etc. Aqueous mixtures are of considerable interest in geochemistry and chemical technology (development of undersea deposits of gas hydrates), industrial technology (electric power generation, extraction process, decontamination), and biochemistry (protein folding, micellization). In particular, the solvation of nonpolar gases exhibits interesting behavior with increasing temperature. The solubility of inert gases in water at room temperature, which is several orders of magnitude smaller than in other liquids such as hydrocarbons, initially decreases with increasing temperature, goes through a minimum, and then exhibits a steep rise at subcritical temperatures (Kennan and Pollack, 1990). Complete miscibility is eventually reached for several nonpolar molecules above the critical temperature of water. This makes supercritical water a useful medium for chemical reactions.

Despite the importance of supercritical aqueous mixtures, the molecular structure of supercritical water in the presence of nonpolar solutes has not been extensively determined experimentally. Recent neutron diffraction studies explored the hydration shell of argon at sub-critical conditions, using distinct isotopes of argon in normal and heavy water (Sullivan *et al.*, 2001; Botti *et al.*, 2003). These data showed structural changes in the hydration shell of the solute, compared to ambient conditions, in agreement with previous MD simulations on mixtures of rare gases and extended simple point charge (SPC/E) water (Guillot and Guissani, 1993). In the presence of a nonpolar solute, reorganization of the water solvent is observed around the hydrophobic solute molecules (Chandler, 2005; Raschke and Levitt, 2005). The ordering of water causes a local decrease of entropy. The nonpolar molecules of the solute tend to aggregate to reduce the local order of the water molecules. The balance between the entropic and the enthalpic terms determines the phenomenon of hydrophobic hydration (Ben-Naim, 1989). It has also been observed that the solubility of rare gases increases as the size of the solute increases (Lynden-Bell and Rasaiah, 1997; Cristofori *et al.*, 2005), which is attributed to the interplay between energetic and entropic contributions to the free energy of solvation. According to the simulation results reported by Guillot and Guissani (1993) with the SPC/E model (Berendsen *et al.*, 1987), the energetic term favors the solubility of larger solutes while the entropic term depresses solubility with increasing size.

Another interesting effect of nonpolar solutes is their influence on the polarization properties of water. The polarization properties of critical and supercritical water in the presence of nonpolar solutes have not been determined experimentally. Polarizable potentials were used in the molecular simulation studies of Cristofori *et al* (2005) and Dyer *et al.* (2008) and references therein. However, these studies were devoted mainly to the question of the solubility of nonpolar solutes in water at very low concentrations. The main aim of this work is to use molecular simulation to investigate the structure of water-nonpolar systems at ambient, critical, and supercritical temperatures and solute mole fractions up to 30%. Previous studies were unable to indicate how the hydration number might vary with the temperature and pressure at which the hydrate was formed. In this work we provide data for the hydration number over a wide range of state points for water plus noble gases and methane. We report results for the solvation shell size, hydration number, and role of the solute particle size on solubility of the solute and their temperature dependence (Shvab and Sadus, 2012a, 2012b).

2.2.1 Methane clathrate

Increasing number of practical applications of water-methane complexes, most importantly from the shale gas mining fuels increasing number molecular dynamic simulations

on water-methane complexes. The question of the solubility of nonpolar particles in water is directly relevant to the formation of clathrate hydrates (Rodger, 1990). Clathrate hydrates are supramolecular compounds of water molecules and guest components without chemical bonds between them. Water molecules form a three-dimensional host structure (the lattice) through hydrogen bonding; this lattice is at sufficiently low density to contain a number of well characterized pores, or "cages" in which other molecules (guests) are trapped. It is reported that, despite having very low chemical reactivity, most of the noble gases form coordination compounds in water (Poling, 1961). The conditions for clathrate hydrate formation depend on temperature, pressure, and the concentration of the solute. Therefore, the knowledge of solute concentrations at which the "cages" are stable is of great importance. Undoubtedly, among the many clathrate hydrates, methane clathrates are of paramount interest for modern industry. Many researchers efforts are being devoted to studying methane clathrates, an crystal-type structures being fromed at high pressures and negative or around zero temperatures, found in the cold waters near the ocean base or in permafrost. Figure 2.8 shows the most common methane clathrate or methane hydrate of sI type.

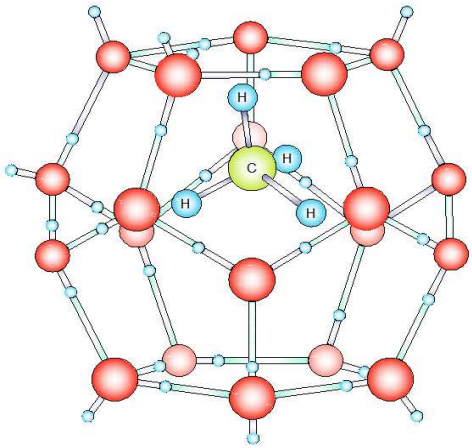

FIGURE 2.8: Methane clathrate.

The phase digram of methane hydrate can be found in Fig. 3 of Lundgaard and Mollerup (1992). As can be seen from this figure, at positive temperatures methane, predominantly, exist in water in form of dissolved gas. However, according to the phase diagram, at pressures higher 10 MPa hydrate structures of type I can be found even at positive temperatures. Stable hydrate structures of differend types (I and II) are being formed at negative temperatures at all pressures. In nature, such conditions exist in the upper layers of lithosphere (at depths less than 2000 m) and sedimentary rocks in polar regions where average surface temperatures are below 0°C. Oceanic sediment at water depths greater than 300 m where the bottom water temperature is around 2°C also contain some amount of methane clathrates. It has been speculated, that deep fresh-water lakes like

Lake Baikal in Siberia may also host gas hydrates (Vanneste *et al.*, 2001). Continental deposits of gas hydrates have been located in Siberia and Alaska in sandstone and siltstone beds at technologically accessible depths (< 800 m). Deposits in ocean seem to be widespread in the continental shelf and may cap even larger deposits of gaseous methane (Kvenvolden, 1995).

2.2.2 Hydrophobic interaction

The interaction of nonpolar solutes with water is accompanied by many unusual changes in water structure and thermodynamic properties (Chaplin, 2013). This kind of interaction has generic name hydrophobic interaction and hydration of nonpolar solutes is called hydrophobic hydration. The term "hydrophobic interaction" refers to the structural and energetic response of water in the vicinity of hydrophobic solutes as shown on Figure 2.9. It describes the interaction of nonpolar molecules with water, each other and the interaction between water molecules in the presence of two or more nonpolar molecules. The hydrophobic hydration is accompanied by following thermodynamic effects (Chaplin, 2013; Mikheev *et al.*, 2007):

- An increase of the solute chemical potential μ, due to its low solubility (Paschek, 2004).
- A local increase in Gibbs free energy G (Ben-Naim, 2009).
- A strong temperature dependence of the enthalpy H of the system, from exothermic at low temperatures to endothermic at high temperatures (Chaplin, 2013; Mikheev *et al.*, 2007).
- A local decrease in entropy S and enthalpy H and decrease in the partial molar volume V (Ben-Naim, 2009), as the solute particle fits into cavities in the water network (Imai and Hirata, 2005).
- A local increase in isobaric heat capacity C_p (Sharp and Madan, 1997).

Precise statistical mechanics expressions for all solvation quantities discussed above and presented on Fig. 2.9 will be given in Chapter 6.

The cause behind all these unusual changes in thermodynamic potentials and other properties, is in H-bond rearrangement around hydrophobic particles. For example, when a hydrophobe is dropped in an aqueous medium, H-bond network will be distorted or even broken to make room for the hydrophobe, since water molecules do not react with hydrophobe. Bond breaking is an endothermic reaction, accompanied by the release of

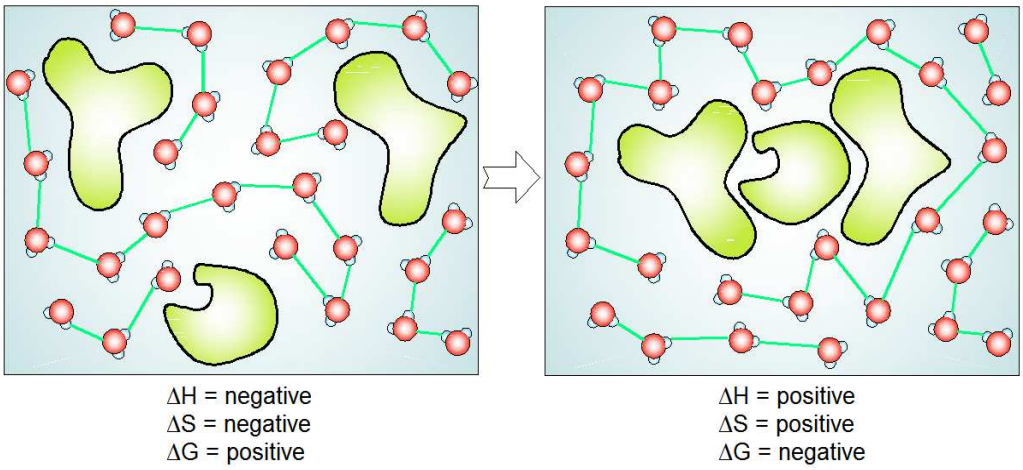

FIGURE 2.9: Formation of hydrophobic interaction and changes in thermodynamic potentials.

heat into the system. Small hidrophobic particles are getting enveloped by the H-bond network of the neighboring water molecules. These new ice-like cage structures are also called a clathrate cages (Chandler, 2005). If nonpolar solutes have radius less than 0.4 nm, the H-bond network is able to rearrange itself around hydrophobe in such a way, that actually local density of water is increasing and decrease of the entropy of the system takes place (-ΔS). In other words, water structure around small hydrophobes is more ordered (Chandler, 2005; Ben-Naim, 2009). The change in enthalpy (ΔH) of the system can be negative, zero, or positive because the new hydrogen bonds can partially, completely, or over compensate for the hydrogen bonds broken by the entrance of the hydrophobe. However, quantitatively, the spontaneity of the reaction is determined largerly by the entropic term (ΔS), as its absolute value is much larger than enthalpic term (ΔH). ΔS is the dominant negative element in the Gibbs free energy formula $\Delta G = \Delta H - T\Delta S$, thus making value of ΔG to be positive. According to the activation state theory (Pitaevskii, Lifshitz, 1981) positive ΔG indicates that the mixing of the hydrophobe and water molecules is not spontaneous. Unfavorable entropy changes drive hydrophobic particles together to form single compound, thus minimising its surface area (see Fig. 2.9). This process causes some portion of the clathrate cage to be broken. Tearing down a H-bond network around hydrophobe increases local disorder, and as a consequence, eventual increase in entropy. It is important to note that the natural tendency of hydrophobic solutes to demix in aqueous medium can be overcomed at special conditions. In the present work, we simulate mixtures of water and hydrophobic solutes at constant density conditions and at temperatures 278 - 750 K (Shvab and Sadus, 2012b). at these conditions mixtures are subject to huge pressures (more than 650 MPa at 650 K for example) which prevent demixing tendencies.

Methane is the simplest hydrocarbon molecule and has often been considered to be a good model for understanding hydrophobic interactions. It is now generally believed that the nature of hydrophobicity is size dependent (Chandler, 2005; Shvab and Sadus, 2012). Small nonpolar molecules such as methane have a hydration free energy near ambient conditions that is largely entropic. That is, it depends more on the number of ways all of the water molecules in the methane hydration shell can form hydrogen bonds rather than their energies. Therefore, the number of water molecules in the solvation shell of small nonpolar molecules is of central importance.

A common theoretical treatment of the hydrophobic interaction has been to study the association of simple hydrophobic solutes (typically Lennard-Jones spheres) in infinitely dilute water solution. Most of these simulation studies show no tendency for the aggregation of the solute molecules, favoring instead the solvent-separated pair (Rashke *et al.*, 2001). These results are in contrast to the "bulk" hydrophobic interaction measured experimentally by solvent transfer, which clearly favors association (Eisenberg and McLachlan, 1986). Experimental neutron diffraction data of methano-water (Geiger *et al.*, 1979) and DMSO water (Rapaport and Scheraga, 1982) mixtures, as well as a number of MD studies (see work of Guillot and Guissani (1993) and ref. therein), have demonstrated that, in the hydrophobic hydration shell, no major restructuring of water occurs, despite earlier claims. Most studies (Shvab and Sadus, 2012b) have also pointed out that the radial distribution functions of the hydrophobic solute with the oxygen and hydrogen atoms of the solvent water have very close maxima, which implies that the water molecules solvating a hydrophobic solute are arranged in such a way that their O-H bonds are parallel to the surface of the solute (tangential hydration). These conflicting theoretical and experimental results have been attributed to differences in the structure and polarizability of the water model used (Shvab and Sadus, 2012b). Considering neon, argon, krypton, xenon, and methane as Lennard-Jones spheres we can establish direct dependency of the thermodynamic and physical properties of aqueous solutions from the mass m, size σ, energy parameter ε, and molar fraction x_s of nonpolar particles. The apolar particles like methane, arguably, possess no dipole moment but there are still interaction between them including short-range repulsive force and the long-range attractive van der Waals force (Szczęśniak *et al.*, 1993).

Water-water interaction has been extensively discussed in the previous sections. The main goal of this work is a thorough investigation of properties of aqueous nonpolar solute mixtures, thus we need to know how polar water molecules interact with nonpolar solutes like neon, argon, krypton, xenon, and methane. Unfortunately, due to very weak solubility of these gases (Kennan and Pollack, 1990), analytical potential function is not known and only different simplification are used. At the moment, simple Lennard-Jones potential is the preferred potential choice for describing water-solute and solute-solute

interaction (Guillot and Guissani, 1993; Shvab and Sadus; 2012). Below we present review of several *ab initio* investigations of water-neon, -argon, -krypton, -xenon and -methane potential energy surfaces available in the literature. Generating the potential surface from such *first principle* calculations becomes a promising alternative to earlier empirical methods as interactions between guest and host molecules can be described in a consistent, quantitative manner.

2.2.2.1 Water-Neon

Several *ab initio* calculation of Ne-H_2O potential-energy surface (PES) have been done. Bagno (1998) performed Gaussian MP2 (Møller-Plesset theory) level calculation using 6-311 basis set. The most stable neon-water arrangement had counterpoise-corrected binding energy of -0.54 kJ/mol with a $R = 3.2$ Å, $\theta = 120°$ as described on Figure 2.10. Hodges *et al.* (2002) using similar technique with MP4 theory obtained similar Ne-O distance distance 3.18 Å but lower binding energy or ground state approximately -0.787 kJ/mol. Earlier Losonczy *et al.* (1973) applied Hartree-Fock approximation for the ground state of the Ne-H_2O dimer. The ground state energy was around -0.669 kJ/mol with the neon atom aligned along one of the O-H axis at distance 3.731 Å.

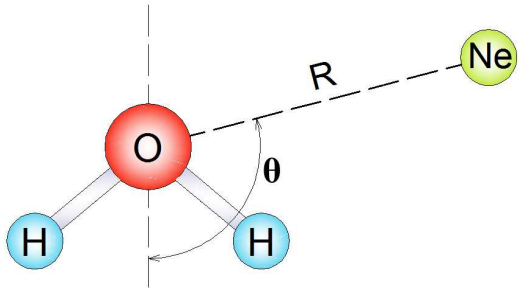

FIGURE 2.10: Definition of the Ne-H_2O coordinate system. R refers to the O-Ne distance, θ is the angle between the O-Ne vector and the C_2 axis.

2.2.2.2 Water-Argon

The Ar-H_2O mixture has proven to be difficult to be observed spectroscopically, which is attributed to its remarkably isotropic intermolecular potential. For a long time, the only detailed experimental studies of the Ar-H_20 dimer have been the molecular-beam scattering measurements of Bicks *et al.* (1975), and Brooks *et al.* (1974), from which isotropic 12-6-type potential-energy surfaces were extracted, indicating a binding energy of 1.495 kJ/mol and the equilibrium distance of 2.9 Å. The common approach to Ar-H_2O interaction was and still is the quantum mechanical calculation of potential energies at different orientations betwen solute-water molecule pair. Chałasiński *et al.* (1991)

calculated all the supermolecular and perturbation interaction terms are performed using the basis set of the whole dimer. The scan of the potential-energy surface was carried out for the coplanar and perpendicular motions of the Ar atom around water. The minimum energy -0.945 kJ/mol was achieved when the argon atom was in the water molecule plane, with the angle $\theta \approx 60°$ with the average distance $R = 3.5$ Å as shown on Figure 2.11.

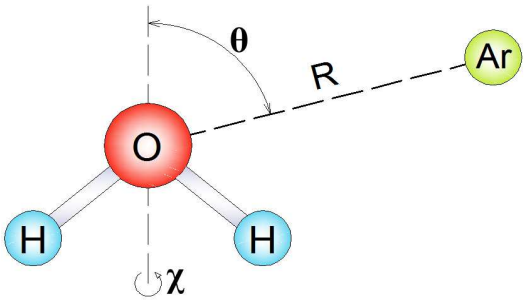

FIGURE 2.11: Definition of the Ar-H_2O coordinate system. R refers to the O-Ar distance, θ is the angle between the O-Ar vector and the C_2 axis, $\chi = 0°$ (coplanar) is the angle between the plane of water and the O-Ar vector.

Alagona and Tani (1980) performed similar *ab initio* self-consistent quantum mechanical calculations of binding energy. Their set included points with an O-Ar distance ranging from 3.3 to 7.7 Å, for seven different approach directions. Their results indicate essentially repulsive nature of argon-water potential. The same authors also applied combination MCY and Lennard-Jones potential to calculate radial distribution and O-Ar angle distribution functions. Their results coincide with the Chałasiński *et al.* (1991) results, with the average O-Ar distance 3.5 Å and O-Ar angle approximately 65°. Radial distribution function analysis shows that water molecules form 1st hydration shell around single Ar atom with mentioned distance 3.5 Å and hydrogen atoms pointing preferably outward. *Ab initio* calculation of Anderson *et al.* (2004) also showed repulsive character of water argon interaction. Anderson *et al.* (2004) compared Lennard-Jones, Kihara, and Exponential-6 potential with their O-Ar *ab initio* data. Repulsive part of Lennard-Jones potential showed best agreement with their data.

2.2.2.3 Water-Krypton

Ab initio calculation of the potential energy surface for the He-, Ne-, Ar-, Kr-, and Xe-H_2O systems performed by Makarewicz (2008) is one of the very few publications with the information about the ground state level Kr-H_2O and Xe-H_2O dimers. The ground state energy corresponding to PES is 2.005 kJ/mol with the Kr atom at distance 3.75 Å from the O atom and at angle $\theta \approx 65 - 70°$ as shown on Figure 2.10. More recent *ab initio* calculation by Lei *et al.* (2012) gives bit higher Kr-O distance 3.969 Å but similar global energy minima 2.033 kJ/mol.

2.2.2.4 Water-Xenon

All noble gases are known to cause genearl anesthesia (Poling, 1961). Xenon can play a role of anesthetic agent by taking part in forming clathrate crystals. In this crystals the xenon atoms occupy chambers in a framework formed by molecules that interact with one another by the formation of hydrogen bonds.The crystal of this sort of interest to us is called xenon hydrate. The xenon hydrate has been shown by x-ray examination to have the same structure as those of other hydrates of small molecules, such as methane or chlorine hydrate. *Ab initio* calculation of Makarewicz (2008) gives the lowest energy corresponding to PES 2.293 kJ/mol with the Xe atom at distance 4.05 Å from the O atom and at angle $\theta \approx 60°$ as shown on Figure 2.10. More recent *ab initio* calculation by Lei *et al.* (2012) gives almost the same Xe-O distance 4.0 Å and similar global energy minima 2.303 kJ/mol. Cristofory *et al.* (2005) performed MD simulation of water-xenon mixture at solute concentartions 2.5 - 6.7% at 300 and 673 K. They used combination of polarizable BSV water model (de Grandis *et al.*, 2002) and Lennard-Jones potential to investigate water-solutes pair correlation functions and their temperature dependence. Preliminary results show the tendency to demix at ambient conditions to a regime of complete solubility in the supercritical region. Noble gases despite having zero dipole moment, nevertheless, have small electronic polarizabilities. Dyer *et al.* (2008) tested five rigid three- and four-site water models in combination with Lennard-Jones and polarization term to predict solubilities of neon, argon, methane, krypton, and xenon in water. In all cases they observed that the use of polarizable solute improves agreement between experimentally observed solubility and simulations.

2.2.2.5 Water-Methane

The interactions between methane and water molecules stand out because of the polyatomic structure of the methane molecule. The real water-methane energy surface is not isotropic in relation to all possible mutual orientations of interacting molecules. Szczęśniak *et al.* (1993) showed that due to the tetrahedral symmetry, CH_4 has three unique directions at which another molecule may approach it. These are the "face," "edge," and "vertex" directions. The water molecule displays a particular ability to form van der Waals bonds when another species approaches it from the two distinct directions: (a) from the oxygen side along the C_2 axis of H_20; (b) from the hydrogen side, along the O-H bond direction. Three selected mutual orientations of CH_4 and H_2O which cover the most representative regions of the PES are shown on Figure 2.12. Case a) shows face - hydrogen orientation, b) edge-hydrogen, and c) vortex-hydrogen orientation. The "vertex" direction provides the most attractive electrostatic and polarization interaction;

however, it is also the most repulsive because it maximizes the Heitler-London (HL) exchange term. On the other hand, "face" seems to be the least favorable electrostatically but, at the same time, it is the most favorable in terms of the exchange repulsion (HL-exchange). The "edge" direction may be thought of as an intermediate between the other two. The a) case appears to have global minima -2.808 kJ/mol with the C-O distance 3.604 Å. The adjacent b) configuration appears to be slightly less favorable. The local PES minima is -2.297 kJ/mol and C-O distance is 3.869 Å. The lowest energy in c) configuration is -2.0563 kJ/mol and the C-O distance is 3.922 Å. Szczęśniak *et al* (1993) even obtained site-site analytical potential for the CH_4-H_2O interaction using nonlinear least-square fitting procedure. The potential is a combination of RWK2 (Reimers *et al.*, 1982) and the Morse type potential, and the summation runs over all C, H, and O, H atoms.

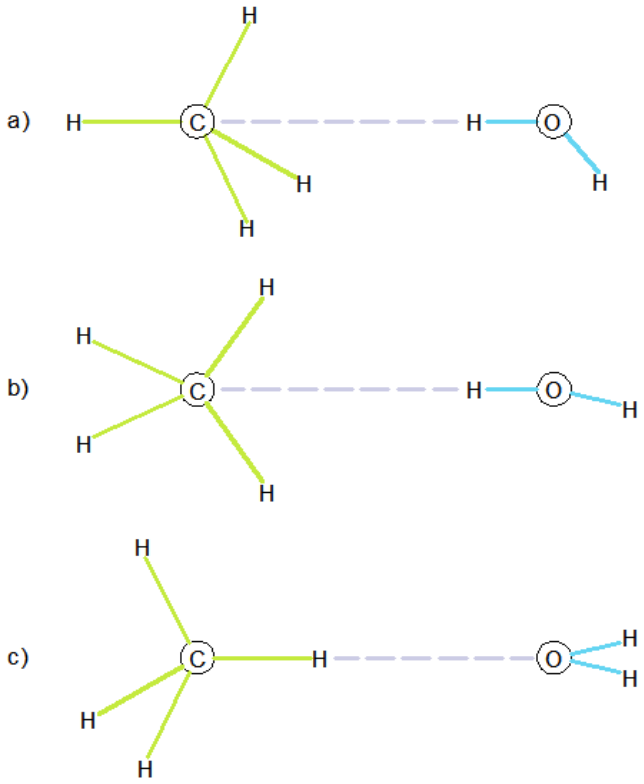

FIGURE 2.12: Definition of the CH_4-H_2O coordinate system.

More recent *ab initio* investigation by Mateus *et al.* shows two general orientations schemes, methane as a proton acceptor (PA) and methane as a proton donor (PD). In PA orientation one of the waters hydrogens points toward the carbon atom (similar to the a) case on Figure 2.12), and in the PD orientation the methane hydrogen points toward the oxygen atom (not shown of on Figure 2.12). Liquid state significantly distorts the alignment of the mentioned pair of atoms in both PA and PD cases comparing to the gas phase. In the PA case the optimized lowest energy is -3.809 kJ/mol and the C-O

distance 3.48 Å. In the PD case the optimized lowest energy is -2.428 kJ/mol and the C-O distance 3.65 Å. Mateus *et al* showed that by adopting the above two genearl orientations, methane plays the role of PD in the 56.4% cases from all selected configurations. On the other hand, for only 13.8% of the selscted configurations methane plays the role of PA. In 7.8% of all configurations methane is both PA and PD.

Cao *et al.* (2001) preformed similar study of CH_4-H_2O PES and orientations in the gas phase. They found orientation similar to b) case from Figure 2.12 to have the lowest energy 3.447 kJ/mol and the C-O separation 3.509 Å.

Increasing number of practical applications of water-methane complexes, most importantly from the shale gas mining, fuels increasing number molecular dynamic simulations on water-methane complexes. As we can see, many research efforts are being devoted to studying methane clathrates, an crystal-type structures being fromed at high pressures and negative or around zero temperatures, found in the cold waters near the ocean base or in permafrost. In this work we will focus on studying properties of water-methane system in the liquid phase. Many MD and MC simulations have been done on dilute water-methane mixtures. In the work of Okazaki *et al.* (1979) internal energy, radial distribution properties and related properties have been evaluated separately for the water in the vicinity of methane molecule and the more distant bulk water. All investigations show that thermodynamic and structural properties of vicinal water to methane differ from those of pure water. Okazaki *et al.* (1979) used combination of ST2 water model (Stilinger and Rahman, 1974) and LJ potential to describe CH_4-H_2O interaction. Docherty *et al.* (2006) applied TIP4P/2005 + LJ with modified Lorentz-Berthelot rules. Lorentz-Berthelot rules were modified in a way to account for polarizability by increasing the cross interaction energy. Errington *et al.* (1998) used SPC/E + LJ potentials to successfully simulate CH_4-H_2O phase diagram, Henry's constant and chemical potential of the dilute CH_4-H_2O system.

Overall one can say that the present knowledge about the most basic aspects of water-nonpolar solutes interactions like ground state energies of dimer configurations, let alone more complex structures, are still not satisfactory. A review of the literature shows considerable disagrement between different *ab initio* studies of the CH_4-H_2O systems in the best case, or very scant data about the less studied Kr-H_2O and Xe-H_2O systems. Without sufficient information about potential energy surface it is impossible to build reliable potential energy curves and to find the analytical fit. As a consequence, choice of the potential energy function looses physical background. Thus, the potentials lack a physical basis, and must be determined *ad hoc* from data from each hydrate system studied. Existing *ab initio* calculations of Ar-H_20 interaction are still in the formation stage and can not be considered conclusive. Many early *ab initio* potentials (Losonczy

et al., 1973; Chałasiński *et al.*, 1991) are very computationally expensive or were applied for the case of very dilute solutions (Dyer *et al.*, 2008). In addition to their theoretical complexity, the common disadvantage of these *ab initio* potentials is their inability to reproduce London dispersion interactions.

As we could see, due to the weak interaction between water and noble gases, which can serve as a model for hydrophobic interactions of water with nonpolar particles, the exact form of the interaction potential is still not known. Nonetheless, the Lennard-Jones potential given by Eq. 2.11 has been commonly used to represent nonpolar solute with considerable success (Botti *et al.* 2003; Rodger, 1990; Bourg and Sposito, 2007, 2008). In this work, for the sake of simplicity and computational economy we can easily apply the LJ potential for water-solute and solute-solute interactions. For the MD simulations, we consider solute particles as points with zero charge. LJ potential parameters used for water-solute and solute-solute pair interactions are shown on Table 2.2.

$$u_{ij} = 4\varepsilon \left[\left(\frac{\sigma}{r_{ij}} \right)^{12} - \left(\frac{\sigma}{r_{ij}} \right)^{6} \right]. \tag{2.11}$$

Here σ is the atomic diameter and ε is the potential well depth, and r_{ij} - solute-oxygen or solute-solute distance. We have chosen the parameters (see Table 2.2) of the LJ potential that are appropriate for solute particles of neon, argon, krypton, xenon, and methane (Guillot and Guissani, 1993). It is well established that the Lennard-Jones potential is a reasonable approximation for the intermolecular interactions of argon, krypton, and xenon. In contrast, increasing quantum influences mean that the parametrization of the potential for neon is likely to be less accurate. Although calculations for mixtures including neon are likely to be less quantitatively accurate than for the other systems, the trends observed are likely to be at least qualitatively correct. Calculations for water-neon are also reported here for the benefit of completeness. As long as hydrogen atoms have zero ε and σ , only oxygen atoms participate in direct LJ interaction with solute particles. Parameters for water-solute interaction are defined by the Lorentz-Berthelot combining rules (Allen and Tildesley, 1989).

$$\sigma_{12} = \frac{\sigma_1 + \sigma_2}{2}, \qquad \varepsilon_{12} = \sqrt{\varepsilon_1 \cdot \varepsilon_2}. \tag{2.12}$$

2.3 Simulation details

The molecular dynamics simulation of any atomic or molecular system in different physical conditions requires different computational approaches. For accurate calculation of system's dynamics appropriate timestep, initial configuration, integrator, thermostat/barostat, etc. have to be chosen. Depending on the complexity of the force calculation and system size, MD simulations can be time consuming and computationally expensive.

2.3.1 Simulation ensemble

As discussed in the beginning of Chapter 2, molecular dynamics simulation incorporates a group of techniques. Usually the entire simulation techniques are determined by the choice of ensembles in a simulation practice. There are five commonly used ensembles for molecular dynamics simulation, i.e. microcanonical (NVE), canonical (NVT), grand canonical (μVT), isoentalpic-isobaric (NpH), and isothermal-isobaric (NPT) ensembles (Allen and Tildesley, 1989; Landau and Lifshitz, 1980). The canonical (NVT) ensemble is chosen in this study.

2.3.2 Equations of motion

In molecular dynamics the movement of N particles is treated as then system of N Newton's laws which should be solved simultaneously. Numerical integration of the system of 3N simultaneous equations is the only viable solution. The set of variables r_{xi}, r_{yi}, r_{zi}, where $i = 1...N$, is governed by a model interaction potential which controls the dynamics of a system. Solution of this system of equations on each time step provides positions $r_i(t)$ and momenta $\mathbf{p}_i(t)$ of each particle during the simulation run. The trajectory of a typical atom at time t, $(r(t), \dot{\mathbf{r}}(t))$, is obtained by integrating the set of first-order differential equations derived from Hamiltonian formulation of mechanics (Goldstein, 1980):

$$\begin{aligned} \dot{\mathbf{r}} &= \frac{\mathbf{p}}{m} \\ \dot{\mathbf{p}} &= \mathbf{F} \end{aligned} \tag{2.13}$$

The Lagrangian formalism (Goldstein, 1980) could be used instead of for finding atomic trajectories as well. However, this approach involves integration of second-order differential equations, which increases computational load, especially with large number of

particles. Hamilton equations Eqs. (2.13) are the most common way to solve systems dynamics and, thus, are accepted in this work. The time evolution of the discretized sequence of states is obtained during the simulation run, by applying appropriate finite-difference integration scheme. Appropriate initial $(t = 0, r(0), \dot{\mathbf{r}}(0))$ boundary conditions, as well as timestep Δt must be applied for this numerical task.

2.3.3 Initial lattice configuration

According to ergodicity principle, system evolving in time which is long enough, will eventually pass trough all possible points in the phase space (Blundel and Blundel, 2009). Thus, over the very long simulation run, the choice of initial configuration for a system does not influences its final configuration. The face centered cubic (f.c.c) lattice have been adopted in our simulations as an initial system configuration at $t = 0$ (Kittel, 2005; Dekker, 1969).

2.3.4 Initial random velocity

Any system in thermodynamic equilibrium has zero overall momentum.

$$\mathbf{P} = \sum_{i=1}^{N} m\dot{\mathbf{r}}_i = 0. \tag{2.14}$$

Thus, the initial distribution of velocities are usually determined from a random distribution with the magnitudes set to the required temperature and directions set in a way that overall momentum $\mathbf{P} = 0$. The velocities are taken randomly from the Maxwell-Boltzmann distribution at given temperature T which gives the probability that an atom i has a velocity $\dot{\mathbf{r}}_{xi}, \dot{\mathbf{r}}_{yi}, \dot{\mathbf{r}}_{zi}$:

$$f_i(\dot{\mathbf{r}}_{\alpha i}) = \left(\frac{m_i}{2\pi kT}\right)^{3/2} \exp\left(-\frac{m_i \dot{\mathbf{r}}_{\alpha i}^2}{2kT}\right), \tag{2.15}$$

where $\alpha = x, y, z$. According to the kinetic theory (Pitaevskii and Lifshitz, 1981), the instantaneous temperature of the ensemble at any time during the simulation run is given by

$$T = \frac{1}{F} \sum_{i=1}^{N} \frac{|f_i|}{2m_i}, \tag{2.16}$$

where N is the number of particles, m_i - mass of the i-th particle, and F - number of degree of freedom in the system.

2.3.5 Constant temperature

In the canonical ensemble temperature of the system is held constant. In nature, such scenarios happen when a system is in contact with some external heath reservoir. In order to mimic this behavior in molecular simulations, different supplemental algorithms were proposed (Allen and Tildesley, 1989). Probably the fastest and the simplest way how to keep the temperature constant during simulation is to use so-called velocity scaling algorithm. At each scaling step, velocities of each molecule in the simulation box are scaled according to the following equation

$$v_i^{new} = v_i^{old} \sqrt{\frac{T_d}{T_a}}, \tag{2.17}$$

where T_d is the target temperature of the NVT ensemble, and T_a is current one given by Formula 2.16. In this study, the frequency of temperature scaling was chosen to be every 10 steps, based on observation of equilibration process.

Another very popular thermostat is the Nose-Hoover thermostat (Nosé, 1984; Hoover, 1985). The idea is to consider the heat reservoir as an integral part of the system by addition of an artificial variable $\tilde{t}$, associated with a "mass" $\tilde{m} > 0$ as well as a velocity $\tilde{v}$. The magnitude of $\tilde{m}$ determines the coupling between the reservoir and the real system an so influences the temperature fluctuations. The artificial variable $\tilde{t}$ plays the role of a time-scaling parameter, more precisely, the timescale in the extended system is stretched by the factor $\tilde{t}$.

2.3.6 Force calculation

The forces given by Eq. (2.13), are derived as gradients of intermolecular potential. If $u(r_{ij})$ and $\mathbf{r}_{ij}$ are the pair-potential and the vector distance between particles i and j, then the force $\mathbf{F}_{ij}$ on particle i from particle j is:

$$\mathbf{F}_{ij} = -\frac{\partial u(r_{ij})}{\mathbf{r}_{ij}}, \tag{2.18}$$

Obviously, according to Newton's third law $\mathbf{F}_{ij} = -\mathbf{F}_{ji}$. The total force exerted on particle i from all other particles in the simulation box is given as $\mathbf{F}_i = \sum_{j=1}^{N} \mathbf{F}_{ij}$.

2.3.7 Integration of motion

The positions and velocities of particles are being calculated numerically on each time step. Numerical algorithms such as leap-frog (Hockney, 1970), Verlet (Verlet, 1967; Press *et al.*, 1992), velocity Verlet (Swope *et al.*, 1982), gear-predictor algorithm (Leach, 2001), Beeman's algorithm (Beeman, 1976) and many more have been developed for this purpose. All of the above integration algorithms assume that the positions, velocities and accelerations can be approximated by a Taylor series expansion. The leap-frog algorithm used in this work is presented in the following set of equations (Li, 2008):

$$\begin{aligned} v\left(t+\delta t/2\right) &= v\left(t-\delta t/2\right)) + (1/m)F(t)\delta t, \\ r(t+\delta t) &= r(t) + v\left(t+\delta t/2\right)\delta t, \end{aligned} \tag{2.19}$$

where $F(t)$ is the force acting on a particle at time t. At the very beginning of the simulation run ($t = t_0$), velocity $v(t_0 - \delta/2)$ is given by

$$v\left(t_0 - \delta t/2\right) = v(t_0) - (1/2m)F(t_0)\delta t, \tag{2.20}$$

In the leap-frog algorithm, the velocities $v(t+1/(2\delta t))$ are calculated first and then used to calculate the positions $r(t+\delta t)$. As one can see from Eq. (2.19) the velocities and coordinates are not calculated at the same time. If represented graphically, the process of calculation of Eq. (2.19) over the simulation time looks like the velocities leap over the positions, then the positions leap over the velocities. The velocities at time t can be approximated as a simple average of velocities at times $t + 1/(2\delta t)$ and $t - 1/(2\delta t)$.

$$v(t) = \frac{1}{2}\left[v(t - 1/(2\delta t)) + v(t + 1/(2\delta t))\right]. \tag{2.21}$$

Simulation practice shows, that the leap-frog algorithm gives more accurate values of velocities and better energy conservation than the Verlet algorithm, however with the higher computation cost (Li, 2008). The leap-frog integration methods can be directly applied to any atomic or molecular system with any intermolecular potential. Real biological systems are usually polyatomic molecules with complex bond structure. Simulation of such objects requires special techniques or constraint methods, which preserve overal geometrical structure and intramolecular bonds of the simulated object.

2.3.8 Constraint method

The SHAKE algorithm is one of the most popular algorithms in molecular dynamics (Li, 2008). The main function of constraint algorythm is the preservation of real bond geometry during molecular dynamic simulation by imposing specific constraints on all intramolecular bonds and angles. The original SHAKE was derived by Ryckaert *et al.* (1977) and was an adaptation of the Verlet algorithm (1967). The first step in the SHAKE algorithm is to obtain the constrained atomic positions $\mathbf{r}_i^c(t+ \triangle t)$.

$$\mathbf{r}_i^c(t+ \triangle t) = 2\mathbf{r}_i^c(t) - \mathbf{r}_i^c(t- \triangle t) + \frac{\triangle t^2}{m_i}\mathbf{f}_i, \tag{2.22}$$

where $\mathbf{f}_i$ is the force acting along the constraint at the i^{th} iteration. These positions are adjusted iteratively until the constraint equations are satisfied to within a specific tolerance. At the i^{th} iterative loop, the atomic coordinates are $\mathbf{r}_i^{old}$. Then the constraint forces act on atoms which form given bond or angle, and yield new position.

$$\mathbf{r}_i^{new} = \mathbf{r}_i^{old} - \lambda_\varpi^I \left(\frac{\partial \sigma_\varpi(\mathbf{r}(t))}{\partial \mathbf{r}_i} \right), \tag{2.23}$$

where the Lagrange multiplier λ_ϖ^i is obtained from the following equation

$$\lambda_\varpi^i = \frac{\sigma_\varpi \mathbf{r}^{old}}{\triangle t^2 \sum_{i=1}^{N_\varpi} \frac{1}{m_i} \left(\frac{\partial \sigma_\varpi(\mathbf{r}^{old})}{\partial \mathbf{r}_i} f_i \right) \left(\frac{\partial \sigma_\varpi(\mathbf{r}(t))}{\partial \mathbf{r}_i} \right)}. \tag{2.24}$$

The obtained multiplier is for the ω^{th} constraints in the i^{th} iteration, with which new guess of positions of all atoms on ϖ^{th} constraint are made. The adjustment iterations stop after the desired degree of accuracy between new and old bonds, or so-called tolerance, is achieved. In our simulations we use tolerance $r_{new} - r_{old} = 0.00001$. The SHAKE algorithm can also be implemented using the leap-frog or predictor-corrector integrators (Li, 2008).

2.3.9 Periodic boundaries

In our simulation we are trying to predict properties of aqueous solutions in a bulk. Such systems usually contain millions of molecules which makes it very difficult to simulate them on a computer not only due to shear number of molecules but also due to surface effects, which real systems have. One possible way to solve the problem with available computational resources is the application of periodic boundary conditions (PBC). With

this method we can consider much smaller number of particles ($N = 50 \sim 1000$) in a cubic simulation box which is replicated throughout space to from an infinite lattice. Using this method we can simulate properties of bulk materials having small number of particles in the simulation box without damage to physiscal and spatial properties of the real object. A molecule that leaves the simulation box is replaced by its image particle in the neighbor cells in the opposite direction, this is clearly shown of Figure 2.13. Such behaviour eliminates unnecessary surface effects which can significantly influence bulk properties (Allen and Tildesley, 1989; Sadus, 1999). In case of polyatomic molecules PBC is applied to all atoms of the given molecule, and the centre of mass is used to judge if the entire molecule leaves the box.

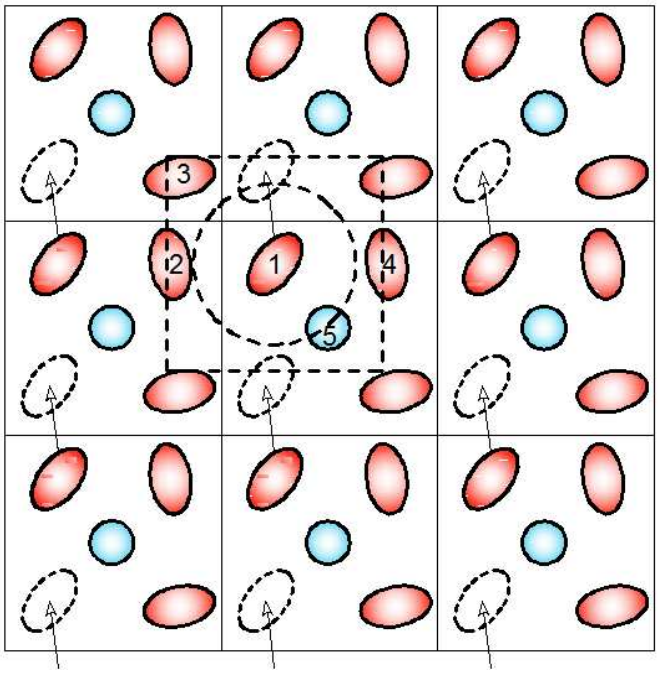

FIGURE 2.13: Diagram showing the periodic boundary conditions, minimum image convention and spherical cutoff radius.

To implement periodic boundary conditions in practice an additional step is needed to reduce the number of particles (real and images) which influence the central particle (particle 1 in Fig. 2.13). This is done by considering an imaginary box around the atom of interest which interacts only with other atoms within the imaginary box. For an imaginary box with the edge lengths l_x, l_y, l_z and $\mathbf{r}_x^{ij}$, $\mathbf{r}_y^{ij}$, $\mathbf{r}_z^{ij}$ of the pair separation vector $\mathbf{r}_{ij}$, one must apply the following condition for every particle on each step of the simulation run:

$$\begin{cases} -\frac{l_x}{2} \leqslant r_x^{ij} \leqslant \frac{l_x}{2} \\ -\frac{l_y}{2} \leqslant r_y^{ij} \leqslant \frac{l_y}{2} \\ -\frac{l_z}{2} \leqslant r_z^{ij} \leqslant \frac{l_z}{2} \end{cases} \tag{2.25}$$

The above described tecnique and Eq. (2.25) form basis for an approximation called "minimum image convention". Depending from the range of the intermolecular potential we can construct a box with the same size as initial box, and calculate interaction with finite number of molecules inside that box, while ignoring molecules outside the box. This approximation greatly reduces total number of pair-interaction from $\frac{1}{2}N(N-1)$ to $\frac{1}{2}N_c(N_c-1)$, where N and N_c are the total number of molecules and number of molecules inside the "minimum image" box. We can further improve computational speed by truncating potential on some cut-off distance r_c, which of course should be big enough not to cut out too much from the potential area and no more than the half of the "minimum image" box length. Minimum image convention box and the cut-off radius are depicted on Figure 2.13 as dotted square and circle respectively.

2.3.10 Treatment of long-range and Coulomb interactions

A potential which does not become equal to zero within any finite distance is considered to be a long-range potential. The most straightforward way to deal this situation is to truncate the potential at some distance r_{cut}, where potential is close to zero (Allen and Tildesley, 1989; Sadus, 1999). The contribution of the ignored tail of the potential $U(r)$ can be estimated to be

$$U_{lrc}(r) = \frac{N}{2}\rho \int_{r_{cut}}^{\infty} u(r) 4\pi r^2 dr, \tag{2.26}$$

where N is the total number of particles and ρ is the number density. The corresponding contribution to the virial is given by

$$P_{lrc}(r) = \frac{1}{6}\rho^2 \int_{r_{cut}}^{\infty} r \frac{du(r)}{dr} 4\pi r^2 dr. \tag{2.27}$$

Tail correction diverges, unless $U(r)$ decays faster than r^{-d}, where d is the dimensionality of the system. In case of the Lennard-Jones potential, the integral (2.26) is absolutely convergent. However, Coulomb potential does not converge with distance, therefore different technique is necessary for treatment of electrostatic forces. Ewald summation method is used in this work (Sadus, 1999; Matthey, 2002).

Ewald summation is perhaps the most popular technique for computing the electrostatic interaction interaction energies of periodic systems (e.g. crystals). Being a special case of the Poisson summation formula, in Ewald method the summation of interaction energies in real space is replaced by an equivalent summation in Fourier space. The advantage of this approach is the rapid convergence of the Fourier-space summation compared to its real-space equivalent. It is maximally efficient to decompose the interaction potential into a short-range component summed in real space and a long-range component summed in Fourier space. According to the periodic boundary condition (see Fig. 2.13), the simulation box or main cell is surrounded by replica cells that fill the whole space. The main cell consist of N particles with charges q_i at position $\mathbf{r}_i$ in a cubic box of length L. A general potential energy function U of a system of N particles with an interaction potential $\phi(\mathbf{r}_{ij}+\mathbf{n})$ and periodic boundary conditions can be expressed as

$$U = \frac{1}{2}\sum_{\mathbf{n}}\sum_{i=1}^{N}\sum_{j=i+1}^{N}\phi(\mathbf{r}_{ij}+\mathbf{n}), \tag{2.28}$$

where $\sum_{\mathbf{n}}$ is the sum over all lattice vectors $\mathbf{n} = (L_x n_x, L_y n_y, L_z n_z)$, $n_{x,y,z} \in \mathbb{N}$, $L_{x,y,z}$ are the dimensions of the unit MD cell, and $\mathbf{r}_{ij} = \mathbf{r}_j - \mathbf{r}_i$.

The Ewald summation method (Sadus, 1999; Matthey, 2002) is in general useful in systems with large, spatial potential differences, where the lattice sum is not absolutely convergent. The lattice sum with the Coulomb potential is given by

$$U^{electrostatic} = \frac{1}{4\pi\varepsilon_0}\frac{1}{2}\sum_{\mathbf{n}}\sum_{i=1}^{N}\sum_{j=i+1}^{N}\frac{q_i q_j}{|\mathbf{r}_{ij}+\mathbf{n}|}. \tag{2.29}$$

To overcome insufficient convergence of Eq. (2.29), the sum is split into two parts by the following trivial identity

$$\frac{1}{r} = \frac{f(r)}{r} + \frac{1-f(r)}{r}. \tag{2.30}$$

The first part in Eq. (2.30) should decay fast and be negligible beyond some cutoff distance, whereas the second part should be smooth for all r, such that its Fourier transform can be represented by a few terms. The assumption is made that each charge is surrounded by a neutralizing charge distribution of equal magnitude but of opposite sign. Typically, a Gaussian charge distribution is used (Sadus, 1999; Matthey, 2002).

$$\rho_i(\mathbf{r}) = \frac{q_i\alpha^3}{\pi^{3/2}}\exp(-\alpha^2\mathbf{r}). \tag{2.31}$$

The new summation then becomes

$$
\begin{aligned}
U^{electrostatic} = & \underbrace{\frac{1}{4\pi\varepsilon_0}\frac{1}{2}\sum_{\mathbf{n}}\sum_{i=1}^{N}\sum_{j=i+1}^{N} q_i q_j \frac{\mathtt{erfc}(\alpha|\mathbf{r}_{ij}+\mathbf{n}|)}{|\mathbf{r}_{ij}+\mathbf{n}|}}_{\texttt{Real-space term}} \\
& + \underbrace{\frac{1}{\varepsilon_0 V}\frac{1}{2}\sum_{\boldsymbol{\kappa}\neq 0}\frac{1}{\boldsymbol{\kappa}^2}e^{-\frac{\kappa^2}{4\alpha^2}}\left[\left|\sum_{i=1}^{N} q_i\cos(\boldsymbol{\kappa}\mathbf{r})\right|^2 + \left|\sum_{i=1}^{N} q_i\sin(\boldsymbol{\kappa}\mathbf{r})\right|^2\right]}_{\texttt{Reciprocal-space term}} \\
& - \underbrace{\frac{1}{4\pi\varepsilon_0}\frac{1}{2}\sum_{j=1}^{N_{mol}}\sum_{k=1}^{N}\sum_{l=k+1}^{N} q_{j_k}q_{j_l}\frac{\mathtt{erf}(\alpha|\mathbf{r}_{j_k j_l}|)}{|\mathbf{r}_{j_k j_l}|}}_{\texttt{Intramolecular self-energy}} \\
& - \underbrace{\frac{\alpha}{4\pi^{\frac{3}{2}}\varepsilon_0}\sum_{i=1}^{N} q_i^2}_{\texttt{Point self-energy}} - \underbrace{\frac{1}{8\varepsilon_0 V\alpha^2}\left|\sum_{i=1}^{N} q_i\right|}_{\texttt{charged system term}} + \underbrace{\frac{1}{6\varepsilon_0 V}\left|\sum_{i=1}^{N} q_i\mathbf{r}_i\right|}_{\texttt{Surface dipole term}} .
\end{aligned}
\tag{2.32}
$$

Here, ε_0 is the permittivity of vacuum and α is the splitting parameter of the real and reciprocal part. Typically, $\alpha = 5/L$ (Sadus, 1999). The intramolecular self-energy term corrects interactions on the same molecule, which are implicitly included in the reciprocal-space term. These self interactions are canceled out by the point self-energy term. The last two terms in Eq. (2.32) are necessary if the total net charge of the system is nonzero and to account for the surface dipole term respectively (Sadus, 1999; Matthey, 2002)). Cautious has to be exercised when applying the surface dipole term, as it is not suited for ions crossing the boundaries. The meaning of the symbols is as follows:

$\mathbf{n}$	lattice vector of periodic cell images
$\boldsymbol{\kappa}$	reciprocal lattice vector of periodic cell images
κ	modulus of $\boldsymbol{\kappa}$
α	real/reciprocal space partition parameter
i, j	absolute indices of all charged sites
k, l	indices of sites within a single molecule
N	total number of charged sites
N_{mol}	total number of molecules
N_j	number of sites on molecule j
q_i, q_j	charge on absolute site i, j
q_{j_k}	charge on site k of molecule j

In this work we use $\alpha = 2.75$ as reported by Shvab and Sadus (2012a, 2012b), and $\boldsymbol{\kappa} = 2\pi\mathbf{n}/L^2$, where L is the length of the simulation box. The Ewald sum (2.32) can

be extended to dipole-dipole intercation (Sadus, 1999). The forces can be obtained by applying classical formula (2.18) to each potential term in Eq. (2.32). In this work we do not calculate forces from intramolecular self-energy term (2.32) due to rigid geometry of water molecules adopted.

Chapter 3

Calculation of Thermodynamic Properties from Molecular Simulation

3.1 Thermodynamic quantities from fluctuation theory

Traditionally, most thermodynamic variables have been calculated by using fluctuation formulas (Sadus, 1999). In molecular simulations, depending from statistical mechanical ensemble, some quantities do not have constant value but fluctuate around mean value. For example, in microcanonical NVE ensemble, internal energy and the volume of the system are constant, while temperature is not. In the canonical NVT ensemble, volume is fixed and temperature is being held constant by using different (artificial) thermostats. In the isobaric-isothermal NpT ensemble pressure and temperature are maintained constant by using different barostats and thermostats, while volume of the system is allowed to fluctuate. Finally, in the grand-canonical μVT ensemble number of particles N is variable, while chemical potential μ, volume V and temperature T are constant (Sadus, 1999). These fluctuations are useful because they can be related to thermodynamic derivatives such as specific heat, isothermal compressibility, thermal expansion coefficient, etc (Allen and Tildesley, 1989; Sadus, 1999). It should be noted also that the fluctuations and the method of calculating thermodynamic derivatives are different in different statistical ensembles. However, Lebowitz *et al.* (1967) and Allen and Tildesley (1989) showed that it is possible to transform thermodynamic quantities calculated in one ensemble to the other. The difference among various ensemble averages is of the order of $1/N$ for an intensive variable in a finite system (Wallace and Staub, 1983).

Before going into details, it is useful to define ensemble and time average of the system, which are the main components of any fluctuation formula. Equilibrium and dynamical properties of a system can be obtained as time averages. The time average of dynamical function $A(t)$ in phase space is (Lebowitz *et al.*, 1967; Sadus, 1999; Allen and Tildesley, 1989)

$$\langle A(t)\rangle = \frac{1}{\tau}\int_{t_0}^{t_0+T} A(\mathbf{r}^N(t),\mathbf{p}^N(t))dt, \tag{3.1}$$

where τ is the time period, and $\mathbf{r}^N, \mathbf{p}^N$ collectively describe all N variables in the systems phase space. It is one of the basic postulates of statistical mechanics that the time average must be equal to the ensemble average at equilibrium.

$$\langle A(t_1)\rangle = \lim_{N\to\infty}\frac{1}{N}\sum_{i=1}^{N} A_i(\mathbf{r}^N(t_1),\mathbf{p}^N(t_1)), \tag{3.2}$$

where t_1 is any specific time when the ensemble average is taken, and N is the number of particles. Both Eqs. (3.1) and (3.2) must give the same result at equilibrium. We can choose either the time average or the ensemble average for the calculation of thermodynamic variables. For its convenience to implement in the simulation and the ability to work near the critical point the ensemble average which uses the statistical formalism is preferable.

It is particularly useful to calculate to calculate the root mean square deviation of an ensemble property, which is used in almost every fluctuation formula

$$\langle \delta A^2\rangle = \langle A^2\rangle - \langle A\rangle^2. \tag{3.3}$$

The fluctuation formula for isochoric heat capacity C_v in the NVT ensemble is given by (Sadus, 1999)

$$C_v = \frac{\left\langle \delta E_{pot}^2\right\rangle_{NVT}}{kT^2} + \frac{3Nk}{2}. \tag{3.4}$$

The thermal pressure coefficient for the canonical ensemble is defined as (Sadus, 1999)

$$\gamma_v = \frac{\langle \delta E_{pot}\delta p\rangle_{NVT}}{kT^2} + \frac{Nk}{V}, \tag{3.5}$$

where E_{pot} is the potential energy and p is the pressure, and $\delta p = p - \langle p \rangle$. Fluctuation formula for isothermal compressibility can be obtained from (Sadus, 1999)

$$\frac{1}{\kappa_T} = \frac{2NkT}{3V} + \langle p \rangle_{NVT} + \frac{\langle F \rangle_{NVT}}{V} - \frac{V \langle \delta p^2 \rangle_{NVT}}{kT}, \tag{3.6}$$

where:

$$F = \frac{1}{9} \sum_i \sum_{j>i} x(r_{ij}), \qquad x(r) = r\frac{dw(r)}{dr}, \qquad w(r) = r\frac{du(r)}{r}, \tag{3.7}$$

and $u(r)$ is the intermolecular potential function. By using Eqs. (3.4 - 3.8), rest of the thermodynamic properties listed in Table 3.1 can be obtained from the well-known relationships (Münster, 1970)

$$\begin{cases} C_p = C_v + k\frac{V}{N}\left(\frac{\gamma_v}{k}\right)^2 \\ \kappa_S^{-1} = \kappa_T^{-1} + \frac{TV\gamma_V^2}{C_v} \\ \mu_{JT} = \frac{1}{k}\frac{(\gamma_v/k) - (\beta/\kappa_T)}{\left(\frac{\beta \cdot N}{\kappa_T V}\right)\frac{C_v}{k} + \left(\frac{\gamma_v}{k}\right)^2} \\ \alpha_p = \frac{\mu_{JT} C_p}{TV} + \frac{1}{T} \\ \omega_0^2 = \frac{V}{N \cdot M \kappa_S} \end{cases} \tag{3.8}$$

where M is the total mass of the system, N is the number of particles, and $\beta = 1/(kT)$.

3.2 Thermodynamic quantities from statistical mechanics theory

As was mentioned in the Chapter 1, fluctuation formulas are ensemble dependent which imposes additional statistical uncertainties on simulation results. Calculations carried out in different ensembles give the same results only for systems with sufficiently large number of particles ($\gtrsim 500$) (Blundel and Blundel, 2009). Furthermore, due to limited computational resources, some biomolecular simulations operate with smaller number of molecules.

Taking this into account, an alternative approach has been applied in this work to calculate thermodynamic properties of water and aqueous solutions. Thermodynamic variables for NVT and related ensembles, based on statistical mechanics derivatives were extensively considered by Lustig (1994, 1998, 2010, 2012). In this work we use statistical

mechanics expressions derived specifically for the canonical NVT ensemble. In short, one needs the canonical partition function

$$\Pi(\beta, V, N) \approx \beta^{-F/2} \int \cdots \int_V e^{-\beta U(\mathbf{q}) d\mathbf{q}}, \tag{3.9}$$

where F is the total number of mechanical degrees of freedom of N particles in the system. The F-fold integral is over the range of all generalized coordinates symbolically collected in $\mathbf{q}$, V is the system volume, $\beta = 1/(kT)$, and k is Boltzmann constant. In statistical mechanics, the logarithm of the partition function $\Pi(\beta, V, N)$ is directly proportional to the Helmholtz energy A/T

$$-\beta A(\beta, V, N) = \ln \Pi(\beta, V, N). \tag{3.10}$$

According to Lustig's formalism (2010, 2012) any thermodynamic property can be obtained from some combination of partial derivatives of the function $\beta A(\beta, V, N)$, or equivalently on the right-hand side of Eq. (3.10). The derivation of this procedure was described in detail by Lustig (2010) and is, therefore, not described here. The basic partial derivative of the partition function $\Pi(\beta, V, N)$ with respect to the independent state variables β and V has the following form

$$\Pi_{mn} = \frac{1}{\Pi} \frac{\partial^{m+n} \Pi}{\partial \beta^m \partial V^n}. \tag{3.11}$$

The general expression of Π_{mn} can be identified with ensemble averages of configurational properties

$$\Pi_{mn} = \left(\frac{F/2}{-\beta}\right)^m \left(\frac{N}{V}\right)^n \left(P_{0,n}^{-N} \sum_{j=0}^{m} \binom{m}{j} P_{0,m-j}^{-F/2} \left\langle \left[\frac{\beta U(\mathbf{q})}{F/2}\right]^j \right\rangle + \right.$$
$$\left. (1-\delta_{0n}) \sum_{j=0}^{m} \binom{m}{j} \sum_{i=1}^{n} P_{0,n-i}^{-N} \sum_{l=1}^{i} P_{-l,m-j}^{F/2} \frac{1}{N^{i-l}} \left\langle \left[\frac{\beta\, U(\mathbf{q})}{F/2}\right]^j \sum_{k=1}^{k_{max}(i,l)} c_{ilk} \frac{V^i W_{ilk}}{N^l} \right\rangle \right), \tag{3.12}$$

where $\langle ... \rangle$ is the NVT ensemble average and δ_{ij} is the Kronecker delta. The $P_{l,m}^k$ polynomial is given in appendix Appendix A, and the term $c_{ilk} W_{ilk}$ is a product of negative volume derivatives $W_{ilk} = -(\partial^i \beta U / \partial V^i)_{\beta,N}$ of the potential energy divided by temperature and is described in detail elsewhere (Meier and Kabelac, 2006; Lustig, 2012).

The formalism outlined above is valid for any assumed intermolecular potential energy function $U(\mathbf{q})$. In this work we restrict ourselves to molecular pair interaction of atomic systems defined as:

$$U(\mathbf{q}) = \sum_{i=1}^{N-1} \sum_{j=i+1}^{N} u_{ij}(r_{ij}), \tag{3.13}$$

where r_{ij} is the distance between atoms j and i. All the volume derivatives of potential energy $U(\mathbf{q})$ necessary for calculation of Eq. (3.11) are given in the subsection 3.3. The resulting thermodynamic state variables used in our study are summarized in Table 3.1.

3.2.1 Thermal pressure coefficient

The thermal pressure coefficient γ_v is one of the fundamental thermodynamic quantities; it is closely related to various properties such as internal pressure, sonic velocity, the entropy of melting, isothermal and adiabatic compressibilities, etc. The thermal pressure coefficient is defined as

$$\gamma_v = \left(\frac{\partial p}{\partial T}\right)_V = \left(\frac{\partial S}{\partial V}\right)_T. \tag{3.14}$$

In terms of derivatives of Helmholtz energy $A(\beta, V, N)$ and partition function $\Pi(\beta, V, N)$, thermal pressure coefficient takes the form (Lustig, 2011)

$$\gamma_v = k\left(\frac{\partial(-A/kT)}{\partial V} - \beta\frac{\partial^2(-A/kT)}{\partial\beta\partial V}\right) = k(\Pi_{01} - \beta[\Pi_{11} - \Pi_{01}\Pi_{10}]), \tag{3.15}$$

where $\beta = 1/(kT)$, and Π_{01}, Π_{10} and Π_{11} are given in the Table 3.1.

3.2.2 Compressibilities

Isothermal (κ_T) and adiabatic (κ_S) compressibilities measure the changes in the volume of the system (i.e., measure the response to the volume to a pressure stimulus) when heated by maintaining the internal energy at constant temperature and entropy respectively. Isothermal and adiabatic compressibilities are defined as:

$$\kappa_T = -\frac{1}{V}\left(\frac{\partial V}{\partial p}\right)_T, \qquad \kappa_S = -\frac{1}{V}\left(\frac{\partial V}{\partial p}\right)_S, \tag{3.16}$$

where $\beta = 1/(kT)$. Transforming expression for κ_T into the one containing Helmholtz energy derivatives we get (Lustig, 2011)

$$\frac{1}{\kappa_T} = -\frac{V}{\beta}\frac{\partial^2(-A/kT)}{\partial V^2} = -\frac{V}{\beta}(\Pi_{02} - \Pi_{01}^2). \tag{3.17}$$

There is a relation between compressibilities and the heat capacities so that if the compressibilities and one of the heat capacities are known the remaining heat capacity can be calculated using the following relation, and vice versa

$$\frac{C_p}{C_v} = \frac{\kappa_T}{\kappa_S}, \tag{3.18}$$

Alternatively we can use the following well-known relation (Münster, 1970) to calculate isothermal compressibility from adiabatic compressibility, isochoric heat capacity C_v and isothermal pressure coefficient γ_v at a given temperature and volume

$$\frac{1}{\kappa_S} = \frac{1}{\kappa_T} + \frac{TV\gamma_v^2}{C_v}. \tag{3.19}$$

Substituting final expressions for C_v and γ_v from Eqs. (3.24) and (3.15) we get the following expression for adiabatic compressibility in terms of the partial derivatives of partition function $\Pi(\beta, V, N)$ (Lustig, 2011)

$$\frac{1}{\kappa_S} = \frac{V}{\beta}\left[\frac{[\Pi_{01} - \beta(\Pi_{11} - \Pi_{01}\Pi_{10})]^2}{\beta^2(\Pi_{20} - \Pi_{10}^2)} - (\Pi_{02} - \Pi_{01}^2)\right]. \tag{3.20}$$

3.2.3 Thermal expansion coefficient

The thermal expansion coefficient α_p is the measure of the tendency of matter to change in volume in response to a change in temperature keeping the pressure constant. Depending from the situationand the shape of the material thermal expansion can be linear (assuming negligible effect of pressure)

$$\alpha_L = \frac{1}{L}\frac{\partial L}{\partial T}, \tag{3.21}$$

area expansion

$$\alpha_A = \frac{1}{A}\frac{\partial A}{\partial T}, \tag{3.22}$$

as well as volumetric expansion. The general expression for volumetric thermal expansion coefficient and its connection with thermal pressure coefficient and isothermal compressibility is given by (Münster, 1970)

$$\alpha_p = \frac{1}{V}\left(\frac{\partial V}{\partial T}\right)_p = \kappa_T \gamma_v. \tag{3.23}$$

3.2.4 Heat capacities

Calculating the heat capacity of water and aqueous solutions is one of the key goals of this work, as it is one of the key properties to understand the nature of solvation (Ben-Naim, 2006, 2009). Heat capacity is the amount of hear needed to raise the temperature of a material by one degree. The measurement could be conducted either at constant volume or pressure. The isochoric heat capacity (C_v) using the first law of thermodynamics $dU = TdS - pdV$ and definition of temperature is defined as

$$C_v = \left(\frac{\partial U}{\partial T}\right)_V = -\beta\left(\frac{\partial S}{\partial \beta}\right)_V, \tag{3.24}$$

where U is the internal energy of the system. The derivative from entropy is expressed in terms of derivative of Helmholtz energy $A(\beta, V, N)$ with respect to $\beta = 1/(kT)$ and consequently as derivatives of partition function $\Pi(\beta, V, N)$ using Eq. (3.10). Similar approach will be adopted to all thermodynamic properties (Lustig, 2011).

$$C_v = k\beta^2 \frac{\partial^2(-A/kT)}{\partial \beta^2} = \frac{k\beta^2}{N}(\Pi_{20} - \Pi_{10}^2). \tag{3.25}$$

Eq. (3.25) shows heat capacity at constant volume in terms of derivatives of partition function $\Pi(\beta, V, N)$, where the values of Π_{20} and Π_{10} are given in Table 3.1. The isobaric heat capacity (C_p) which denotes the temperature variation of enthalpy $H = U + pV$ is defined as

$$C_p = \left(\frac{\partial H}{\partial T}\right)_P. \tag{3.26}$$

Enthalpy derivative is transformed to derivatives of type $(\partial.../\partial\beta)_V$ and $(\partial.../\partial V)_\beta$ which result in (Lustig, 2011)

$$C_p = -\beta^2 \frac{\left(\frac{\partial H}{\partial \beta}\right)_V \left(\frac{\partial p}{\partial V}\right)_T - \left(\frac{\partial H}{\partial V}\right)_T \left(\frac{\partial p}{\partial \beta}\right)_V}{\left(\frac{\partial p}{\partial V}\right)_T}. \tag{3.27}$$

Again applying Massieu-Planck system of thermodynamic we get the following expression for isobaric heat capacity (Lustig, 2011)

$$\begin{aligned} C_p &= \frac{\beta^2}{N} \frac{\partial^2(-A/kT)}{\partial \beta^2} - \frac{\left(\frac{\partial(-A/kT)}{\partial V} - \beta \frac{\partial^2(-A/kT)}{\partial \beta \partial V}\right)^2}{N \frac{\partial^2(-A/kT)}{\partial V^2}} \\ &= \frac{k}{N} \left[\beta^2(\Pi_{20} - \Pi_{10}^2) - \frac{[\Pi_{01} - \beta(\Pi_{11} - \Pi_{01}\Pi_{10})]^2}{\beta^2(\Pi_{02} - \Pi_{01}^2)} \right], \end{aligned} \tag{3.28}$$

where N is the total number of particles in the system.

3.2.5 Speed of sound

Due to the high accuracy of the experimental data for the speed of sound in different liquids, this property provides a very sensitive test in the course of developing an equation of state (Wagner, 1995) and so validity of simulations. The thermodynamic speed of sound at zero frequency is related to the propagation of an adiabatic pressure wave. The zero frequency speed of sound is related to the zero frequency bulk modulus, it is a derivative of the pressure with respect to mass density at constant entropy (Lustig, 2011). The speed of sound at zero frequency is defined as (Lustig, 2011)

$$\omega_0^2 = -\frac{V^2}{N \cdot M} \left(\frac{\partial p}{\partial V}\right)_S = \frac{V}{N \cdot M \kappa_S}. \tag{3.29}$$

where M is the molar mass and N is the total number of molecules. In terms of the partial derivatives of function $\Pi(\beta, V, N)$ this can be written as (Lustig, 2011)

$$\omega_0^2 = \frac{v^2}{\beta M \cdot N} \left[\frac{[\Pi_{01} - \beta(\Pi_{11} - \Pi_{01}\Pi_{10})]^2}{\beta^2(\Pi_{20} - \Pi_{10}^2)} - (\Pi_{02} - \Pi_{01}^2) \right]. \tag{3.30}$$

3.2.6 Joule-Thomson coefficient

The Joule-Thomson expansion, or throttling, of a fluid of constant composition is a closed-system process occurring between initial and final states at pressures p_0 and p_1,

with $p_0 > p_1$, for which the system enthalpy remains constant (Lustig, 2011; Lísal *et al.*, 2003). The sign of Joule-Thomson coefficient μ_{JT} at any given state determines whether the fluid is cooled ($\mu_{JT} > 0$) or heated ($\mu_{JT} < 0$) for a small change in pressure at constant enthalpy. The Joule-Thomson coefficient is defined as

$$\mu_{JT} = \left(\frac{\partial T}{\partial p}\right)_H . \tag{3.31}$$

Temperature derivative is transformed to derivatives of type $(\partial.../\partial\beta)_V$ and $(\partial.../\partial V)_\beta$ which results in (Lustig, 2011)

$$\frac{1}{\mu_{JT}} = k\beta^2 \frac{\left(\frac{\partial p}{\partial \beta}\right)_V \left(\frac{\partial H}{\partial V}\right)_T - \left(\frac{\partial p}{\partial V}\right)_T \left(\frac{\partial H}{\partial \beta}\right)_V}{\left(\frac{\partial H}{\partial V}\right)_T}. \tag{3.32}$$

Applying Massieu-Planck system of thermodynamic we get the following expression usable for practical MD simulations (Lustig, 2011)

$$\mu_{JT} = \frac{1}{k} \frac{V(\Pi_{02} - \Pi_{01}^2) + [\Pi_{01} - \beta(\Pi_{11} - \Pi_{01}\Pi_{10})]}{\beta^2(\Pi_{02} - \Pi_{01}^2)(\Pi_{20} - \Pi_{10}^2) - [\Pi_{01} - \beta(\Pi_{11} - \Pi_{01}\Pi_{10})]^2}. \tag{3.33}$$

As we already know, depending on state conditions the Joule-Thomson coefficient may be positive, negative or zero (Lísal, 2003). If μ_{JT} is positive, reduction in pressure causes reduction in temperature. This will happen at lower initial pressure. If the coefficient is negative, reduction in pressure causes increase in temperature. This will happen if the initial pressure is high. Therefore, temperature increases with increasing pressure for an isenthalpic process, reaches a maximum point and then starts to decrease with increasing pressure. The temperature corresponding to this maximum point (i.e., the crossover from heating to cooling) at which $\mu_{JT} = 0$ is referred as the "inversion point". The inversion curve is the locus of these inversion points on a p-T graph (Miller, 1970).

Formulas for all fundamental thermodynamic quantities which are used in this work are summarized in Table 3.1.

3.3 Calculation of thermodynamic quantities in the NVT ensemble

The equations for thermodynamic variables given above can be directly applied in molecular dynamic simulation. Explicit calculation of the derivatives Π_{mn} in Table 3.1 using Eq. (3.12) can be written in the following final form (Lustig, 2011):

TABLE 3.1: Summary of thermodynamic functions in terms of partial derivatives of partition function $\Pi(\beta, V, N)$.

Thermodynamic quantities	Expression in terms of Π_{mn}
p	Π_{01}/β
C_v	$\frac{k\beta^2}{N}(\Pi_{20} - \Pi_{10}^2)$
C_p	$\frac{k}{N}\left[\beta^2(\Pi_{20} - \Pi_{10}^2) - \frac{[\Pi_{01} - \beta(\Pi_{11} - \Pi_{01}\Pi_{10})]^2}{\beta^2(\Pi_{02} - \Pi_{01}^2)}\right]$
κ_T^{-1}	$-\frac{V}{\beta}(\Pi_{02} - \Pi_{01}^2)$
κ_S^{-1}	$\frac{V}{\beta}\left[\frac{[\Pi_{01} - \beta(\Pi_{11} - \Pi_{01}\Pi_{10})]^2}{\beta^2(\Pi_{20} - \Pi_{10}^2)} - (\Pi_{02} - \Pi_{01}^2)\right]$
γ_v	$k(\Pi_{01} - \beta[\Pi_{11} - \Pi_{01}\Pi_{10}])$
α_p	$\gamma_v \kappa_T$
ω_0^2	$\frac{v^2}{\beta M \cdot N}\left[\frac{[\Pi_{01} - \beta(\Pi_{11} - \Pi_{01}\Pi_{10})]^2}{\beta^2(\Pi_{20} - \Pi_{10}^2)} - (\Pi_{02} - \Pi_{01}^2)\right]$
μ_{JT}	$\frac{1}{k}\frac{V(\Pi_{02} - \Pi_{01}^2) + [\Pi_{01} - \beta(\Pi_{11} - \Pi_{01}\Pi_{10})]}{\beta^2(\Pi_{02} - \Pi_{01}^2)(\Pi_{20} - \Pi_{10}^2) - [\Pi_{01} - \beta(\Pi_{11} - \Pi_{01}\Pi_{10})]^2}$

$$\Pi_{10} = \left(-\frac{\beta}{F/2}\right)^{-1}\left[1 + \left\langle\frac{\beta U}{F/2}\right\rangle\right], \tag{3.34}$$

$$\Pi_{20} = \left(-\frac{\beta}{F/2}\right)^{-2}\left[\left(1 + \frac{1}{F/2}\right) + 2\left\langle\frac{\beta U}{F/2}\right\rangle + \left\langle\left(\frac{\beta U}{F/2}\right)^2\right\rangle\right], \tag{3.35}$$

$$\Pi_{01} = \frac{N}{V} + \left\langle-\frac{\partial\beta U}{\partial V}\right\rangle, \tag{3.36}$$

$$\Pi_{02} = \left(\frac{N}{V}\right)^{-2}\left(1 - \frac{1}{N}\right) + 2\frac{N}{V}\left\langle-\frac{\partial\beta U}{\partial V}\right\rangle + \left\langle-\frac{\partial^2\beta U}{\partial V^2}\right\rangle + \left\langle\left(-\frac{\partial\beta U}{\partial V}\right)^2\right\rangle, \tag{3.37}$$

$$\Pi_{11} = \left(-\frac{\beta}{F/2}\right)^{-1}\left[\frac{N}{V}\left(1 + \left\langle\frac{\beta U}{F/2}\right\rangle\right) + \left(1 - \frac{1}{F/2}\right)\left\langle-\frac{\partial\beta U}{\partial V}\right\rangle + \left\langle\frac{\beta U}{F/2}\left(-\frac{\partial\beta U}{\partial V}\right)\right\rangle\right]. \tag{3.38}$$

In summary, thermodynamic properties in the NVT ensemble are given by ensemble (simulation) averages of type $\langle\partial^p U/\partial V^p \times \partial^q U/\partial V^q \times \ldots \partial\rangle$ with $p, q \geq 0$. The results so far are generally valid for any assumed intermolecular interaction energy $U(\mathbf{q})$. The

volume derivatives $\partial^p U/\partial V^p$, however, have to be worked out case by case. In this work we apply this formalism to the SPC/E and TIP4P/2005 pair-potentials which are described in detail in Chapter 2. The intermolecular energy function $U(\mathbf{q})$ has the form

$$U(\mathbf{q}) = \sum_{i=1}^{N-1} \sum_{j=i+1}^{N} u_{ij}(r_{ij}), \tag{3.39}$$

where the radial distances r_{ij} between atoms i and j are the only generalized coordinates in $\mathbf{q}$. If the system is contained in a cubic box of volume V the distance between the particles implicitly depend on the volume of the system. To remove this dependence we will introduce the scaled distance $\acute{r}_{ij}$ with a transformation $r_{ij} = V^{1/3}\acute{r}_{ij}$. The scaled distance r_{ij} do not depend on the volume of the system

$$\frac{\partial r_{ij}}{\partial V} = \frac{1}{3} V^{-2/3} \acute{r}_{ij} = \frac{r_{ij}}{3V}. \tag{3.40}$$

applying this rule, the first volume derivative of U is standard and given by (Meier and Kabelac, 2006)

$$\frac{\partial U}{\partial V} = \frac{1}{3V} \sum_{i=1}^{N-1} \sum_{j=i+1}^{N} r_{ij} \frac{\partial u_{ij}}{\partial r_{ij}}. \tag{3.41}$$

The second-order derivative, required here is given by (Meier and Kabelac, 2006)

$$\frac{\partial^2 U}{\partial V^2} = \frac{1}{9V^2} \sum_{i=1}^{N-1} \sum_{j=i+1}^{N} \left(-2 r_{ij} \frac{\partial u_{ij}}{\partial r_{ij}} + r_{ij}^2 \frac{\partial^2 u_{ij}}{\partial r_{ij}^2} \right). \tag{3.42}$$

in general, the nth volume derivative of the potential energy is given by

$$\frac{\partial^n U}{\partial V^n} = \frac{1}{3^n V^n} \sum_{i=1}^{N-1} \sum_{j=i+1}^{N} \sum_{k=1}^{n} a_{nk} r_{ij}^k \frac{\partial^k u_{ij}}{\partial r_{ij}^k}. \tag{3.43}$$

The coefficients $a_{n,k}$ can be constructed by the recursion relation

$$\begin{aligned} a_{n,k} &= a_{n-1,k-1} + (-3(n-1)) + k) a_{n-1,k}, \\ a_{n,1} &= \prod_{l=0}^{n-1} (-3l+1), \qquad a_{nn} = 1. \end{aligned} \tag{3.44}$$

Chapter 4

Molecular Structure and Hydrogen Bonding in Aqueous Solutions

As was described in Chapter 2, water exhibits a number of unusual properties starting from well known density anomalies (density maximum, expansivity behavior) to thermodynamical (high heat capacity and entropy of vaporization), physical (high viscosity and surface tension), and material anomalies (high dielectric constant, low solubility of nonpolar solutes, at least 15 crystalline polymorphs), etc. (Chaplin, 2013; Ball, 2008). Many of these anomalies are transferred to aqueous solutions (Ben-Naim, 2006). Apart from exclusively water anomalies, the picture becomes even more complicated when solute molecules are added (Feig, 2010). Aqueous solutions of different solutes, e.g. solutions of ionic and nonpolar solutes are two big overlapping branches of physical chemistry. Aqueous solutions of biological molecules is another research field with most focus from scientific community. Since the dawn of simulation studies of water (Eisenberg and Kauzmann, 1969) it is assumed that the main part of all mentioned anomalies is caused by unique water structure, namely ability to form extensive H-bond network.

In this chapter we will elucidate the main aspects of water molecular structure and structure of several aqueous nonpolar solute mixtures. Probably the most straightforward way to investigate the structure of any molecular or atomic liquid is to use the pair correlation functions. The best function for investigation of structural and density variations is so-called Radial Distribution Function (RDF). The radial distribution function $g(r)$ in a system of particles (atoms, molecules, colloids, etc.), describes how density varies as a function of distance from a reference particle. If a given particle is taken to be at the origin O, and if $\rho = N/V$ is the average number density of particles, then the local time-averaged density at a distance r from O is $\rho \cdot g(r)$. This simplified definition holds for a homogeneous and isotropic system. The function $g(r)$ is shown below

$$g(r) = \frac{V}{4\pi r^2 N(N-1)} \left\langle \sum_i n_i(r)\Delta r \right\rangle, \tag{4.1}$$

where V is the system volume, and $n(r)\Delta r$ is the number of particles which exist in the region between r and $r + \Delta r$. Figure 4.1 presents the general scheme of function $g(r)$ calculation.

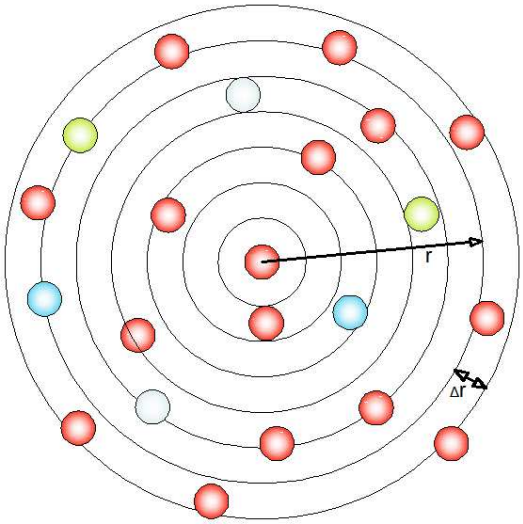

FIGURE 4.1: Diagram presenting radial distribution function calculation.

It is clear that $g(r)$ should go to 1 at large r. At very short r the radial distribution function must be zero, because two particles cannot occupy the same space. The water RDF has oscillating decaying behavior, with 2 - 3 distinctive peaks. Each peak represents region with higher number density comparing to adjacent minima, which correspondingly represent region with smaller number density. The surplus of particles in the first highest peak causes a lack of particles a little bit further on, explaining the first minimum of $g(r)$ and so on. For polyatomic molecules, all the different combinations of RDFs, give relative positions of molecules as well as the intermolecular bonding information. By using RDFs we can calculate any desirable coordination number n_{ij} which is the mean number of atoms/molecules within the coordination sphere limited by r_1 and r_2. The first-order coordination number can be estimated by taking integration limits $r_1 = 0$ and r_2 being the position of the first RDF peak. In the present study we will be using mainly first order coordination numbers given by formula

$$n_{ij}(r) = 4\pi\rho \int_0^{r_{min}} g_{ij}(r) r^2 dr. \tag{4.2}$$

The ij subscript in $g_{ij}(r)$ stands for different kinds of interatomic RDFs we are interested in, for example, O-H, O-O, Ne-O, Ar-O, CH_4-O, etc.

The first purpose of the present study is to examine the effects of temperature and density on the structure and dynamics of bulk water and aqueous nonpolar solutions for a wide range of states using molecular dynamics (MD) calculations. As we already know, most of the peculiarities of water behavior are ascribed to the hydrogen bond (H-bond) and the ability of water molecules to form three-dimensional networks. At ambient conditions, the first peak of the oxygen-hydrogen radial distribution function around 1.8 Å is a manifestation of hydrogen bonding between molecules. Despite some ambiguity in H-bond definition, computer calculations with common empirical potential models have successfully reproduced this hydrogen-bonding peak for ambient water (Berendsen *et al.*, 1987; Abascal and Vega, 2005, Li *et al.*, 2007). To investigate the properties of the hydrogen bonds at extreme conditions, studies have been extended to the supercritical state (Shvab and Sadus, 2012a; Yoshii *et al.*, 1998; Dyer and Cummings, 2008). The region of supercritical temperatures and pressures is where most of the discrepancy between MD data and experiments arises.

The questions of preservation of H-bond network at critical and supercritical conditions, and the H-bond lifetime are the most intriguing and crucial for our study of water structure. The *ab initio* calculations of Kang *et al.* (2011) indicate a conservation of 50% of H-bonds above 800 K. Molecular dynamics calculation with the TIP4P model indicated that 70% of the hydrogen bonds found at ambient conditions remain at temperatures up to 1130 K (Mountain, 1989). However, neutron diffraction experiments using the isotopic substitution technique (NDIS) of Soper show that the first peak of oxygen-hydrogen RDF completely disappears in the supercritical state at 673 K and densities of 0.58 and 0.66 g/cm^3 (Soper, 2000). This suggests that the hydrogen bonding network do not exist at supercritical conditions despite the fact that the hydrogen-bonding energy is well above thermal energy at 673 K. Tromp *et al.* (1994) suggested that the reason for this discrepancy is due to the deficiency of pairwise additive potentials such as TIP4P. Alternatively, Loffler *et al.* (1994) claimed that the discrepancy arises from the inelasticity correction to the neutron data, which is particularly large for the light water sample.

Recent in situ x-ray diffraction (XRD) experiments of Ikeda *et al.* (2010) and Weck *et al.* (2009) are in better agreement with the calculation results. However, the picture of hydrogen bonding in water at elevated temperatures and pressures is still different between calculations and experiments. A possible reason for our poor understanding of water structure at critical conditions comes from specific nature of modern water models. The properties of water are most commonly obtained using fixed point charge models (Berendsen *et al.*, 1987; Mountain, 1989). Typical examples are the SPC/E, SPC/Fw, and TIP4P models described in the Chapter 2. The parameters for such potentials are optimized to reproduce the properties of liquid water at the ambient conditions of temperature 298 K and density of 1 g/cm^3. Except from being fine-tuned, these models

describe interaction in water in somewhat simplified way, usually having nonadditive corrections implicitly incorporated into the potential function. For example in case of SPC/E and TIP4P models accounting for nonadditive contributions like polarization was achieved by increasing values of charges on hydrogen and oxygen sites (SPC/E) or shifting charged site slightly from oxygen atom (TIP4P). If one wants to investigate water structure and properties in the wide temperature-pressure region he has to adopt more realistic approach and try to calculate not only pair-wise interactions but also polarization and three-body interactions explicitly.

4.1 Simulation details

All simulation results presented in Chapters 4 - 7 were performed in canonical NVT molecular dynamics simulations (Sadus, 1999) using the Shake constraint algorithm (see Eqs. (2.22 - 2.24) in Chapter 2) for the total number of 500 molecules. In the case of pure water a cubic periodic simulation cell was used with fixed box lengths of 2.466, 2.654, and 2.921 Å for the 1, 0.8, and 0.6 g/cm^3 isochores, respectively. In case of binary mixtures all simulations were performed at standart density 0.998 g/cm^3 for mixtures with solute concentrations x_s = 1, 2, 4, 6, 10, 15, 20, and 30%. All simulations were commenced from an initial face centered cubic lattice with a time step of 2 fs (Chapters 4 - 6) and 1 fs (Chapter 7). The systems were equilibrated for 500 ps before any ensemble averages were determined. At each temperature, the total simulation time was at least 2 ns, which corresponds to 1 $\times$ 10^6 time steps. The equations of motion were integrated using a leap-frog algorithm (see Eqs. (2.19 - 2.21) in Chapter 2). The Ewald summation method was used to evaluate the long-range part of the Coulomb potential (see Eqs. (2.28 - 2.32) in Chapter 2). The convergence parameter for the Ewald sum was α = 5.0/L, with summation over 5×5×5 reciprocal lattice vectors, where L is the box length. A cutoff of L/2 was applied to the SPC/E (Berendsen *et al.*, 1987), SPC/Fw (Wu *et al.*, 2006), TIP4P/2005 (Abascal and Vega, 2005) additive two-body potentials, as well as two-body part of MCYna potential (Matsuoka *et al.*, 1976). The three-body part of the MCYna potential was truncated at L/4.

During the pre-equilibration stage, the temperature was held constant by rescaling the velocities every ten steps, which we found to be equivalent to results obtained using a Gaussian thermostat. To determine the induced dipole moment (Eq. (2.8) in Chapter 2), a direct solver, namely, the conjugate gradient method (Karniadakis and Kirby, 2003), was used. All ensemble averages were obtained by analyzing post-equilibrium configurations at intervals of 100 time steps and standard deviations were determined. The introduction of the induced dipole calculation and the Axilrod-Teller term (Eq. (2.6) in

Chapter 2) significantly increases the computation load, requiring the implementation of a modified force decomposition algorithm (Li *et al.*, 2006) to parallelize the calculation. It was implemented with the MPI library, with more than 98% of the computational load distributed among 32 processors.

4.2 Molecular structure and hydrogen bonding in bulk water

As was clearly suggested in the comprehensive review of Vega and Abascal (2011), a realistic model should include the polarization effect of the molecule to accurately describe the inter-molecular interaction in the sub- and supercritical states. Kang *et al.* (2011) and Dyer *et al.* (2008) reported a first principle studies of sub- and supercritical water which account for the state dependence of intermolecular interactions. These workers calculated the structure factors and polarization distribution in water. However, the method used is computationally expensive and involves a very small number of particles (32 - 64 molecules). We need simpler models to investigate the properties of water over a wide range of thermodynamic states. A natural improvement of the empirical potential models is to explicitly introduce nonadditive many-body interactions such as three-body and polarizable contributions. In this work, we apply an *ab initio* MCYna potential model (see Eq. (2.4 - 2.7), Chapter 2) for investigation of structural and polarization properties of bulk water and compare results with the previous *ab initio* and MD results as well as with available experimental data. This water model was introduced by Li *et al.* (2007) and contains an *ab initio* description of two-body additive interactions plus nonadditive contributions from both three-body interactions and polarization.

4.2.1 Structural properties along the isochore at 1 g/cm^3.

Analysis have been carried out for bulk water along the isochores 1, 0.8, and 0.6 g/cm^3 in the temperature range from 278K to 750K. Fig. 4.2 shows the temperature dependence of oxygen-oxygen (g_{oo}), oxygen-hydrogen (g_{oh}), and hydrogen-hydrogen (g_{hh}) RDFs for the isochore $\rho = 1$ g/cm^3 or in other word at normal density. For g_{oo} at 298 K the positions of the first peak, second peak, and first minimum are at 2.74, 4.53, and 3.36 Å, respectively, which are in good agreement with X-ray scattering (Allesch *et al.*, 2011; Sorenson *et al.*, 2000), neutron diffraction measurements (Soper, 2000), and *ab initio* simulation of the infra-red spectrum of bulk water (Heyden *et al.*, 2010). Such positions of the 2nd and the 1st peaks are ascribed to the local tetrahedral ice-like structure of the water. Thus, the peaks implicitly indicate the three-body correlation of oxygen atoms (Li

et al., 2007). As temperature increases the 1st peak of g_{oo} broadens considerably but its position remains essentially fixed with only a small outward shift. The second peak and the first minimum shift considerably from 4.53 and 3.36 Å at 298 K to 6.01 and 4.59 Å at 750 K, respectively. At 298 K the 1st g_{oo} coordination shell is very thin spanning from 2.74 to 3.36 Å, which suggests a layer of water molecules rather than a shell. In contrast at T = 750 K the 1st g_{oo} coordination shell is much thicker spanning from 2.74 to 4.59 Å which is the middle of the 2nd shell at ambient temperature. Such behavior suggests that the local structure changes significantly with temperature. When the temperature rises above the normal boiling temperature, the second peak gradually flattens out and almost disappears in the supercritical region. Such temperature dependence of the 2nd peak indicates a gradual merging of the first and second coordination shells of water molecules with increasing temperature and pressure. This, in turn, indicates a significant reorganization of the H-bond network. Namely, the partial breaking of the total number of H-bonds and consequent transition of water structure from tetrahedral to more closely packed geometry. The ratio of the second peak position to the first one gives a measure of the local structure in the fluid. At 298 K, the ratio is 1.65, which is ascribed to the local tetrahedral coordination of the water molecules mentioned above. On the other hand, at 750 K, the ratio is 2.1, which is equivalent to that of simple liquids such as argon (John *et al.*, 1975).

The temperature dependence of the oxygen-hydrogen (g_{oh}) and hydrogen-hydrogen (g_{hh}) radial distribution functions illustrated in Fig. 4.2 is similar to that of oxygen-oxygen (g_{oo}). When temperature and pressure are increased, the peaks broaden significantly and gradually shift towards larger intermolecular distances. The behavior of the g_{oh} first peak is the most interesting. Increasing the temperature results in the peak flattening out and eventually disappearing at T $\geq$ 650 K. The very sharp separation between the two O-H shells and their position relative to the 1st O-O peak at ambient conditions indicates a regular order in O-H covalent bonds orientations. For example, the 1st O-H peak is located at 0.922 Å (the length of the O-H covalent bond in this model is 0.975 Å) behind the 1st O-O peak, which means that the H atoms are orientated almost radially toward the O atom of the central water molecule. Increasing thermal energy diminishes the separation between the O-H shells and at T $\geq$ 650 K they appear to merge into one shell. This means that most H atoms no longer have a preferred orientation relative to the neighboring molecules and are free to rotate around their own oxygen atom. The observed temperature dependence of g_{oh} indicates the collapse of H-bond network at T $\geq$ 650 K for the MCYna model.

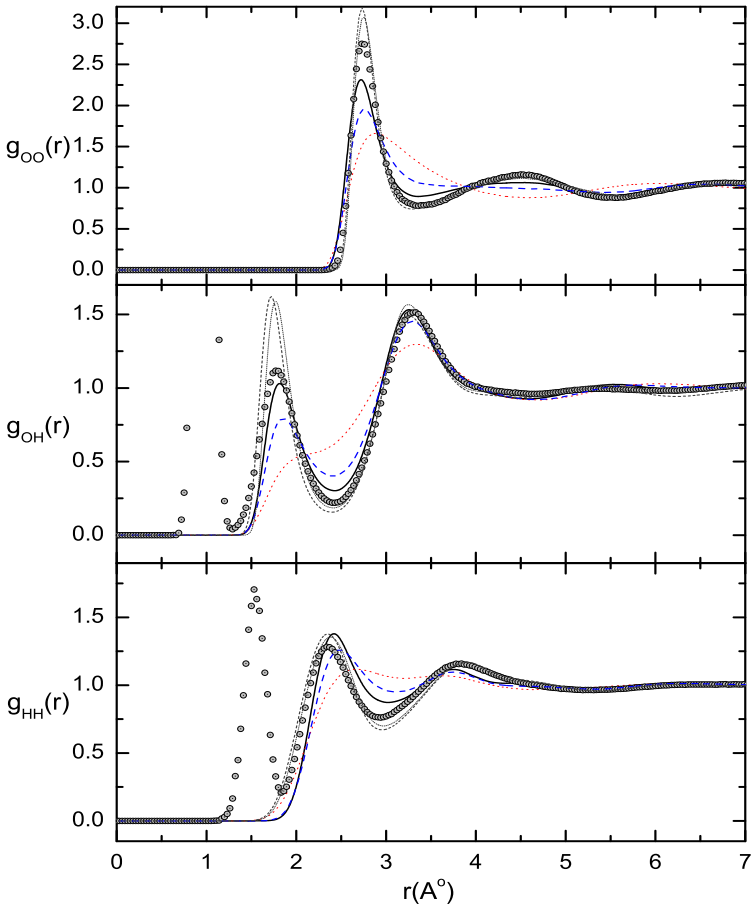

FIGURE 4.2: Temperature dependence of the oxygen-oxygen, oxygen-hydrogen, and hydrogen-hydrogen RDFs along the 1 g/cm^3 isochore obtained from the MCYna model (298 K, thick black line; 400 K, dashed blue line; 750 K, dotted red line). At T = 298 K and ρ = 1.0 g/cm^3 experimental data (Soper, 2000) are available (gray circles) and a comparison at this temperature is also given for the SPC/E (gray short dotted line), and SPC/Fw (gray short dashed line) models.

4.2.2 Structural properties along the isochore at 0.8 g/cm^3.

Our investigation would be incomplete without data about water structure at lower densities. Fig. 4.3 illustrates the temperature dependence of RDFs along the isochore ρ = 0.8 g/cm^3. The effect of reduced density can be immediately seen on the overall shape of the curves. The 1st g_{oo} peak at 573 K is only 2.1 high with almost vanished 2nd peak, which indicates distorted water structure and weaker H-bond network. At 573 K and higher, H-bond network is already distorted with a large number of broken hydrogen bonds and water behaves much like simple liquid. With increasing temperature the first and second peaks are broadening only slightly, while the 1st oxygen-hydrogen minima is disappearing completely. The average intermolecular distance for this isochore is larger than at ρ = 1 g/cm^3 which manifests in peaks slightly shifted to the right. It is interesting to note, that at smaller densities average intermolecular distance is not proportionally bigger that at normal density. Experimental observations (Soper, 2000) show that the

average distance is about the same, but water structure changes from the extensive H-beond network towards one with more localized spatially closed clusters. Another effect caused by the reduced density is the smaller 1st g_{oh} peak and faster disappearance of the 1st g_{oh} minima with temperature. For example, at 0.8 g/cm^3 this minimum vanishes at approximately 550 K, whereas at 1 g/cm^3 they disappear at 650 K. Smaller 1st g_{oh} peak obviously indicates smaller number of H-bonds between in the 1st coordination shell.

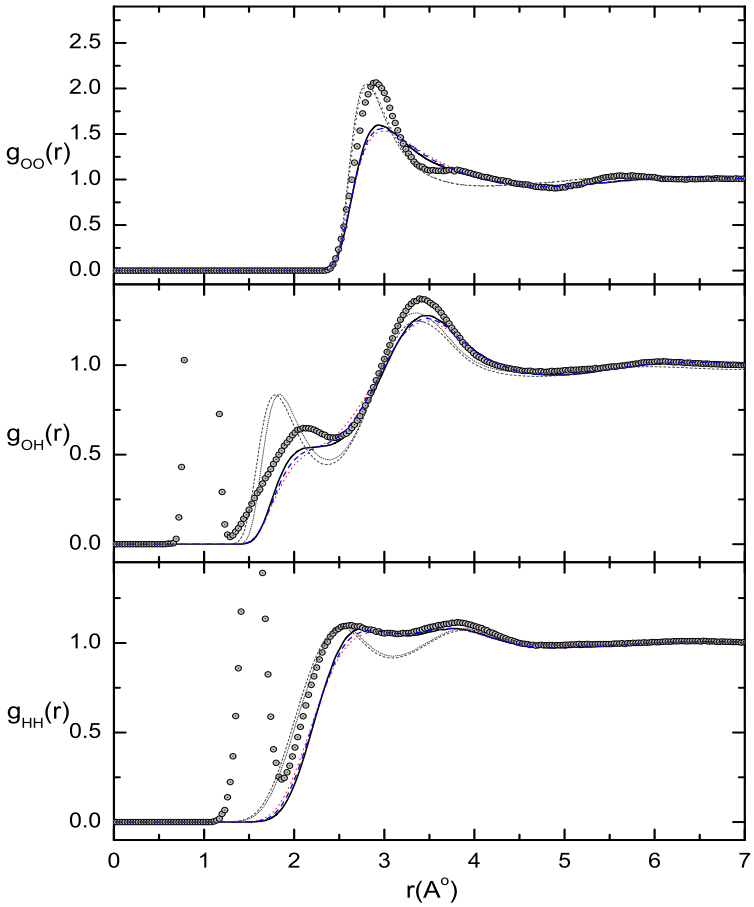

FIGURE 4.3: Temperature dependence of oxygen-oxygen, oxygen-hydrogen, and hydrogen-hydrogen RDFs along the 0.8 g/cm^3 isochore (573 K, thick black line; 650 K, blue dashed line; 750 K, red dotted line). At 573 K and $\rho = 0.78$ g/cm^3 , experimental data (Soper, 2000) are available (gray circles) and a comparison at this temperature is also given for the SPC/E (gray short dotted line), and SPC/Fw (gray short dashed line) models. Sharp peaks on the experimental g_{oh} and g_{hh} curves represent oxygen and hydrogen atoms of the same molecule.

4.2.3 Structural properties along the isochore at 0.6 g/cm^3.

Fig. 4.4 illustrate the temperature dependence of RDFs along the isochore $\rho = 0.6$ g/cm^3. At such a small density water structure is significantly distorted with little resemblance to the classical tetrahedral structure at ambient conditions. The 1st g_{oo} peak at 550 K is only about 1.6 high indicating even smaller 1st hydration shell and nonexistent 2nd shell.

The absence of the 2nd and furher shells means absence of any long-range correlations at these conditions. The RDFs behave very much like in the case of ρ = 0.8 g/cm^3 with very little changes to g_{oo} and g_{oh} peaks. Weak temperature dependence of water RDFs at reduced densities indicates and high temperatures distorted spatial structure of water. While at ambient conditions water exhibits extensive H-bond network with large free volume inside the network, at extreme conditions the H-bond network is significantly distorted, and the volume is occupied with the clusters with smaller surface area. The 1st g_{oo} peak is shifted to the right by some 0.3 Å from the same peak at 0.8 g/cm^3 and by 0.6 Å from the 1st peak at 1.0 g/cm^3. Another effect caused by the reduced density is the faster disappearance of the 1st g_{oh} minima with temperature. For example, at ρ = 0.6 g/cm^3 this minimum vanishes at approximately 450 K, whereas at 1 g/cm^3 they disappear at 650 K.

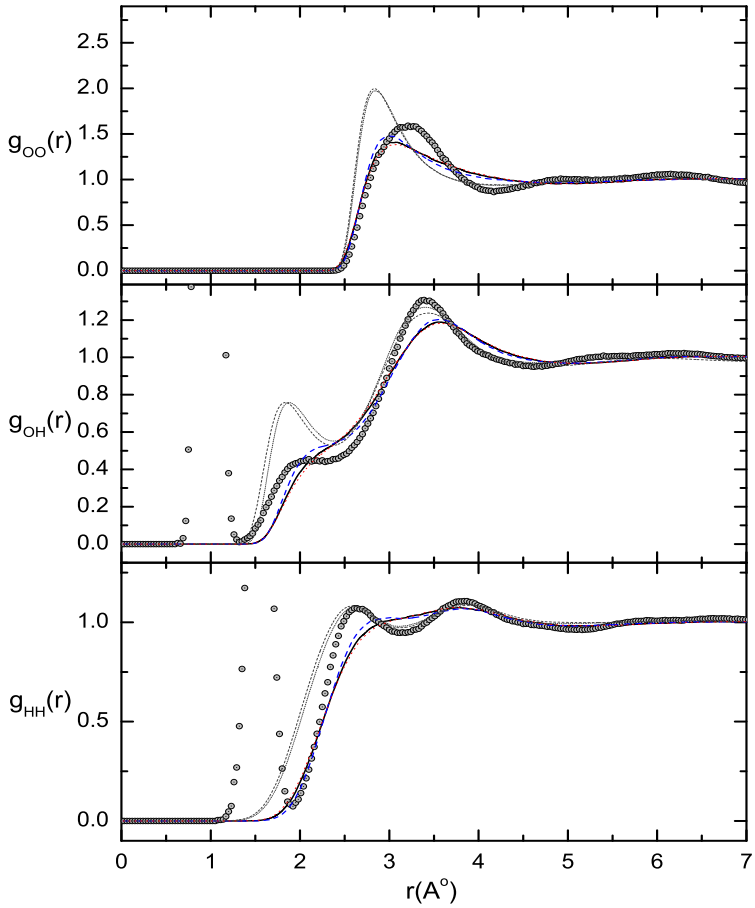

FIGURE 4.4: Temperature dependence of oxygen-oxygen, oxygen-hydrogen, and hydrogen-hydrogen RDFs along the 0.6 g/cm^3 isochore (550 K, blue dashed line; 673 K, thick black line; 750 K, red dotted line). At 673 K and ρ = 0.58 g/cm^3, experimental data (Soper, 2000) are available (gray circles) and a comparison at this temperature is also given for the SPC/E (gray short dotted line), and SPC/Fw (gray short dashed line) models. Sharp peaks on the experimental g_{oh} and g_{hh} curves represent oxygen and hydrogen atoms of the same molecule.

In Figs. 4.2-4.4, simulations are compared with available NDIS experimental data (Soper, 2000) as well as with data from the SPC/E (Beendsen *et al.*, 1987) and SPC/Fw (Wu *et al.*, 2006) models. In general, RDFs for the 1 g/cm^3 isochore coincide with experimental curves except the case of a smaller first g_{oo} peak. This feature was noticed by Niesar *et al.* (1990) and can be explained by the fact that the MCY potential is too repulsive. This is due to the fact that very few configuration state functions were used for the computation of water dimers energies to obtain a good fit. However, the g_{oh} and g_{hh} values obtained from the MCYna model show much better agreement with experimental curves than the corresponding RDFs from non-polarizable SPC/E and SPC/Fw models. RDFs for the 0.8 g/cm^3 and 0.6 g/cm^3 isochores show qualitative agreement with NDIS curves. Overall, comparing MD RDFs with the experimental data we observed much greater preservation of the 1st and the 2nd water shells at smaller densities than is predicted by MD simulations. These discrepancies can be attributed to the parametrization of the *ab initio* MCY model (Matsuoka *et al.*, 1976). Originally this model was developed with the help of configuration-interaction method to describe water properties at normal conditions.

4.2.4 Shell structure

Oxygen-hydrogen (n_{oh}) coordination numbers together with RDFs allow better understanding of shell structure and H-bonding of water molecules at different densities and temperatures. Since the molecular structure in liquid water differs greatly from a regular crystal configuration, it is difficult to unambiguously define a fixed upper limit r_{min} in the integral (4.2). In fact, the n_{oh} coordination number depends largely on the choice of this value. In this work we accept position of the first $g_{oh}(r)$ minima as r_{min}. Thus, r_{min} means the size of the 1st oxygen-hydrogen solvation shell. Oxygen-hydrogen (n_{oh}) coordination numbers for water along the isochores 1, 0.8, and 0.6 g/cm^3 are presented on Fig. 4.5.

Starting from the values of 2.71, 2.544, and 2.215 at 278 K they gradually decrease to 1.336 at 650 K, 1.366 at 550 K, and 1.409 at 450 K respectively. Interruption of n_{oh} is taking place due to the vanishing of the 1st g_{oh} minima at approximately 650 K, 550 K, and 450 K along each respective isochore. This behavior of the 1st g_{oh} minima indicates the merging of water shells as a consequence of complete collapse of the H-bonding network. This indication of complete collapse of H-bonding network seems to be premature and a characteristic only of the MCYna potential. We cannot infer the complete collapse of H-bond network from RDFs alone. More sophisticated calculations are required in order to estimate the number of remaining H-bonds. Molecular dynamics simulation results at $\rho = 1$ g/cm^3 for other polarizable models show much better

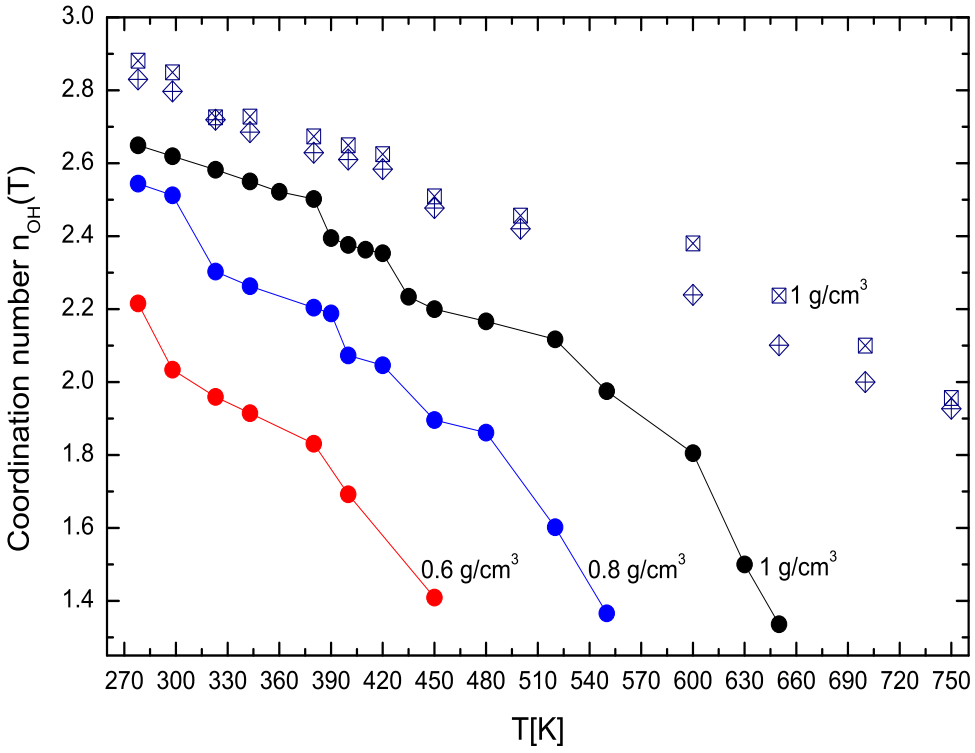

FIGURE 4.5: Evolution of the first oxygen-hydrogen coordination numbers with temperature along the 1, 0.8, and 0.6 g/cm^3 isochores. Comparison is between MCYna (circles), SPC/E (crossed squares), and SPC/Fw (crossed diamonds).

conservation of H-bond structure. For example, according to the *ab initio* simulation of Kang *et al.*(2011) the tetrahedral H-bond network exhibits collapse above 800 K whereas calculation with TIP4P model (Mountain, 1989) indicates that 70% of hydrogen bonds still remain at temperatures up to 1130 K. The number of hydrogen bonds obtained from non-polarizable models like SPC/E (see Fig. 4.5) keep gradually decreasing well beyond 650 K. According to the MCYna potential, at T $\geq$ 650 K (ρ = 1 g/cm^3), almost half of the H-bonded molecules transform to be interstitial molecules. The reason for the discrepancy between the potential models is due to the definition of hydrogen bond. It is important to note that the n_{oh} coordination number is not exactly the number of hydrogen bonds. Eq. (4.5) defines average number of molecules, which lie within a distance r_{min} from the central water molecule. As was shown by Kalinichev and Bass (1994), this number coincides with number of H-bonds only at T $\leq$ 500 K. At higher temperatures and pressures geometrical criteria alone used in Eq. (4.5) are not sufficient. More elaborate criteria are required for the definition of H-bonds over wider range of state points (Yoshii *et al.*, 2011; Kalinichev and Bass, 1994). Taking such factors into consideration and despite the fact the quantitative assessment of the degree of hydrogen bonding is still a matter of debate, we can say that in real water at least some part of H-bond network still exists even at supercritical temperatures. The evaluation of oxygen-hydrogen coordination numbers along the 1g/cm^3 isochore has also been performed for the rigid

SPC/E and flexible SPC/Fw models. The comparison with the flexible water model is particularly important at high temperatures when the energy of intermolecular vibrations is comparable with k_BT. Incorporation of flexibility is intended to produce more realistic dynamic behavior of hydrogen bonds. It is apparent from Fig. 4.5 that these models give values of n_{oh} higher by approximately 0.4 and keep gradually decreasing well beyond 650 K. Introduction of bond flexibility does not significantly n_{oh} change compared to the rigid SPC/E model. However, as discussed above, SPC based models overestimate the water structure, resulting in a 1st OH peak that is too high and an unrealistically sharp separation between the water shells, especially at lower densities. Taking into account the comparison between MD and experimental RDFs from Figs. 4.2 - 4.5, it is apparent that the MCYna model yields more accurate n_{oh} values than the SPC-based models. It is also important to note that at lower densities it is difficult to calculate reliable n_{oo} and n_{oh} for non-polarizable water models due to strong local density fluctuations.

We also calculated oxygen-oxygen coordination numbers (n_{oo}) along the isochores 1, 0.8, and 0.6 g/cm^3 (see Table 4.1). In the 278-373 K temperature region the n_{oo} have very similar values, only increasing slowly with an increase on temperature. Along the 1 g/cm^3 isochore n_{oo} starts from the classical value of 4.6 at 278 K and increases to approximately 4.9 at T = 373 K. For the 0.8 g/cm^3 isochore n_{oo} increases from 4.076 to 5.5. For the 0.6 g/cm^3 isochore n_{oo} has values from 3.7 at 278 K to 4.5 at 373 K. The closeness of these coordination numbers in this temperature region indicates the presence of tetrahedral structure in water along the isochore 0.8 and possibly 0.6 g/cm^3. However, in the temperature region shortly after normal boiling temperature and until approximately 400 K a very sharp rise in the n_{oo} values occurs. After 400 K, n_{oo} slowly decreases to values of 12∼13 at supercritical temperatures (John and Eyring, 1975). The reason for this discontinuity in n_{oo} values can be seen in the temperature dependence of oxygen-oxygen RDFs. In this region of intermediate temperatures these RDFs (g_{oo}) show characteristics that are specific to only the MCYna model. As is clearly seen from the g_{oo} values in Fig. 4.2 the 2nd peak, which represents the second coordination shell, vanishes with increased temperature and pressure. This indicates that the first two coordination shells are merging into one shell with much more closely packed molecular structure. Merging shells make impossible proper determination of the integration limit r_{min} (see Eq. (4.2)). The positions of the first O-O and O-H minima along the 1, 0.8, and 0.6 g/cm^3 isochores are presented in the Table 4.1. Many authors (Yoshii *et al.*, 1998; Kang *et al.*, 2011; Mountain, 1989) take positions of the 1st OO and OH minima at 25°C as criteria of H-bond forming. However, as is apparent from the data in Table 4.1, these positions are not fixed but are temperature and density dependent. This effect imposes additional uncertainty on the choice of H-bond criteria.

TABLE 4.1: Positions of the first minima of the MCYna RDFs together with n_{oo} values along the 1, 0.8, and 0.6 g/cm^3 isochores.

	1 g/cm^3			0.8 g/cm^3			0.6 g/cm^3		
T[K]	O-O r_{min} [Å]	n_{oo}	O-H r_{min} [Å]	O-O r_{min} [Å]	n_{oo}	O-H r_{min} [Å]	O-O r_{min} [Å]	n_{oo}	O-H r_{min} [Å]
298	3.375	4.605	2.419	3.566	4.337	2.571	3.742	3.869	2.574
343	3.437	4.912	2.419	3.667	4.824	2.538	3.816	4.111	2.574
373	3.468	5.090	2.419	3.699	5.040	2.504	3.888	4.374	2.574
450	-	-	2.358	-	-	2.438	4.217	5.952	2.464
500	4.763	14.560	2.358	4.727	12.790	2.339	4.473	7.043	-
550	4.670	13.561	2.327	4.727	11.989	2.272	4.692	8.230	-
650	4.608	13.021	2.173	4.794	11.939	-	4.984	9.513	-
750	4.608	13.009	-	4.827	12.173	-	4.947	9.532	-

4.3 Molecular structure and hydrogen bonding in aqueous nonpolar solute mixtures

As was discussed in Chapter 2, the interaction of nonpolar solutes with water is accompanied by many unusual changes in water structure and thermodynamic properties (Chaplin, 2013; Ball, 2008). This kind of interaction has the generic name "hydrophobic interaction" and hydration of nonpolar solutes is called "hydrophobic hydration". The term "hydrophobic interaction" refers to the structural and energetic response of water in the vicinity of hydrophobic solutes as shown on Figure 2.9 in Chapter 2. It describes the interaction of nonpolar molecules with water, each other and the interaction between water molecules in the presence of two or more nonpolar molecules. The "hydrophobic effect" of hydrophobic solutes in water (such as non-polar gases) is primarily a consequence of changes in the clustering in the surrounding water rather than water-solute interactions (Fisicaro *et al.*, 2010). In this chapter the calculation of aqueous nonpolar solutes is performed with the help of combined MCYna + LJ potential model (see Eqs. (2.4 - 2.7), Chapter 2) and the Lorentz-Berthelot combination rules (see Eqs. (2.12), Chapter 2). The Lennard-Jones parameters ε and σ of neon, argon, methane, krypton, and xenon are given in Table 4.2.

TABLE 4.2: Lennard-Jones potential parameters used for water-solute and solute-solute pair interactions (Guillot and Guissani, 1993).

	ε/k_b [K]	σ [nm]
H_2O	78.22 (O)	0.3136 (O)
Ne	18.56	0.3035
Ar	125.0	0.3415
CH_4	147.5	0.3730
Kr	169.0	0.3675
Xe	214.7	0.3975

Below we present results from MD simulations of water-neon, -argon, -methane, -krypton, and -xenon mixtures at solute molar fractions $x_s = 1 - 30\%$ in the single phase region and temperature range 298-750 K.

4.3.1 Water-solute radial distribution functions

To define the inner structure of these systems we studied RDFs at 298 K and x_s = 20% for Ne and Ar, x_s = 15% for CH_4, x_s = 10% for Kr and 6% for Xe. Fig. 4.6 shows solute-oxygen (g_{so}) radial distribution functions. From this figure we can see that the solute-oxygen curves start at distances proportional to the parameter σ, in the

following order $\sigma_{Ne} < \sigma_{Ar} < \sigma_{CH_4} < \sigma_{Kr} < \sigma_{Xe}$. The position of the 1st peaks allows us to identify the radius of the 1st solvation shell water molecules form around solute particles. The approximate radii for the given values of x_s and temperature are: r_{Ne} = 0.313, r_{Ar} = 0.332, r_{CH_4} = 0.334, r_{Kr} = 0.35, and r_{Xe} = 0.365 nm. Simulations performed for higher temperatures show that the size of the solvation shells decrease slightly with increasing temperature. One of the main tasks of the present work was to investigate the distortion of the structure of water caused by the inert solutes. Fig. 4.7 compares oxygen-oxygen (g_{oo}), oxygen-hydrogen (g_{oh}), and hydrogen-hydrogen (g_{hh}) RDFs for pure water with RDFs of water-Ne, water-Ar, and water-CH4 systems at T = 298 K and x_s = 20%. It is apparent from Fig. 4.7 that the presence of the nonpolar solute increases and slightly widens the 1st O-O, O-H, and H-H peaks. Water-argon and water-methane O-O and O-H first peaks are higher than in the case of pure water (dash curve). We can conclude that increasing the concentration of a large nonpolar solute particle like Ar or CH_4, compresses the water structure because of solute-oxygen repulsion. The second O-O peak is flattening out and almost disappears in the presence of 15 - 20% solute particles, which indicates a significant distortion of the usual water shell structure by solute particles at distances larger than 4 nm. The effect of the solutes on $g_{oh}(r)$ is to increase the 1st minima and decrease the 2nd minima. In general, data from Fig. 4.7 suggest that the solute particles slightly distort the 1st shell while the distortion of water structure at longer distances is much more significant. Similar indications of nonpolar solutes induced distortion of water structure were obtained for dilute aqueous mixtures of Ar (Botti *et al.*, 2003; Alagona and Tani, 1980), CH_4 (Okazaki *et al.*, 1979), He (Botti *et al.*, 2003), and Kr (Botti *et al.*, 2003).

By analyzing the distribution functions from Figs. 4.6 and 4.7 we can infer the shape of the solvation shell around solute particles. For example, by comparing the 1st Ne-O and Ne-H peaks positions we can see that the 1st Ne-H peak is located some 0.95 nm closer to the Ne atom than the 1st Ne-O peak, which is almost equal to the length of O-H covalent bond (0.9752 nm for the MCYna model). Taking this into account, we can infer that the hydrogen atoms of the water molecules, which form a shell around Ne atoms, are oriented almost radially inward. This orientation of H-atoms is in agreement with the Hartree-Fock calculations of Losonczy *et al.*, (1973) which indicate that the water-neon pair potential has a minimum when the Ne atom is located in the water molecule plane along one of the O-H axes. RDFs for larger solute particles show similar behavior. The hydrogen atoms of water molecules in the 1st solvation shell are orientated slightly toward the central solute particle, however, not completely radially like it is in the case of the small Ne atom.

The 2nd peaks of $g_{ArO}(r)$, $g_{CH_4O}(r)$, $g_{KrO}(r)$, and $g_{XeO}(r)$ are located at a shorter distance than the 2nd peaks of the corresponding solute-hydrogen functions (0.615 nm

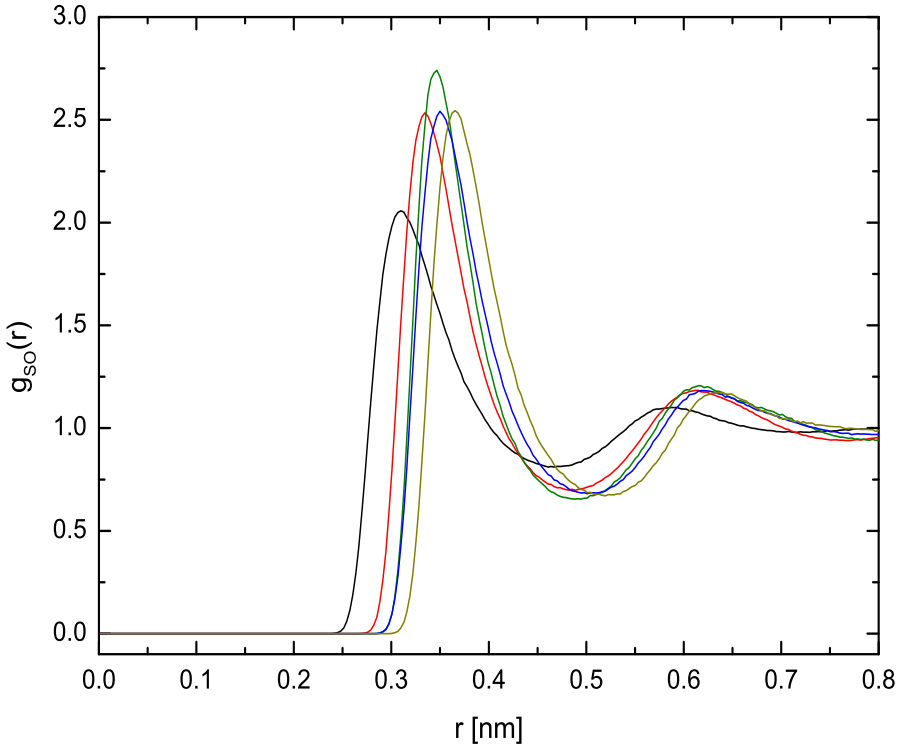

FIGURE 4.6: Solute-oxygen $g_{so}(r)$ RDFs for water-solute systems at 298 K. Starting from left to the right, the solutes are Ne (black $x_s = 20\%$), Ar (red $x_s = 20\%$), CH_4 (green $x_s = 15\%$), Kr (blue $x_s = 10\%$), and Xe (olive $x_s = 6\%$).

for Ar-O vs. 0.64 nm for Ar-H, 0.638 nm for CH_4-O vs. 0.66 nm for CH_4-H, 0.62 nm for Kr-O vs. 0.665 nm for Kr-H, and 0.583 nm for Xe-O vs. 0.63 nm for Xe-H for the values of x_s indicated in Fig. 4.6). This means that the water molecules of the 2nd shell point their oxygen atoms preferentially towards the solute and the hydrogen atoms towards the bulk, while in the 1st shell H atoms are pointed from the bulk and toward the solute particle. This enclathration mechanism, or encagement phenomenon, has been viewed in several simulation studies (Shvab and Sadus, 2012b; De Grandis *et al.*, 2003; Cristofori *et al.*, 2005; Alagona and Tani, 1980) on hydrophobic solutes in water and it is one of the most important feature of hydrophobic hydration at the atomic level.

4.3.2 Structure of the solvation shells

We studied the evolution of water-nonpolar solute solvation shells using the water-argon system as the example. Aqueous solutions of CH_4 and Ne have similar phase behavior at $x_s \leq 30\%$ and exhibit similar temperature dependence of the solvation shells. Fig. 4.8 presents the 1st order coordination numbers for water-argon system calculated by Eq. (4.2). Since the molecular structure in liquid water differs from a regular configuration of crystal as in ice, it is difficult to unambiguously define a fixed upper limit r_{min} in integral (4.2). In fact, the coordination number n_{ij} depends largely on the choice of this

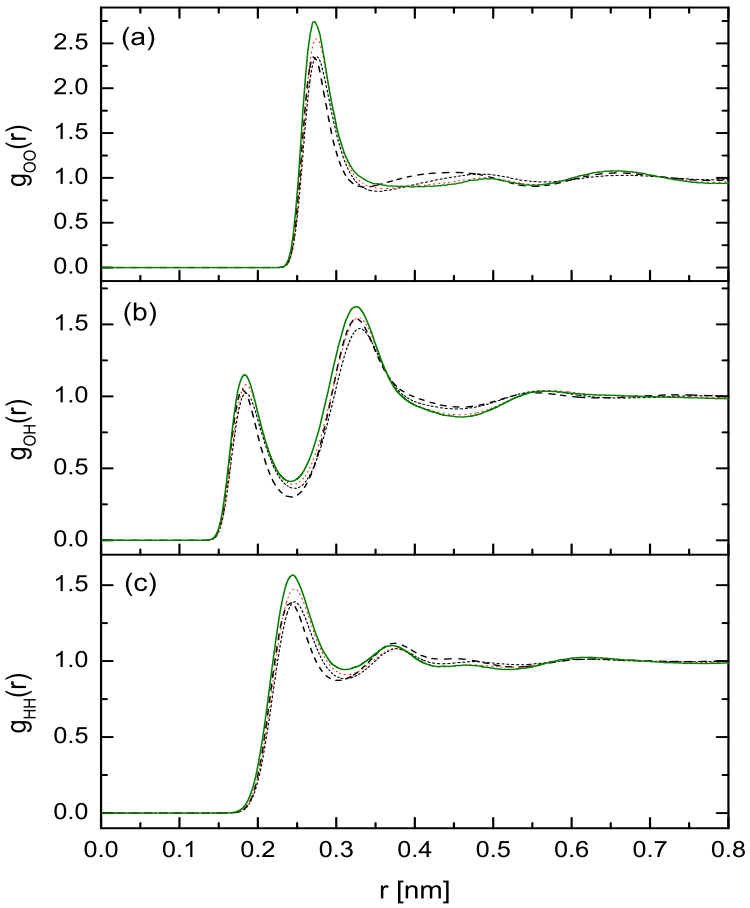

FIGURE 4.7: Oxygen-oxygen, oxygen-hydrogen, and hydrogen-hydrogen distribution functions of pure water (dashed black line) and aqueous solutions of Ne (short dashed line x_s = 20%), Ar (dotted red line x_s = 20%), and CH_4 (continuous green line x_s = 15%) at T = 298 K.

value. In this work we accept the position of the first $g_{ij}(r)$ minima as a r_{min}. Thus, r_{min} represents the size of the 1st solvation shell. Each curve in Fig. 4.8a represents the argon-oxygen coordination number n_{ArO} or the so-called hydration number at different x_s in the one phase region. In general, n_{ArO} slowly decreases with temperature reaching stable values at $T \geq 650$ K. At argon mole fractions $\leq 20\%$ and $T < 400$ K the number of water molecules forming a solvation shell around an argon atom is approximately 15∼17 and slowly decreases to 14 at supercritical temperatures. This compares with hydration values of 15∼14 for water-neon (x_s = 20%), 16∼17 for water-methane (x_s = 20%), 18 for water-krypton (x_s = 10%) and 19∼20 for water-xenon (x_s = 6%). These values lie within the range of hydration numbers reported in the literature (Okazaki *et al.*, 1979; Dec *et al.*, 2006).

The oxygen-oxygen coordination numbers n_{oo} for water-argon systems are presented in Fig. 4.8b. At temperatures up to the normal boiling temperature, the presence of Ar atoms increases n_{oo}. For example, the generally accepted value of n_{oo} for pure water at

298 K is 4.6 whereas at $x_s = 10\%$ it is 5.1 and for $x_s = 20\%$ it is 5.96. This increase in the number of water molecules inside the 1st coordination shell can be explained by the formation of a more densely packed H-bond network due to significant repulsion from Ar atoms. Confirmation of this effect is explicitly seen in Fig. 4.7b where the first solute-oxygen peaks at solute concentrations of 20% are clearly higher than that of pure water. This is possible in part because of the incorporation of water molecules from the 2nd shell into the 1st one. Our simulations show that at temperatures up to the boiling temperature values of n_{oo} at $x_s = 10\%$ are close to n_{oo} of pure water. Naturally, with increasing number of Ar atoms the tetrahedral water structure becomes increasingly distorted until at some point it collapses completely. By analyzing values of n_{oo} with higher solute concentrations we can infer that the tetrahedral structure collapses at solute concentrations $> 20\%$.

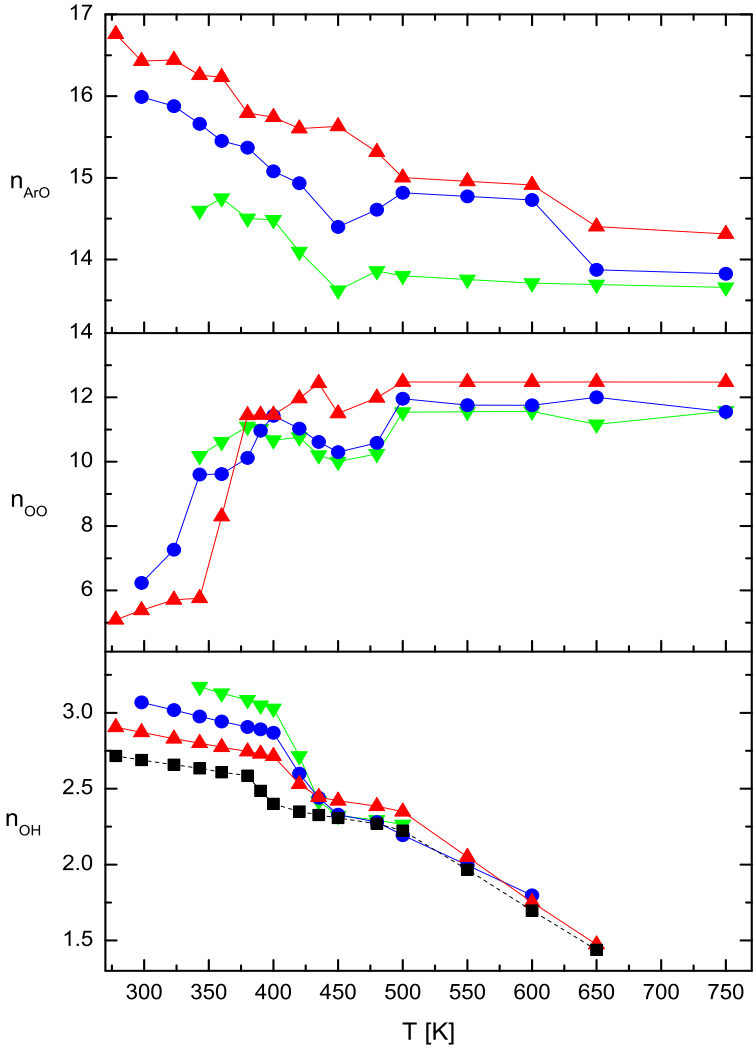

FIGURE 4.8: Temperature dependence of (a) argon-oxygen, (b) oxygen-oxygen, and (c) oxygen-hydrogen coordination numbers at argon mole fractions of 0% (black ■), 10% (red ▲), 20% (blue ◯), and 30% (green ▼).

The evolution of the oxygen-hydrogen coordination number (n_{oh}) of the water-argon system is the most interesting one. The O-H coordination numbers for x_s = 10, 20, and 30% together with corresponding values for pure water are presented in Fig. 4.8c. We have calculated these coordination numbers using Eq. (4.2) which requires the position of the O-H 1st minima as an upper integration limit. It is important to note that the n_{oh} coordination number is not exactly the number of hydrogen bonds. Eq. (4.2) defines the average number of molecules which are within a distance r_{min} from the central water molecule. As was shown by Kalinichev and Bass (1994) this number coincides with the number of H-bonds only at T $\leq$ 500 K. At higher temperatures and pressures more elaborate criteria are required for the definition of H-bonds over a wider range of state points. Nevertheless, n_{oh} can serve as a good approximation of H-bond number, especially at T $\leq$ 500 K. As we can clearly see from Fig. 4.8c the presence of Ar atoms increase n_{oh}. Many authors (Guillot and Guissani, 1993; Alagona and Tani, 1980; Okazaki *et al.*, 1979) suggest that small concentrations of inert solutes strengthen the water structure by increasing the number of H-bonds in the first hydration shell.

Analyzing the data from Figs. 4.7a, and b and 4.8c we can infer that some short-range strengthening of the H-bond network in the vicinity of the solute particle occurs in systems with $x_s \leq 30\%$. However, at the same time, the data from Figs 4.7a, and b also show a negative influence of nonpolar solutes on the structuring of water molecules in the second hydration shell, especially at $x_s \geq 20\%$ and at distances larger than 4 nm from the solute particle. The n_{oh} values at x_s = 30, 20, and 10% are higher than that of pure water at T < 400 K. In the region 400 - 450 K a significant drop in n_{oh} is observed and after T = 450 K all oxygen-hydrogen coordination numbers merge into one and have values that are very close to that of pure water. At T < 400 K, where the tetrahedral structure still exists, the increase in n_{oh} can be explained by the formation of a more densely packed solvation shell due to repulsion from solute atoms. The n_{oh} curve is interrupted at 650 K where the 1st g_{oh} minimum disappears. At this temperature the 1st and 2nd O-H shells merge and it becomes difficult to unambiguously define a fixed upper limit r_{min} in integral (4.2). We believe that more than half of the H-bond network breaks at T $\geq$ 650 K. In the case of $x_s > 30\%$ irrespectively of solute size, the solute particles largely block water molecules from forming either H-bonds or any kind of cluster formations.

Fig. 4.9 presents coordination numbers of water plus Ne, Ar, CH_4, Kr, and Xe systems at 298 K as a function of solute concentrations. This figure can be interpreted as the dependence of coordination numbers on the size of the solute particles. All three coordination numbers solute-oxygen, oxygen-oxygen, and oxygen-hydrogen show a clear dependence on the σ parameter of solute particles. Coordination numbers from Fig. 4.9 follow the dependence $\sigma_{Xe} > \sigma_{Kr} > \sigma_{CH_4} > \sigma_{Ar} > \sigma_{Ne}$. This dependence has a

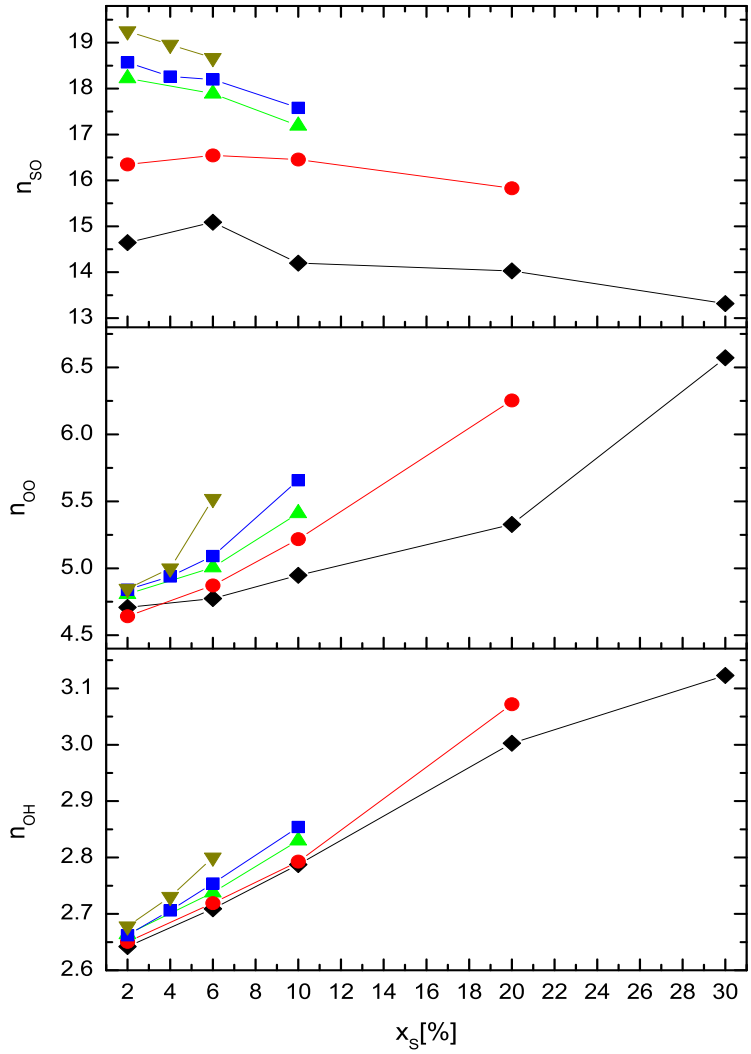

FIGURE 4.9: Coordination numbers of aqueous solutions of Ne (black ♦), Ar (red ◯), CH_4 (green ▲), Kr (blue ■), and Xe (olive ▼) at T = 298 K as a function of solute concentration.

very simple explanation, larger particles require larger solvation shell, smaller particles - smaller shell. n_{oo} and n_{oh} start from values close to that of pure water at small x_s and increase with increasing solute concentrations. In contrast to n_{oo} and n_{oh} solute-oxygen coordination numbers n_{so} decrease with increasing solute concentrations.

We have compared the internal energies of pure water and water-argon mixtures with argon concentrations 2, 6, 10, and 20% at the same number densities and at T = 298 K. The internal energy of the 2% water-argon system is smaller by -3.181 kJ/mol than that of pure MCYna water. This result is in agreement with the results from Okazaki *et al.* (1979) and Alagona and Tani (1980) and indicates energetic stabilization of vicinal water molecules by solute atoms. However, at higher concentrations, even at x_s = 6%, the water-argon internal energy becomes larger than in pure water, gradually increasing with x_s. This change in internal energy can be explained by the cost of incorporating

argon atoms into the H-bond network. Only in very dilute mixtures can the few solute atoms be easily incorporated into the existing water tetrahedral structure without causing significant perturbation. At higher x_s, solute atoms cause more and more perturbations to the structure of water. Despite the somewhat strengthening effect on the 1st surrounding water shell (mainly more dense packing of water molecules), excessive numbers of solute particles destabilize the cohesiveness of the water structure.

4.3.3 One-phase region

All simulation data for water and aqueous solutions presented in this work belong to the single-liquid phase region at constant density 1g/cm^3. Knowing the very small solubility of nonpolar gases like Ne, Ar, Kr, Xe, and CH_4 in water (Kennan and Pollack, 1990) at ambient and near ambient conditions one may naturally question the stability of the phase state.

Solute concentration and size also affect the solubility of the given substances in water. Our simulations indicate a tendency for the large Xe and Kr atoms to demix at concentrations higher than 6% and 10%, respectively. Medium sized Ar and CH_4 tend to demix at $x_s > 30\%$ while small Ne atoms remain in a single phase with water even at higher concentrations. The solubility of these particles also depends on temperature. At $x_s \leq 10\%$ all the water-solutes systems appear to be in one phase throughout the entire temperature region of 278 - 750 K irrespective of the size of the solute particles. At ambient temperatures, both water-Ar and water-CH_4 systems separated into two phases when $x_s = 20\%$. At $x_s = 30\%$ water-argon and water-methane systems do not tend to mix at temperatures up to 340 K and 450 K respectively. Therefore, all results presented in the given work belong to the ranges of x_s and temperature where full water-solute miscibility is attained.

We report calculations for the homogeneous phase at elevated temperatures, involving solute concentrations up to 30%. These phase conditions obtained at constant volume (NVT ensemble) should not be confused with the very small solubility of noble gases and methane in water at ambient conditions. Extensive experimental studies of various aqueous solutions of nonpolar solutes conducted by Franck *et al.* (1974) confirm the existence of a single homogeneous phase at $x_s = 30\%$ and even higher concentrations at near critical and supercritical temperatures. For example, Fig. 10 in Franck (1987) and Fig. 2 in Wu *et al.* (1990) clearly show phase equilibrium isopleths and isotherms at solute concentrations up to 30% at near critical temperatures for water-methane and water-argon systems, respectively. Although the existence of a single phase for water mixtures of relatively high non-polar solute concentrations ($x_s \geq 30\%$) has been observed

experimentally at high temperatures and high pressures, the extent of miscibility at low temperatures (T < 500 K) and high pressures remains unclear.

The very low methane solubility in water at T < 500 K and p < 100 MPa has been amply demonstrated by both experimental (Franck, 1987; Wu *et al.*, 1990; Japas and Franck, 1985; Zheng *et al.*, 2012) and simulation data (Errington *et al.*, 1998). However, most measurements have been reported for the methane in the gas state, e.g., a density of 0.00068 g/cm^3 at T = 288 K, p = 0.1 MPa. In contrast, for the NVT simulations reported here, the density of the whole mixture is held constant at 1g/cm^3, which is more than 1000 times larger than reported by Zheng *et al.* (2012) and Errington *et al.* (1998). As a result of this confinement, the pressures observed in our simulations are much higher, resulting in increased solubility. For example, our pressures at the same methane concentrations reported in by Errington *et al.* (1998) (Figs. 4.6 - 4.9) are greater than 200 MPa (423 K), 420 MPa (523 K), and 600 MPa (603 K). This compares with pressures less than 100 MPa at low methane concentration at these temperatures (Errington *et al.*, 1998). In the work of Culberson and McKetta (1951) (Fig. 2), a pressure-composition diagram for methane + water is reported based on some experimental observations at 298 K. It should be noted that this diagram is at best semi-quantitative, and as such considerable caution should be exercised in its use. Nonetheless, with this important caveat in mind, it appears to identify a single-phase liquid region for methane concentrations of up to 15% and pressures up to 1 GPa.

To check the stability of the mixtures, we conducted additional simulations for water-neon and water-methane at x_s = 20% and 30% using boxes elongated two-fold in one direction with the clearly separated water-rich and solute-rich phases. We also compared the miscibility range of the MCYna + LJ system with that of the nonpolarizable SPC/E + LJ model. In the elongated simulation box, all systems were equilibrated for 1 ns with another 1 ns dedicated for accumulation of ensemble averages. All systems showed the same mixing behavior as in the original cubic simulation box with the same values of dielectric constant and dipole moment. We found that the single homogeneous phase for the nonpolarizable SPC/E + LJ system is restricted to smaller solute concentrations than can be observed for the MCYna + LJ system. For water-methane, the highest solute concentrations at which a single phase was obtained using SPC/E + LJ are x_s = 20% at T > 650 K and x_s = 15% at T > 400 K. For the water-Ne system the highest single-phase conditions are x_s = 30% at T > 650 K and x_s = 20% at T > 400 K. In contrast, the MCYna + LJ calculations yield a single phase at solute concentrations up to 30% for both systems. As the solute particles are modeled by the same LJ potential, the differences observed can be attributed to the water potential. The average MCYna water-water intermolecular energy is -39.0 kJ/mol, which compares with a value of -47.0 kJ/mol for the SPC/E potential. This suggests that the more loosely attracted, MCYna

water molecules allow solute particles to diffuse inside the hydrogen-bond network to a greater extent than SPC/E water molecules. Differences in the structure of water obtained by the two different potentials are apparent in the oxygen-oxygen RDFs (Shvab and Sadus, 2012a). The SPC/E O-O peak reaches value 3.2 at T = 298 K while the MCYna O-O peak has a value of 2.5. This again indicates a much more strongly connected water shell structure of the SPC/E model. As shown elsewhere (Shvab and Sadus, 2012a) SPC/E provides better prediction of water's structure at $T < 373$ K, while significantly overestimating its structure at $T > 373$ K, particularly at low densities. The MCYna model underestimates water molecules ordering at ambient conditions, but at the same time it is much better in predicting the dielectric constant, dipole moment, and to some extent hydrogen bonding (see Figs. 2-4 in (Shvab and Sadus, 2012a)), which are properties of interest in this work.

Chapter 5

Polarization Properties of Aqueous Nonpolar Solute Mixtures

The polarization properties of polar substances like water are usually described in terms of the dielectric constant and dipole moment (Fröhlich, 1958; Feldman *et al.*, 2006; Böttcher *et al.*, 1973). For most materials these quantities are independent of the strength of the electric field over a wide range of the latter, but in the case of alternating fields depend on the frequency. They also depends on parameters, such as the temperature, which define the state of the material. In the macroscopic (phenomenological) theory, which will be summarized in the next paragraph, the dielectric constant is supposed to be known empirically. Throughout this work we shall be interested only in internal electric fields created by all water molecules in the system.

The simulation details were given in Chapter 4.

5.1 Current theories of dielectrics

In a dielectric, two essentially different types of interaction forces should be distinguished. Forces due to chemical bonds, van der Waals attraction, repulsion forces, and others are all short ranged, and usually interactions between nearest neighbors only need be considered. Comparing with these interactions, dipolar interaction forces have a very long range (Fröhlich, 1958). Water is a strong dielectric with dielectric constant ε = 78.65 at 25°C and 0.1 MPa, and the dipole moment $\boldsymbol{\mu} \approx$ 2.2 - 3 D. Due to the long range nature of the dipolar forces an accurate calculation of dipole-dipole interaction is complicated. Here we present major theories of polarization properties of water and

binary mixtures, and formulas for dielectric constant and dipole moment applicable for molecular dynamic simulations.

When a body is placed in a uniform electric field $\mathbf{E}_o$ in vacuum, caused by a fixed charge distribution, its dipole moment will in general change. The difference between the dipole moments before and after the application of the field $\mathbf{E}_o$ is called the induced dipole moment $\boldsymbol{\mu}^{ind}$, and the body in this case is called polarizable (Böttcher *et al.*, 1973). In most cases polarizable bodies are polarized linearly, that is, the induced moment $\boldsymbol{\mu}^{ind}$ is proportional to $\mathbf{E}_o$. In this case one has

$$\boldsymbol{\mu}^{ind} = \alpha \mathbf{E}_0, \tag{5.1}$$

where ε is the dielectric constant, α is the polarizability of the body and a scalar quantity. The fundamental equation which defines the dielectric constant ε from the internal electric field inside any dielectric material is given by (Fröhlich, 1958; Feldman *et al.*, 2006)

$$\frac{\varepsilon - 1}{4\pi}\mathbf{E} = \sum_k N_k \left[\alpha_k (\mathbf{E}_i)_k + \frac{\boldsymbol{\mu}_k^2}{3kT}(\mathbf{E}_d)_k\right], \tag{5.2}$$

where summation is over all species k and $\mathbf{E}_i$ is the internal electric field. It is defined as the total electric field at the position of the particle minus the field due to the particle itself. In Eq. (5.2) the $\mathbf{E}_d$ is a so-called directing field, part of the total electric field $\mathbf{E}$ tending to direct the permanent dipoles $\boldsymbol{\mu}_k$. For a nonpolar system the fundamental equation for the dielectric constant is simplified to the famous Clausius-Mosotti formula (Fröhlich, 1958)

$$\frac{\varepsilon - 1}{\varepsilon + 2} = \frac{4\pi}{3}\sum_k N_k \alpha_k. \tag{5.3}$$

In this case, only the relation between the internal field $\mathbf{E}_i$ and the Maxwell field $\mathbf{E}$ has to be determined. In old Debye theory the internal field $\mathbf{E}_i$ and directing field $\mathbf{E}_d$ were not distinguished from each other. Insteed of both fields in the square brackets in Eq. (5.2), Debye used the Lorentz field $\mathbf{E}_L$.

$$\mathbf{E}_L = \frac{\varepsilon + 2}{3}\mathbf{E}. \tag{5.4}$$

Substituting this expression into Eq. (5.2) we can find

$$\frac{\varepsilon - 1}{\varepsilon + 2} = \frac{4\pi}{3} \sum_k N_k \left[\alpha_k + \frac{\boldsymbol{\mu}_k^2}{3kT} \right]. \tag{5.5}$$

This is generally called the Debye equation (Fröhlich, 1958; Feldman *et al.*, 2006). It was the first relationship that made the connection between the molecular parameter of the substance being tested and the phenomenological (macroscopic) parameter that can be experimentally measured. It works well for gases at normal pressures. However, in many other cases the Debye equation is in considerable disagreement with the experiment.

In the case of spherical molecules Onsager has shown that it is possible to go one step further in the approximate calculation of the dielectric constant (Fröhlich, 1958). The interaction between molecules will no longer be entirely neglected, but one component of it, namely the long-range dipolar interaction, will be taken into account. The following assumptions are made (Fröhlich, 1958; Feldman *et al.*, 2006):

- A molecule occupies a sphere of radius a and its polarizability is isotropic;
- The short range interaction energy is negligible (i.e. $\ll kT$ per molecule).

As was shown above, when a molecule with permanent dipole strength $\boldsymbol{\mu}$ is surrounded by other particles, the inhomogeneous field of the permanent dipole polarizes its environment, and as aconsequence, orientation of the dipole moment is influenced. A simple model has been proposed to calculate this effect: an ideal dipole in a center of a spherical cavity. The field of the dipole in such a cavity polarizes the surrounding matter, which in turn gives rise to a so-called reaction field $\mathbf{R}$. It can be shown that the the reaction field $\mathbf{R}$ is

$$\mathbf{R} = \frac{1}{\frac{2\varepsilon+1}{2(\varepsilon-1)} - \frac{\alpha}{a^3}} \frac{\boldsymbol{\mu}}{a^3}, \tag{5.6}$$

where a is the radius of the cavity. The internal field is now given by

$$\mathbf{E}_i = \mathbf{E}_d + \langle \mathbf{R} \rangle \,, \tag{5.7}$$

where $\langle \mathbf{R} \rangle$ is is the average reaction field connected with the permanent part of the dipole moment $\boldsymbol{\mu}$. Taking into account Clausius-Mossotti formula (5.3) for polar systems in high-frequency alternating fields (Fröhlich, 1958; Feldman *et al.*, 2006):

$$\frac{\varepsilon_\infty - 1}{\varepsilon_\infty + 2} = \frac{4\pi}{3} \sum_k N_k \alpha_k, \tag{5.8}$$

and performing further algebraic transformations we can get

$$\frac{(\varepsilon - \varepsilon_\infty)(2\varepsilon + \varepsilon_\infty)}{\varepsilon(\varepsilon_\infty + 2)^2} = \frac{4\pi\rho}{9kT}\boldsymbol{\mu}^2, \tag{5.9}$$

where ρ is the number density and the ε_∞ is the dielectric constant at a frequency at which the permanent dipolescan no longer follow the changes of the field but where the atomic and electronic polarization are still the same as in static fields. For most natural materaials $\varepsilon_\infty \approx n^2$, where n is the optical refractive index. The Eq. (5.9) is generally called the Onsager equation (Fröhlich, 1958; Feldman *et al.*, 2006).

Kirkwood applied methods of statistical mechanics to find macroscopic quantities when the properties of the molecules and the molecular interactions are known. The electric polarization $\mathbf{P}$ is defined as $\mathbf{P} = \mathbf{D} - \varepsilon_0\mathbf{E}$, where $\mathbf{D}$ is the electric displacement field inside some material, and ε_0 is the permittivity of vacuum. When the higher multipole interactions may be neglected the electronic polarizability $\mathbf{P}$ is equal to dipole density:

$$\mathbf{P}V = \langle \mathbf{M} \rangle , \tag{5.10}$$

where V is the volume of the dielectric under consideration an $\langle \mathbf{M} \rangle$ is its statistical mechanical average of the total dipole moment. In case of isotropic system the $\mathbf{D} = \varepsilon\mathbf{E}$. Thus we can write (Fröhlich, 1958; Feldman *et al.*, 2006):

$$(\varepsilon - 1)\mathbf{E} = \frac{4\pi}{V} \langle \mathbf{M} \rangle , \tag{5.11}$$

Using statistical mechanics distribution functions for total dipole moment $\mathbf{M} = \sum \boldsymbol{\mu}$ in the end we obtain famous Kirkwood equation for dielectric constant

$$\varepsilon - 1 = \frac{4\pi\rho\boldsymbol{\mu}^2}{3kT} g_k, \tag{5.12}$$

where $\boldsymbol{\mu}$ is the permanent dipole of a molecule and g_k is the so-called Kirkwood factor. This factor can be obtained from the fluctuation of the total dipole moment of the system

$$g_k = \frac{\left\langle \left[\sum_{i=1}^{N} \left(\boldsymbol{\mu}_i + \boldsymbol{\mu}_i^{ind} \right) \right]^2 \right\rangle}{N\boldsymbol{\mu}^2} = \frac{\langle M^2 \rangle}{N\boldsymbol{\mu}^2}, \tag{5.13}$$

where $\langle M^2 \rangle$ is the ensemble average of the square total dipole moment of the system. The total molecular dipole moment $\boldsymbol{\mu}_m$ which has contributions from both the partial

charge permanent electric dipole $\boldsymbol{\mu}_i$ and the induction interaction $\boldsymbol{\mu}_i^{ind}$, is averaged over the entire molecular system. If there is no specific correlations one has $g_k = 1$. If the dipole correlations are not negligible, more detailed information about the molecular interactions is required in order to calculate g_k (Neumann, 1983, 1986). The average molecular dipole moment is given by

$$\boldsymbol{\mu}_m = \frac{1}{N} \sum_{i=1}^{N} \left(\boldsymbol{\mu}_i + \boldsymbol{\mu}_i^{ind} \right). \tag{5.14}$$

In this work we are using polarizable MCYna water model described in Chapter 2. The $\boldsymbol{\mu}^{ind}$ in this model is defined in Eqs. (2.7 - 2.9) from Chapter 2. Thus, having induced dipole moment we can calculate total dipole of a single molecule $\boldsymbol{\mu}_m = \boldsymbol{\mu}^{ind} + 2.1936$. The 2.1936 D is the permanent dipole moment in the MCYna water model. Having total dipole moment we can calculate dielectric constant of any polar liquid. In this work we are using Kirkwood formula (5.12) to find dielectric constants of water and aqueous solutions (Shvab and Sadus, 2012a, 2012b).

For the representation of a dielectric consisting of polarizable molecules with a permanent dipole moment, Fröhlich introduced a continuum with dielectric constant ε_∞ in which point dipoles with a moment $\boldsymbol{\mu}_d$ are embedded. According to this model the polarizability of the molecules can be imagined as smeared out to form a continuum with dielectric constant ε_∞. After splitting polarization $\mathbf{P}$ into induced and orientational parts, and performing necessary algebraic transformations Kirkwood formula (5.12) can be rewritten in the following way

$$g_k \mu^2 = \frac{9kT}{4\pi} \frac{(\varepsilon - \varepsilon_\infty)(2\varepsilon + \varepsilon_\infty)}{\varepsilon(\varepsilon_\infty + 2)^2}, \tag{5.15}$$

where g_k is the Kirkwood factor given by Eq. (5.13). Equation (5.15) is called the Kirkwood-Frhölich equation, and it is used mainly for polar systems with short-range interactions (Fröhlich, 1958; Feldman *et al.*, 2006).

5.2 Polarization properties of bulk water

The dipole moment of an isolated water molecule in vapor is 1.85 D (Haynes *et al.*, 2013). However, in condensed phases, the electrostatic field from the other molecules reorganizes the charge distribution in the molecule. The self-consistent induction calculations give an average total dipole moment of ice Ih 3.09 D (Batista *et al.*, 1998). In the fluid phase, the dipole moment must have intermediate values between those in the gas and

the ice. Therefore, it is not sufficient to describe the properties of water over a wide range of physical states based upon this kind of fixed-charge potential model. Instead, a realistic model should include the polarization effect of the molecule to describe the intermolecular interaction in the sub- and supercritical states. Car-Parrinello *ab initio* MD (Car and Parinello, 1985) is one of the best methods to account for the state dependence of intermolecular interactions. Kang *et al.* (2011) and Dyer *et al.* (2006) reported a first principle study of sub- and supercritical water. These workers calculated the structure factors and polarization distribution in water. However, the method used is computationally expensive and involves a very small number of particles (32-64 molecules). In this sense, we need simpler models to investigate the properties of water over a wide range of thermodynamic states. A natural improvement of the empirical potential models is to explicitly introduce nonadditive many-body interactions such as three-body and polarizable contributions. In this work we apply an *ab initio* MCYna potential model for investigation of structural and polarization properties of bulk water and compare results with available experimental data. This model was introduced by Li *et al.* (2007) and contains an *ab initio* description of two-body additive interactions plus nonadditive contributions from both three-body interactions and polarization. The nonadditive multibody influence arises because the induced dipole of each molecule generates an electric field that affects all other molecules. The molecular induced dipole moments are determined self-consistently with the electrostatic field reflecting the configuration of the fluid that depends on the physical state. A comparison is also made with SPC/E water model (Berendsen *et al.*, 1987).

5.2.1 Dielectric constant

Molecular dynamics and experimental dielectric constants (Fernandez *et al.* 1997) are presented in Fig. 5.1. As expected, ε_r is lower for higher temperatures. The temperature driven decrease of ε_r is due to the reduction of molecular ordering. One of the main reasons for the high dielectric constant of water is that the extensive H-bond network enables a fast (within 10 ps) reorientation of the molecular dipoles in response to a field.

Increasing the temperature increases the randomizing thermal fluctuations that oppose dipole alignment by an electrostatic field. Values of the dielectric constant ε_r gradually decrease along all isochores. The decrease of ε_r at lower densities is caused by strong local density fluctuations, and is a consequence of a broken H-bond network and reduced polarizability of water.

Comparison with the experimental values of dielectric constant from elsewhere (Fernandez *et al.* 1997) shows that MCYna model underestimates ε_r by approximately 5% at

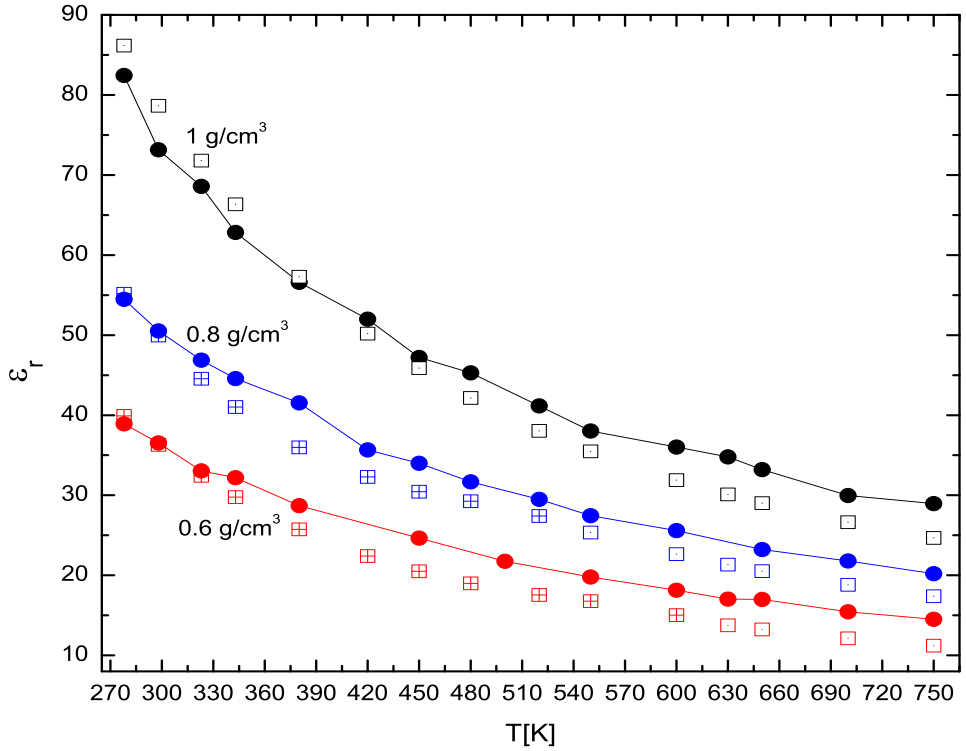

FIGURE 5.1: Temperature dependence of the dielectric constant ε_r. MD data along the 1, 0.8, and 0.6 g/cm^3 isochores (all ◯). A comparison is given with both direct experimental data (Fernandez *et al.* 1997) (open ⊡) and interpolated experimental data (Uematsu and Franck, 1980) (crossed ⊞).

temperatures lower than 343 K, and overestimates ε_r for the temperatures greater than 450 K. In the temperature range 343 - 450 K MCYna predictions and experimental data almost coincide. Experimental results for isochores 0.8 and 0.6 g/cm^3 are available only in temperature regions 550 - 750 K and 630 - 750 K respectively. For lower temperatures we used an interpolation equation based on the experimental data collected in the work of Uematsu and Franck (1980). In the case of smaller water densities, MD results deviate more from experimental data than it was in case of $\rho = 1$ g/cm^3.

Comparison with dielectric constants obtained from the SPC/E model is presented in Table 5.1. The MCYna model gives better agreement with experiment for temperatures up to 400 K than the SPC/E model, which can be at least partly attributed to polarization interaction. Above the critical temperature, both polarizable MCYna and non-polarizable SPC/E models give similar values of the dielectric constant. This trend can be explained by the fact that water at supercritical conditions behaves like simple fluid, due to the collapse of the shell structure and significant reduction of the H-bond network.

TABLE 5.1: Dielectric constants for the MCYna and SPCE models along the 1, 0.8, and 0.6 g/cm^3 isochores.

	1 g/cm^3			0.8 g/cm^3			0.6 g/cm^3		
T[K]	Exp. ε_r [38]	MCYna	SPC/E	Exp. ε_r [38]	MCYna	SPC/E	Exp. ε_r [38]	MCYna	SPC/E
278	86.175	82.435	70.161	-	54.484	-	-	38.919	-
298	78.65	73.161	66.380	-	50.537	-	-	36.528	-
323	71.80	68.583	61.109	-	46.870	-	-	33.052	-
343	66.34	62.833	57.824	-	44.567	-	-	32.189	-
380	57.29	56.609	52.213	-	41.530	-	-	28.703	-
400	53.53	53.205	49.647	-	37.890	40.116	-	27.287	-
450	45.875	47.210	44.237	-	33.990	35.786	-	24.644	-
500	40.00	43.102	40.027	-	30.490	32.299	-	21.758	-
600	31.89	36.021	33.528	22.65	25.586	27.052	-	18.132	20.532
650	29.015	33.196	31.013	20.54	23.220	25.072	13.235	16.990	19.071
750	24.66	28.947	27.021	17.38	20.207	21.873	11.210	14.507	16.641

5.2.2 Dipole moment

The effect of temperature on polarization properties of liquid water is presented by the distribution of dipole moment of water molecules on Fig. 5.2. These distributions are obtained from an instantaneous snapshot at the end of the simulation run. The standard deviations for the 298, 480, and 700 K (isochore 1 g/cm^3) are 0.36, 0.29, and 0.28 respectively and a comparison is given with the normal Gaussian distribution. The deviation from the Gaussian distribution reflects local fluctuation of molecular dipole at the given instance. The shape of the distributions, relative to the normal distribution, was found to be widened towards the larger values of dipole moments. Peaks are also found to be shifted to the left from the mean values. These effects could be caused by the rigidity of the MCYna water molecule. Distributions from real *ab initio* simulations (Dyer and Cummings, 2006; Sun *et al.*, 2010) are usually quite close to the normal Gaussian distributions. As was shown in *ab initio* simulations (Dyer and Cummings, 2006; Allesh *et al.*, 2004) flexing of the molecule enhances the occurrence of the dipoles at the tails of the distribution. As temperature raises distributions become sharper and mean values shift towards smaller values of dipole moment. Comparing a given dipole distributions with the ones obtained from other *ab initio* (Kang *et al.*, 2011; Dyer and Cummings, 2006) and MD simulations (Yoshii *et al.*, 1998), we found the MCYna distributions to be much wider. They begin from a minimum value of 2.1936 D, which is assigned to the isolated water molecule according to MCY model20 and span up to a value of 4.5 D. A similar trend was observed for dipole distributions of water along the isochores of 0.6 and 0.8 g/cm^3, which agree with previous *ab initio*10 and MD8 results.

Fig. 5.3 shows the variation of average dipole moment at different densities as a function of temperature. Values of dipole moments gradually decrease with the temperature rising, slowly approaching stable values at supercritical temperatures. From Fig. 5.3 it is clearly seen that the average dipole moments are decreasing with decreasing density of water. This result is in qualitative agreement with recent *ab initio* simulations (Dyer *et al.*, 2006; Ikeda *et al.*, 2010; Sharma *et al.*, 2007) and MD simulations (Yoshii *et al.*, 1998). The dipole moment calculated by Eq. (5.14) contains contribution from both the permanent dipole moment $|\boldsymbol{\mu}_i| = 2.1936$ D plus the induced dipole moment $|\boldsymbol{\mu}_{ind}|$. In condensed phases of water, the internal electric field arising from the interaction of water molecules with surrounding ones polarizes the molecules which leads to a large values of $\boldsymbol{\mu}_{ind}$ and, correspondingly, large total dipole moment $\boldsymbol{\mu}$ (see Eq. (5.14)) relative to that in the gas phase. As discussed above, at densities $\rho < 1$ g/cm^3 average intermolecular distances are larger than at ambient conditions, and, therefore, polarization energy and average dipole moment should be smaller and slowly approach the vapor value of 1.89

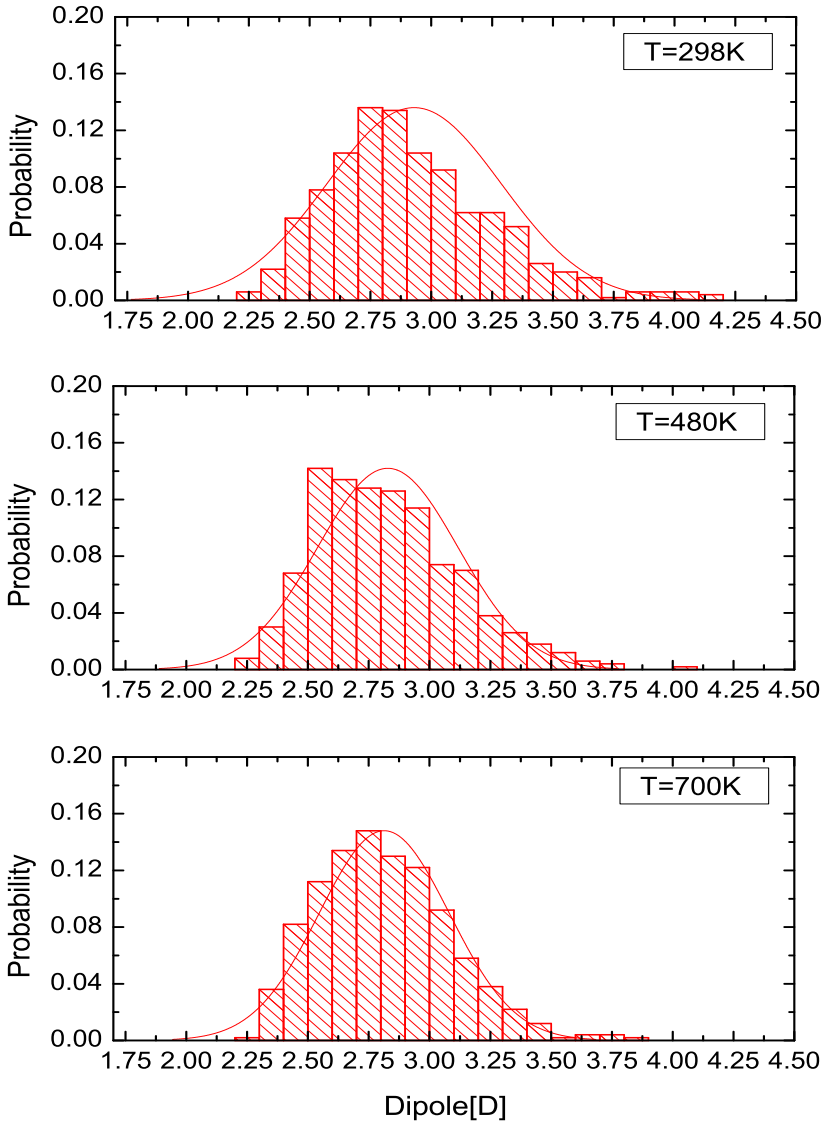

FIGURE 5.2: Distribution of dipole moments for water at 1g/cm^3 and temperatures 298, 480, and 700 K obtained from a single snapshot at the end of the simulation. Smooth curves show the corresponding Gaussian distributions.

D. The absence of reliable experimental data for the given temperatures and densities does not allow us to firmly establish correct temperature and density dependence of $\boldsymbol{\mu}$.

5.3 Polarization properties of aqueous nonpolar solute mixtures

After calculating dielectric constant and dipole moment of bulk water at normal and reduced densities (Shvab ansd Sadus, 2012b) the next step is to investigate the same properties for binary aqueous solutions of neon, argon, methane, krypton, and xenon. All these solutes are have zero dipole moment and exhibit very similar interaction with

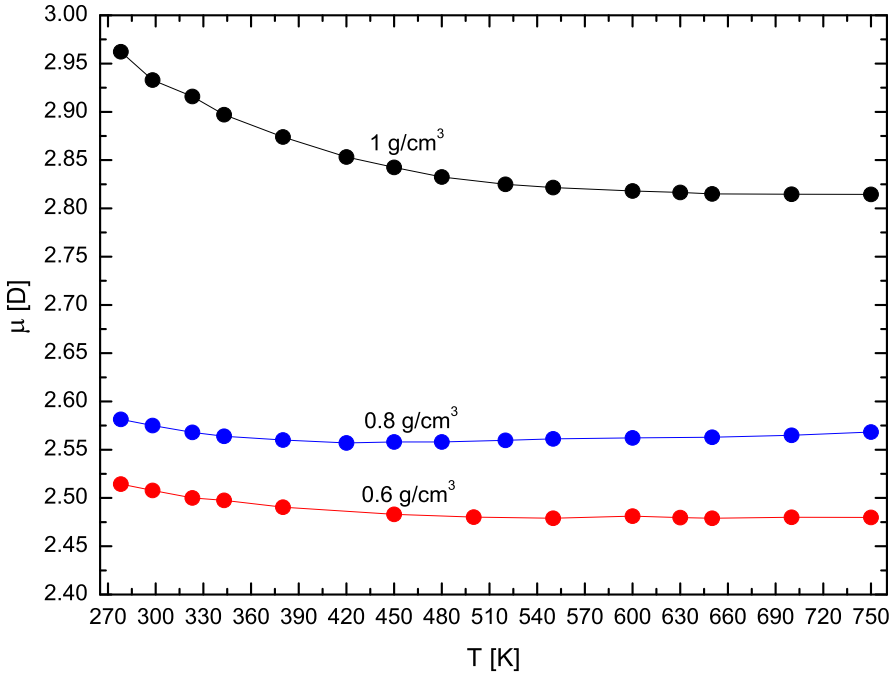

FIGURE 5.3: Temperature dependence of average dipole moments along the 1, 0.8, and 0.6 g/cm^3 isochores.

water, called "hydrophobic interaction". For a water-solute system, the total dipole moment should contain contributions from all species (Skaf and Ladanyi, 1995)

$$M^2 = \sum_i n_i M_i^2 = n_s M_s^2 + n_w M_w^2, \tag{5.16}$$

where x_s and x_w are mole fractions of solute and water, respectively. Because the nonpolar solute particles do not have a permanent dipole moment, only water molecules contribute to the total dipole moment of the system $\boldsymbol{\mu}_m$.

5.3.1 Dielectric constant

We calculated the dielectric constants ε_m for water plus neon, argon, methane, krypton, and xenon mixtures. For this calculation we have used the classical fluctuation formula of Kirkwood (Gray and Gubbins, 1984; Sadus, 1999). Despite the fact that the system consists of 2 molecules, the second molecule is nonpolar and has zero dipole moment. Therefore, only water molecules make a contribution to the total dipole moment of the system used in Eq. (5.16). The temperature dependence of the dielectric constants ε_m in the one-phase region for pure water and water plus Ne, Ar, and CH_4 systems is presented in Fig. 5.5.

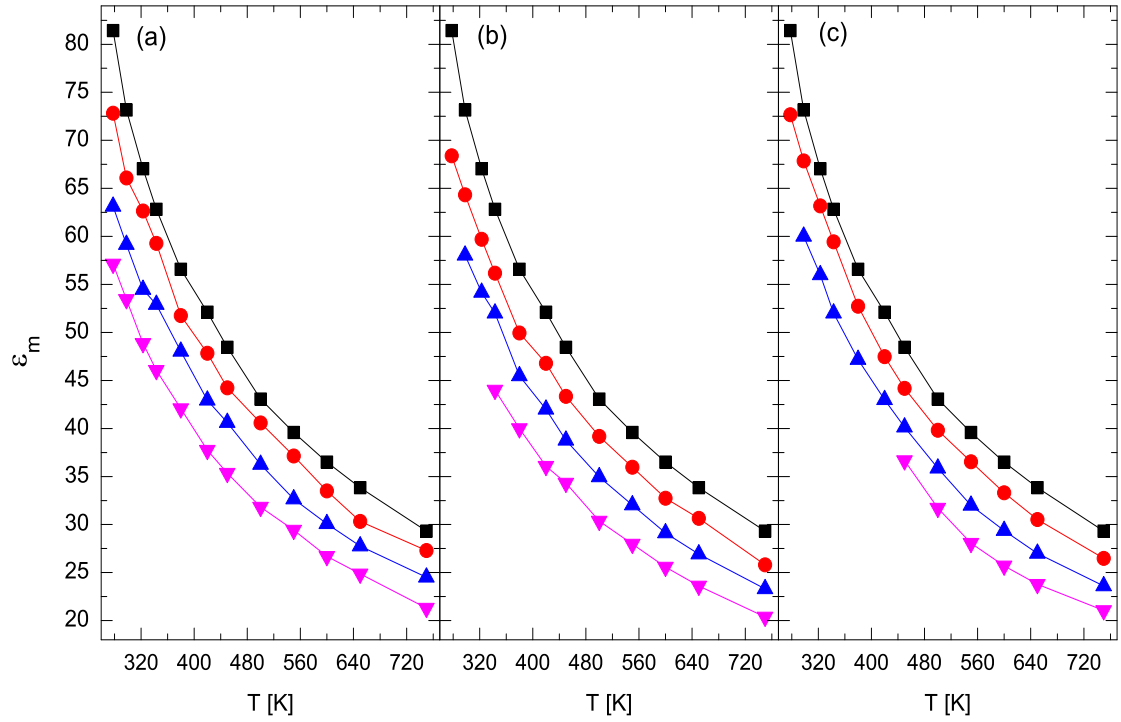

FIGURE 5.4: Temperature dependence of the dielectric constants of (a) water-neon, (b) water-argon, and (c) water-methane systems at solute concentrations 0% (black ■), 10% (red ◯), 20% (blue ▲), and 30% (pink ▼).

It is apparent, that all values of ε_m gradually decrease with temperature and x_s. The decrease in ε_m with increasing solute concentration is primarily due to solute-hydration effects. For aqueous solutions, the formation of hydration shells around nonpolar solutes prevents the "shell-bounded" water molecules from being oriented in the external field. These water molecules are excluded from creating the effective dipole moment of the system, thus causing a decrease of polarization and dielectric constant. A further increase in solute concentration leads to a water deficit and to a redistribution of water molecules in the hydration layers. Despite the significant difference in the Ne, Ar, and CH_4 size and energy parameters, the dielectric constants of these three systems are almost identical for a given temperature and x_s. The difference in ε_m values is within ±1-1.5%. The absence of experimental data for the dielectric properties of water-nonpolar solute systems makes it impossible to validate the predictions of the MCYna + LJ potential. However, it has been previously reported (Shvab and Sadus, 2012a) that the MCYna potential provides a good prediction of the dielectric properties of pure water over a wide range of temperatures. The discrepancy between simulations (Shvab and Sadus, 2012a) and experiment was typically 5%, which suggests that we can have a reasonable degree of confidence in the reliability of the mixture calculations.

Fig. 5.5 presents dielectric constants ε_m for the various water mixtures as functions of x_s at T = 298 K. In general, the dielectric constants decrease with increasing concentration

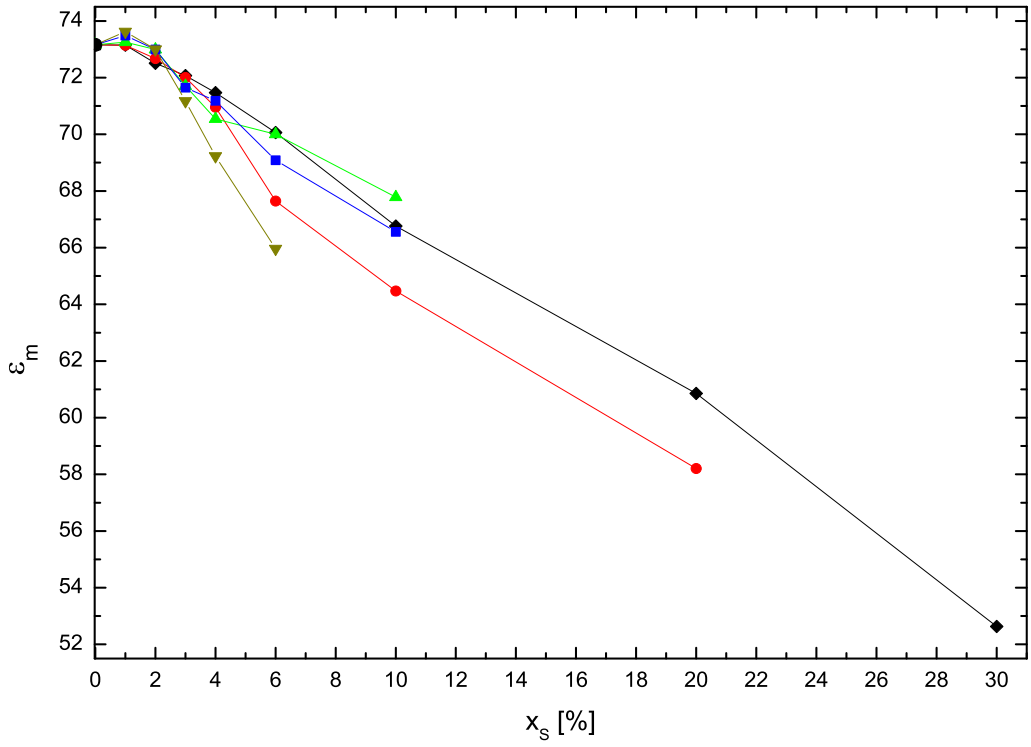

FIGURE 5.5: Dielectric constants of aqueous solutions of Ne (black ♦), Ar (red ◯), CH_4 (green ▲), Kr (blue ■), and Xe (olive ▼) at T = 298 K as functions of solutes concentration.

of the solute. It is natural to expect values of ε_m for very dilute mixtures ($x_s < 2\%$) to be very close to that of pure water. Indeed examining Fig. 5.5 in the direction of decreasing solute concentration x_s we can clearly see that the values of ε_m for all mixtures converge to the dielectric constant value of pure water ($x_s = 0\%$) at 298 K. It is noteworthy that there is a small but nevertheless noticeable peak at approximately $x_s = 1\%$ for mixtures containing either krypton or xenon. While more extensive simulations are always preferable for better convergence of the dielectric constant, this observation may be directly connected with the nature of the hydrophobic hydration of krypton and xenon. As was elaborated by Chandler (2005), solvation of the single particles which excludes water molecules from a spherical volume less than 0.5 nm across does not require the breaking of hydrogen bonds. Water molecules can adopt orientations that allow hydrogen-bonding patterns to go around the solute in such single cavities. Therefore, at very dilute concentrations large nonpolar particles like krypton and xenon enhance local water ordering, which may lead to a small increase in dielectric constant and dipole moment. Enhanced local water ordering in dilute solutions has also been observed by Cristofori *et al.* (2005), and Okazaki *et al.* (1979). The situation is different for $x_s > 2\%$ where solute particles tend to aggregate, forming large hydrophobic cavities with low curvature making it impossible for water molecules to maintain a complete hydrogen-bonding network.

5.3.2 Comparison of MD and analytical calculations of dielectric constants

It is of interest to compare the dielectric constants for the water + methane mixture predicted by the combined MCYna + LJ potential with the results obtained using simple analytical mixing rules developed by Harvey and Prausnitz (1987) and other empirical formulas (Van Beek, 1967). The Harvey-Prausnitz linear and quadratic mixing rules are based on the calculation of pure components polarizations obtained at the reduced density of the mixture, insuring that all molar volumes are physically appropriate.

$$p_m = \sum_i^n \Phi_i^{\pm} p_i^{\pm}. \tag{5.17}$$

Here $p_i^{\pm}$ is the polarizability of the ith component and $\Phi_i^{\pm}$ is the volume fraction based on pure-component molar volumes

$$\Phi_i^{\pm} = x_i \nu_i / \sum_i^n x_j \nu_j, \tag{5.18}$$

where x_i is the molar fraction and ν_i is the molar volume of species i.

A quadratic mixing rule was developed to account for increased or decreased degree of correlation between neighboring molecules in the mixture:

$$p_m = \sum_{i=1}^n \sum_j^n \Phi_i^{\pm} \Phi_j^{\pm} p_{ij}^{\pm}. \tag{5.19}$$

where $p_{ij} = \frac{1}{2}(p_i^{\pm} + p_j^{\pm})\xi$, ξ is an adjustable parameters used to optimize agreement between theory and experiment. Analysis of the binary mixture critical curve indicates that a value of $\xi = 0.92$ is appropriate for methane + water interactions. The dielectric constant of the mixture ε_m is obtained from Kirkwood's expression for polar fluids:

$$p_m = \frac{(\varepsilon_m - 1)(2\varepsilon_m + 1)}{9\varepsilon_m} \tag{5.20}$$

Several formulas are available for the calculation of dielectric constant of mixture of liquids but these appertain essentially to the dielectric constant at DC or low frequency alternating voltage. Further, the formulas available are independent of temperature and therefore they are presumably applicable at room temperature or at a given constant

temperature (Van Beek, 1967). Denoting the two components by subscripts 1 and 2, we summarize some formulas as below:

Lichtenecker formula

$$\varepsilon_m = \exp\left[V_1 \ln \varepsilon_1 + V_2 \ln \varepsilon_2\right], \tag{5.21}$$

Loyenga formula

$$\varepsilon_m = \left[\varepsilon_1^{1/3} + V_2(\varepsilon_2^{1/3} - \varepsilon_1^{1/3})\right]^3, \tag{5.22}$$

Bottcher formula

$$\varepsilon_m = \ln \varepsilon_1 + \frac{3V_2\varepsilon_m(\varepsilon_2 - \varepsilon_1)}{2\varepsilon_m + \varepsilon_2}, \tag{5.23}$$

Rayleigh formula

$$\varepsilon_m = \varepsilon_1 \frac{\frac{2\varepsilon_1+\varepsilon_2}{\varepsilon_2-\varepsilon_1} + 2V_2 - \frac{1.575(\varepsilon_2-\varepsilon_1)}{4\varepsilon_1+3\varepsilon_2}V_2^{10/3}}{\frac{2\varepsilon_1+\varepsilon_2}{\varepsilon_2-\varepsilon_1} - V_2 - \frac{1.575(\varepsilon_2-\varepsilon_1)}{4\varepsilon_1+3\varepsilon_2}V_2^{10/3}}, \tag{5.24}$$

where V_1 and V_2 are the dimensionless volume fractionals of the dispersed (solute) components, ε_m, ε_1, and ε_2 are the dielectric constants of mixture as a whole and components 1 and 2 respectively. Of the various alternatives presented above and summarized by Van Beek (1967), we found that the Rayleigh formula (5.24) yielded values of ε_m closest to our MD simulations. The derivation of Eq. (5.24) assumes a cubical array of spheres (ε_2) enclosed in a medium (ε_1), which appears to be a reasonable approximation for methane in water. Furthermore, the dielectric constants of methane and noble gases at T $>$ 278 K are very close to 1 so it is natural to expect very small contribution to the total dielectric constant of the mixture from the solute component. For example, according to the Harvey-Prausnitz approach, at $x_s = 10\%$ and T $<$ 373 K methane contributes less than 1% to the total dielectric constant of the mixture and it makes an even smaller contribution at higher temperatures.

It is important to note that particles like methane and xenon have relatively high electronic polarizabilities of 2.6 and 4.11 Å^3, respectively. Some authors (Mateu *et al.*, 2011; Rosato *et al.*, 2012) suggest that single methane molecules can acquire a small induced dipole moment upon hydration, which can affect the solvation process and consequently dielectric constant of the mixture. However, Mateus *et al.* (2011) found no difference between the average monomeric dipole moment of bulk water and that of water in close interaction (within the first hydration layer) with methane. A proper account of solute polarizability requires a thorough *ab initio* approach and is beyond the scope of the present study. Comparison of the ε_m from the given polarizable potential model with the Harvey-Prausnitz mixing rules, Rayleigh's formula (5.24), and non-polarizable SPC/E + LJ potential model for the water-methane system at methane concentrations 10, 20,

and 30% is presented in Fig. 5.6. This comparison indicates that Eq. (5.17) with linear volume-fraction mixing at x_s = 10% and 20% slightly overestimates ε_m at T < 343 and 370 K respectively. At higher temperatures all analytical formula underestimate ε_m. The quadratic mixing rule (5.19) and Rayleigh's Eq. (5.24) under estimate MD results for all temperatures and solute concentrations. One of the reasons for this difference between MD and analytical results at elevated temperatures is the quite high dipole moment of the MCYna water molecule, which contributes to ε of pure water higher by 5% compared to experimental data. Deviation between MD data and the quadratic mixing rule Eq. (5.19) can be explained by the fact that this rule was developed to improve agreement over the linear rule for water-alcohol systems. These systems are fully soluble and possess stronger correlation between the neighboring molecules, which is obviously not the case for hydrophobic solutes like methane or noble gases. In general, we can conclude that the Harvey-Prausnitz linear mixing rule and the predictions of MCYna + LJ model are in qualitative agreement along all temperatures and solute concentrations.

5.3.3 Dipole moment

Fig. 5.7 shows the temperature dependence of the average water molecule dipole moment $\mathbf{m}_m$ at different mole fractions of water plus Ne, Ar, and CH_4 systems. At temperatures up to 500 K all dipoles slowly decrease while at higher temperatures dipoles of water-Ar and water-CH_4 systems are almost constant. In contrast to Ar and CH_4 mixtures, dipole moments of the water-Ne system at supercritical temperatures exhibit small but steady increases. Values of $\boldsymbol{\mu}_m$ for the given systems differ much more than in the case of dielectric constants. For example, $\boldsymbol{\mu}_m$ of the water-CH_4 system are clearly higher than $\boldsymbol{\mu}_m$ of water-Ar system, and the difference increases with x_s, from 1% for x_s = 10% to 2.5% for x_s = 30%. Dipoles for water-Ne system appear to be higher than for Ar and CH_4 and the distance between the curves of constant x_s is smaller. A possible explanation of this weak deviation of water-Ne system dipoles from pure water could be partly attributed to the parameters used for Ne. The Lennard-Jones parameters σ = 0.3035 nm and especially ε/k_b = 147.5 K from Table 4.2 in Chapter 4 appear to be disproportionally small compared to Ar, CH_4, Kr, and Xe. Having such a small ϵ, which basically defines the depth of the LJ potential well, means that Ne atoms interact very weakly with water molecules.

Fig. 5.8 shows the probability distribution of individual dipole moments at T = 450 K for pure MCYna water and water-methane systems with x_s = 10, 20, and 30%. These distributions were obtained from an instantaneous snapshot at the end of the simulation. Deviation from the normal distribution reflects local fluctuation of molecular dipole at the given instance. From this figure we can see that the mean values, height and width

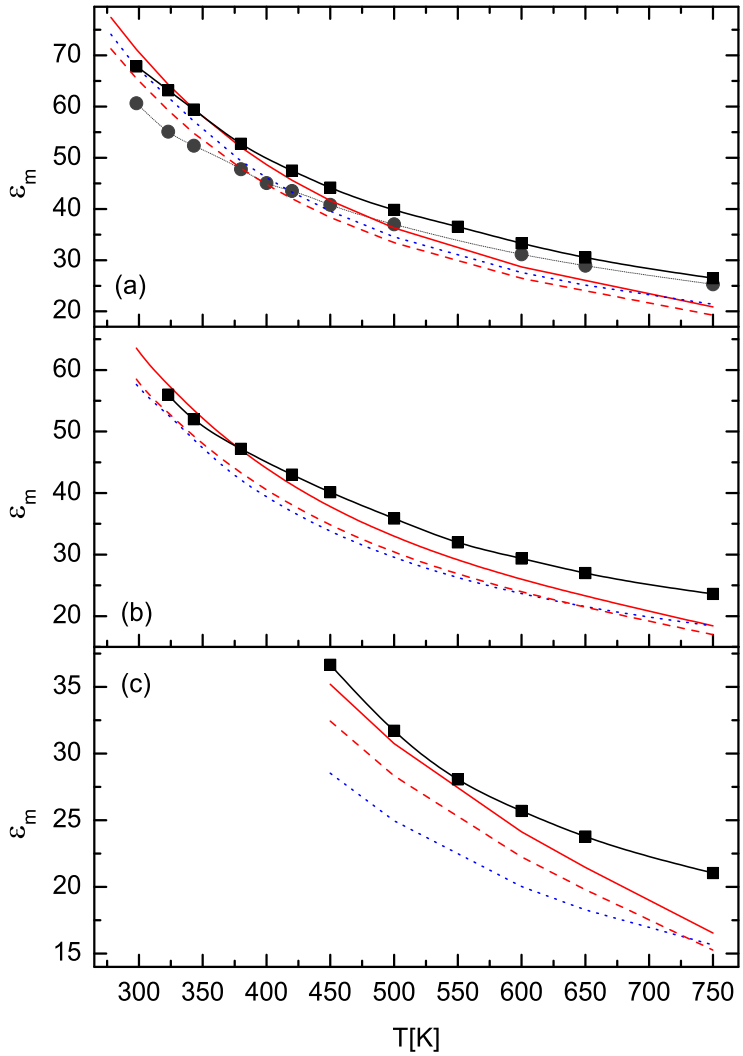

FIGURE 5.6: Comparison of the dielectric constants of the water-methane (c) system at solute concentrations (a) 10%, (b) 20%, and (c) 30% obtained from MD simulations of MCYna + LJ model (■), SPC/E + LJ model (grey ◯), linear mixing rule Eq. (5.17) (continuous red line), quadratic mixing rule Eq. (5.19) (dashed red line), and Eq. (5.24) (dotted blue line).

of the distributions gradually decrease with increasing x_s. In accordance with Fig. 5.8, the mean values of the distributions become progressively shifted to the left with increasing concentration. This dependence seems to have a simple explanation. Namely, the neutral solute particles especially at high concentrations repel water molecules and weaken the intermolecular electric field. As a consequence, at decreasing electric field, the induction contribution $\boldsymbol{\mu}^{ind}$ to the total molecular dipole moment is also vanishing. Dipole distributions for water-neon and water-argon systems show the same behavior.

The solute concentration dependence of the dipole moments of water mixtures at T = 298 K is illustrated in Fig. 5.9. In common with the dielectric constants (see Fig. 5.7), the average dipole moment decreases with increasing solute concentration. We observe

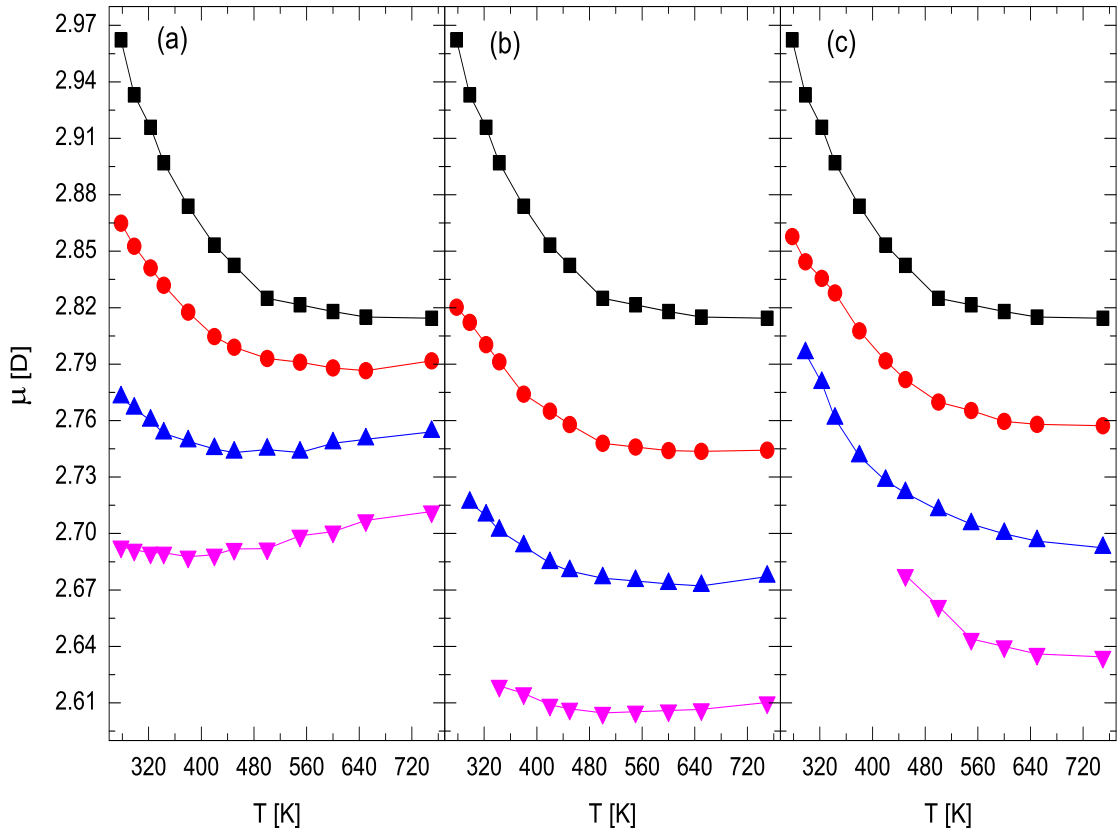

FIGURE 5.7: Temperature dependence of the average dipole moments of (a) water-neon, (b) water-argon, and (c) water-methane systems at solute concentrations 0% (black ■), 10% (red ◯), 20% (blue ▲), and 30% (pink ▼).

a distinct peak in the dipole moment at $x_s < 3\%$ for the water-xenon curve and a slight increase for the water-neon curve. The reason for the small increase of the average dipole moment in the presence of xenon atoms is the same as it was for the dielectric constant, namely, local strengthening of the water structure. The small deviation of the water-neon properties from the general trend can probably be attributed to the less accurate parameterization of the neon potential due to quantum influences. Excluding the water-neon mixture, the dipole moments of the mixtures exhibit a dependency on the size of the solute as judged by the value of the σ parameter (Table 4.2 in Chapter 4). The dipole moment is larger in mixtures with larger solutes. That is, $\boldsymbol{\mu}_m$ values decrease in the following order: Xe > CH_4/Kr > Ar.

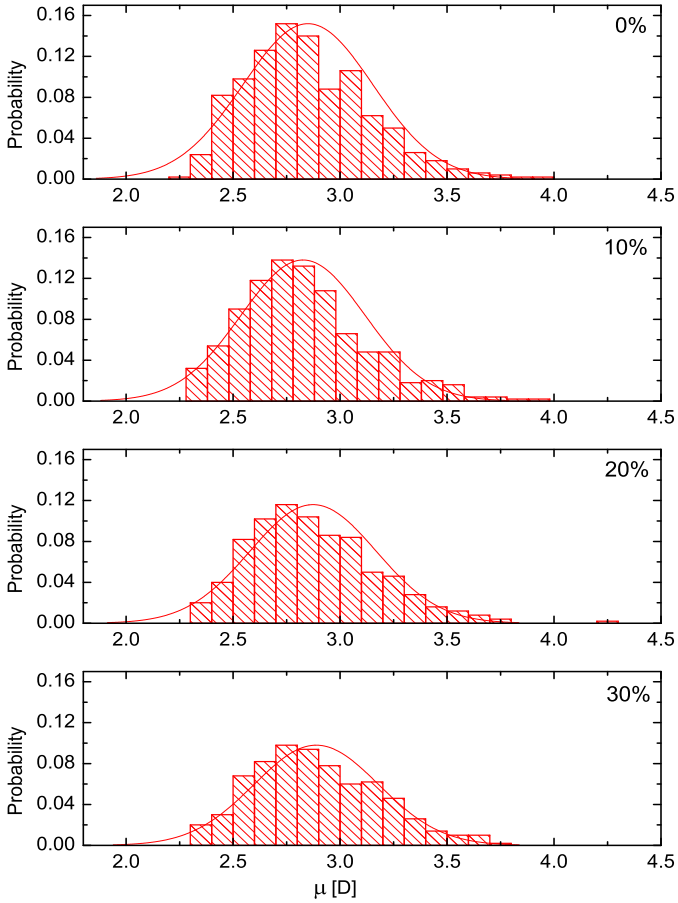

FIGURE 5.8: Instantaneous snapshots of the distribution of dipole moments for the water-methane system at T = 450 K and solute concentrations of 0%, 10%, 20%, and 30%. Smooth curves show corresponding Gaussian distributions.

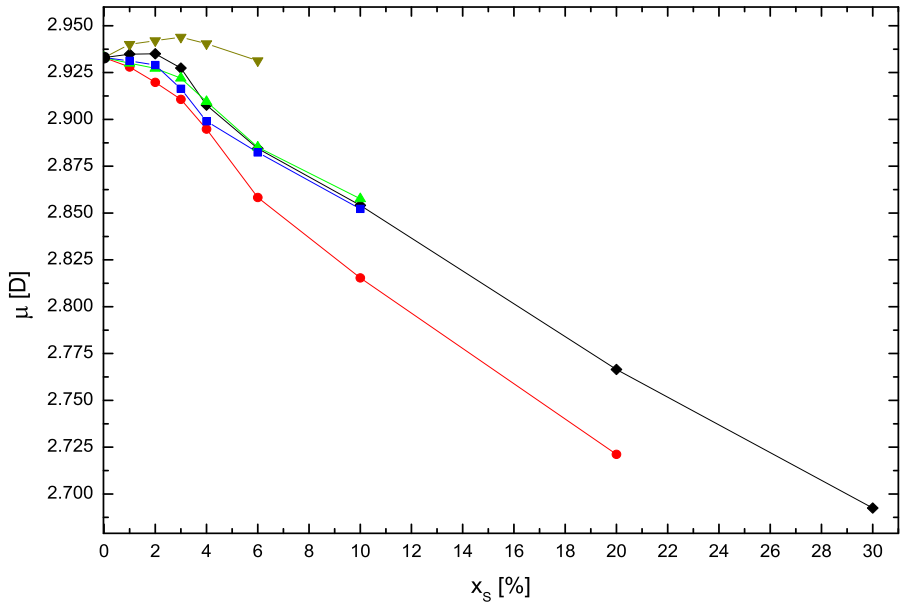

FIGURE 5.9: Average dipole moments of aqueous solutions of Ne (black ♦), Ar (red ◯), CH_4 (green ▲), Kr (blue ■), and Xe (olive ▼) at T = 298 K as a function of solute concentration.

Chapter 6

Thermodynamic Properties of Water and Aqueous Nonpolar Solute Mixtures

As was stated in the Aims section of the Chapter 1, investigation of the thermodynamic properties of water and aqueous nonpolar solute mixtures is one of the main goals of the present research project. Surprisingly enough, as it is shown in critical reviews of Vega and Abascal (2011), Wu *et al.* (2006), Mao and Zhang (2012), modern water models are much less successful in predicting thermodynamic properties like heat capacities, compressibilities, expansion coefficients, etc. than predicting physical properties like dielectric constant, diffusion coefficient, enthalpy of vaporisation, etc (Vega and Abascal, 2011; Guillot, 2002). Most of the thermodynamic variables are still largely omitted from the mainstream focus of the simulation community, moreover, properties like speed of sound and Joule-Thomson coefficient are, to the best of our knowledge, nonexistent in simulation literature. Researchers are still focused on improving existing water models and prediction of water-ice phase digram, structural and polarization properties. Unlike water, thermodynamic properties of some gases (natural gas, carbon dioxide) have been calculated using fluctuation formulas in works of Lagache *et al.* (2001, 2004) and Colina *et al.* (2003).

There are several reasons for such a situation. The generally accepted point of view is that the existing water models were not designed to reproduce thermodynamic properties (Vega and Abascal, 2011). In the context of the present work and some recent investigations (Yigzawe and Sadus, 2013; Kiss and Baranyai, 2013), this statement seems questionable, because some water models (TIP4P/2005 (Abascal and Vega, 2005), MCYna (Li *et al.*, 2007), BKd3 (Kiss and Baranyai, 2013), and SPC/E (Berendsen *et al.*, 1987))

do predict some thermodynamic properties with reasonable accuracy. Another significant deficiency of the most commonly used rigid water models like TIP4P/2005 and SPC/E is the absence of nonadditive interaction terms, namely polarization and multi-body terms intrinsic to most quantum-mechanical systems (Eisenberg and Kauzmann, 1969).

Table 6.1 presents experimental and simulation data of the most popular water models at 298 K and 0.1 MPa. The large value range for all properties of interest indicates different abilities of different water model to correctly predict thermodynamic properties of water, and, as a consequence, absence of one most suitable for these purposes water model. In addition to the choice of potential, a large discrepancies in simulation results is caused also by force-field implementations and calculation techniques. Comparative studies performed by Mao and Zhang (2012), Wu *et al.* (2006), and Vega and Abascal (2011), unexpectedly show different results obtained from the same water models. For example, implementation of Ewald method or PPPM technique (Sadus, 1999) gives different value of isochoric C_v and isobaric C_p heat capacities (Mao and Zhang, 2012). Therefore, it is necessary to develop special simulation techniques for particular thermodynamic quantities within particular ensembles. Such techniques have been developed in a series of works by Lustig (1994abc, 1998, 2011, 2012) and is described in the Chapter 3. All thermodynamic properties presented in this Chapter are calculated with the help of formulas given Table 3.1 of Chapter 3.

The solvation of nonpolar solutes in water is a fundamental problem for the understanding of the thermodynamics of gas clathrate formation, membrane formation, and protein folding. Low solubility of nonpolar solutes like methane or noble gases in water is known as a hydrophobic effect. Despite more than half-century of experimental and simulation research since the introduction of "iceberg" concept in the middle of 20th century, the picture of hydrophobic solvation is still not clear. Moreover, so far modelling of some thermodynamic properties has received more attention than others, for example constant volume isochoric heat capacity C_v. Despite extensive experimental investigation of various aqueous solutions at water critical temperature, pressure, and constant volume conditions in the works of Abdulagatov *et al.* (2005), references about thermodynamic properties at other state points are very scarce and mostly limited to ambient conditions. This situation is rather strange if one takes into account unusual behavior of thermodynamic potentials observed upon dissolution of polar and nonpolar solutes (Ben-Naim, 1980, 2006, 2009). For example, hydration of nonpolar particles is accompanied by unusual large loses in entropy ($-\Delta S$), increase in constant pressure heat capacity ($+\Delta C_p$), and as a consequence unfavorable increase in enthalpy ($+\Delta H$). At the same time hydration of most of the polar and ionic groups is followed by negative change in constant pressure heat capacity ($-\Delta C_p$) and local decrease of entropy (Sharp and Madan, 1997; Chaplin, 2013). Most of the studies of ΔC_p changes have been

limited to the system containing only one nonpolar particle at ambient conditions. In addition to this there are several theoretical definitions of hydrophobic solvation process as well there is no clear statistical mechanical formulation of solvation thermodynamic quantities (Ben-Naim, 2009; Sharp and Madan, 1997). The question of ΔC_v and ΔC_p changes in the range from ambient to supercritical temperatures and wide range of solute concentrations still remain unanswered.

The results presented in this Chapter are divided into two parts. Firstly, we calculate thermodynamic properties of pure water using two nonpolarizable rigid water models SPC/E and TIP4P/2005. This will allow us to check the ability of these popular water models to predict thermodynamic properties in the extended temperature-pressure range. additionally, we compare our results with the most recent data obtained by Yigzawe and Sadus (2013) from MD simulations of liquid water in the NVE ensemble. These authors employed nonadditive *ab initio* MCYna (Li *et al.*, 2007) potential to calculate similar thermodynamic properties. This comparison will allow us to elucidate influence of nonadditive interactions, like polarization and three-body interaction, on prediction of thermodynamic properties of water. All liquid water data are thoroughly compared against the highly accurate data obtained from International Association for the properties of Water and Steam (IAPWS-95) software developed by Wagner (1995) to calculate thermodynamic quantities at isochoric conditions.

Secondly, having calculated thermodynamic properties for pure water we can extend our investigation for aqueous solutions. In this research we have simulated water-methane mixture in the NVT ensemble at constant density 0.998 g/cm^3 in the temperature range 298 - 650 K. The water-methane binary mixture was chosen as a model system which within a framework of SPC/E + LJ potential model can describe general trends in the solvation of nonpolar solutes like noble gases in water. Another reason in favor of methane is the great importance of methane compounds in water for modern energy industry (Kvenvolden, 1995). At constant density conditions, and at ever increasing temperature and pressure, mixtures remain in the stable liquid phase (Franck, 1987; Shvab and Sadus, 2012b). In this work we used the combined SPC/E + LJ potential model to describe water-methane mixtures, since both SPC/E and TIP4P/2005 models give quite similar results for pure water. Furthermore, the SPC/E model is the most common starting choice for investigation of dilute aqueous nonpolar solutions (Guillot and Guissani, 1993; Paschek, 2004; Dyer *et al.*, 2008).

The simulation details were given in Chapter 4.

6.1 Thermodynamics of solvation

The solvation also sometimes called "dissolution", is the process of attraction and association of molecules of a solvent with molecules or ions of a solute. As solute particles dissolve in a solvent they spread out and become surrounded by solvent molecules. Generally speaking, the solvation process is defined as the process of transferring a single molecule from a fixed position in an ideal gas phase to a fixed position in a liquid (Ben-Naim, 2009). In most cases the solvation is happening at constant temperature and pressure conditions. Brief description of solvation changes in thermodynamic potentials upon solvation of nonpolar solutes is given below.

Historically, the first law that defined the solubility of gases in liquid was Henry's law formulated in 1803. Henry's law can be put into mathematical terms (at constant temperature) as

$$p = k_H c, \tag{6.1}$$

where p is the partial pressure of the solute in the gas above the solution, c is the concentration of the solute and k_H is a constant with the dimensions of pressure divided by concentration. The constant, known as the Henry's law constant, depends on the solute, the solvent and the temperature. Henry's law is a limiting law that only applies for 'sufficiently dilute' solutions. The range of concentrations in which it applies becomes narrower the more the system diverges from ideal behavior. Typically, Henry's law is only applicable to gas solute mole fractions less than 0.03 (Prausnitz *et al.*, 1999).

The first theories that attempted to explain the thermodynamics of water with nonpolar gases were (Ben-Naim, 2009): Eley's theory (1944) based on a lattice model for water and Frank and Evan's (1945) theory of iceberg formation. Apart from the lattice postulate, Eyley's model had restriction on the number of holes solute particle can occupy in this lattice. Frank and Evans (1945) introduced somewhat artificial idea that when a nonpolar solute is inserted in water, "icebergs" are formed around it. Although there was no proof for the iceberg formation, the idea gained significant popularity (Eisenberg and Kauzmann, 1969).

The first molecular interpretation of the process of solution proposed a two-step process. On the first step the cavity that can accommodate the solute is formed, and on the second step, the solute is introduced into this cavity. Based on this, for each thermodynamic quantity of solution, say enthalpy and entropy, we can write (Ben-Naim, 2009)

$$\begin{cases} \Delta H = \Delta H^c + \Delta H^{int} \\ \Delta S = \Delta S^c + \Delta S^{int} \end{cases} \tag{6.2}$$

where c means cavity and int stands for interaction. Experiments revealed large negative values of enthalpies and entropies of solution of inert gases in water (Frank, Evans, 1945). For example, the entropy of solution of two moles of argon in water is -60.4 cal/mol·K (Ben-Naim, 2009). This large negative entropy of solvation is generally perceived as a results of a local ordering effect. The solubility of nonpolar solutes is usually measured by the Ostwald absorption coefficient (Kennan and Pollack, 1990)

$$\gamma_s = \left(\frac{n_s^l}{n_s^g} \right)_{eq}, \tag{6.3}$$

where n_s^l and n_s^g are number densities of solute s in the liquid and gaseous phases at equilibrium. The low solubility of nonpolar solute in water has led to the concept "hydrophobic" solute. The solvation Gibbs energy of solute in liquid is directly related to the Ostwald coefficient γ_s

$$\Delta G_s = kT \ln \gamma_s. \tag{6.4}$$

Thus, low solubility of nonpolar solutes in water, in terms of γ_s, is equivalent to a large positive value of solvation Gibbs energy ΔG_s. For instance, ΔG_s of methane and argon in water at 25°C is approximately +2000 cal/mol·K (Ben-Naim, 2009). It is intersting to note that the solvation Gibbs energy of small nonpolar molecules like neon or argon in heavy water D_2O is smaller than in H_2O. From the definition of solvation process, it follows that the change in the solvation Gibbs energy associated with the solvation process is

$$\Delta \mu_s \underset{ig \to l}{=} \Delta G_s = \mu_s^l - \mu_s^{ig}, \tag{6.5}$$

where μ_s^l and μ_s^{ig} is the chemical potential of solute in a liquid (l) and in an ideal gas (ig) phase respectively. Thus, from the solvation Gibbs energy given by Eq. (6.4) and the vapor pressure of pure solute, we can calculate the solubility of solute s in a liquid l.

The unique properties of water and aqueous nonpolar solutions can be best described by the so-called 'solvation quantities', or changes of thermodynamic potentials and related extensive and intensive variables in mixture compared to pure substance. As was shown

by Ben-Naim (2009, 1980), solvation quantities are important mainly for two reasons. First, the solvation Gibbs energy ΔG_s determines the solubility of a solute. The second application is to determine the equilibrium constant of a chemical reaction in a liquid phase.

The statistical mechanical expression for the solvation Helmholtz energy in the NVT ensemble is given by (Ben-Naim, 2009)

$$\Delta A_s = kT \ln \langle \exp(-\beta B_s) \rangle \,, \tag{6.6}$$

where $\beta = 1/kT$ and B_s is defined by

$$B_s(\mathbf{R}_s, \mathbf{X}^N) = U_{N+1}(\mathbf{R}_s, \mathbf{X}^N) - U_N(\mathbf{X}^N) = \sum_{i=1}^{N} U(\mathbf{R}_s, X^i). \tag{6.7}$$

The $B_s(\mathbf{R}_s, \mathbf{X}^N)$ is the total binding energy of solute s to all the N water molecules at a specific configuration $\mathbf{X}^N = X^1 ... X^i ... X^N$, and U_N is internal energy of the system. The solute s is presumed to be at some fixed position $\mathbf{R}_s$. It is interesting to note that the statistical mechanical expression for ΔG_s in NpT ensemble has the same form like right-hand side of the Eq. (6.6).

The solvation entropy ΔS_s in NVT ensemble is obtained by taking the temperature derivative of Eq. (6.6)

$$\Delta S_s = k \ln \langle \exp(-\beta B_s) \rangle_0 + \frac{1}{T} \left(\langle B_s \rangle_s + \langle U_N \rangle_s - \langle B_N \rangle_0 \right), \tag{6.8}$$

where symbols $\langle ... \rangle_s$ and $\langle ... \rangle_0$ mean an average over all mixture including solute s and an average over pure water in the absence of s.

The solvation energy is obtained from Eqs. (6.6) and (6.8)

$$\Delta E_s = \Delta A_s + T\Delta S_s = \langle B_s \rangle_s + \langle U_N \rangle_s - \langle U_N \rangle_0 \,. \tag{6.9}$$

Finally, using the first law of thermodynamic, we get the following expression for solvation enthalpy ΔH_s:

$$\Delta H_s = \Delta E_s + p\Delta V_s. \tag{6.10}$$

Another unusual property of aqueous solutions of nonpolar solutes is the relatively large partial molar heat capacity of the solute in water. The partial molar heat capacities of a solute s in solute-water mixture at constant volume and pressure are defined by

$$\begin{aligned} C_v &= \left(\frac{\partial U_s}{\partial T}\right)_{V,N_s,N_w} \\ C_p &= \left(\frac{\partial H_s}{\partial T}\right)_{p,N_s,N_w} \end{aligned} \tag{6.11}$$

where U_s is the internal energy of the mixture, N_s and N_w denote number of solute and water molecules. In this work we are studying thermodynamic properties of aqueous solutions of noble gases and methane. At ambient conditions these nonpolar solutes behave much like an ideal gas. The heat capacity of noble gases in the ideal gas phase is due to the translational degrees of freedom only, and this does not change upon transferring from the ideal gas phase into liquid. It is well known that isobaric C_p and isochoric C_v heat capacities of ideal gas is equal to $5R/2$ and $3R/2$ respectively. The heat capacities of solvation of s is defined by (Ben-Naim, 2009)

$$\begin{aligned} \Delta C_v &= \left(\frac{\partial \Delta U_s}{\partial T}\right)_{V,N_s,N_w} \\ \Delta C_p &= \left(\frac{\partial \Delta H_s}{\partial T}\right)_{p,N_s,N_w} \end{aligned} \tag{6.12}$$

For example, ΔC_p of methane in water is 53 cal/mol·K. The effect of solute solvation is usually accompanied by volume change of the whole aqueous solution. This solvation volume change is defined as (Ben-Naim, 2009)

$$\Delta V_s = \left(\frac{\partial \Delta G_s}{\partial p}\right)_T . \tag{6.13}$$

Zheng *et al.* (2012) experimentally observed dissolution process of methane gas bubbles in water at different temperatures and pressures. Their data clearly show reduction in total volume upon dissolution of methane bubbles. In the present work we use exclusively canonical NVT ensemble, therefore the volume of the system is fixed by definition. Thus, having identified general expressions for thermodynamic solvation quantities, all other thermodynamic properties like pressure coefficient, compressibilities, expansion coefficient etc., can be found like simple derivatives with respect to p, V, or T (Lustig, 2010).

TABLE 6.1: Comparison with experiment for the thermodynamic properties of several water models at 298K and 0.1 MPa.

Water model	C_v [J/mol·K]	C_p [J/mol·K]	κ_T [1/GPa]	κ_S [1/GPa]	γ_v [MPa/K]	α_p [10^{-4}/K]	μ_{JT} [K/MPa]	w_0 [m/s]	Ref.
SPC	62.350[a]	76.674	0.461	0.3748*	1.629*	7.51	-0.2034*	1635.7*	Wu *et al.* (2006)
SPC/E	79.325	80.385	0.476	0.4699	0.731	3.482	-0.2006	1460.1	this work
SPC/Fw	-	114.592	0.458	-	1.107*	2.00	-	-	Wu *et al.* (2006)
TIP4P	82.089[a]	88.975[a]	0.590	0.5443*	0.746*	4.4	-0.1872*	1357.4*	Chaplin *et al.* (2013)
TIP4P/2005	81.797	82.582	0.497	0.4923	0.618	3.076	-0.1937	1427.2	this work
TIP5P	118.239[a]	90.587[a]	0.410	0.535*	1.177*	6.3	-0.1275*	1369.0*	Chaplin *et al.* (2013)
GCPM	-	94.0	-	-	-	4.20	-	-	Chialvo and Cummings (1998)
MCY	70.800[b]	-	-	-	-	-	-	3040.0	Yigzawe and Sadus (2013)
MCYna	74.357	74.636	0.448	0.4465	0.383	2.63	-0.2295	1498.4	Yigzawe and Sadus (2013)
BK3d	-	88.0	0.450	-	0.488*	2.20	-	-	Kiss and Baranyai (2013)
IAPWS-95	74.836	75.770	0.448	0.4458	0.567	2.54	-0.2215	1499.7	Wagner (1995)
Experiment	**74.440**	**75.312**	**0.458**	**0.425**	**0.436**	**2.00**	**-0.2215**	**1496.7**	Wagner and Pruß (2002)

[a] Mao and Zhang (2012)

[b] O'Shea and Tremain (1980)

* values obtained using conversion relations (6.14) (Münster, 1970).

6.2 Reference data for water

Most of the experimental data for water reported in the literature (Wagner and Pruß, 2002; Debenedetti, 2003) are at isobaric conditions whereas the MD simulations in the NVT ensemble yield isochoric values. Therefore, we must either convert the data or find an accurate alternative to the experimental values. For this purpose, we have used the International Association for the Properties of Water and Steam (IAPWS-95) software developed by Wagner (1995) to calculate thermodynamic quantities at isochoric conditions. The IAPWS-95 is based on a highly accurate empirical equation of state (Wagner and Pruß, 2002) for water and allows researchers easily obtain many thermodynamic properties of water and other liquids at different densities, temperatures and pressures. However, the IAPWS-95 can only be used to directly calculate pressure P, heat capacities C_v and C_p, Joule-Thomson coefficient μ_{JT}, and the speed of sound w_0. The remaining thermodynamic quantities, namely κ_T, κ_S, γ_v, and α_p are then calculated using the following well-known relationships (Münster, 1970):

$$\begin{cases} \kappa_S = \frac{V}{w_0^2 M} \\ \kappa_T = \frac{\kappa_S C_p}{C_v} \\ \gamma_v^2 = \frac{C_v(\kappa_S^{-1} - \kappa_T^{-1})}{TV} \\ \alpha_p = \frac{\mu_{JT} C_p}{TV} + \frac{1}{T} \end{cases} \tag{6.14}$$

where M is the total mass of the system.

Comparison of simulation data of aqueous nonpolar mixtures with experiment is very difficult due to high scarcity of available experimental results. The work of Abdulagatov *et al.* (2005) is one the few extensive reviews of the thermodynamic properties of binary water-hydrocarbons mixtures. The experimental and simulation data about thermodynamic properties of aqueous nonpolar mixtures is even more dispersed and limited to solute concentrations $\leq 1\%$ at only few state points (Sharp and Madan, 1997; Ben-Naim, 2009).

6.3 Pressure

We start our investigation by correctly identifying temperature and pressure range in which we are going to study water and water-methane properties. The temperature-pressure conditions of water in the liquid phase are shown in Fig. 6.1. The IAPWS-95 reference data (Wagner, 1995) increases nonlinearly up to the water normal boiling

temperature, at which point afterwards the data increases almost linearly. The initial trend is probably caused by a reorganization of the water structure, namely a gradual retreat from classical tetrahedral structure, and increasing thermal fluctuations of the H-bond network.

Both the SPC/E and TIP4P/2005 potentials show good agreement with the IAPWS-95 reference data. Simulated pressures from both water potentials show a close to a linear trend for the whole range of temperatures. These potentials slightly overestimate reference data for the entire temperature range. From 298 K and up to 420 K the discrepancy is slightly higher which may be due to the excessive rigidity of the nonpolarizable SPC/E and TIP4P/2005 models. In contrast, the isochore calculated from the MCYna potential is in much better agreement with the reference data over the entire range of temperatures, being only slightly lower at supercritical temperatures (Yigzawe and Sadus, 2013).

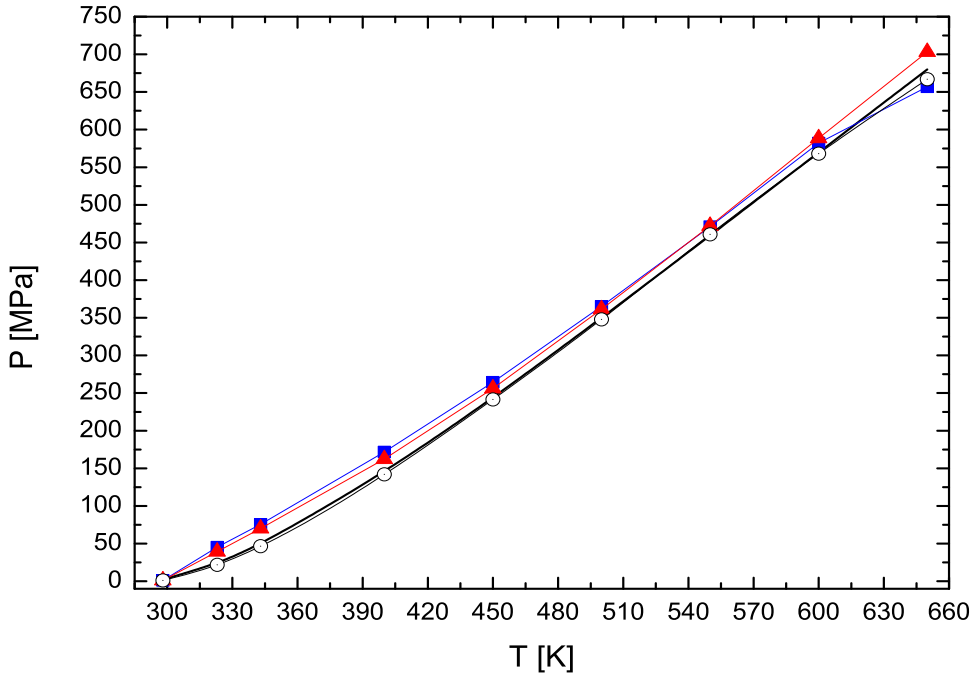

FIGURE 6.1: Isochores of liquid water (0.998 g/cm^3) predicted by the SPC/E (blue ■), TIP4P/2005 (red ▲) and MCYna potential (⊙) and compared to IAPWS-95 reference data for water (—). The lines through the data points are given only for guidance.

Fig. 6.2 shows isochores of water-methane mixtures with methane molar fractions x_s = 0, 6, 10, and 15% in the liquid phase and temperature range 298 - 650 K. Simulated pressures of water-methane mixtures (x_s = 6, 10, and 15%), calcuated with the help of the combined SPC/E + LJ potential, show trend closer to linear in the whole temperature region. It is clearly seen that the pressure is increasing significantly with temperature and solute concentration. This effect is predominantly caused by the constraint imposed on systems volume (NVT ensemble). At these conditions and at increasing temperature, water molecules experience significan Lennard-Jones repulsion from the methane

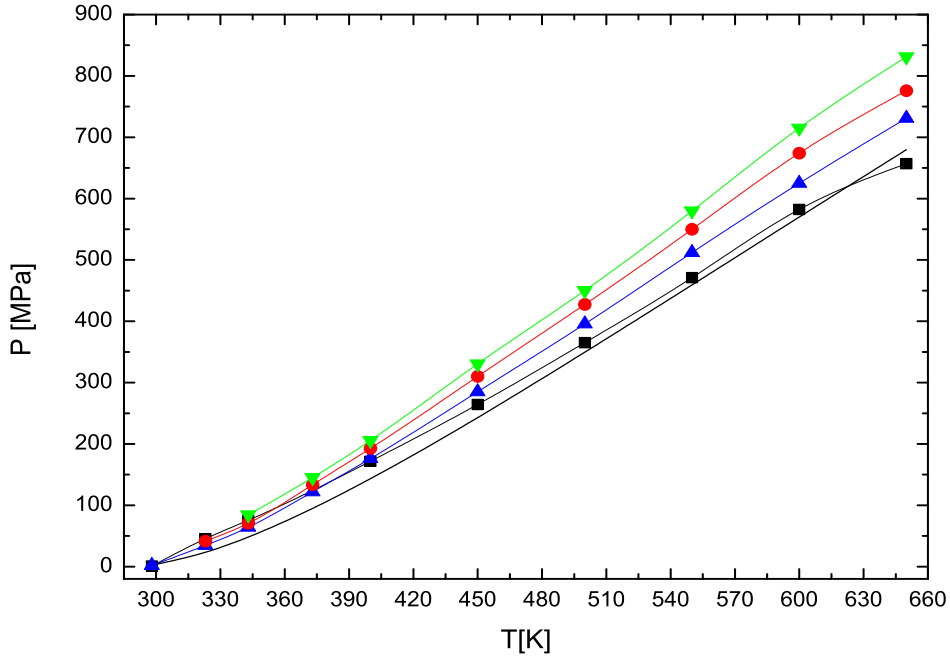

FIGURE 6.2: Isochores (0.998 g/cm^3) of liquid water and water-methane mixtures at methane concentrations 0% (black ■), 6% (blue ▲), 10% (red ◯), 15% (green ▼), and IAPWS-95 reference data for pure water (—). The simulation data are obtained from the SPC/E + LJ model. The lines through the data points are given only for guidance.

molecules, which obviously increases with increasing methane concentration. The uniform dissolution of methane molecules in water and absence of any stable methane clusters or assemblies with the size of more than 1 nm at all solute concentrations was confirmed by both a careful analysis of radial distribution functions and visualization of the simulation box during the equilibration stage.

At high pressures and temperatures significant reorganization of H-bonding inside the aqueous solution is taking place. As many believe, it is this reorganization of H-bond network around hydrophobic solutes which is responsible for all specific changes in solvation quantities (Chaplin, 2013; Chandler, 2006). Introduction of nonpolar solutes disturbs H-bond structure around the solute particles, and changes energy balance of the mixture. The rate of changes to the structure is defined by the interplay between two components of Gibbs free energy $\Delta G = \Delta H - T\Delta S$, as well as amount of solute particles and their size. Most of the previous MD simulations of hydrophobic interaction were done for systems containing only one nonpolar particle, or very dilute solutions (Paschek, 2004ab, Docherty *et al.*, 2006; Botti *et al.*, 2003). Most of the researchers (Okazaki *et al.*, 1979; Alagona and Tani, 1980; Cristofori *et al.*, 2005) agree that in very small quantities hydrophobic solutes strengthen water structure or, in other words, increase the average number of H-bonds per water molecule. Chandler (2005) in his review summarizes the

main aspects of hydrophobic hydration. In case of small solute particles (<0.5 nm) hydration process is driven by entropically dominated free energy, when for larger solute particles or their clusters (>1 nm), hydration is driven by enthalpically dominated free energy. Negative entropy change (ΔS) inside hydration shells and the reordering of H-bond network around solute particles moves them to form aggregates with smaller total surface. With increasing number of solute particles this eventually leads to phase separation. However, this is not the case in our simulations. Under constant volume and density conditions, and high pressures as shown on Fig. 6.1, water-methane mixtures remain in a single liquid phase. The maintaining of a one-phase region prohibits formation of any large solute assemblies, which could lead to phase separation. At sufficiently high pressures as shown on Fig. 6.2, external forces overwhelm the finite driving force to assemble, making methane molecules to remain dispersed in the solution.

6.4 Thermal pressure coefficient

The thermal pressure coefficient γ_v is one of the fundamental thermodynamic quantities; it is closely related to various properties such as internal pressure, sonic velocity, the entropy of melting, isothermal compressibility and expansibility, etc. The thermal pressure coefficient is defined as the differential dependence of pressure on temperature of a system perturbed by a change in temperature where the volume remains constant.

The thermal pressure coefficient as a function of temperature is illustrated in Fig. 6.3. γ_v for the SPC/E and TIP4P/2005 potentials start from values of 0.731 and 0.618 MPa/K respectively, and increases almost linearly until the boiling temperature. After this, γ_v starts slowing down, peaking at around 550 - 580 K with a further tendency to decrease. Both SPC/E and TIP4P/2005 potentials give higher values of γ_v compared to the reference data throughout the whole temperature range, with TIP4P/2005 potential being slightly closer to the reference data then SPC/E. Our observations are consistent with results reported in the reviews of Wu *et al.* (2006) and Vega and Abascal (2011). All nonpolarizable water models vastly overestimate pressure coefficient at 298 K. The over estimation of the experimental value γ_v = 0.436 MPa/K by some 30 - 200% strongly indicates that all nonpolarizable water models reported in (Vega and Abascal, 2011; Wu *et al.*, 2006) fail to describe the temperature dependence of pressure at ambient conditions.

It is apparent from the comparison given in Fig. 6.3 and Table 6.1 that the MCYna potential yields the closest agreement with the reference data. This may reflect the better description of interatomic interactions given by MCYna potential, namely the contributions from nonadditive terms. Experimentally, the thermal pressure coefficient becomes

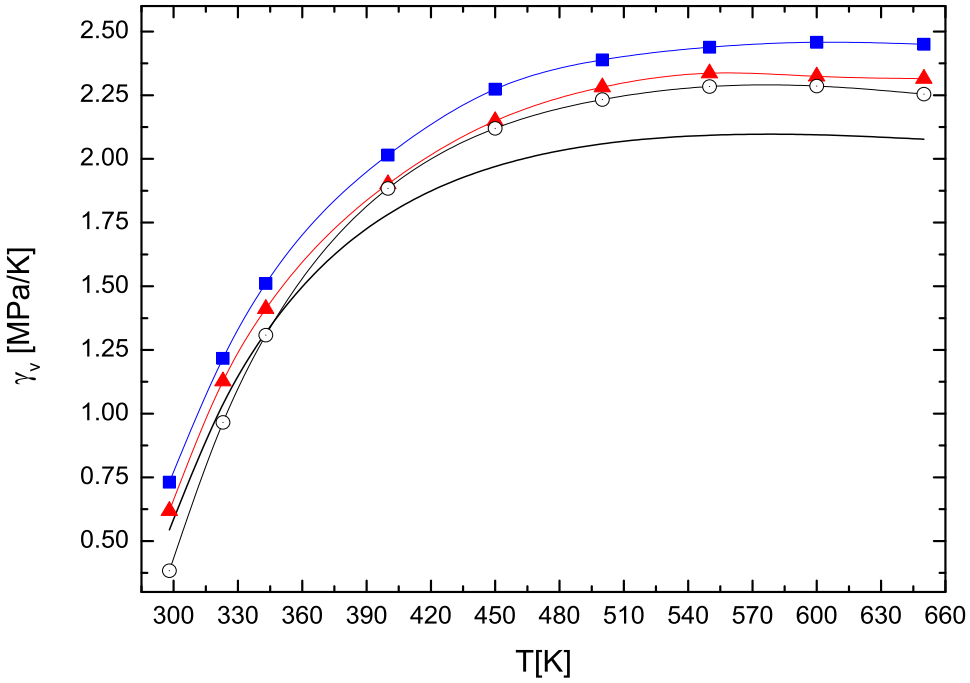

FIGURE 6.3: Thermal pressure coefficient as a function of temperature predicted by the SPC/E (blue ■), TIP4P/2005 (red ▲) and MCYna potential (⊙) and compared to IAPWS-95 reference data for water (—). The lines through the data points are given only for guidance.

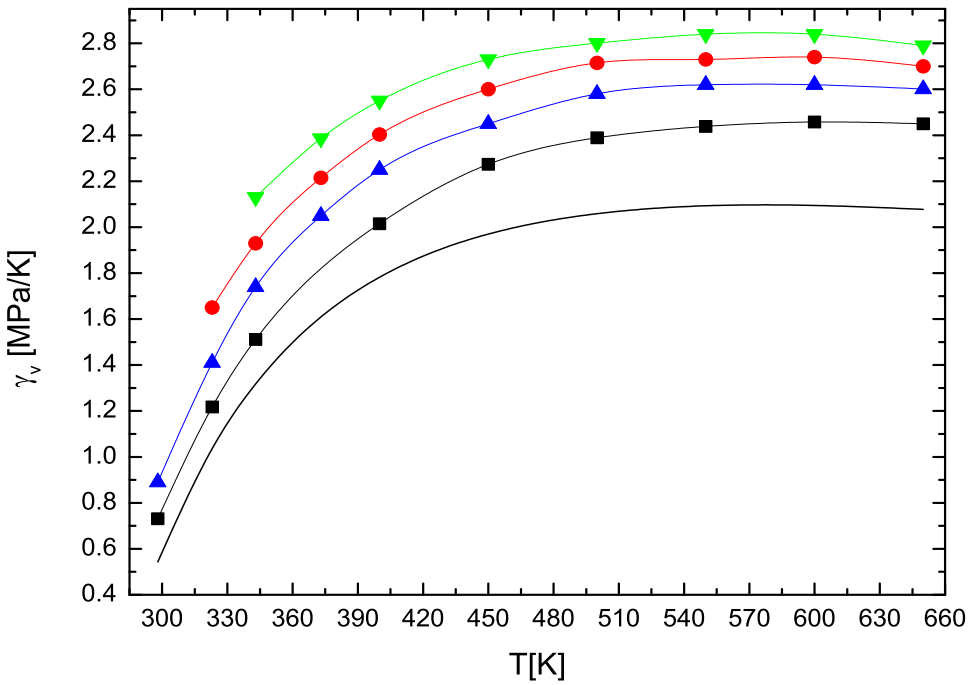

FIGURE 6.4: Thermal pressure coefficient of the water-methane mixtures (0.998 g/cm^3) at methane concentrations 0% (black ■), 6% (blue ▲), 10% (red ◯), 15% (green ▼), and IAPWS-95 reference data for pure water (—). The simulation data are obtained from the SPC/E + LJ model. The lines through the data points are given only for guidance.

negative at temperature less than 277 K with anomalous density behavior (Münster, 1970). Positive values of the thermal pressure coefficient in the entire simulation region implies that water does not show anomalies at a density of 0.998 g/cm^3.

Fig. 6.4 shows temperature dependence of the water-methane thermal pressure coefficient γ_v obtained from the SPC/E + LJ model. One can see, that thermal pressure coefficients of water-methane mixtures at solute concentrations x_s = 6, 10, and 15% are higher than in case of pure water (x_s = 0%). Such behavior is closely related to higher internal pressures of water-methane mixtures compared to pure water, as it is shown on Fig. 6.2. To the best of our knowledge, there are no previous MD simulations or analytical calculations of thermal pressure coefficient of aqueous nonpolar solutions. Higher γ_v of sea water ($\approx$ 0.7 MPa/K at ambient conditions) comparing to fresh water (0.436 MPa/K) can serve as indirect proof obtained here general trend (Safarov *et al.*, 2009).

6.5 Isothermal and adiabatic compressibilities

The isothermal and adiabatic compressibilities reflect how the density of the system changes with pressure. Compressibility has a complex dependence from local density of water and water clusters and the H-bond strength. Both isothermal and adiabatic compressibilities start from a value of 0.459 GPa^{-1} at ambient conditions, which reflects the cohesive nature of the extensive H-bonding. Due to strong thermal fluctuations with increasing temperature, the structure of water starts collapsing, opening up large cavities inside the H-bond network, or in other words, shifting the water structure to more open one. As a consequence, compressibility of water decreases with increasing temperature and pressure.

Simulation results for κ_T and κ_S as functions of temperature are compared with reference data in Figs. 6.5 and 6.8 respectively. The SPC/E and TIP4P/2005 potentials at 298 K have values of κ_T = 0.476 and 0.497 GPa^{-1} respectively, which is consistent with previous calculations (Berendsen *et al.*, 1987; Wu *et al.*, 2006; Vega and Abascal, 2011). As reported by Wu *et al.* (2006) and Abascal and Vega (2011) most rigid potentials of the SPC and TIP families have thermal compressibilities higher than that of real water. In contrast, flexible SPC/Fw (Wu *et al.*, 2006) and F3C (Levitt *et al.*, 1997) models have smaller κ_T, which indicate the influence of internal degrees of freedom. Unlike the constant pressure data (Debenedetti, 2003), κ_T and κ_S at a constant density of 0.988 g/cm^3 keep gradually decreasing not showing any minima. At temperatures up to the boiling temperature, the isothermal and adiabatic compressibilities predicted by the both SPC/E and TIP4P/2005 potentials overestimates corresponding values from the IAPWS-95 reference data. Data from these potentials gradually decrease with temperature,

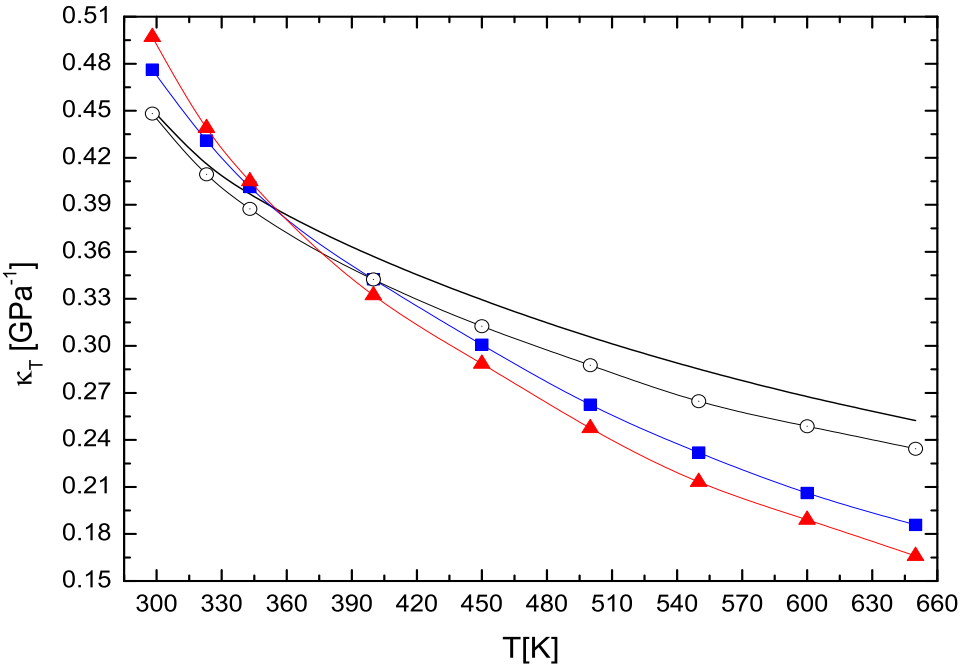

FIGURE 6.5: Isothermal compressibility as a function of temperature predicted by the SPC/E (blue ■), TIP4P/2005 (red ▲) and MCYna potential (⊙) and compared to reference data for water (—). The lines through the data points are given only for guidance.

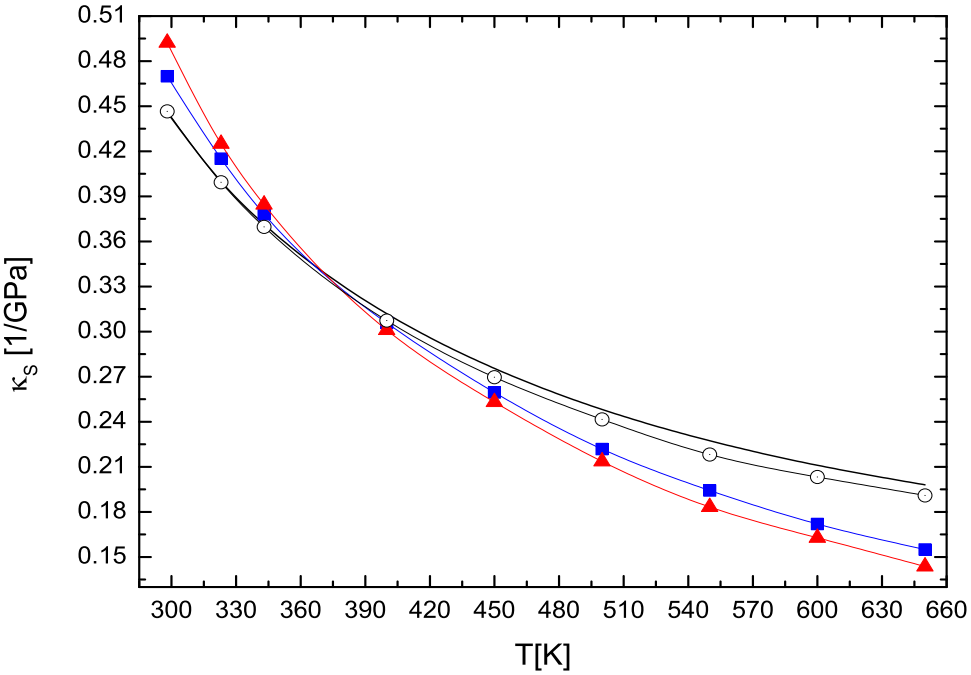

FIGURE 6.6: Adiabatic compressibility as a function of temperature predicted by the SPC/E (blue ■), TIP4P/2005 (red ▲) and MCYna potential (⊙) and compared to reference data for water (—). The lines through the data points are given only for guidance.

levelling off with the reference data at around 355 and 373 K for κ_T and κ_S respectively. After 373 K, the curves on both figures keep descending below the reference data. We do not have a simple explanation for these results.

Figs. 6.5 and 6.6 also present the most recent data obtained from the MCYna potential (Yigzawe and Sadus, 2013). The comparison shows that the MCYna results are in much better agreement with the reference curve for both κ_T and κ_S. This underestimation of κ_T and κ_S of water for nonpolarizable SPC/E and TIP4P/2005 potentials and to a smaller extent MCYna potential can be attributed to inadequate temperature dependence of the water structure at high temperatures provided by these potentials. As was shown recently (Shvab and Sadus, 2012a, 2012b) nonpolarizable potentials from the SPC-family underestimate the level of water structure at temperatures approaching the critical temperature, particularly number of hydrogen bonds.

It is well known (Soper, 2000) that water at critical conditions maintains a much more stable shell structure and higher level of H-bonding then predicted by any potential model. Svischev and Kusalik (1994), and Shiga and Shinoda (2005) identified a specific feature of SPC based models that could be responsible for underestimating H-bonded configurations. The rotational self-diffusion coefficient (Svischev and Kusalik, 1994) in the H-bonding plane for the SPC/E potential is half the value observed for other planes. That is, the angle between the intra-molecular H-O covalent bond and intermolecular O$\cdots$O vector (H-O$\cdots$O) for the H-bonded pair can fall into narrow range of values. Path integral molecular dynamics (PIMD) simulations have revealed (Shiga and Shinoda, 2005) that the quantum corrections significantly broaden the H-O$\cdots$O angle distribution in both liquid and solid phases, allowing for better H-bonding. Although quantum correction calculations remains computationally and theoretically challenging, accounting for polarisation interactions or bond vibrations can improve predictions of the density dependent properties such as compressibilities, thermal expansion and thermal pressure coefficients for a wide range of state points. The MCYna potential, which takes into account non-additive effects like polarization, gives a better description of the H-bond network and shell structure even at high temperatures.

Isothermal κ_T and adiabatic κ_S compressibilities of water-methane mixtures obtained from the SPC/E + LJ model are shown in Figs. 6.7 and 6.8 respectively. The κ_T and κ_S of the water-methane mixtures obtained from the combined SPC/E + LJ potential are expectedly smaller than those of pure water. Both κ_T and κ_S decrease with temperature and are proportional to solute molar fraction x_s. In absence of experimental data or similar MD results we can only compare our predictions with theoretical calculations and other aqueous solutions. Analytical calculations by Zaytsev *et al.* (2010) of aqueous solutions of potassium chloride confirm the temperature and solute molar fraction

dependence of both κ_T and κ_S. Isothermal compressibility of sea water is also smaller than in pure water (Safarov *et al.*, 2009).

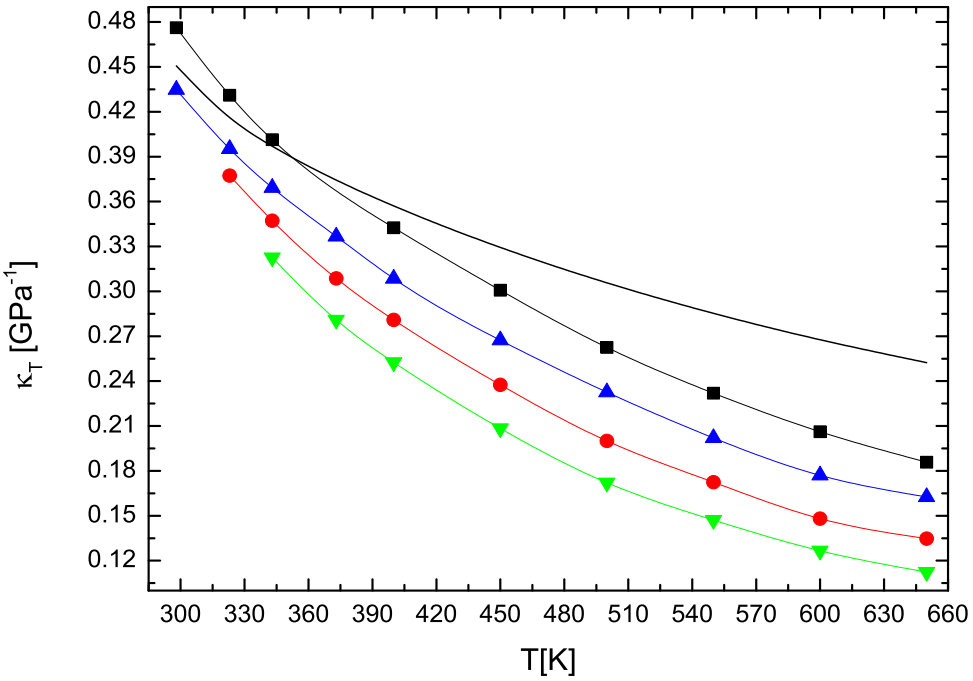

FIGURE 6.7: Isothermal compressibility of the water-methane mixtures (0.998 g/cm^3) at methane concentrations 0% (black ■), 6% (blue ▲), 10% (red circles), 15% (green ▼), and IAPWS-95 reference data for pure water (—). The simulation data are obtained from the SPC/E + LJ model. The lines through the data points are given only for guidance.

6.6 Thermal expansion coefficient

The thermal expansion coefficient is the measure of the tendency of matter to change volume in response to a change in temperature. While anomalous volume behavior of water and ice in the temperature region from -4 until +4°C are well known, the present data gives information about temperature dependence of α_p at constant volume. Unlike the constant pressure data (Wagner, Pruß, 2002), values of α_p at constant volume increase more slowly, starting to slow down after 350 K and eventually peaking at around 425-450 K. The initial increase in α_p can be attributed to the temperature driven collapse of water structure rather than lowering of water density. Later decrease in thermal expansion coefficient is caused by the constraint imposed on systems volume.

Simulation results for α_p are compared with reference data for water in Fig. 6.9. Values of α_p calculated from the method described in this work at 298 K for SPC/E (3.482 10^{-4}/K) and TIP4P/2005 (3.076 10^{-4}/K) models are in much better agreement with the experimental value 2.56 10^{-4}/K than most of the water models reported (Wu *et al.*,

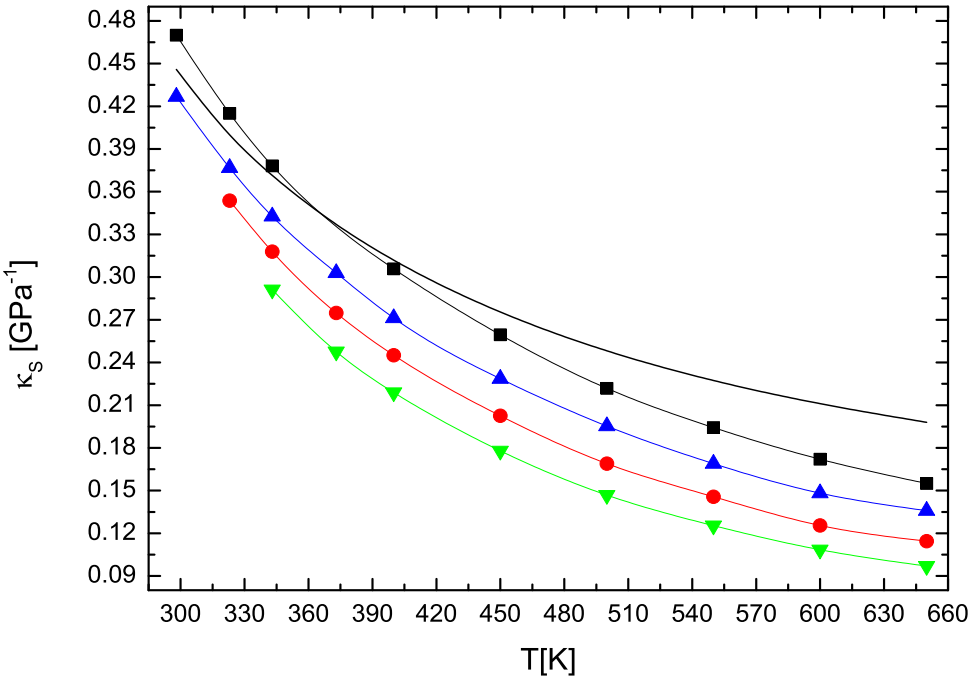

FIGURE 6.8: Adiabatic compressibility of the water-methane mixtures (0.998 g/cm^3) at methane concentrations 0% (black ■), 6% (blue ▲), 10% (red ◯), 15% (green ▼), and IAPWS-95 reference data for pure water (—). The simulation data are obtained from the SPC/E + LJ model. The lines through the data points are given only for guidance.

2006; Vega and Abascal, 2011). For example, the value of α_p for the SPC/E potential obtained from the fluctuation formula is 5.14 10^{-4}/K. In the temperature range of 298 K to 425 K, the thermal expansion coefficients obtained using the SPC/E and TIP4P/2005 water potentials again overestimate the reference data. Peaking at around 425 K both curves start to decrease, significantly deviating from the reference data. It is apparent that MCYna potential most closely mimics the behavior of the IAPWS-95 curve.

The temperature trend is caused by the interplay between isothermal compressibility κ_T and pressure coefficient γ_V (see Table 3.1 in Chapter 3). According to the classical fluctuation formula (Abascal and Vega, 2005), κ_T is proportional to volume fluctuations. As can be seen from Figs. 6.5 and 6.6, the density constraint means that, shortly after the normal boiling temperature, local volume fluctuations decrease with temperature and outweigh the increase in pressure. This temperature dependence of local volume fluctuations is a characteristic of the NVT ensemble and plays important role in other density dependent properties, such as the Joule-Thomson coefficient and speed of sound.

Thermal expansion coefficient of water-methane mixtures obtained from the SPC/E + LJ model is presented on Fig. 6.10. As we can see the mixture curves repeat the general trend of pure water. However, they also exhibit significantly different temperature dependence of the α_p peaks, as they are progressively shifted to the left, as methane

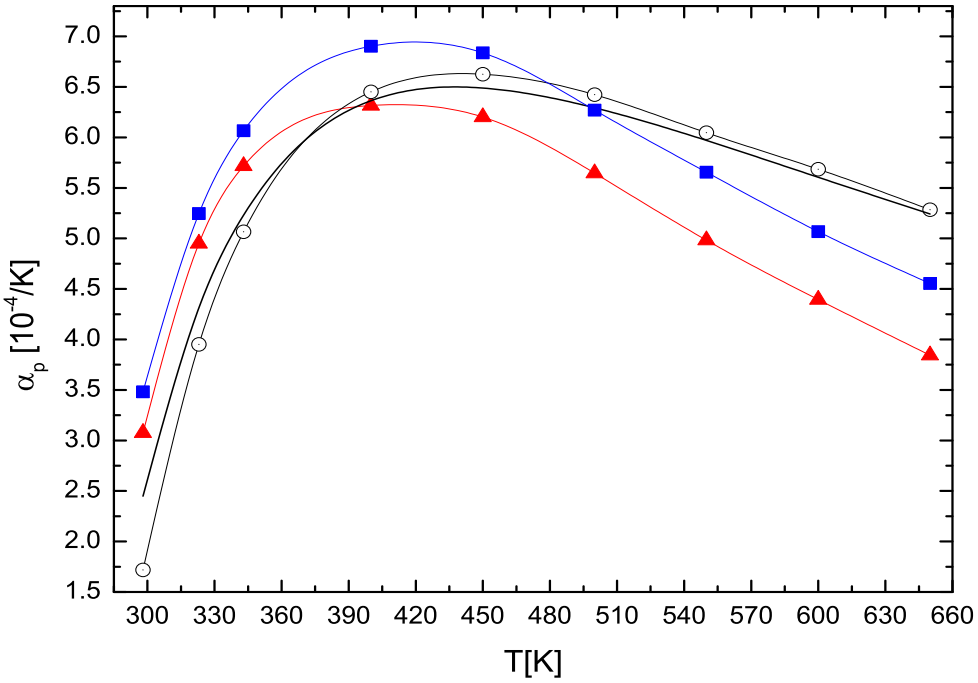

FIGURE 6.9: Thermal expansion coefficient as a function of temperature predicted by the SPC/E (blue ■), TIP4P/2005 (red ▲) and MCYna potential (⊙) and compared to IAPWS-95 reference data for water (—). The lines through the data points are given only for guidance.

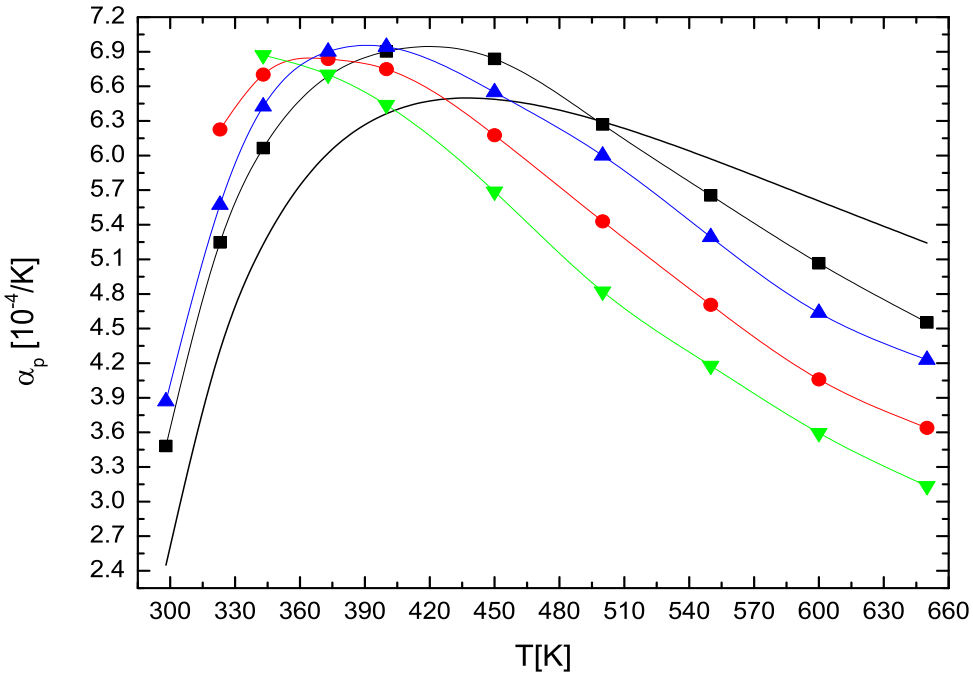

FIGURE 6.10: Thermal expansion coefficient of the water-methane mixtures (0.998 g/cm^3) at methane concentrations 0% (black ■), 6% (blue ▲), 10% (red ◯), 15% (green ▼), and IAPWS-95 reference data for pure water (—). The simulation data are obtained from the SPC/E + LJ model. The lines through the data points are given only for guidance.

concentration increases. This means that the expansion coefficient increases with the addition of nonpolar solutes at temperatures up to 400 K. Analytical calculations of α_p for urea (x_s = 2.5%) (Korolev, 2010) and aqueous solution of propylene glycol measurements (x_s = 0 - 60%) (Conde, 2011) also yield higher values of α_p than in pure water. Experimental curves of water-propylene glycol mixtures reported in shorter temperature interval also indicate gradual shift of α_p temperature maximum to the left, with increasing x_s (Korolev, 2010).

6.7 Isochoric and isobaric heat capacities

The isochoric and isobaric heat capacities of water as a function of temperature from our simulation and reference data are illustrated in Figs. 6.11 and 6.12, respectively. Both curves decrease progressively with increasing temperature, following each other rather closely. The TIP4P/2005 potential gives slightly higher values of C_v and C_p than the SPC/E curve at ambient conditions and slightly lower at critical conditions. The behavior of C_p curve is especially interesting since it does not show any minimum. The presence of a shallow C_p minimum at around 309 K and subsequent increase with temperature, at constant pressure conditions (Wagner and Pruß, 2002) is caused by rearrangement in water clustering and consequential increase of enthalpy. However, at constant volume, the values of C_p gradually decrease for the whole temperature range. At high pressures and temperatures the water structure apparently keeps deteriorating and the enthalpy decreases. While agreement with IAPWS-95 data is quite good for isochoric heat capacity, with the exception of too high values at 298 K, the isobaric heat capacity curve deviates from the reference data much more. As is evident from the relationships in Table 3.1 from Chapter 3, the isobaric heat capacity is derived from the values of isochoric heat capacity and compressibilities. Therefore, an error in either of these thermodynamic quantities will be reflected in the results for the isobaric heat capacity.

Extensive data for other potentials at different temperatures are not available in the literature. As can be seen from the Table 6.1 and the recent review by Mao and Zhang (2012), all nonpolarizable potentials over-predict values of C_v and C_p at 298 K and 0.1 MPa, by at least 7%. This inadequacy has been observed for quite some time and it has not been rectified by the development of new rigid or flexible water models.

It is sometimes suggested that the over-prediction of C_p is caused by a failure to address quantum influences (Shiga and Shinoda, 2005; Vega *et al.*, 2010), bond vibrations (Lobaugh and Voth (1997; Wu *et al.*, 2006), and polarization effects. Shiga and Shinoda (2005) performed extensive PIMD calculations of vapor, liquid and ice using a flexible

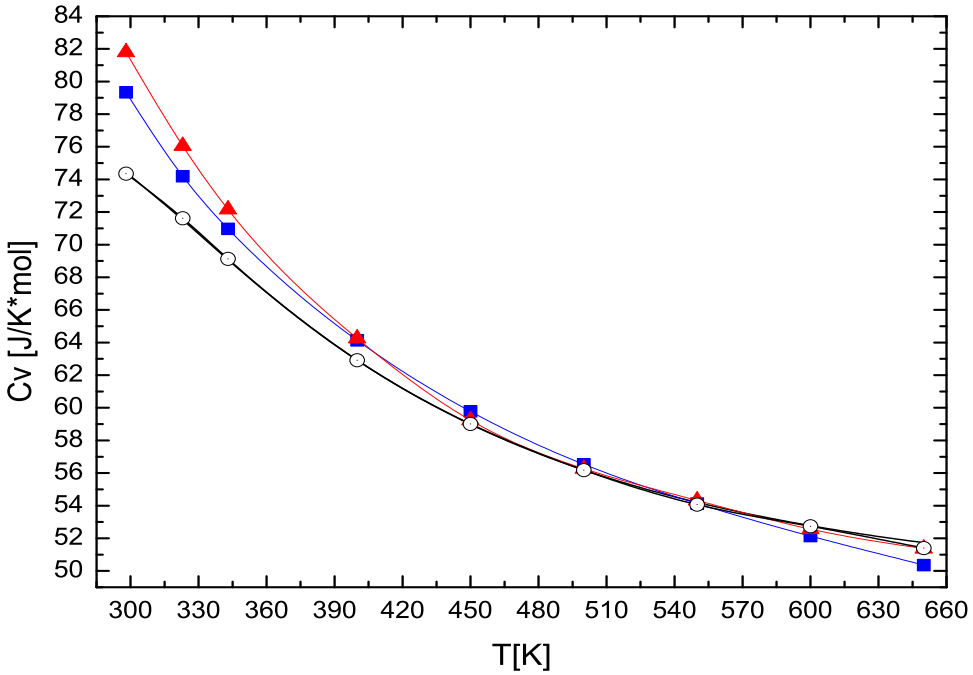

FIGURE 6.11: Isochoric heat capacity as a function of temperature predicted by the SPC/E (blue ■), TIP4P/2005 (red ▲) and MCYna potential (⊙) and compared to IAPWS-95 reference data for water (—). The lines through the data points are given only for guidance.

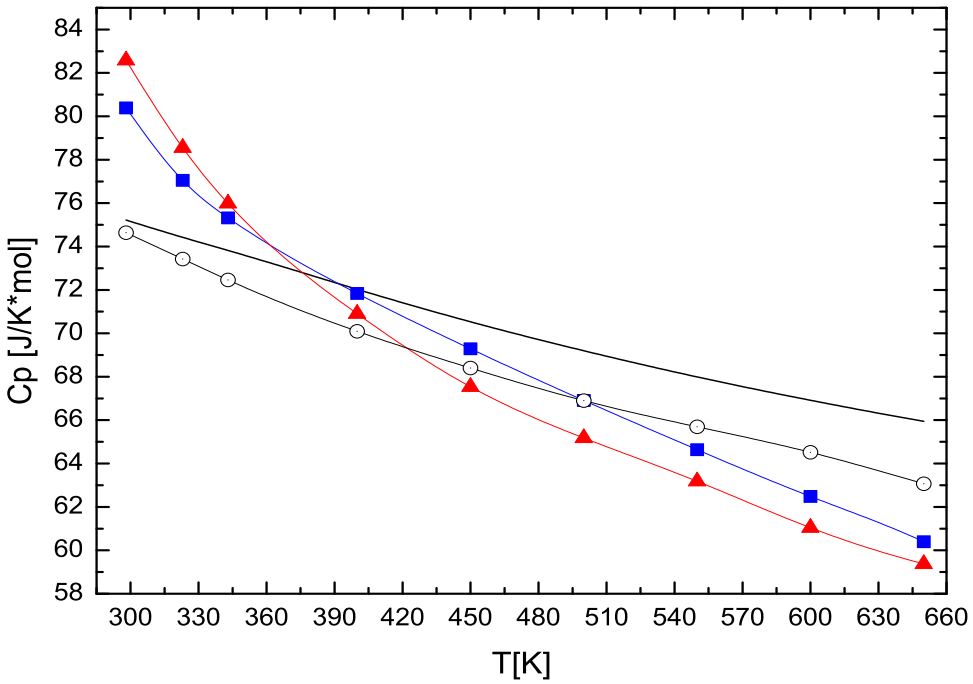

FIGURE 6.12: Isobaric heat capacity as a function of temperature predicted by the SPC/E (blue ■), TIP4P/2005 (red ▲) and MCYna potential (⊙) and compared to IAPWS-95 reference data for water (—). The lines through the data points are given only for guidance.

SPC/F water model (Lobaugh and Voth, 1997). The C_v of ice and vapour was accurately reproduced whereas C_v for liquid water was 23% smaller than the experimental value 74.44 J/mol·K. Nonetheless, this is a significant improvement over the classical SPC/F value of 116.395 J/mol·K. Vega *et al.* (2010) used a quantum corrected version of the TIP4P/2005 potential and obtained a value of C_p that was approximately only 5.8% less than the experimental value 75.312 J/mol·K. Shiga and Shinoda (2005) observed that success in predicting C_v for vapor and ice indicates that the vibrational heat capacity is predicted correctly, whereas underestimation in liquid phase means an inadequate description of hydrogen-bonded configurations.

Accounting for polarisation effects is a viable alternative to costly PIMD simulations because the classical treatment of intermolecular bond vibrations causes significant overestimation of heat capacity (Wu *et al.* (2006); Lobaugh and Voth, 1997). Abascal and Vega (2005) showed that including the self-energy correction (Berendsen *et al.*, 1987) helps to bring values of heat capacity C_p and heat of vaporisation (ΔH_v) significantly closer to experimental values by reducing non-corrected values of C_p and ΔH_v by more than 11% each. However, the self-energy correction $\Delta E_{pol} = (\boldsymbol{\mu}_l - \boldsymbol{\mu}_g)^2/2\alpha$ for the SPC/E and TIP4P/2005 is constant because the liquid $\boldsymbol{\mu}_l$ and the gas $\boldsymbol{\mu}_g$ phase dipole moments of these models are constant. Increasing deviations of C_p in the high temperature region on Fig. 6.12 indicates that constant ΔE_{pol} alone cannot improve heat capacity predictions in the wide temperature range.

Heat capacities obtained from the MCYna water potential, which explicitly accounts for polarization interaction via induced dipole moment (see Eqs. (2.5 - 2.9) in Chapter 2), are also presented in Figs. 6.11 and 6.12. The MCYna potential gives remarkably good agreement of the vales of C_v with IAPWS-95 data, while C_p values underestimate the reference data throughout the whole temperature range. As discussed above the under-estimation of values of C_p is connected with low values obtained for κ_T. It is apparent from the comparison of the isobaric heat capacities (Table 6.1 and Figs. 6.11 and 6.12) that the MCYna potential nonetheless yields the best agreement with experiment. The superiority of the MCYna results over SPC/E and TIP4P/2005 results clearly demonstrate the importance of polarization as a key contributing factor. The MCYna calculations did not need to invoke quantum corrections to obtain good agreement with experiment.

Isochoric and isobaric heat capacities of water-methane mixtures obtained from the SPC/E + LJ model are presented on Figs. 6.13 and 6.14. The C_v and C_p of pure water ($x_s = 0\%$) are also shown on these figures so we can immediately see the difference between mixtures and pure water. From the Figs. 6.13 and 6.14 it becomes immediately clear that C_v and C_p of water-methane mixtures are smaller than those of pure water.

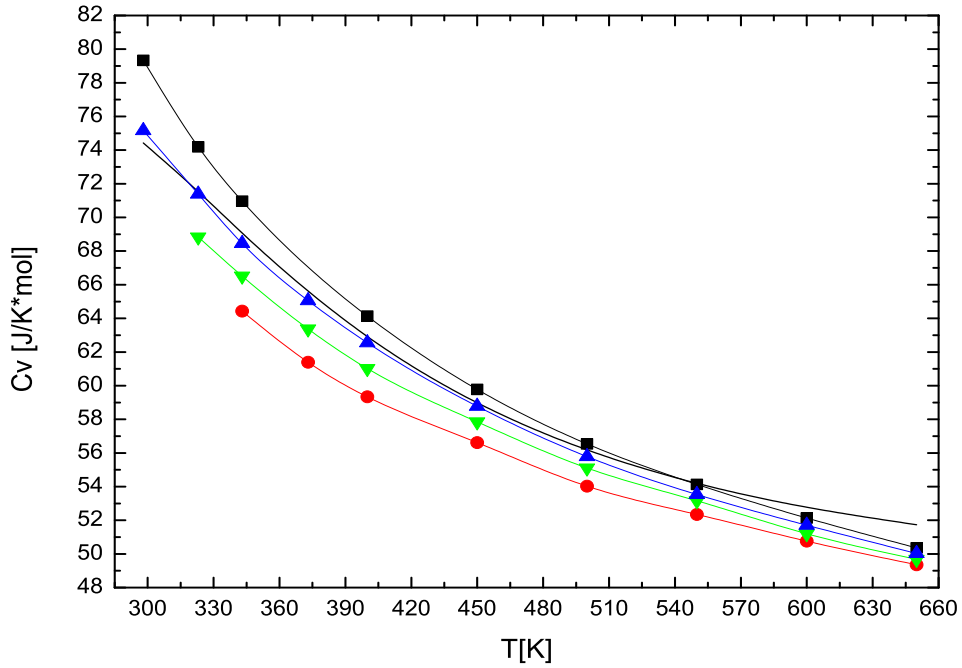

FIGURE 6.13: Isochoric heat capacity of the water-methane mixtures (0.998 g/cm^3) at methane concentrations 0% (black ■), 6% (blue ▲), 10% (red ◯), 15% (green ▼), and IAPWS-95 reference data for pure water (—). The simulation data are obtained from the SPC/E + LJ model. The lines through the data points are given only for guidance.

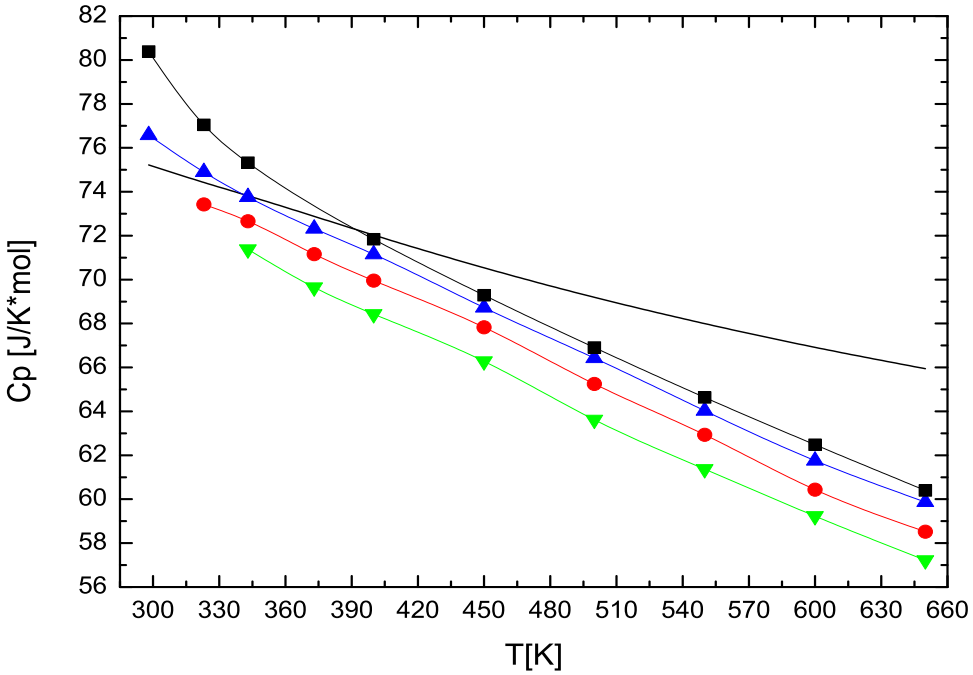

FIGURE 6.14: Isobaric heat capacity of the water-methane mixtures (0.998 g/cm^3) at methane concentrations 0% (black ■), 6% (blue ▲), 10% (red ◯), 15% (green ▼), and IAPWS-95 reference data for pure water (—). The simulation data are obtained from the SPC/E + LJ model. The lines through the data points are given only for guidance.

This indicates negative heat capacity solvation changes ($-\Delta C_{v,p}$). Available experimental data on solvation heat capacity of alcohols (Kuroki *et al.*, 2001; Kitajima *et al.*, 2003) also shows negative ΔC_p. However, experimental ΔC_p exhibits more diverse behavior. Due to absence of direct water-methane heat capacity measurements, we can only compare our MD results with experimental measurements of ΔC_p of highly soluble alcohols and ammonia available in the literature. For instance, C_p of water-ammonia system is higher than C_p of pure water and is increasing with increasing number of ammonia molecules (positive ΔC_p) (Fujita *et al.*, 2008). At the same time, C_p of water-methanol system show initial increase, after which it starts decreasing eventually becoming smaller than C_p of pure water (negative ΔC_p). Obviously solvation processes of methane, ammonia, and methanol are completely different and only qualitative conclusions can be made comparing these cases. One possible unifying factor here is C_p of pure solute component. For example, methane and methanol have smaller C_p than pure water, thus C_p of aqueous solutions of these substances tend to be smaller than in pure water. Ammonia, however, has higher C_p and as a consequence water-ammonia mixtures also have higher C_p.

To date there is no clear understanding of solvation of not only nonpolar solutes, but also polar and ionic groups. As was shown by Sharp and Madan (1997) hydration of a single nonpolar particle like CH_4 or Ar is accompanied by the short-range reorganization of the water structure in the 1st and the 2nd hydration shells. It was shown that these hydration shells contain smaller population of H-bonded water molecules pairs with high H-bond angle and high H-bond length, which indicates a decrease of disorder in water structure. In other words, one can say that these hydration shells have more ordered water structure than pure water. At the same time, hydration of single polar or small ionic solute (Sharp and Madan, 1997) shows an increase in mean H-bond length and H-bond angle. Constant pressure solvation heat capacity of polar and nonpolar groups, as was shown by Sharp and Madan, also have opposite sign, being positive for nonpolar group and negative for polar. The values of solvation heat capacity of single hydrophobic particle obtained by Sharp and Madan are still significantly smaller than experimental results. The opposite signs of ΔC_p in case of hydration of a single methane molecule, and in case of solvation of large number of methane molecules presented in this work should not be confused. The large positive values of ΔC_p ($\sim$209 J/mol·K) for methane reported in the literature (Chandler, 2005; Ben-Naim, 2009; Sharp and Madan, 1997) were calculated as the difference between C_p of the 1st hydration shell around methane and C_p of bulk water. In a sense, this is the excess heat capacity of the 1st hydration shell. This result may be interpreted in terms of a simplified two-state model, where the system has only two energy levels, activated (molecules in the hydration shell) and ground level (bulk molecules) separated by an energy gap ΔE (Sharp and Madan, 1997). In this work we simply compare the thermodynamic properties of pure water and water-methane

mixtures at different concentrations (e.g. Figs. 6.13 and 6.14). In our simulations, C_p is averaged over the whole ensemble because methane molecules at constant volume and high pressures are uniformly dissolved.

6.8 Speed of sound

The speed of sound in water at zero frequency (Pfeiffer and Heremans, 2005; Santucci *et al.*, 2006) as a function of temperature is illustrated in Fig. 6.15. The thermodynamic properties at constant volume behave quite differently than at constant pressure. Similar to many other thermodynamic properties, the speed of sound at isobaric conditions goes through a peak at around 348 K and than decreases with temperature (Wagner and Pruß, 2002). At isochoric conditions sonic speed does not have a minimum, and is simply decreasing with temperature. The thermodynamic speed of sound w_0 is related to the propagation of an adiabatic pressure wave. As can be seen from the Table 3.1 in Chapter 3, w_0 is inversely proportional to the square root of the adiabatic compressibility κ_S, and therefore, keeps freely increasing with temperature and pressure.

Results from the TIP4P/2005 and SPC/E potentials shown in Fig. 6.15 are in qualitative agreement with the reference data. Starting from values of 1420 and 1460 m/s at 298 K for TIP4P/2005 and SPCE models respectively, simulation results cross the reference data at approximately 373 K. Both curves keep increasing linearly with temperature, much above the reference curve, almost doubling their values at 650 K. The speed of sound is inversely proportional to square root of density and adiabatic compressibility κ_S of water (see Table 3.1 in Chapter 3). While the overall density of a system remains constant, it is the adiabatic compressibility (see Fig. 6.6) that determines the temperature dependence speed of sound. The high values of w_0 for both water models could be attributed to specific structure and local density behavior of TIP4P/2005 and SPC/E models. It has been shown (Santucci *et al.*, 2006), that over a range of high frequencies (>4 nm^{-1}) liquid water behaves as though it is a glassy solid rather than a liquid and sound travels at about twice its normal speed ($\sim$3200 m/s, similar to the speed of sound in ice Ih). The SPC/E model is known for strong oxygen-oxygen attraction and strong oxygen-oxygen solvation shells (Shvab and Sadus, 2012).

It is apparent from Fig. 6.15 that the MCYna potential yields the best agreement with the reference data for temperatures between 298 K and 400 K. For T $>$ 400 K the MCYna potential also over-predicts the speed of sound, however, to a much smaller extent than the nonpolarizable potentials. It is interesting to note that the original MCY potential (see Eq. 2.4 in Chapter 3), significantly over-predicts the sonic speed (see Table 6.1). The

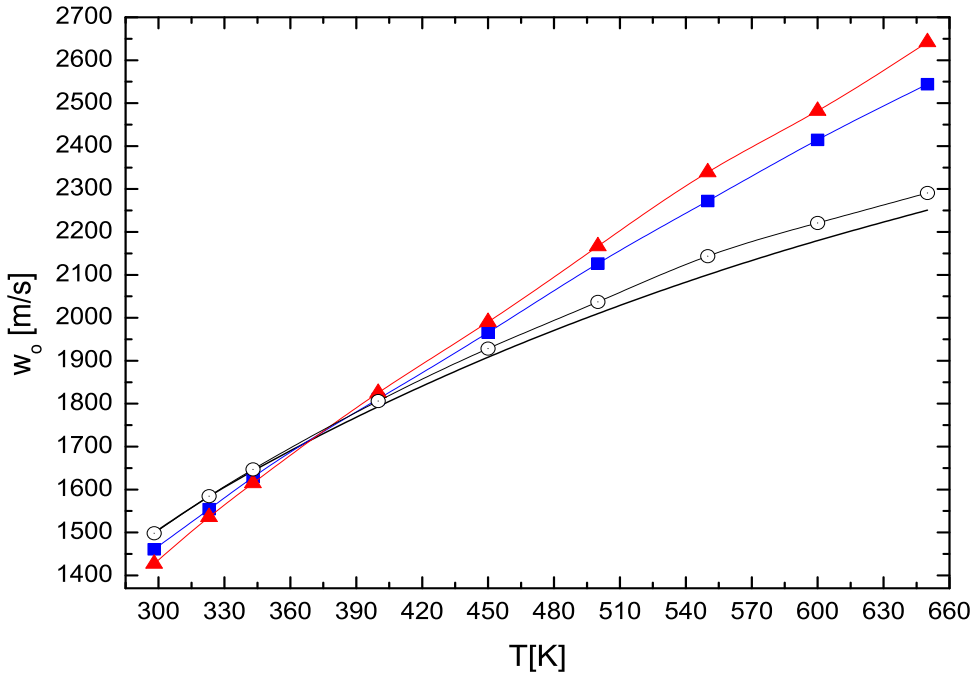

FIGURE 6.15: Speed of sound as a function of temperature predicted by the SPC/E (blue ■), TIP4P/2005 (red ▲) and MCYna potential (⊙) and compared to IAPWS-95 reference data for water (—). The lines through the data points are given only for guidance.

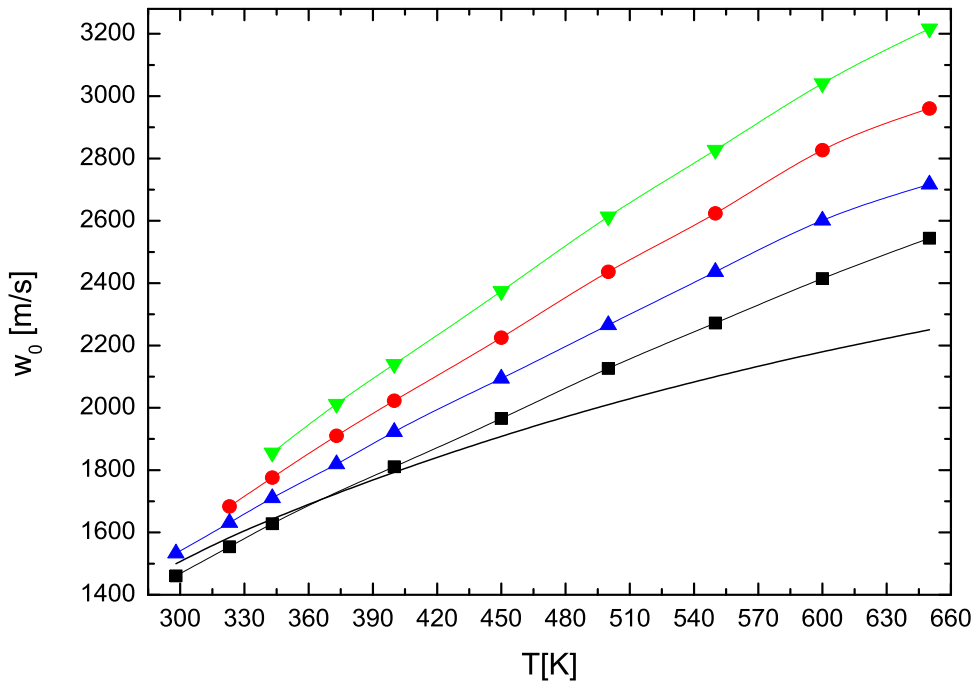

FIGURE 6.16: Speed of sound at zero frequency of the water-methane mixtures (0.998 g/cm^3) at methane concentrations 0% (black ■), 6% (blue ▲), 10% (red ◯), 15% (green ▼), and IAPWS-95 reference data for pure water (—). The simulation data are obtained from the SPC/E + LJ model. The lines through the data points are given only for guidance.

main difference between the MCYna and MCY potentials is the inclusion of nonadditive polarization and three-body interaction terms in the former.

Simulation results for water-methane mixtures obtained from the SPC/E + LJ model are shown on Fig. 6.16. Starting from value 1460 m/s at 298 K, simulation results are crossing reference data at approximately 373 K. Both curves keep linearly increasing with temperature, much above the reference curve. We can see that the presence of methane molecules significantly increases speed of sound in the mixture. Numerous experimental measurements performed for aqueous solutions of potassium chloride, sodium citrates, metal halides etc. confirm the general trend of increased sonic speed (Ernst and Manikowski, 1996, 1997; Sadeghi *et al.*, 2010).

6.9 Joule-Thomson coefficient

The Joule-Thomson expansion (Lustig, 2011; Li'sal *et al.*, 2003), or throttling of a fluid of constant composition is a closed-system process occurring between initial and final states at pressures p_0 and p_1 , with $p_0 > p_1$, for which the system enthalpy remains constant. The sign of the Joule-Thomson coefficient μ_{JT} at any given state determines whether the fluid is cooled ($\mu_{JT} > 0$) or heated ($\mu_{JT} < 0$) for a small change in pressure at constant enthalpy. Joule-Thomson heating of water is of particular interest in industry because it has a significant influence on temperature in and around injection wells.

The simulation results are compared with reference data in Fig. 6.17. The Joule-Thomson coefficient is negative for the entire simulation region, which naturally indicates heating of water at increased pressures. All three potentials fail to correctly reproduce temperature dependence of μ_{JT}. Both the TIP4P/2005 and SPC/E potentials give too high values of μ_{JT} at temperatures up to 420 - 500 K. After this temperature region, results from both nonpolarizable potentials start to decrease almost linearly. Only the MCYna potential qualitatively reproduces the behavior of the reference data at all temperatures, although the value of the Joule-Thomson coefficient is under-predicted. The disparity increases with increasing temperature. Using well-known thermodynamic relationships (Münster, 1970) we can rewrite the formula for μ_{JT} from Table 3.1 in Chapter 3 in the following form

$$\mu_{JT} = \left(\frac{\partial T}{\partial P}\right)_H = \frac{V}{C_p}(T \cdot \alpha_p - 1), \tag{6.15}$$

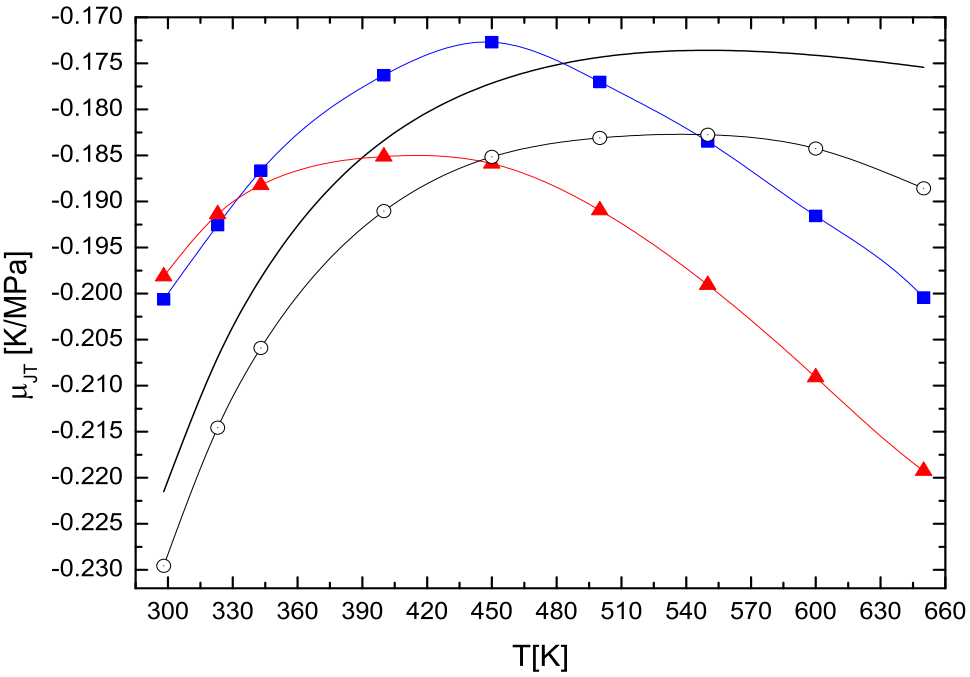

FIGURE 6.17: Joule-Thomson coefficient as a function of temperature predicted by the SPC/E (blue ■), TIP4P/2005 (red ▲) and MCYna potential (⊙) and compared to IAPWS-95 reference data for water (—). The lines through the data points are given only for guidance.

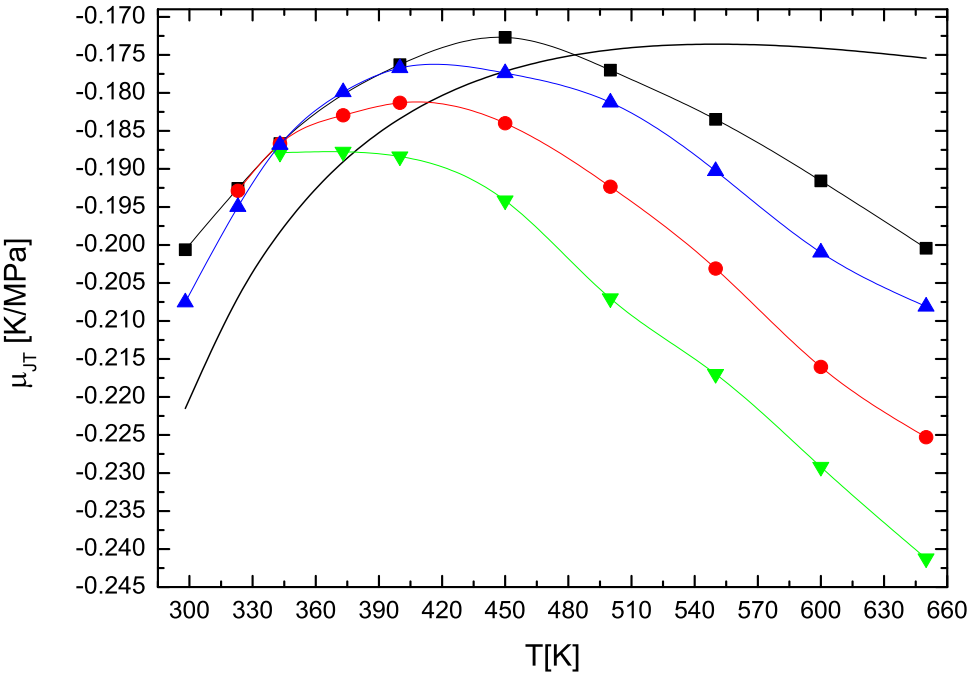

FIGURE 6.18: Joule-Thomson coefficient of the water-methane mixtures (0.998 g/cm^3) at methane concentrations 0% (black ■), 6% (blue ▲), 10% (red ◯), 15% (green ▼), and IAPWS-95 reference data for pure water (—). The simulation data are obtained from the SPC/E + LJ model. The lines through the data points are given only for guidance.

and it becomes immediately apparent that the observed temperature dependence of the Joule-Thomson coefficients is consistent with the trend observed for the thermal expansion coefficient α_p (see Fig. 6.9).

The simulation results for Joule-Thomson coefficient of water-methane mixtures obtained from the SPC/E + LJ model are presented on Fig. 6.17. The Joule-Thomson coefficient μ_{JT} is negative for the entire simulation region, which indicates that there is no inversion curve (locus of μ_{JT}) for water-methane mixtures at higher densities. The combined SPC/E + LJ potential fails to correctly reproduce temperature dependence of μ_{JT}. Results for pure water ($x_s = 0\%$) overestimate experimental data at temperatures up to 420 - 500 K, after which μ_{JT} for pure water start to decrease almost linearly. The disparity increases with increasing temperature. Joule-Thomson coefficients of mixtures repeat general trend, with peaks being shifted to the left. As well as in the case of pure water ($x_s = 0\%$), taking into consideration Eq. (6.15), we can see that the observed temperature dependence of water-methane Joule-Thomson coefficients is consistent with the trend observed for the thermal expansion coefficient α_p (Fig. 6.10). The presence of solute shifts μ_{JT} temperature maximum of the left in a similar fashion as α_p. Being proportional to the expansion coefficient and inversely proportional to the isobaric heat capacity, μ_{JT} incorporates the uncertainties from all of these quantities.

Chapter 7

Transport Properties

As was stated in the Chapters 2 and 6 solvation of nonpolar solutes in water is accompanied by large reorganization of water structure around solute particle. Apart from studying physical and thermodynamic properties of such solutions it is important to know the changes in the dynamic of water molecules brought upon by the solvation of nonpolar solutes (Mehrer and Stolwijk, 2009). Hydrodynamic transport processes in fluids play fundamental roles in many areas of science, engineering, geochemistry, and every day life. The knowledge of the transport coefficients in the fluid region of the phase diagram and elementary understanding of the transport mechanisms on the molecular scale are essential requirements for modelling hydrodynamic transport processes. This chapter aims is to calculate diffusion coefficients and velocity autocorrelation functions of water and aqueous nonpolar solute mixtures over the wide temperature-pressure range. The SPC/E and SPC/E + LJ potentials will be applied for water and mixtures respectively. Dynamic properties of aqueous solutions of neon, argon, krypton, xenon, and methane will be investigated in detail.

The simulation details were given in Chapter 4.

7.1 Diffusion theories

Diffusion is one of several transport phenomena that occur in nature. A distinguishing feature of diffusion is that it results in mixing or mass transport, without requiring bulk motion. Diffusion of mass is due to differences in concentration, temperature, and pressure (Reid *et al.*, 1987). The general expression for diffusive flux of one dilute gas in another at low velocities is (Landau and Lifshitz, 1987)

$$J_i = -\rho_o \left[D_{AB} \nabla \left(\frac{\rho_A}{\rho_o} \right) + \frac{D_T}{T} \nabla T + \frac{D_p}{p_o} \nabla p_o \right], \tag{7.1}$$

where J_i is the diffusive mass flux of gas A, D_{AB} is the mutual diffusion coefficient of gas A in gas B, D_T the coefficient for "thermodiffusion", T the temperature, and D_p the coefficient of "barodiffusion". Thermodiffusion and barodiffusion are usually small compared with concentration diffusion. Equation (7.1) holds in a reference frame where the center of mass velocity of the gas mixture is zero. In an environment where temperature and total pressure change little, and the vapor concentration is low, the concentration diffusion J_i would be simply described by the well-known Fick's first law:

$$J_i = -D_i \nabla c_i, \tag{7.2}$$

where c_i is the concentration of substance i and where D_i is the diffusion coefficient of substance i. Fick's second law predicts how diffusion causes the concentration to change with time.

$$\frac{\partial c_i}{\partial t} = D_i \nabla^2 c_i. \tag{7.3}$$

Depending from type of the substance studied, several theories of diffusivity have been developed. For example, mobility of dilute gases and ions in other gases or liquids, diffusion in polymer-solvent mixture, and mass transfer caused by chemical reactions all have different expressions for D based on different theoretical assumptions (Tyrell and Harris, 1984; Hildebrand, 1977). In this work we compare simulation results of diffusion coefficient of methane in water with theoretical predictions. A brief overview of several diffusion theories and their underlying principles is given below.

Hydrodynamic theory

The success of the kinetic theory of molecules developed in works of Maxwell, Boltzmann, and Einstein led to first attempts to quantitatively predict diffusivity of dilute gases (Mehrer and Stolwijk, 2009; Pitaevskii, Lifshitz, 1981). The hydrodynamic theory (Ramshaw, 1993; Verwoerd and Kulasiri, 2003) originates from the earlier kinetic theory of gases. According to the Nernst-Einstein equation (Einstein, 1905), a single spherical particle which moves through a stationary medium has diffusion coefficient:

$$D = kT \frac{\mathbf{v}_a}{\mathbf{f}_a}, \tag{7.4}$$

where $\mathbf{v}_a$ is the particle speed caused by force $\mathbf{f}_a$, T and k are temperature and Boltzmann coefficient respectively. Given that the flow is very slow (Reynolds number $\mathrm{Re} \ll 1$), force $\mathbf{f}_a$ becomes a function of particle's radius R_A, viscosity of the medium η_B, and the coefficient of sliding friction (Tyrrell and Harris, 1984). Two limiting cases of the Stokes-Einstein equation (7.4) are of practical interest (Huang, 2012):

- If the friction coefficient between particles is infinite, or in other words, there is no slip of fluid at the interface with particle, then fundamental Eq. (7.4) can be simplified to the following form:

$$D = \frac{kT}{6\pi\eta_B R_A}, \tag{7.5}$$

  This scenario describes diffusion of large spherical particles or molecules in a liquid which can be treated as a continuum.

- In the opposite case of very small friction coefficient, there is no tendency for the fluid to stick at the interface with the particle, and the Eq. (7.4) takes the form:

$$D = \frac{kT}{4\pi\eta_B R_A}, \tag{7.6}$$

Formulas (7.5) and (7.6) which are two limiting cases of the general Stokes-Einstein formula (7.4) (Einstein, 1905), are by far the basis and standard for testing of other formulas. As shown above, the diffusion coefficient is in inverse relation with viscosity. The Stokes-Einstein equation works well when the ratio of solute molecular radius to solvent molecular radius is greater than 5 (Longsworth, 1955). However, when this ratio decreases, the formula error becomes bigger. The Stokes-Einstein theory describes the diffusion of hard-sphere particles through the medium of smaller hard-sphere particles, with the friction being the only kind of interaction between particles. Several attempts were made to modify the Stokes-Einstein theory, in such a way, that it better accounts for viscosity, group viscosity and solute molecular radius (Arkhipov, 2011; McKee, 1981).

Kinetic theory

The kinetic theory is a further development of Stokes-Einstein diffusion theory (Yang, 1949). In short, molecules in this theory are treated as hard spheres randomly moving around and occasionally colliding with other hard spheres at low density. Application of the original kinetic diffusion theory for the calculation of diffusion coefficients requires a number of simplifying assumptions such as: only two-body interactions, no potential iterations during the free flight time, collisions are completely elastic, and as such there is no correlation between positions and velocities of colliding particles. Despite all these

assumptions, kinetic theory explains macroscopic properties of gases (pressure, temperature or volume) in terms of their molecular composition and motion, as well as diffusion coefficients of dilute spherical gases, mean free path of a particle in dilute media, heat capacities and other thermodynamic properties of gases close to ideal gas (Pitaevskii, Lifshitz, 1981; Yang, 1949). In the framework of kinetic theory, the diffusion coefficient of a single solute molecule in a dense hard-sphere fluid is given by the Enskog relation (Tyrell and Harris, 1984; Bourg and Sposito, 2007)

$$D = \frac{3}{8\rho R_{io}^2} \frac{1}{g_{io}(R_i + R_o)} \left(\frac{kT}{2\pi\mu_{io}} \right)^{0.5}, \tag{7.7}$$

where ρ is the total number density of the mixture, $g_{io}(R_i + R_0) \approx 1$ is the value of the solute radial distribution function at the point of contact of solute and solvent molecules, R_0 is the solvent molecule radius, $R_{i0} = (R_i + R_0)/2$ and $\mu_{io} = m_i m_o/(m_i + m_o)$ is the reduced solute-solvent molecular mass. Although kinetic theory was initially intended to be used for prediction of diffusion coefficients of gas, it has been used for many other areas. Davis (1987) used the Enskog's kinetic theory of dense hard sphere fluids and modified it allow long-ranged attractive interactions in a mean field sense to derive the tracer diffusion of the inhomogeneous fluid. More recently, Bourg and Sposito (2007, 2008) successfully applied Enskog formula (7.7) to predict kinetic isotope fractionation during the diffusion of ionic species and noble gases in liquid water.

Activated state theory

The diffusion theories discussed so far are applicable to systems of noninteracting or weakly interacting hard spheres. However, it has been known for a long time that many chemical reactions are accompanied by significant mass transfer. The activated state theory originates from the general transition state theory, a theory that describes chemical equilibrium between reactants and activated transition state chemicals. According to the original Eyring theory (1935), liquid is described as a lattice in which each molecule has a certain position (Eyring, 1935). Based on several empirical schemes, the assumption was made that only a small part of molecules can reach the 'activation energy'. When reached these molecules are in so-called "transition state" and, according to the statistic distribution of the thermal energy, can start diffusive motion. The Eyring's formula for diffusion coefficient in liquids has the following exponential form:

$$D = \frac{kT\lambda^2}{h} \exp\left[-\frac{\Delta G}{RT} \right], \tag{7.8}$$

where h is Plank coefficient, λ is the elementary "jump distance" with the order of average intermolecular distance, R is gas coefficient and ΔG is the difference in Gibbs energy between molecules in ground state and in 'activated' state. The ΔG is often called diffusion activation energy, and the expression in front of exponent is often written as D_0. Jähne *et al.* (1987) measured diffusion coefficients of several noble gases, methane, and carbon dioxide in water at ambient conditions, and gave values of ΔG and D_0 suitable for this temperature region. This theory has been used in the past with some success, due to the fact that diffusion motion in some chemical and osmotic processes is observed to follow exponential dependence over wide temperature range (Eyring, 1935; Alder and Hildebrand, 1973).

However, as pointed out by Petrowsky *et al.* (2012), and Alder and Hilderbrand (1973), this approach has conceptual difficulties. Tyrrell and Harris (1984) concluded that observed activation energies and their use in difffusion theories lack rigorous physical basis. In addition, the jump distance λ, an important parameter in Eq. (7.8) may also be incorrect (Ruby *et al.*, 1975). Currently, the activated state theory of diffusion is mostly used for extrapolation of data but not for prediction of D from first principles (Huang, 2012).

Free volume theory

Penetrant diffusion in polymer systems is another special case where unique approach is necessary. Complex motion patterns of long-chain polymers in medium can be explained by introducing concepts of occupied volume and free volume (Rodriguez *et al.*, 2003). The concept of free volume, or volume which can not be occupied by some molecules due to presence of other molecules, has proved to be very useful tool in description of many processes happening in condensed media. For example, low polymer molecular weight and thermal expansion coefficient calculated in Chapter 6 are due to high free volume ratio. Batchiniski (1913) found that the relationship between the viscosity and molar volume for non-associated liquids is linear. The equation is given by (Huang, 2012):

$$\frac{1}{\eta} = B\frac{V_B - V_\eta}{V_\eta}, \tag{7.9}$$

where B is a coefficient which depend on the solvent, V_B is the liquid molar volume and V_η is the hypothetical liquid molar volume at infinite viscosity. It has been found that similar relationship can be found if apply the same reasoning for diffusion coefficient (Hildebrand, 1977):

$$D = B\frac{V_B - V_D}{V_D}, \tag{7.10}$$

where V_D is the molar volume at its melting point at which diffusion is considered to cease. Thus, the diffusion coefficients predicted by the theory are strongly dependent on the "space-filling" properties of both the penetrant and the medium. Free volume theory has been used intensively in predicting the diffusivities of gases in polymers (Hong, 1995). However, later investigations of this theory produced very controversial results (Vrentas, Vrentas, 2002).

7.1.1 Trajectory analysis

Diffusion theories presented so far are macroscopic theories which allow to calculate diffusion coefficients if one knows temperature, viscosity, masses of particles, etc. In practice most of these properties are not known, and only approximate values are used. However, on a fundamental level, the coefficient of diffusion is the product of mean velocity and mean free path, with a prefactor that can be temperature dependent (Einstein, 1905). Molecular dynamics is a universal tool that can allow one to calculate diffusion coefficient of any atomic/molecular system based on direct trajectory analysis of every particle. MD approach is free from different assumptions imposed by theoretical models and, thus, is extensively used to predict diffusivity of molecular systems with increasing success. The mean velocity depends only on temperature; the mean free path is inversely proportional to the density of the gas. Molecular dynamics calculation can provide the coordinate and velocity of each atom (or group) in a system at each step. The change of atom coordinate with time presents the moving routes of atoms in the system. The moving route is called trajectory. In molecular dynamics calculation, the velocity of atoms reflects moving speed and direction. Normally, the coordinates and velocity of all atoms in the access system are calculated and saved once every 10 or 20 steps for the purpose of analysis. From the calculation of some physical properties based on this saved trajectory, a great amount of information can be obtained such as heat, statistical and dynamic information.

In the molecular dynamics simulations, particles keep moving from their initial position to a different position at each point of time. The average of the square of the particle displacement is called mean-square displacement (MSD) (Allen and Tildesley, 1987).

$$MSD = \left\langle |\mathbf{r}_i(t) - \mathbf{r}_i(0)|^2 \right\rangle, \tag{7.11}$$

where $\mathbf{r}_i(t)$ is the position of i-th molecule at time t, and the angle brackets $\langle ... \rangle$ denotes ensemble average. According to statistical mechanics principles, if the number of molecules is infinitely big and time is inffinitely long, any moment of the system can be

viewed as time zero and the average values calculated are always the same. Normally, when the motion time t is very small, MSD increases exponentially, but when t is getting larger, MSD increases almost linearly. Mean-square displacement is directly connected with diffusion coefficient D. According to the Einstein diffusion theory (1905) the diffusion coefficient was calculated from the mean-square displacement of the center of mass of the molecule (Allen and Tildesley, 1987):

$$D = \lim_{t\to\infty} \frac{\left\langle |\mathbf{r}_i(t) - \mathbf{r}_i(0)|^2 \right\rangle}{6t}, \tag{7.12}$$

where $\mathbf{r}_i(t)$ is the position of the i-th molecule at the time t. In this work we are using Eq. (7.12) to calculate all the diffusion coefficients of water and aqueous nonpolar solutions.

7.1.2 Correlation function

The dynamic properties of solute particles can be examined via the so-called velocity autocorrelation functions (VACF). Time-correlation functions are an effective and intuitive way of representing the dynamics of a system, and are one of the most common tools of time-dependent molecular dynamics. They provide a statistical description of the time-evolution of a variable for an ensemble at thermal equilibrium. They are generally applicable to any time-dependent process for an ensemble, but are commonly used to describe random (or stochastic) and irreversible processes in condensed phases. The simplest definition of a time-correlation function is: if $A_1(t)$ is a time dependent quantity at time t and $A_2(t')$ is another related quantity at some later time t', then average of the product of A_1 and A_2 over some equilibrium ensemble is the time-correlation function (Zwanzig, 1965). The assumptions on which any correlation function must be calculated are (Ahmed, 2010):

- Simulation time must be longer than the relaxation time of the system (Haile, 1997).
- Correlation length of the spatial correlation function of the system must be converged and well below the simulation box length. The correlation length can be estimated from the rate of decay of time-correlation function (Hansen and McDonald, 1986).
- Unavoidable surface effects must be appropriately minimized (Allen and Tildesley, 1987).

The velocity autocorrelation function (VACF) is a prime example of a time dependent correlation function, and is important because it reveals the underlying nature of the dynamical processes operating in a molecular system. In the short initial time period of particle motion, particle velocity is correlated to its initial value (at $t = 0$), and the VACF has big positive values. This regime is called ballistic motion. Over the time, due to random collisions, VACF slowly decays to zero, and particle velocity is not correlated to its initial velocity anymore. This regime is called diffusive motion. VACF often decays in oscillating manner (in case of ions) acquiring negative values. Since particle velocity is a vector, the negative sign represents the direction that is opposite to initial velocity. As one the most important function in statistic mechanics, correlation function in various forms can be used to calculate the average value of time and many physical properties. For example, the VACF (Allen and Tildesley, 1987) can also be used to calculate the diffusion coefficient. The normalized VACF for the i-th particle is defined as:

$$VACF = \frac{\langle \mathbf{v}_i(t) \cdot \mathbf{v}_i(0) \rangle}{\langle \mathbf{v}_i(0)^2 \rangle}, \tag{7.13}$$

where $\mathbf{v}_i(t)$ is the speed of the i-th molecule at the time t. In this work we use Eq. (7.13) to calculate VACFs of aqueous nonpolar solute mixtures.

7.2 Diffusion coefficients of aqueous nonpolar solute mixtures

The solvation of nonpolar and polar solutes is a fundamental problem encountered in a wide range of biological and chemical systems (Lynden, 1997). In particular, the manner in which water solvates alkali cations is relevant to problems such as the protein folding (Rashke *et al.*, 2001; Eisenberg and McLachlan, 1986). Hydrogen-bond structure and dynamics play very important roles in the solvation processes of many chemical and biochemical reactions (Chandler, 2005). An understanding of the orientational dynamics of water is essential in a wide range of processes, such as the rearrangement of water hydrogen-bond network (Chandler, 2005), biomolecular hydration (Fisicaro *et al.*, 2010; Bouazizi and Nasr, 2011) and drag-protein recognition (Bagchi, 2005). Therefore, accurate details about the local structures, the hydrogen-bonding network and the dynamics of aqueous solutions have been widely investigated both theoretically and experimentally. Numerous studies, for instance, have been carried out about the diffusion coefficient of different aqueous solutions of noble gases (Bourg and Sposito, 2008; Jähne *et al.*, 1987), Lennard-Jones systems (Varanasi *et al.*, 2012), and ions (Bourg and Sposito, 2007; Koneshan *et al.*, 1998; Bouazizi and Nasr, 2011). SPC/E (Berendsen *et al.*, 1987) and SPC/Fw

(Wu *et al.*, 2006) models in combination with Lennard-Jones potential have been used in all of these simulation studies. In unison with investigations presented in Chapters 4, 5, and 6 in this Chapter we calculated self-diffusion coefficient of pure SPC/E water and aqueous solutions of Ne, Ar, Kr, Xe, and CH_4 at solute concentrations x_s = 0 - 15 %. Diffusion coefficients of water-methane and water-krypton as functions of tempearture and solute concentration have been investigated.

In principle, diffusion coefficients of nonpolar solutes can be calculated by MD simulation, with an accuracy limited only by the quality of the water-water and solute-water intermolecular potentials used. Due to lack of experimental data previous simulations of noble gases diffusion coefficients have been limited to very dilute mixtures at ambient conditions (Bourg and Sposito, 2007, 2008; Varanasi *et al.*, 2012). In the present work we calculated diffusion coefficients of aqueous solutions at tangible concentrations up to 15% and tempeartures up to 650 K. Due to constant volume condition and very high pressures (as shown on Fig. 6.2 of Chapter 6) binary mixtures of H_2O with CH_4 or Kr even at concentrations up to 15% are in a single liquid phase (for this potential model).

Figs. 7.1 and 7.2 present temperature variation of diffusion coefficient of water-methane and water-krypton mixtures at solute molar fractions x_s = 0, 6, 10, and 15%. Data are obtained from the combined SPC/E + LJ potential, where SPC/E describes water-water interactions, and LJ potential is responsible for water-solute and solute-solute interactions. Hence, in this work we consider solute particles like Lennrad-Jones nonpolar spheres. Fig. 7.1a gives a comparison of diffusion coefficient of pure SPC/E water with experimental data (Krynicki *et al.*, 1978) over the temperature range 278 - 650 K. Data obtained from SPC/E model (Berendsen *et al.*, 1987) fit the experimental values fairly well almost up to the boiling temperature. At higher temperatures the deviation starts to increase giving values of self-diffusion coefficients about 35% smaller than the experimental ones. We would like to stress out that the experimental data of Krynicki *et al.* (1978) shown on Figs. 7.1 and 7.2 are only for qualitative comparison with simulation results. Direct comparison with our results is impossible due to nonmatching values of pressure. The reason why simulation values of D in the high temperature region are lower then experimental partly lays on the much higher pressures of the constantnt volume NVT simulations comparing to constant pressure experimental values of diffusion coefficient. It is well known (Krynicki *et al.*, 1978; Raabe and Sadus, 2012) that the diffusion coefficients are decreasing with increasing pressure, especially at near and supercritical temperatures. So, taking this into consideration, in the appropriate pressure range we can expect better agreement between simulations and experiment. Recent experiment on self-diffusion coefficients of light and heavy water (Yoshida *et al.*, 2005) shows values of D up to 8% smaller from data given by Krynicki *et al.* (1978). Nevertheless, data of Krynicki *et al.* cover wide enough p-T region to estimate the general trend between

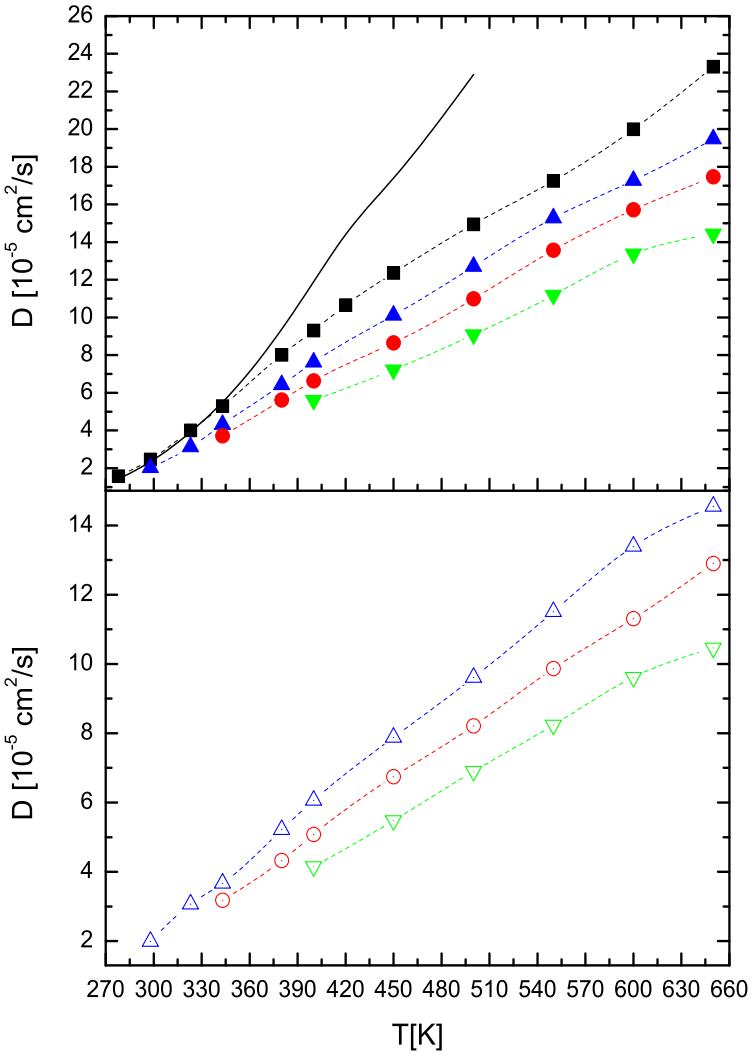

FIGURE 7.1: Diffusion coefficients of (a) water and (b) methane at constant density 0.998 g/cm^3 at methane concentrations 0% (black ■), 6% (blue ▲), 10% (red ⊙), and 15% (green ▼). Experimental self-diffusion coefficients for pure water are given for comparison (Krynicki *et al.*, 1978). The dashed lines through the data points are given only for guidance.

experiment and simulations. As was shown by Habershon *et al.* (2009), accounting for quantum effects, namely coupling between nuclear quantum effects and bond flexibility results in some increase of translational diffusion and orientational relaxation of water.

Recent experimental studies (Mancinelli *et al.*, 2007; Laenen and Thaller, 2001) of aqueous ionic solutions show that the dynamics of water in concentrated solutions differ significantly from those of pure water. As the solute concentration increases, the degree of hydrogen bonding in water decreases (Shvab and Sadus, 2012b), whereas the coordination number of water in the solution increases if compared with pure water. In contrast to polar and ionic solutions, structure and dynamics of aqueous nonpolar mixtures at high temperatures and pressures are studied much less. In order to get better understanding

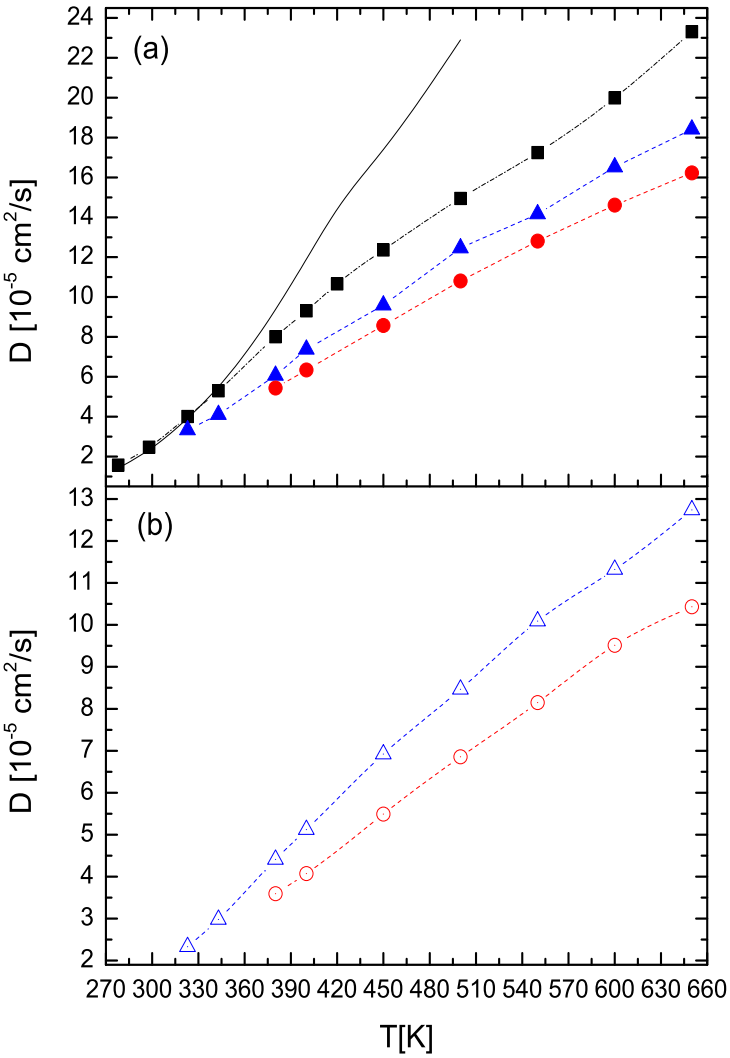

FIGURE 7.2: Diffusion coefficients of (a) water and (b) krypton at constant density 0.998 g/cm^3 at krypton concentrations 0% (black ■), 6% (blue ▲), and 10% (red ⊙). Experimental self-diffusion coefficients for pure water are given for comparison (Krynicki *et al.*, 1978). The dashed lines through the data points are given only for guidance.

of the properties of such solutions we conducted MD simulations of H_2O-CH_4, -Ne, -Ar, -Kr, and -Xe systems, to study the temperature, mass and solute particles atomic diameter dependence of diffusion coefficients these systems over the wide temperature range and the solute molar fraction x_s up to 15%.

Reliable experimental data on diffusion coefficients of noble gases are available only in the narrow temperature range from 278 - 308°C for very dilute mixtures (Jähne *et al.*, 1987). For example, experimental diffusion coefficients of Ne, CH_4, Kr, and Xe at 298 K are 4.16, 1.84, 1.84, and $1.47 \cdot 10^{-5}$ cm^2/s respectively. Our simulations at solute molar fraction x_s = 1% and T = 298 K give diffusion coefficients 3.95 (Ne), 2.51 (CH_4), 1.94 (Kr) and 1.55 (Xe) which are close to experimental data and gives validity to our results. Molecular dynamic diffusion coefficient of methane overestimates experimental data by

27%. This deviation is caused by more complex nature of water-methane interaction than in the case of noble gases. The methane molecule due to four hydrogen atoms can temporary acquire small dipole moment and as a consequence create week chemical bonds with water (Mateus *et al.*, 2011).

As we can see from the Figs. 7.1 and 7.2, presence of nonpolar particles slow down the dynamics of water molecule in the aqueous solution comparing to pure water (curve $x_s = 0\%$ on Fig. 7.1a and 7.2a). This deceleration is proportional to solute particles atomic diameter σ (see Table 4.2 from Chapter 4) and the solute molar fraction x_s. Nonpolar particles do not form chemical bonds with water and are surrounded by large solvation shells with higher local density. Koneshan *et al.* (1998) calculated the 'residence time' or average time water molecules spend in the first solvation shell of the solute particle. They have found almost linear dependence of the residence time from the nonpolar solute size σ, with residence time being bigger for larger solute particle. Our simulations support this finding, as the diffusion coefficients of the water molecules in the water-krypton mixture are in general smaller than those of water-methane mixture (comparing curves with the same x_s), which in turn are smaller than corresponding coefficients of water-neon mixture (not shown here). These findings, supported with other similar studies (Koneshan *et al.*, 1998; Bouazizi and Nasr, 2011) indicate that the diffusion of the whole system is defined by the slowest solute component. Solute particles heavier than water not only diffuse much slower but also, in sufficiently large quantities ($> 2\%$) decrease average diffusion coefficient of surrounding water molecules.

As we know from investigations of water-methane and -krypton shell structures in Chapter 4, methane and krypton acquire large first hydration shells which contain around 18 - 20 water molecules. Diffusion coefficients of methane and krypton in the mentioned mixtures are also presented on the Figs. 7.1b and 7.2b. Methane and krypton particles show much smaller diffusion coefficients which means they have much smaller mean-square displacement than water molecules. Slow motion of solute particles is caused by large hydration shells encompassing these particles.

Diffusivity D of solute species in any solvent medium depends on a number of factors such as temperature T, solvent diameter σ, solute-solvent interaction strength ε, presence of long-range electrostatic interaction between solute and solvent, viscosity η, etc. Dependence of diffusivity on some of these factors has been well understood, for example, like in hydrodynamic and kinetic theories (Tyrrell and Harris, 1984; Alder and Hildebrand, 1973). We have calculated diffusion coefficients of methane molecule in water using Stokes-Einstein Eq. (7.5), Enskog Eq. (7.7), and Eyring Eq. (7.8). For the corresponding calculations we have used viscosity $\eta = 0.896$ cp at 298 K and 0.1 MPa (Vega and Abascal, 2011), and water-methane R_{io} was obtained from Table 4.2 in Chapter 4.

The Stokes-Einstein Eq. (7.5) gives diffusivity 0.777, Enskog Eq. (7.7) - 1.715, while the experimental value of methane diffusion coefficient is $D = 1.84 \cdot 10^{-5}$ cm^2/s at T = 298 K (Jähne *et al.*, 1987). At the same time, as shown on Fig. 7.3, equations (7.5) and (7.7) give very weak temperature dependence of the diffusion coefficient, significantly underestimating D at higher temperatures. The Eyring Eq. (7.8) gave the best agreement with experiment (Jähne *et al.*, 1987) at ambient conditions. However, this can be explained by fitted parameters, in particular activation energy $\Delta G = 18.36$ kJ/mol, and exponential prefactor $D_0 = 3047\ 10^{-5}$ cm^2/s (Jähne *et al.*, 1987). The Eyring formula (7.8) keeps exponentially increasing with temperature, overpreding the simulation resultsts (methane concentration 1%) at 650 K by order of 10. For better visual representation vertical axis in Fig. 7.1 has been brocken from 20 to 98 10^{-5} cm^2/s. One obvious reason for such significant overprediction is insufficient experimental data on methane diffusion coefficient. To the best of our knowledge, experimental values of D of noble gases, methane, and carbon dioxide in water, are available only for temperatures 278 - 308 K (Jähne *et al.*, 1987). Naturally, activation energy ΔG or exponential prefactor D_0 in Eq. (7.8) at critical tempeartures differ from those at ambient conditions.

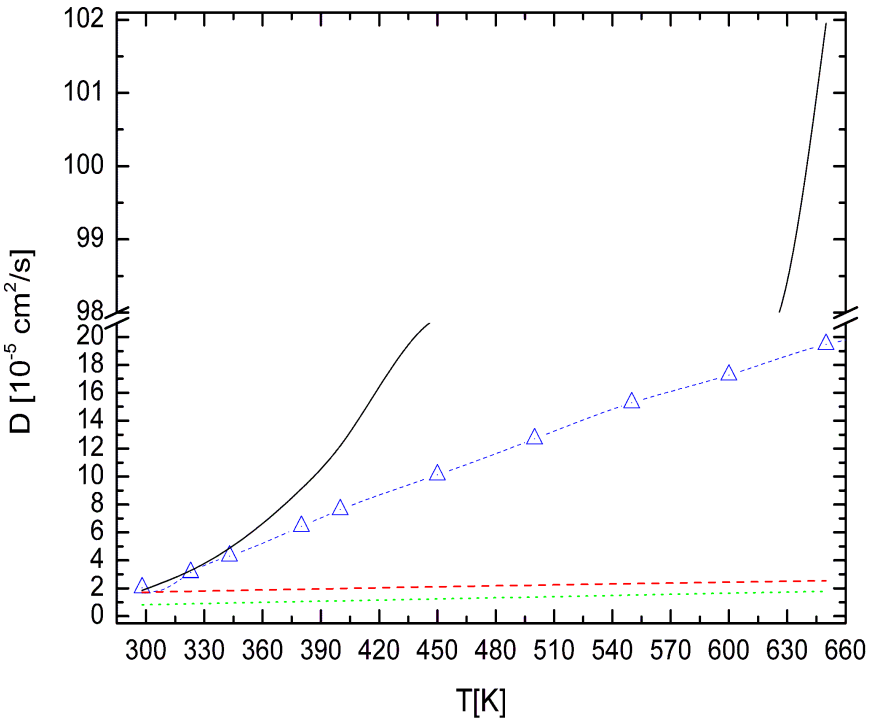

FIGURE 7.3: Temperature dependence of methane diffusion coefficient in water. Simulations at methane concentration 1% - (blue triangles), Eyring Eq. (7.8) - (black line), Enskog Eq. (7.7) - (red dashed line), Stokes-Einstein Eq. (7.5) - (green dotted line).

According to the kinetic and hydrodynamic theories (see Eqs. (7.5 - 7.7)), diffusion coefficient of molecules is also implicitly dependent from the size of the solvent and solute molecules. Comparison of diffusion coefficients of Ne, Ar, CH_4, Kr at solute

concentration $x_s = 10\%$, Xe at $x_s = 6\%$, and pure H_2O obtained from MD simulations in one-phase region at T = 400 K is given on Fig. 7.4. It is clearly seen that the smaller the atomic diameter is the higher the diffusion coefficient is. The only exception from this trend is CH_4 which has diffusion coefficient in between Ar and Kr despite having bigger parameter σ than the later two. The obvious reason for this deviation lies, according to formula (7.7), in much smaller mass of methane molecule comparing to krypton and argon.

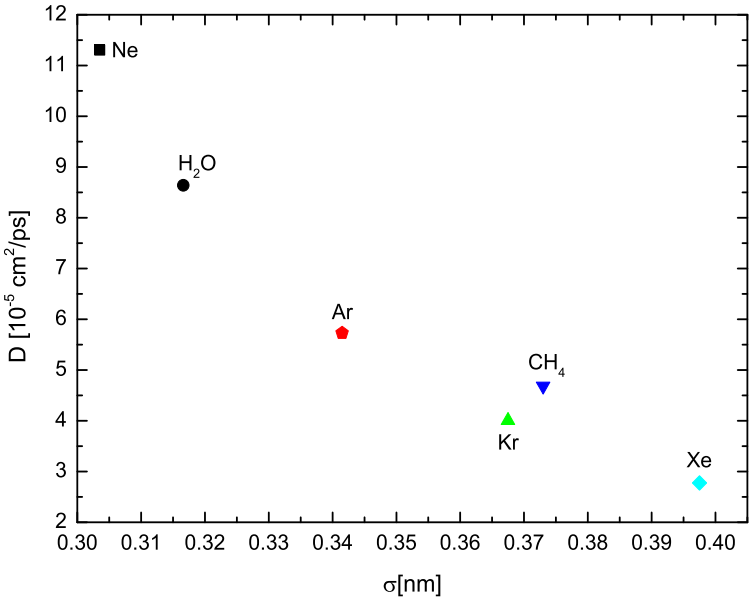

FIGURE 7.4: Diffusion coefficients of aqueous solutions of noble gases and methane at T = 400 K as a function of atomic diameter σ. Values are calculated for the mixtures with concentrations of Ne, Ar, CH_4, Kr - 10%, and Xe - 6%.

Unlike the nonpolar solutes studied in this work, solvation and dynamics of ionic species in water exhibit much more complex behavior. Due to strong Coulomb interaction between anions and cations with water molecules, forms large solvation shells with the O-H covalent bonds pointed towards anion, or in opposite direction in case of cation (Koneshan *et al.*, 1998). Highly soluble ionic substances like NaCl, for example, dissolve into positive Na^+ and negative Cl^-. Na^+ and Cl^- exhibit smaller diffusion coefficients than water molecules, with Cl^- having bit higher D than Na^+ (Bouazizi and Nasr, 2011). Residence time of water molecules inside the solvation shell of ions differs significantly from the solvation shell of nonpolar solutes. Residence time as a function of solute size shows distinct minima for cations and continuous decrease for anions (Koneshan *et al.*, 1998).

7.3 VACF and the shell structure

The diffusion can be alternatively calculated by integrating linear velocity autocorrelation functions (see Eq. (7.13)). Mathematically this is expressed as

$$D = \frac{1}{3} \lim_{\tau \to \infty} \int_0^\tau \mathbf{v}_i(t)\mathbf{v}_i(0)d\tau, \tag{7.14}$$

where $\mathbf{v}_i(t)$ is the speed of the i-th molecule at the time t. In this connection, it is expedient to investigate properties of VACF of aqueous nonpolar solute mixtures. Velocity autocorrelation functions provide information on a shell structure and its dynamic in time. This information is complimentary to the one obtained with the help of radial distribution functions and coordination numbers of aqueous solutions of Ne, Ar, CH_4, Kr, and Xe in Chapter 4. These properties allows us to understand the picture of solvation shells and their temperature dependence. VACF of water-methane and water-krypton mixtures at T = 400 K are presented on Figs. 7.5 and 7.6.

The water curves show the same behavior for all aqueous solutions of nonpolar solutes considered in this work, regardless of solute atomic diameter or mass. Water VACFs from Figs. 7.5(a) and 7.2(a) show the first positive minima which are deepening up with increasing x_s, and then very shallow second minima. The decrease in water VACF values with increasing x_s means slowing down of the water molecules motion. With increasing x_s solvation shells around hydrophobic particles also increase in size (Shvab and Sadus, 2012b) consuming more water molecules for the shell formation. It is well known (Shvab and Sadus, 2012b; Botti *et al.*, 2003; Alagona and Tani, 1980; De Grandis *et al.*, 2003) that such shells have higher local density and stronger H-bonds than the bulk water. As was shown by Koneshan *et al.* (1998) water molecules spend in average longer time in the first solvation shell around large nonpolar solute which reduces the mobility of water molecules. All these changes in water's structure induced by the hydration of hydrophobic solutes contribute to the smaller values of the diffusion coefficients and VACF which we observe on Figs. 7.1, 7.2, 7.5(a), and 7.6(a).

Figs. 7.5(b) and 7.6(b) present velocity autocorrelation functions of CH_4 and Kr inside the mixture. These curves exhibit single negative minima which are moving slightly leftward with increasing solute mole fraction. The minima of methane VACF on Fig 7.1b is located at 0.11 ps time when the krypton minima is at 0.24 ps. Methane molecule being five times lighter than the krypton atom is much easier to reverse its motion during the course of intermolecular collisions. This effect finds its reflection in deep negative part of the methane VACF from Fig. 7.5(b). Consequently, much heavier krypton shows shallow minima (see Fig. 7.6(b)) which indicate significant slowing down rather than complete

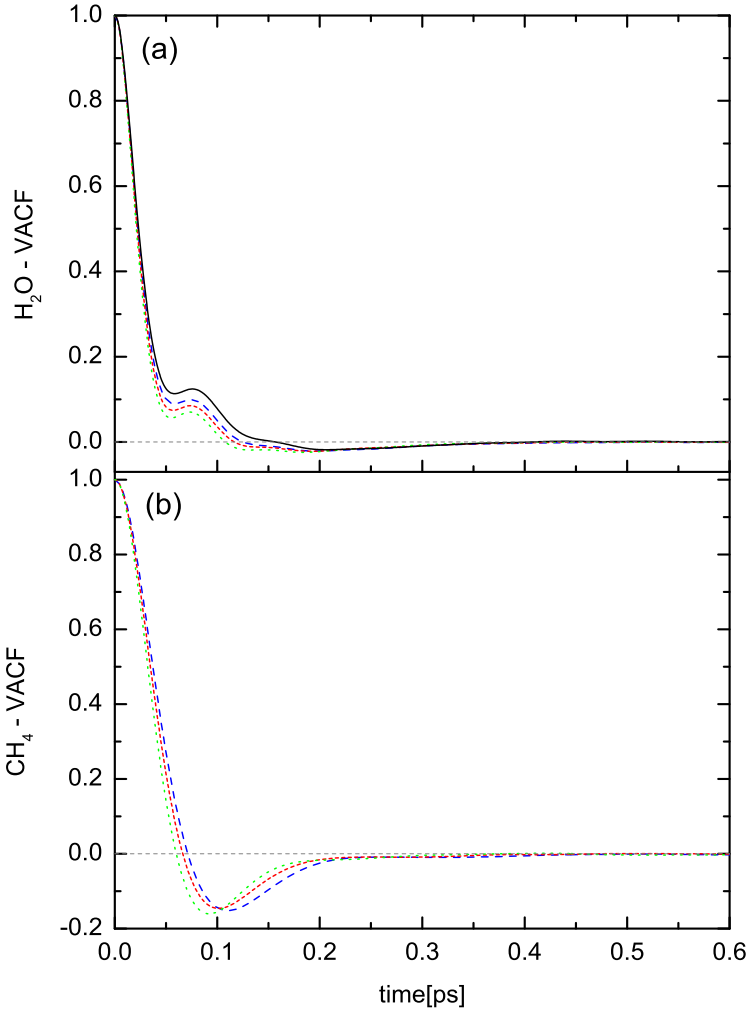

FIGURE 7.5: The velocity autocorrelation functions for H_2O (a) and CH_4 (b) in the H_2O-CH_4 mixtures at T = 400 K and CH_4 molar fractions x_s = 0% (black line), 6% (blue dashed line), 10% (red short dashed line), and 15% (green dotted line).

reverse of the particles motion. Methane solutes follow ballistic motion (nonzero velocity correlations) up to approximately 0.35 ps after which the motion became diffusive with no memory of initial velocity. Heavy krypton atoms preserve correlation of initial and current velocities up to 0.55 ps.

As well as diffusion coefficients, VACF of ionic solutes inside aqueous solution behave much differently from the VACF and diffusion coefficients of nonpolar solutes. Most of the VACFs for the ionic solutes exhibit clear oscillating behavior for the time intervals up to 0.4 ps with the amplitudes proportional to atomic diameter and mass (Koneshan *et al.*, 1998). The reason for such different scenarios obviously lies in the nature of water-solute and solute-solute interactions. Again, there is significant difference in velocity correlations of anions and cations. For example Na^+ exhibits stronger oscillations and faster transition to diffusive motion - 0.32 ps (VACF $\approx$ 0). At the same time Cl^- in aqueous NaCl solution exhibits only one peak, approaching diffusive regime of motion

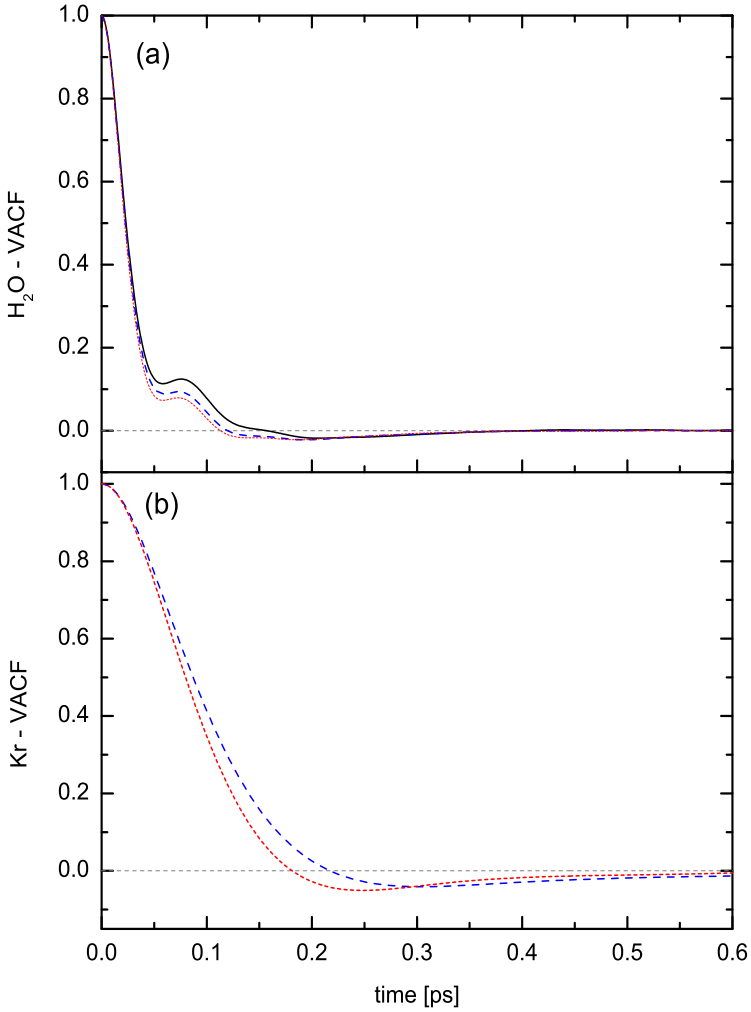

FIGURE 7.6: The velocity autocorrelation functions for H_2O (a) and Kr (b) in the H_2O-Kr mixtures at T = 400 K and CH_4 molar fractions x_s = 0% (black line), 6% (blue dashed line), and 10% (red short dashed line).

at 0.65 ps (Bouazizi and Nasr, 2011). Oscillations of ionic VACFs are caused by a long-ranged Coulomb potential, whereas single minima for nonpolar VACFs, like on Figs. 7.5(b) and 7.6(b) are caused by short-ranged Lennard-Jones repulsion. Charged particles being strongly attached to water molecules also have much smaller diffusion coefficients than nonpolar particles (Koneshan *et al.*, 1998).

Chapter 8

Conclusions and Recommendations

In this work we examined the structure, polarization, thermodynamic and transport properties of water and aqueous solutions of nonpolar solutes like Ne, Ar, Kr, Xe, and CH_4. Several water models were employed for MD simulation of water properties. In particular we have used *ab initio* polarizable MCYna model (Li *et al.*, 2007; Matsuoka *et al.*, 1976), rigid SPC/E (Berendsen *et al.*, 1987) and TIP4P/2005 (Abascal and Vega, 2005) models, and flexible SPC/Fw (Wu *et al.*, 2006) model. Properties of aqueous nonpolar solutions were investigated with the help of MCYna + LJ and SPC/E + LJ combined potentials. To the best of our knowledge, the simulation result presented here are one of the first attempts to cover all basic properties of pure water and aqueous nonpolar solutions at industrially relevant solute concentrations (x_s = 1 ... 30%) in the liquid phase and at constant density conditions (NVT ensemble). Comparisons with experimental data and theoretical predictions have been made where possible.

Structure of water and aqueous nonpolar solutions.
Changes in water structure caused by reduced density and high temperature and pressure were the starting point of this research project. It is well known that most of the water anomalies as well as concomitant properties of aqueous solutions are determined by the specific changes in H-bond network in water coordination shells and hydration shell around solutes (Shvab and Sadus, 2012a, 2012b). Proper understanding of H-bond network as a function of temperature and its behavior when nonpolar solutes are added is imperative for further investigations of physical and thermodynamic properties of these molecular systems. In particular, we paid special attention to the effect of structural change of the pure water at densities 1, 0.8, and 0.6 g/cm^3 in the range from the normal boiling temperature up to the critical temperature. RDFs, presented in Chapter 4, in general show good agreement with neutron diffraction experiments using the isotopic

substitution technique (NDIS) results (Ikeda *et al.*, 2010; Soper, 2000). Although SPC-based models yield better agreement with experiment for the height of the 1st OO peak, the MCYna model gives much better agreement of the 1st OH peak with the experimental curve, while SPC models significantly overestimate the peak height. In comparison to the MCYna model, nonpolarizable SPC-based models tend to overestimate structuring of water, particularly at high temperatures and low densities. Including polarizability improves the density-induced behavior of RDFs, although the 1st OH peaks still remain higher than observed experimentally. Along the 1 g/cm^3 isochore, the structure of water changes from a tetrahedral ice-like structure at room temperature to a simple liquid-like structure at higher temperatures. Although ice-like three-body correlation of water molecules largely vanishes at T = 373 K, simple H-bonding between two molecules persists up until the critical temperature and beyond. At this temperature, the first peak of the oxygen-hydrogen RDF vanishes, which makes impossible calculation of the oxygen-hydrogen coordination number. We conclude that up to 50% of the H-bonds are disrupted. Values of the first oxygen-oxygen coordination numbers along the 0.8 and 0.6 g/cm^3 isochores are reasonably close to values obtained at 1.0 g/cm^3 and temperatures less than or equal to 373 K. This indicates the presence of tetrahedral structure and H-bond network in bulk water at these densities and temperatures (Shvab and Sadus, 2012a).

A combination of polarizable MCYna and Lennard-Jones potential was chosen for investigation of binary mixtures of water and nonpolar solutes with Lorentz-Berthelot combining rules. The MCYna + LJ model reproduces the experimentally observed homogeneous phase region of both water-methane and water-noble gas systems more accurately than the SPC/E + LJ model. At solute percentage mole fractions $x_s \leq 30\%$, some strengthening of vicinal water structure was observed. This strengthening is manifested mainly by increasing numbers of water molecules in the 1st solvation shell around solute particles and consequent increases in the O-O and O-H coordination numbers. At $x_s > 30\%$, excessive number of solute particles starts to play a destructive role on water's tetrahedral structure, preventing water molecules from forming H-bonds. Coordination numbers follow the same dependence as the parameter σ, $\sigma_{Xe} > \sigma_{Kr} > \sigma_{CH4} > \sigma_{Ar} > \sigma_{Ne}$. The n_{oo} and n_{oh} start from values close to that of pure water at small x_s and increase with increasing solute concentrations. In contrast to n_{oo} and n_{oh} , solute-oxygen coordination numbers decrease with increasing solute concentrations (Shvab and Sadus, 2012b).

As a recommendation we would like to stress the importance of more precise definition of hydrogen bond. In the present work we were calculating 1st order OH coordination numbers which, as was shown by Kalinichev and Bass (1994), are close to the real number of H-bonds only at T $\leq$ 500 K. These coordination numbers were obtained based on geometrical definition, or the average distance between central O-atom and the closest

H-atoms of the 1st coordination shell. If we want to calculate the number of H-bonds based on more rigorous physical considerations, and at critical temperatures, we need to amplify geometric criteria with energetic criteria, and certain limitations on spatial orientation of two water molecules. For example, in works of Swiatla-Woicik *et al.* (2008) and Kalinichev and Bass (1994), only those molecules were considered to be H-bonded whose pair-potential energy is more than -10 kJ/mol, H-bond distance is less than 2.3 Å and the deviation from the straight O-H$\cdots$O is less than 25° (all parameters depend from the water model choice and T-p conditions). In addition, we would like to point out the ability of polarizable water models to mimic varying temperature and density conditions, compared with rigid models. The use of polarizable models is proving to be a promising tool in investigation of water properties in the wide range of state points.

Polarization properties.

According to the second aim of this research project, we have calculated polarization properties of water and aqueous nonpolar solute mixtures (Chapter 5). The dielectric constant and average dipole moment of pure water are changing continuously along isochores 1, 0.8, and 0.6 g/cm^3. Calculations confirmed the gradual decrease of the dielectric constant and average dipole moment with temperature and density. This trend is caused by a reduction of polarizability of the system, which in turn is caused by the collapse of the H-bond network and resulting thermal fluctuations that oppose dipole alignment by an electrostatic field. Dielectric constants calculated for water at normal density, and temperatures less than 450 K, agree within 5% of experimental values. Average dipole moments for water at ambient conditions seem to be in good agreement with *ab initio* calculations (Dyer and Cummings, 2006; Ikeda *et al.*, 2010). However, we also observed a very weak temperature dependence of the MCYna dipole moments at temperatures higher than 450 K. Calculated dipoles for $\rho = 1$ g/cm^3 never fall below 2.81 D, while the dipole moments obtained from *ab initio* simulations dipoles fall to 2.6 D (Shvab and Sadus, 2012a).

The dielectric constant ε_m and average dipole moment $\boldsymbol{\mu}_m$ of water-nonpolar solute systems also have been calculated. The calculations confirmed the gradual decrease of dielectric constant and average dipole moment with temperature and solute concentration. At high temperatures, this trend is caused by the reduction of polarizability of the system, which in turn is caused by the collapse of the H-bond network and resulting thermal fluctuations that oppose dipole alignment by an electrostatic field. In case of high solute concentration, the trend is caused by the "negative" influence of solute particles on cooperative response of water molecules on the external field. Dielectric constants ε_m calculated in the given MD simulation are in good agreement with the analytical approach of calculating ε_m of aqueous solutions at small solute concentrations x_s and temperatures up to the boiling temperature of water. At higher temperatures and solute

concentrations, analytical calculations underestimate ε_m compared to MD results (Shvab and Sadus, 2012b).

Polarizable potentials, by definition, are superior to nonpolarizable ones when it comes to calculation of dielectric constants or dipole moments. However, there is still significant room for improvement here. First of all, it is highly desirable to have water models with as few adjustable parameters as possible. Simulation data about water dipole moments at reduced density is very scant (Shvab and Sadus, 2012a). When there is no experimental data on water dipoles at lower densities, *ab initio* and MD simulations could give us insight on water properties at these conditions. The incorporation of solute polarizability could improve simulation prediction of properties of aqueous solutions. Despite being electrically neutral, noble gases and methane do have electronic polarizability, and, as was already shown in some simulations (Dyer *at al.*, 2008; Paschek, 2004a, 2004b), incorporation of this effect into calculations can improve predicted values of solubility, enthalpy, and chemical potential.

Thermodynamic properties.
Thermodynamic properties of pure water were obtained in Chapter 6 using two most popular water models SPC/E and TIP4P/2005. Water-methane mixture has been chosen as a model system, to study changes in thermodynamic properties of pure water, induced by solvation of nonpolar solutes (Chapter 6). Results for both the TIP4P/2005 and SPC/E potentials are only in semi-quantitative agreement with reference data of water. At temperatures greater than 400 K, the TIP4P/2005 and SPC/E potentials fail to correctly reproduce thermodynamic properties of liquid water. This is consistent with other work (Wu *et al.*, 2006; Vega and Abascal, 2011; Mao and Zhang, 2012), which indicated that all nonpolarizable water models give values of heat capacities, compressibilities, and thermal expansion coefficient which are in poor agreement with experiment even at 298 K and 0.1 MPa. To the best of our knowledge, our values of the Joule-Thomson coefficient and the speed of sound of SPC/E and TIP4P/2005 potentials are the only data available for these potentials.

It is difficult to unambiguously differentiate between the SPC/E and TIP4P/2005 for thermodynamic properties. Although both potentials fail at high temperatures, at temperatures up to 400 K both models reproduce the overall experimental trend, with the SPC/E results being slightly closer to the IAPWS-95 reference data (Wagner, 1995). Deviations observed in the high temperature and pressure region can be attributed to the following reasons. Non-polarizable potentials like TIP4P/2005 and SPC/E significantly underestimate the water structure and H-bond network at high temperatures. According to these models, at high temperatures, water has a very small 1st oxygen-hydrogen solvation shell and an almost vanished 2nd solvation shell. However, recent in

situ x-ray diffraction experiments of Ikeda *et al.* (2010) and Weck *et al.* (2009) indicate much better conservation of water shell structures and H-bonding at extreme pressures and temperatures. Furthermore, the *ab initio* calculations of Kang *et al.* (2011) indicate a conservation of 50% of H-bonds above 800 K. From a thermodynamic point of view, properties such as $\kappa_{T,S}$, α_p, γ_v, and w_0, which are largely determined by $\partial V/\partial p$, $\partial V/\partial T$, $\partial p/\partial T$, and $\partial p/\partial V$, respectively are significantly affected by the changes in the H-bond network and spatial packing of molecules at high T and p. By contrast, C_v and C_p strongly depend on temperature driven fluctuations of U and H. Accurate prediction of C_p and μ_{JT} requires use of intermolecular potential models that fully account for configuration effects (solvation shell structure) and different energy contributions (polarization, many-body interactions and quantum corrections) over a the wide range of state points. D is determined by the dynamics of water and solute molecules and the stability of solvation shells.

An important factor for improving MD results for polar liquids like water is the inclusion of interaction terms that better describe changes in physical conditions at variable temperature and pressure. Quantum corrections could potentially improve prediction of thermodynamic properties of water, however few calculations in this direction have been done so far (Shiga and Shinoda, 2005; Vega *et al.*, 2010). As was shown on the examples of SPC/E (Berendsen *et al.*, 1987) and TIP4P/2005 (Abascal and Vega, 2005) water models, accounting for the self-energy correction certainly improves calculations of heat capacity and vaporization enthalpy, however this correction remains effective only at ambient or near ambient conditions, where average dipole moment of water is high.

Recent success of different *ab initio* models (Bukowski *et al.*, 2007; Kang *et al.*, 2011; Mountain, 1989) and polarizable potentials (Yigzawe and Sadus, 2013; Shvab and Sadus, 2012a, 2012b; Kiss and Baranyai, 2013) demonstrate the need to use more complex potential models. Vega and Abascal (2011) suggested including polarizability to improve agreement with experiment and our analysis strongly supports this conclusion. Our comparison with the most recent simulation data (Yigzawe and Sadus, 2013) obtained from the polarizable MCYna potential indicates that very good agreement with reference data over the entire liquid range of temperatures is possible when polarization effects are included. Indeed, in some cases, the effect of including polarization is to transform poor agreement with experiment to near perfect agreement. Significantly, this is achieved without any arbitrary optimization of theory with experimental data. Such a striking results clearly indicate the superiority of polarizable water models over nonpolarizable SPC/E and TIP4P/2005 potentials in predicting thermodynamic properties of water.

Transport properties.

Diffusion coefficients and velocity-autocorrelation functions (VACF) of pure water-neon, -argon, -krypton, -xenon, and -methane mixtures were studied in Chapter 7. Self-diffusion coefficient D of SPC/E water is in good agreement with experimental data till boiling temperature, after which simulated D starts to underestimate experimental values. It is suggested that this deviation is partly due to the experimental data obtained at smaller pressures (Krynicki *et al.* (1978)). Diffusion coefficients of both water molecules and solute particles, according to the modern theories of diffusion, gradually increase with temperature. At the same time presence of nonpolar solutes decreases mobility of water molecules which reflects itself in smaller diffusion coefficients in aqueous solution comparing to pure water. Simulation results show clear dependency of the diffusivity from the solute particle size σ and mass. In agreement with kinetic theory lighter and smaller solutes have bigger diffusion coefficient than large solutes.

Dynamics of molecules inside the solution have been investigated by velocity autocorrelation function. VACF of pure water and aqueous nonpolar solutions show significant reorganization of the shell structure and changes in velocities of water molecules due to formation of the large solvation shells around nonpolar particles. Simulations show that heavy solute particles like Kr have longer correlation times comparing to lighter particles. Large solutes acquire large solvation shells which reflects in decreased diffusivity of water molecules around them, compared to water molecules in pure water.

As a recommendation, we would like to say that more efforts are needed for better prediction of the dynamic properties of nonpolar solutes in water. From the Fig. 7.1 in Chapter 7 we could see that SPC/E model underestimate diffusion coefficient at T $>$ 373 K. Apparently, computer models inadequately describe mobility and bonding of water molecules in high temperature-pressure region. Different efforts were made to circumnavigate this problem. Raabe and Sadus (2012) showed that account for intramolecular degrees of freedom improves diffusion coefficient predictions. Bourg and Sposito (2008) claims that use of Lorentz-Berthelot rules, modified in such a way that potential energy parameter ε_{ij} is larger than it would be in classical Lorentz-Berthelot case, gives better agreement of diffusion coefficient of noble gases with experiment. Thus, modern simulation studies and available experimental data indicate more complex picture of water-nonpolar solute interaction than is used in the present simulation studies.

Bibliography

Abascal J. L. F. and C. Vega, A general purpose model for the condensed phases of water: TIP4P/2005. J. Chem. Phys. **124**, 024503 (2005).

Abascal J. L. F., E. Sanz, R. García Fernández, and C. Vega, A potential model for the study of ices and amorphous water: TIP4P/Ice. J. Chem. Phys. **122**, 234511 (2005).

Abdulagatov I. M., A. I. Abdulagatov, and A. N. Kalamov, *Thermophysical Properties of Pure Fluids and Aqueous Systems at High Temperatures and High Pressures.* (Begell House, 2005).

Afanasiev V. N., A. N. Ustinov, and I. Yu. Vashurina, State of Hydration Shells of Sodium Chloride in Aqueous Solutions in a Wide Concentration Range at 273.15-373.15 K. J. Phys. Chem. B. **113**, 212 (2009).

Ahlstrotm P., A. Wallqvist, S. Engstrom, and B. Jonsson, A molecular dynamics study of polarizable water. Mol. Phys. **68**, 563 (1989).

Alagona G. and A. Tani, Structure of a dilute aqueous solution of argon. A Monte Carlo simulation. J. Chem. Phys. **72**, 580 (1980).

Alder B. J. and T. E. Wainwright, Phase Transition for a Hard Sphere System. J. Chem. Phys. **27**, 1208 (1957).

Alder B. J. and J. H. Hildebrand, Activation energy: Not involved in transport processes in liquids. Industrial and Engineering Chemistry. Fundamentals. **12**, 387 (1973).

Ahmed A., Molecular Simulation of Solid-Liquid Phase Equilibria and Shear Viscosity. PhD thesis. Swinburne University of Technology (2010).

Allen M. P. and D. J. Tildesley, *Computer Simulation of Liquids* (Oxford University Press, 1989).

Allesch M., E. Schwegler, F. Gygi, and G. Galli, A first principles simulation of rigid water. J. Chem. Phys. **123**, 5192 (2004).

Anderson B. J., J. W. Tester, and B. L. Trout, Accurate Potentials for Argon-Water and Methane-Water Interactions via *Ab initio* Methods and Their Application to Clathrate Hydrates. J. Phys. Chem. B. **108**, 18705 (2004).

Arkhipov V. P., A method for calculating the self-diffusion coefficients of molecules in multicomponent mixtures of liquids. Rus. J. Phys. Chem. A. **85**, 423 (2011).

Axilrod M. and E. Teller, Interaction of the van der Waals type between three atoms. J. Chem. Phys. **11**, 299 (1943).

Baez L. A. and P. Clancy, Existence of a density maximum in extended simple point-charge water. J. Chem. Phys. **101**, 9837 (1994).

Bagchi B., Water dynamics in the hydration layer around proteins and micelles. Chem. Rev. **105**, 3197 (2005).

Bagno A., The *ab initio* neon-water potential-energy surface and its relationship with the hydrophobic hydration shell. J. Chem. Soc. Faraday Trans. **94**, 2501 (1998).

Ball P., Water: Water - an enduring mystery. Nature, **452**, 291 (2008).

Baranyai A. and P. Kiss, A transferable classical potential for the water molecule. J. Chem. Phys. **133**, 144109 (2010).

Batchinski A. J., Investigations on the internal frictions of fluids. Zeit. Phys. Chem. **68**, 206 (1913).

Batista E. R., S. S. Xantheas, and H. Jonsson, Molecular multipole moments of water molecules in ice Ih. J. Chem. Phys. **109**, 4546 (1998).

Beeman D., Some multistep methods for use in molecular dynamics calculations. J. Comp. Phys. **20**, 130 (1976).

Ben-Naim A. and F. H. Stillinger, Aspects of the Statistical-Mechanical Theory of Water, in *Structure and Transport Processes in Water and Aqueous Solutions.* (Wiley Sons, New York, 1972).

Ben-Naim A., *Molecular Theory of Solutions* (Oxford University Press, Oxford, 2006).

Ben-Naim A., *Molecular Theory of Water and Aqueous Solutions, Part I: Understanding Water* (World Scientific, Singapore 2009).

Ben-Naim A., *Hydrophobic Interactions* (Plenum, New York, 1980).

Ben-Naim A., Solvent-induced interactions: Hydrophobic and hydrophilic phenomena. J. Chem. Phys. 90, 7412 (1989).

Berendsen H. J. C., J. P. M. Postma, W. F. van Gunsteren, and J. Hermans, in *Intermolecular Forces*, edited by B. Pullman (Reidel, Dordrecht, 1981).

Berendsen H. J. C., J. R. Grigera, and T. P. Straatsma, The missing term in effective pair potentials. J. Phys. Chem. **91**, 6269 (1987).

Berendsen H. J. C., J. P. M. Postma W. F. Vangunsteren, A. Dinola, and J. R. Haak, Molecular-Dynamics with Coupling to an External Bath. J. Chem. Phys. **81**. 3684 (1984).

Bernal J. D. and R. H. Fowler, A Theory of Water and Ionic Solution, with Particular Reference to Hydrogen and Hydroxyl Ions. J. Chem. Phys. **1**, 515 (1933).

Bickes R. W., G. Duquette, C. J. N. van den Meijdenberg , A. M. Rulis, G. Scoles, and K. M. Smith, Molecular beam scattering experiments with polar molecules: measurement of differential collision cross sections for H_2O+H_2, He, Ne, Ar, H_2O and NH_3+H_2, He, NH_3. J. Phys. B **8**, 3034 (1975).

Blundel S. and K. Blundel, *Concepts of Thermal Physics* (Oxford University Press, 2009).

Böttcher C. J. F., O. C. van Belle, P. Bordewijk, and A. Rip, *Theory of electric polarization.* (Amsterdam, New York, Elsevier Scientific Pub. Co., 1978).

Botti A., F. Bruni, A. Isopo, G. Modesti, C. Oliva, M. A. Ricci, R. Senesi, and A. K. Soper, Water structure in supercritical mixtures of water and rare gases. J. Chem. Phys. **118**, 235 (2003).

Bourg I. C. and G. Sposito, Isotopic fractionation of noble gases by diffusion in liquid water: Molecular dynamics simulations and hydrologic applications. Geochim. Cosmochim. Acta. **72**, 2237 (2008).

Bourg I. C. and G. Sposito, Molecular dynamics simulations of kinetic isotope fractionation during the diffusion of ionic species in liquid water. Geochim. Cosmochim. Acta. **71**, 5583 (2007).

Bouazizi S. and S. Nasr, Self-diffusion coefficients and orientational correlation times in aqueous NaCl solutions: Complementarity with structural investigations. J. Mol. Liq. **162**, 78 (2011).

Brooks R., F. Kalos, and A. E. Grosser, Intermolecular potential for Ar + D_2O from differential cross sections. Mol. Phys. **27**, 1071 (1974).

Brooks B. R., C. L. Brooks III, A. D. Mackerell, L. Nilsson, R. J. Petrella, B. Roux, Y. Won, G. Archontis, C. Bartels, S. Boresch A. Caflisch, L. Caves, Q. Cui, A. R. Dinner,

M. Feig, S. Fischer, J. Gao, M. Hodoscek, W. Im, K. Kuczera, T. Lazaridis, J. Ma, V. Ovchinnikov, E. Paci, R. W. Pastor, C. B. Post, J. Z. Pu, M. Schaefer, B. Tidor, R. M. Venable, H. L. Woodcock, X. Wu, W. Yang, D. M. York, and M. Karplus, CHARMM: The Biomolecular simulation Program. J. Comp. Chem. **30**, 1545 (2009).

Bukowski R.,K. Szalewicz, G. C. Groenenboom, and Ad van der Avoird, Predictions of the Properties of Water from First Principles. Science **315**, 1249 (2007).

Bukowski R.,K. Szalewicz, G. C. Groenenboom, and Ad van der Avoird, Polarizable interaction potential for water from coupled cluster calculations. I. Analysis of dimer potential energy surface. J. Chem. Phys. **128**, 094313 (2008).

Cağin T. and J. R. Ray, Fundamental treatment of molecular-dynamics ensembles. Phys. Rev. A. **37**, 247 (1988).

Cao Z., J. W. Tester, and B. L. Trout, Computation of the methane-water potential energy hypersurface via *ab initio* methods. J. Chem. Phys. **115**, 2550 (2001).

Car R. and M. Parrinello, Unified approach for molecular dynamics and density-functional theory. Phys. Rev. Lett. **55**, 2471 (1985).

Cencek W., K. Szalewicz, C. Leforestier, R. van Harreveltc, and Ad van der Avoird, An accurate analytic representation of the water pair potential. Phys. Chem. Chem. Phys. **10**, 4716 (2008).

Chałasiński G., M. M. Szczęśniak, and S. Scheiner, *Ab initio* study of the intermolecular potential of Ar-H_2O. J. Chem. Phys. **94**, 2807 (1991).

Chaplin M. F., Water Structure and Science, London South Bank University. URL http://www.lsbu.ac.uk/water/models.html.

Chandler D., Interfaces and the driving force of hydrophobic assembly. Nature **437**, 640 (2005).

Chialvo A. A. and P. T. Cummings, Engineering a simple polarizable model for the molecular simulation of water applicable over wide ranges of state conditions. J. Chem. Phys. **105**, 8274 (1996).

Chialvo A. A. and P. T. Cummings, Simple transferable intermolecular potential for the molecular simulation of water over wide ranges of state conditions. Fluid Phase Equilibria **150-151**, 73 (1998).

Colina C. M., C. G. Olivera-Fuentes, F. R. Siperstein, M. Lisal, and K. E. Gubbins, Thermal Properties of Supercritical Carbon Dioxide by Monte Carlo Simulations. Mol. Sim. **29**, 405 (2003).

Conde M., Thermophysical Properties of Brines. Properties of Working Fluids (2011).

Coulson C. A. and D. Eisenberg, Interactions of H_2O molecules in ice. I. The dipole moment of an H_2O molecule in ice. Proc. R. Soc. London, Ser. A **291**, 445 (1966).

CPMD, URL http://www.cpmd.org/ Copyright IBM Corp 1990-2008, Copyright MPI für Festkörperforschung Stuttgart 1997-2001.

Cristofori P., P. Gallo, and M. Rovere, Local order in aqueous solutions of rare gases and the role of the solute concentration: a computer simulation study with a polarizable potential. Mol. Phys. **103**, 501 (2005).

Culberson O. L. and J. J. McKetta Jr., Phase equilibria in water-hydrocarbon systems. II - The solubility of ethane in water at pressures to 10,000 psi. Trans. Am. Inst. Min. Metall Pet. Eng. 192, 223 (1951).

Dang L. X., The nonadditive intermolecular potential for water revised. J. Chem. Phys. **97**, 2659 (1992)

Dang L. X. and T-M. Chang, Molecular dynamics study of water clusters, liquid, and liquid-vapor interface of water with many-body potentials. J. Chem. Phys. 106, 8149 (1997).

Davis H. T., Kinetic theory of inhomogeneous fluid: Tracer diffusion. J. Chem. Phys. **86**, 1474 (1987).

Debenedetti P. G., Supercooled and glassy water. J. Phys.: Condens. Matter. **15**, R1669 (2003)

Dec S. F., K. E. Bowler, L. L. Stadterman, C. A. Koh, and E. D. Sloan Jr., Direct Measure of the Hydration Number of Aqueous Methane. J. Amer. Chem. Soc. **128**, 414 (2006).

De Grandis V., P. Gallo, and M. Rovere, Computer simulation of structural properties of dilute aqueous solutions of argon at supercritical conditions. J. Chem. Phys. **118**, 3646 (2003).

Docherty H., A. Galindo, C. Vega, and E. Sanz, A potential model for methane in water describing correctly the solubility of the gas and the properties of the methane hydrate. J. Chem. Phys. **125**, 074510 (2006).

Dyer P. J. and P. T. Cummings, Hydrogen bonding and induced dipole moments in water: Predictions from the Gaussian charge polarizable model and Car-Parrinello molecular dynamics. J. Chem. Phys. **125**, 144519 (2006).

Dyer P. J., H. Docherty, and P. T. Cummings, The importance of polarizability in the modeling of solubility: Quantifying the effect of solute polarizability on the solubility of small nonpolar solutes in popular models of water. J. Chem. Phys. **129**, 024508 (2008)

Einstein A., Uber die von der Molekularkinetischen Theorie der Warme Geforderte Bewegung von in Ruhenden Flussigkeiten Suspendierten Teilchen. Annalen der Physik. **17**, 549 (1905).

Eisenberg D. and W. Kauzmann, *The Structure and Properties of Water* (Clarendon Press, Oxford, 1969).

Eisenberg D. and A. D. McLachlan, Solvation energy in protein folding and binding. Nature. **319**, 199 (1986).

Eley D. D., The structure of water in aqueous solutions. Trans. Faraday Soc. **40**, 184 (1944).

Ernst S. and R. Manikowski, Measurements of the Speed of Sound and Density of Aqueous Solutions of the First-Row Transition Metal Halides. 1. Apparent and Molar Compressibilities and Volumes of Aqueous $CoCl_2$ and $CoBr_2$ within the Temperature Range 291.15 K to 297.15 K. J. Chem. Eng. Data **41**, 397 (1996).

Ernst S. and R. Manikowski, Measurements of the Speed of Sound and Density of Aqueous Solutions of the First-Row Transition-Metal Halides. 2. Apparent and Molar Compressibilities and Volumes of Aqueous $NiCl_2$ and $NiBr_2$ within the Temperature Range 291.15 K to 297.15 K. J. Chem. Eng. Data **42**, 647 (1997).

Errington J. R., G. C. Boulougouris, I. G. Economou, A. Z. Panagiotopoulos, and D. N. Theodorou, Molecular simulation of phase equilibria for water-methane and water-ethane mixtures. J. Phys. Chem. B. **102**, 8865, (1998).

Eyring H., The activated complex in chemical reactions. J. Chem. Phys. **3**, 107 (1935).

Fawzi R. M., Advanced Methods in *Ab-initio* Molecular Dynamics. PhD thesis. ETH ZURICH (2006).

Feig M., *Modeling Solvent Environments: Applications to Simulations of Biomolecules.* (Wiley-VCH Verlag GmbH and Co. KGaA, 2010).

Feldman Y., A. Puzenko, and Y. Ryabov, Dielectric Relaxation Phenomena in Complex Materials. Adv. Chem. Phys. **133**, 1 (2006).

Fernandez D. P., A. R. H. Goodwin, E. W. Lemmon, J. M. H. Levelt Sengers, and R. C. Williams, A formulation for the static permittivity of water and steam at temperatures

from 238 K to 873 K at pressures up to 1200 MPa, including derivatives and Debye-Hückel coefficients. J. Phys. Chem. Ref. Data, **26**, 1125 (1997).

Fisicaro E., C. Compari, and A. Braibanti, Hydrophobic hydration processes. General thermodynamic model by thermal equivalent dilution determinations. Biophys. Chem. **151**, 119 (2010).

Fichthorn K. A. and W. H. Weinberg, Theoretical foundations of dynamical Monte Carlo simulations. J. Chem. Phys. **95**, 1090 (1991).

Franck E. U., H. Lentz, and H. Welsch, The system water-xenon at high pressures and temperatures. Z. Phys. Chem. Neue. Folge. **93**, 95 (1974).

Franck E. U., Fluids at high pressures and temperatures. Pure Appl. Chem.**59**, 25 (1987).

Frank H. S. and Evans M. W, 1945. Free volume and entropy in condensed systems. III. Entropy in binary liquid mixtures; partial molal entropy in dilute solutions; structure and thermodynamics in aqueous electrolytes. J. Chem. Phys. **13**, 507 (1945).

Franks F., in *Water. A Comprehensive Treatise*, edited by F. Franks (Plenum Press, New York, 1972), Vol. 1.

Frenkel D. and B. Smit, *Understanding Molecular Simulation: From Algorithms to Applications.* (Academic Press, 2002)

Fröhlich H., *Theory of Dielectrics: Dielectric Constant and Dielectric Loss.* (Clarendon Press, 1958)

Fujita I., T. Suzuki, and M. Uematsu, Isobaric specific heat capacity of xH_2O + (1 - x)NH_3 with x = (0.0000, 0.1566, 0.1597, 0.3030, 0.3048, 0.4956, 0.7061, and 0.8489) at T = (280, 300, 320, and 360) K over the pressure range from (0.1 to 15) MPa. J. Chem. Thermod. **40**, 260 (2008).

Geiger A., A. Rahman, and F. H. Stillinger, Molecular dynamics study of the hydration of LennardâĂŘJones solutes. J. Chem. Phys. **70**, 263 (1979).

Goldstein H., *Classical Mechanics.* (Reading, MA, Addison-Wesley Pub. Co., 1980).

González M. A. and J. L. F. Abascal, A flexible model for water based on TIP4P/2005. J. Chem. Phys. **135**, 224516 (2011).

Gray G. and K. E. Gubbins, *Theory of Molecular Fluids* (Vol. 1, Clarendon, Oxford, 1984).

Guevara-Carrion G., J. Vrabec, and H. Hasse, Prediction of self-diffusion coefficient and shear viscosity of water and its binary mixtures with methanol and ethanol by molecular simulation. J. Chem. Phys. **134**, 074508 (2011).

Guillot B., A reappraisal of what we have learnt during three decades of computer simulations on water. J. Mol. Liq. **101**, 219 (2002).

Guillot B. and Y. Guissani, A computer simulation study of the temperature dependence of the hydrophobic hydration. J. Chem. Phys. **99**, 8075 (1993).

Guillot B. and Y. Guissani, How to build a better pair potential for water. J. Chem. Phys. **114**, 6720 (2001).

Habershon S., T. E. Markland, and D. E. Manolopoulos, Competing quantum effects in the dynamics of a flexible water model. J. Chem. Phys. **131**, 024501 (2009).

Haile, J. M., *Molecular Dynamics Simulation : Elementary Methods*. (Wiley, New York, 1997).

Hansen, J.-P. and I. R. McDonald, *Theory of Simple Liquids*. (Academic, London, 1986).

Harvey A. H. and J. M. Prausnitz, Dielectric constants of fluid mixtures over a wide range of temperature and density. J. Solution Chem. **16**, 857 (1987).

Haynes W. M., D. R. Lide, and T. J. Bruno, *CRC Handbook of Chemistry and Physics* 93rd Edition (CRC Press, Boulder, 2013).

Hernández-Cobos J., H. Saint-Martin, A. D. Mackie, L. F. Vega, and I. Ortega-Blake, Water liquid-vapor equilibria predicted by refined ab initio derived potentials. J. Chem. Phys. **123**, 044506 (2005).

Heyden M., J. Sun, S. Funkner, G. Mathias, H. Forbert, M. Havenith, and D. Marx, Dissecting the THz spectrum of liquid water from first principles via correlations in time and space. PNAS **107**, 12068 (2010).

Hildebrand J. H., *Viscosity and Diffusivity: A Predictive Treatment*. (John Wiley and Sons Inc. 1977).

Hodges M. P., R. J. Wheatley, and A. H. Harvey, Intermolecular potentials and second virial coefficients of the water-neon and water-argon complexes. J. Chem. Phys. **117**, 7169 (2002).

Hockney R. W., The potential calculation and some applications. Meth. Comput. Phys. **9**, 136 (1970).

Hong S-U., Prediction of Polymer/Solvent Diffusion Behavior Using Free-Volume Theory. Ind. Eng. Chem. Res. **34**, 2536 (1995)

Hoover W. G., Canonical dynamics: Equilibrium phase-space distributions. Phys. Rev. A. **31**, 1695 (1985).

Horn H. W., W. C. Swope, J. W. Pitera, J. D. Madura, T. J. Dick, G. L. Hura, and T. Head-Gordon, Development of an improved four-site water model for biomolecular simulations: TIP4P-Ew. J. Chem. Phys. **120**, 9665 (2004).

Huang T., Molecular Dynamics Simulation of Carbon Dioxide in Aqueous Electrolyte Solution. PhD thesis. Swinburne University of Technology (2012).

Ikeda T., Y. Katayama, H. Saitoh, and K. Aoki, Communications: High-temperature water under pressure. J. Chem. Phys. **132**, 121102 (2010).

Imai T. and F. Hirata, Hydrophobic effects on partial molar volume. J. Chem. Phys. **122**, 094509 (2005)

Jähne B., G. Heinz, and W. Dietrich, Measurement of the Diffusion Coefficient of Sparingly Soluble Gases in Water. J. Geophys. Res. **92**, 10,767 (1987).

Japas M. L. and E. U. Franck, High pressure phase equilibria and PVT-data. of the water-nitrogen system to 673 K and 250 MPa. Ber. Bunsenges. Phys. Chem. **89**, 793 (1985).

John M. S. and H. Eyring, Liquid theory and the structure of water. Ann. Rev. Phys. Chem. **27**, 45 (1976).

Jorgensen W. L., J. Chandrasekhar, J. D. Madura, R. W. Impey, and M. L. Klein, Comparison of simple potential functions for simulating liquid water. J. Chem. Phys. **79**, 926 (1983).

Kalinichev A. G. and J. D. Bass, Hydrogen bonding in supercritical water: a Monte Carlo simulation. Chem. Phys. Letters **231**, 301 (1994).

Kang D., J. Dai, and J. Yuan, Changes of structure and dipole moment of water with temperature and pressure: A first principle study. J. Chem. Phys. **135**, 024505 (2011).

Karniadakis G. and R. M. Kirby, *Parallel Scientific Computing in C and MPI: A Seamless Approach to Parallel Algorithms and their Implementation* (Cambridge University Press, Cambridge, 2003).

Kennan R. P. and G. L. Pollack, Pressure dependence of the solubility of nitrogen, argon, krypton, and xenon in water. J. Chem. Phys. **93**, 2724 (1990).

Kennedy D. and C. Norman, What don't we know. Science, **309**, 75 (2005).

Kioupis L. I. and E. J. Maginn, Pressure-enthalpy driven molecular dynamics for thermodynamic property calculation I. Methodology. Fluid Phase Equilibria **200**, 75 (2002).

Kiss P. T. and A. Baranyai, A systematic development of a polarizable potential of water. J. Chem. Phys. **138**, 204507 (2013).

Kiss P. T. and A. Baranyai, Cluster of classical water models. J. Chem. Phys. **131**, 204310 (2009).

Kitajima H., N. Kagawa, H. Endo, S. Tsuruno, and J. W. Magee, Isochoric Heat Capacities of Alkanols and Their Aqueous Mixtures. J. Chem. Eng. Data. **48**, 1583 (2003).

Hohenberg P. and W. Kohn, Inhomogeneous electron gas. Physical Review **136**, B864 (1964).

Koneshan S., J. D. Rasaiah, R. M. Lynden-Bell, and S. H. Lee, Solvent Structure, Dynamics, and Ion mobility in Aqueous solutions at 25°C. J. Phys. Chem. B. **102**, 4193 (1998).

Korolev V. P., Thermal coefficients and internal pressure of aqueous urea. concentration, temperature, and isotopy effects. J. Struct. Chem. **51**, 76 (2010).

Krynicki K., C. D. Green, and D. W. Sawyer, Pressure and Temperature Dependence of Self-diffusion in Water. Disscuss. Farad. Soc. **66**, 199 (1978).

Kuroki T., N. Kagawa, H. Endo, S. Tsuruno, and J. W. Magee, Specific Heat Capacity at Constant Volume for Water, Methanol, and Their Mixtures at Temperatures from 300 K to 400 K and Pressures to 20 MPa. J. Chem. Eng. Data. **46**, 1101 (2001).

Kvenvolden K., A review of the geochemistry of methane in natural gas hydrate. Org. Geochem. **23**, 997 (1995).

Lagache M., P. Ungerer, A. Boutina, and A. H. Fuchs, Prediction of thermodynamic derivative properties of fluids by Monte Carlo simulation. Phys. Chem. Chem. Phys. **3**, 4333 (2001).

Lagache M., P. Ungerer, and A. Boutina, Prediction of thermodynamic derivative properties of natural condensate gases at high pressure by Monte Carlo simulation. Fluid Phase Equilibria **220**, 211 (2004).

Landau L. D. and E. M. Lifshitz, *Statistical Physics (Course of Theoretical Physics, Vol. 5)* (3rd Ed. Pergamon Press, Oxford, 1980).

Laenen R. and A. Thaller, Water in the vicinity of solvated ions: modified dynamical and structural water properties resolved by sub-picosecond IR-spectroscopy. Chem. Phys. Let. **349**, 442 (2001).

Leach A. R., *Molecular Modeling: Principles and Applications*, (2nd Ed., Prentice Hall, Harlow, 2001).

Leder F., newblock Three-body contributions to the thermodynamic properties of supercritical argon. J. Chem. Phys. **82**, 1504 (1985).

Legon A. C. and D. J. Millen, Angular geometries and other properties of hydrogen-bonded dimers: a simple electrostatic interpretation of the success of the electron-pair model. Chem. Soc. Rev. **16**, 467 (1987).

Lei J., Y. Zhou, D. Xie, and H. Zhu, A new ab initio intermolecular potential energy surface and predicted rotational spectra of the Kr-H_2O complex. J. Chem. Phys. **137**, 224314 (2012).

Leonard P. J. and J. A. Barker, in *Theoretical Chemistry: Advances and Perspectives*, edited by H. Eyring and D. Henderson (Academic, London, 1975), Vol. 1.

Levine I. N. *Quantum Chemistry.* (4th Ed. Englewood Cliffs, New Jersey: Prentice Hall. 1991).

Levitt M., M. Hirshberg, R. Sharon, K. Laidig, and V. Daggett, Calibration and Testing of a Water Model for Simulation of the Molecular Dynamics of Proteins and Nucleic Acids in Solution. J. Phys. Chem. B **101**, 5051 (1997).

Li J., Non-additive Effects in Liquid Water by Parallel Molecular Dynamics Simulation. PhD thesis. Swinburne University of Technology (2012).

Li J., Z. Zhou, and R. J. Sadus, Role of nonadditive forces on the structure and properties of liquid water. J. Chem. Phys. **127**, 154509 (2007).

Li J., Z. Zhou, and R. J. Sadus, Modified force decomposition algorithms for calculating three-body interactions via molecular dynamics. Comput. Phys. Commun. **175**, 683 (2006).

Li M. and W. L. Johnson, Fluctuations and thermodynamic response functions in a Lennard-Jones solid. Phys. Rev. B. **46**, 5237 (1992).

Lisal M., W. R. Smith, and K. Aim, Direct molecular-level Monte Carlo simulation of Joule-Thomson processes. Mol. Phys. **101**, 2875 (2003).

Lie G. C. and E. Clementi, Molecular-dynamics simulation of liquid water with an *ab initio* flexible water-water interaction potential. Phys. Rev. A **33**, 2679 (1986).

Lipkowitz K. B., D. B. Boyd, R. J. Bartlett, J. F. Stanton. Applications of Post-Hartree-Fock Methods: A Tutorial. Rev. Comp. Chem. **5** (2007)

Lobaugh J. and G. A. Voth, A quantum model for water: Equilibrium and dynamical properties. J. Chem. Phys. **106**, 2400 (1997).

Loffler G., H. Schreiber, and O. Steinhauser, Computer simulation as a tool to analyze neutron scattering experiments: Water at supercritical temperatures. Ber. Bunsenges. Phys.Chem. **98**, 1575 (1994).

Longsworth L. G., *Diffusion in liquids and the Stokes-Einstein relation.* (John Wiley and Sons, Inc., New York, N.Y., 1955).

Losonczy M., J. W. Moskowitz, and F. H. Stillinger, Hydrogen bonding between neon and water. J. Chem. Phys. **59**, 3264 (1973).

Lundgaard L. and J. Mollerup, Calculation of Phase Diagrams of Gas-Hydrates. Fluid Phase Equilibria. **76**, 141 (1992).

Lustig R., Statistical thermodynamics in the classical molecular dynamics ensemble. I. Fundamentals. J. Chem. Phys. **100**, 3048 (1994).

Lustig R., Statistical thermodynamics in the classical molecular dynamics ensemble. II. Application to computer simulation. Journal of Chemical Physics, **100**, 3060 (1994).

Lustig R., Statistical thermodynamics in the classical molecular dynamics ensemble. III. Numerical results. J. Chem. Phys. **100**, 3068 (1994).

Lustig R., Microcanonical Monte Carlo simulation of thermodynamic properties. J. Chem. Phys. **109**, 8816 (1998).

Lustig R., Direct molecular NVT simulation of the isobaric heat capacity, speed of sound and Joule-Thomson coefficient. Mol. Sim. **37**, 457 (2011).

Lustig R., Statistical analogues for fundamental equation of state derivatives. Mol. Phys. **110**, 3041 (2012).

Lynden-Bell R. M. and J. C. Rasaiah, From hydrophobic to hydrophilic behaviour: A simulation study of solvation entropy and free energy of simple solutes. J. Chem. Phys. **107**, 1981 (1997).

Mahoney M. W. and W. L. Jorgensen, A five site model of liquid water and the reproduction of the density anomaly by rigid, nonpolarizable potential functions. J. Chem. Phys. **112**, 8910 (2000).

Mahoney M. W. and W. L. Jorgensen, Diffusion constant of the TIP5P model of liquid water. J. Chem. Phys. **114**, 363 (2001).

Mancinelli R., A. Botti, F. Bruni, M. A. Ricci, and A. K. Soper, Perturbation of water structure due to monovalent ions in solution. Phys. Chem. Chem. Phys. **9**, 2959 (2007).

Mao Y. and Y. Zhang, Thermal conductivit, shear viscosity and specific heat of rigid water models. Chem. Phys. Lett. **542**, 37 (2012).

Marcelli G. and R. J. Sadus, A link between the two-body and three-body interaction energies of fluids from molecular simulation. Journal of Chemical Physics, **112**, 6382-6385 (2000).

Marcelli G. and R. J. Sadus, Molecular simulation of the phase behavior of noble gases using accurate two-body and three-body intermolecular potentials. J. Chem. Phys. **111**, 1533 (1999).

Makarewicz J., *Ab initio* intermolecular potential energy surfaces of the water-rare gas atom complexes. J. Chem. Phys. **129**, 184310 (2008).

Mateus M. P. S., N. Galamba, B. J. C. Cabral, K. Coutinho, and S. Canuto, Electronic properties of a methane-water solution. Chem. Phys. Lett. **506**, 183 (2011).

Matsuoka O., E. Clementi, and M. Yoshimine. CI study of the water dimer potential surface. J. Chem. Phys. **64**, 1351 (1976).

Matthey T., Framework Design, Parrallelization and Force Computation in Molecular Dynamics. PhD thesis. University of Bergen (2002)

Mas E. M., R. Bukowski, and K. Szalewicz *Ab initio* three-body interactions for water. I. Potential and structure of water trimer. J. Chem. Phys. **118**, 4386 (2003).

Mausbach P. and R. J. Sadus, Thermodynamic properties in the molecular dynamics ensemble applied to the Gaussian core model fluid. J. Chem. Phys. **134**, 114515 (2011).

Mehrer H. and N. A. Stolwijk, Heroes and Highlights in the History of Diffusion. Diffusion Fundamentals **11**, 1 (2009).

Meier K. and S. Kabelac, Pressure derivatives in the classical molecular-dynamics ensemble, J. Chem. Phys. **124**, 064104 (2006).

Metropolis N., A.W. Rosenbluth, M.N. Rosenbluth, A.H. Teller, and E. Teller, Equation of State Calculations by Fast Computing Machines. J. Chem. Phys. **21**, 1087 (1953).

McKee R. A., A generalization of the nernst-Einstein equation for self-diffusion in high defect concentration solids. Proceedings of the International Conference on Fast Ionic Transport in Solids. **5**, 133 (1981)

Mikheev Y. A, L. N. Guseva, E. Y. Davydov, and Y. A. Ershov, The hydration of hydrophobic substances. Russ. J. Phys. Chem. A **81**, 1897 (2007).

Miller D. G., Joule-Thomson inversion curve, corresponding state, and simple equation of state. Industr. Chem. Eng. Fund. **9**, 585 (1970).

Mountain R. D., Molecular dynamics investigation of expanded water at elevated temperatures. J. Chem. Phys. **90**, 1866 (1988).

Münster A., *Classical Thermodynamics*, translated by E. S. Halberstadt (Wiley, London, 1970).

Nada H. and J. J. M. van der Eerden, An intermolecular potential model for the simulation of ice and water near the melting point: a six-site model of H_2O, J. Chem. Phys., **118**, 7401 (2003).

Nada H. and Y. Furukawa, Anisotropy in growth kinetics at interfaces between proton-disordered hexagonal ice and water: a molecular dynamics study using the six-site model of H_2O, J. Cryst. Growth. **283**, 242 (2005).

Narten A. H. and H. A. Levy, Liquid water: molecular correlation functions for x-ray diffraction. J. Chem. Phys. **55**, 2263 (1971).

Neumann M., Dipole moment fluctuation formulas in computer simulations of polar systems. Mol. Phys. **50**, 841 (1983).

Neumann M., Dielectric relaxation in water. Computer simulations with TIP4P potential. J. Chem. Phys. **85**, 1567 (1986).

Niesar U., G. Corongiu, E. Clementi, G. R. Kneller, and D. K. Bhattacharya, Molecular dynamic simulation of liquid water using the NCC *ab initio* potential. J. Phys. Chem. **94**, 7949 (1990).

Nosé S., A unified formulation of the constant temperature molecular dynamics methods. J. Chem. Phys. **81**, 511 (1984).

Okazaki S., K. Nakanishi, H. Touhara, Y. Adachi, Monte Carlo studies on the hydrophobic hydration in dilute aqueous solutions of nonpolar molecules. J. Chem. Phys. **71**, 2421 (1979).

O'Shea S. F., P. R. Tremaine, Thermodynamics of liquid and supercritical water to 900°C by a Monte-Carlo method. J. Phys. Chem. **84**, 3304 (1980).

Paricaud P., M. Predota, and A. A. Chialvo, From dimer to condensed phases at extreme conditions: Accurate predictions of the properties of water by a Gaussian charge polarizable model. J. Chem. Phys. **122**, 244511 (2005).

Parr, R. G. and Yang, W., *Density-Functional Theory of Atoms and Molecules.* (New York: Oxford University Press. 1989).

Paschek D., Heat capacity effects associated with the hydrophobic hydration and interaction of simple solutes: A detailed structural and energetical analysis based on molecular dynamics simulations. J. Chem. Phys. **120**, 10605 (2004).

Paschek D., Temperature dependence of the hydrophobic hydration and interaction of simple solutes: An examination of five popular water models. J. Chem. Phys. **120**, 6674 (2004).

Petrowsky M., A. Fleshman, M. Ismail, D. T. Glatzhofer, D. N. Bopege, and R. Frech, Molecular and System Parameters Governing Mass and Charge Transport in Polar Liquids and Electrolytes. J. Phys. Chem. B, 2012, **116**, 10098 (2012).

Pi H. L., J. L. Aragones, C. Vega, E. G. Noya, J. L. F. Abascal, M. A. Gonzalez, and C. McBride, Anomalies in water as obtained from computer simulations of the TIP4P/2005 model: density maxima, and density, isothermal compressibility and heat capacity minima. Mol. Phys. **107** 365 (2009).

Pitaevskii L. P. and E. M. Lifshitz, *Physical Kinetics (Course of Theoretical Physics, Vol. 10)*. (Pergamon Press, Oxford, 1981).

Poling L., A Molecular Theory of General Anesthesia. Science. **134**, 15 (1961).

Prausnitz J. M., R. N. Lichtenthaler, and E. G. de Azevedo, *Molecular Thermodynamics of Fluid Phase Equilibria*. (Prentice Hall, 3rd ed., 1999).

Press, S. A., A. W. Teukolsky, A. W. T. Vetterling, and B. P. Flannery, *Numerical recipes in C: The Art of Scientific Computing*. (Cambridge University Press, New York, 1992).

Raabe G. and R. J. Sadus, Molecular dynamics simulation of the dielectric constant of water: The effect of bond flexibility. J. Chem. Phys. **134**, 234501 (2011).

Raabe G. and R. J. Sadus, Molecular dynamics simulation of the effect of bond flexibility on the transport properties of water. J. Chem. Phys. **137**, 104512 (2012).

Rahman A. and F. H. Stillinger, Molecular dynamics study of liquid water. J. Chem. Phys. **55**, 3336 (1971).

Ramshaw J. D., Hydrodynamic Theory of Multicomponent Diffusion and Thermal Diffusion in Multitemperature Gas Mixtures. J. Non-Equil. Thermod. **18**, 121 (1993).

Rapaport D. C. and H. A. Scheraga, Hydration of inert solutes. A molecular dynamics study. J. Phys. Chem. **86**, 873 (1982)

Raschke T. M., J. Tsai, and M. Levitt, newblock Quantification of the hydrophobic interaction by simulations of the aggregation of small hydrophobic solutes in water. PNAS **98**, 5965 (2001).

Raschke T. M. and M. Levitt, Nonpolar solutes enhance water structure within hydration shells while reducing interactions between them. PNAS **102**, 6777 (2005).

Reid R. C., Prausnitz J. M., and Poling B. E, *The properties of gases and liquids.*(4th Ed. McGraw-Hill Co., New York, NY, 1987).

Reimers J. R., R. O. Watts, and M. L. Klein, Intermolecular potential functions and the properties of water. Chent Phys. **64**, 95 (1982).

Rick S. W., S. J. Stuart, and B. J. Berne, Dynamical fluctuating charge force fields: Application to liquid water. J. Chem. Phys. **101**, 6141 (1994).

Rick S. W., Simulation of ice and liquid water over a range of temperatures using the fluctuating charge model. J. Chem. Phys. **114**, 2276 (2001).

Rodger P. M., Stability of gas hydrates. J. Phys. Chem. **94**, 6080 (1990).

Rodriguez F., C. Cohen, C. K. Ober, and L. A. Archer, *Principles of Polymer Systems.* (5th ed., CRC Press, 2003).

Rossato L., F. Rossetto, and P. L. Silvestrelli, Aqueous Solvation of Methane from First Principles. J. Phys. Chem. B, 116, 4552 (2012).

Rozmanov D. and Peter G. Kusalik, Transport coefficients of the TIP4P-2005 water model. J. Chem. Phys. **136**, 044507 (2012).

Ruby S. L., J. C. Love, P. A. Flinn, and B. J. Zabransky, Diffusion of iron ions in a cold liquid: Evidence against a "jump" model. Appl. Phys. Let. **27**, 320 (1975).

Ryckaert J-P., G. Ciccotti, and H. J. C. Berendsen, Numerical Integration of the Cartesian Equations of Motion of a System with Constraints: Molecular Dynamics of n-Alkanes. J. Comp. Phys. **23**, 327 (1977).

Sadeghi R., R. Golabiazar, and E. Parsi, Vapor-Liquid Equilibria, Density, and Speed of Sound of Aqueous Solutions of Sodium Dihydrogen Citrate or Disodium Hydrogen Citrate. J. Chem. Eng. Data **55**, 5874 (2010).

Sadus R. J., *Molecular simulation of fluids: Theory, Algorithms and Object-Orientation* (Elsevier, Amsterdam, 1999).

Safarov J., F. Millero, R. Feistel, A. Heintz, and E. Hassel, Thermodynamic properties of standard seawater. Ocean Sci. Discuss. **6**, 689 (2009).

Sharma M., R. Resta, and R. Car, Dipolar correlations and the dielectric permittivity of water. Phys. Rev. Lett. **98**, 247401 (2007).

Sharp K. A. and B. Madan, Hydrophobic effect, Water Structure, and Heat Capacity Changes. J. Phys. Chem. B. **101**, 4343 (1997).

Shiga M. and W. Shinoda, Calculation of heat capacities of light and heavy water by path-integral molecular dynamics. J. Chem. Phys. **123**, 134502 (2005).

Shmonov V. M., R. J. Sadus, and E. U. Franck, High-pressure phase equilibria and supercritical pVT data of the binary water + methane mixture to 723 K and 200 MPa. J. Phys. Chem. **97**, 9054 (1993).

Smith W., T.R. Forester, and I.T.Todorov, The DL_POLY Classic User Manual. Daresbury Laboratory, United Kingdom (2012). URL http://www.ccp5.ac.uk/DL_POLY_CLASSIC/.

Soper A. K., The radial distribution functions of water and ice from 220 to 673 K and at pressures up to 400 MPa. Chem. Phys. **258**, 121 (2000).

Sorenson J. M., G. Hura, R. M. Glaeser, and T. Head-Gordon, What can x-ray scattering tell us about the radial distribution functions of water? J. Chem. Phys. **113**, 9149 (2000).

Skaf M. S. and B. M. Ladanyi, Molecular dynamics simulation of the wave vector-dependent static dielectric properties of methanol-water mixtures. J. Chem. Phys. **102**, 6542 (1995).

Stern H. A., F. Rittner, B. J. Berne, and Richard A. Friesner, Combined fluctuating charge and polarizable dipole models: Application to a five-site water potential function. J. Chem. Phys. **115**, 2237 (2001).

Stillinger F. H. and A. Rahman, Molecular dynamics study of temperature effects on water structure and kinetics. J. Chem. Phys. **57**, 1281 (1972).

Stillinger F. H. and A. Rahman, Improved simulation of liquid water by molecular dynamics. J. Chem. Phys. **60**, 1545 (1974).

Sullivan D. M., G. W. Neilson, and H. E. Fischer, Hydrophobic hydration of argon at high temperatures. J. Chem. Phys. **115**, 339 (2001).

Sun J., D. Bousquet, H. Forbert, and D. Marx, Glycine in aqueous solution: solvation shells, interfacial water, and vibrational spectroscopy from ab initio molecular dynamics. J. Phys. Chem. **133**, 114508 (2010).

Svishchev I. M. and P. G. Kusalik, Dynamics in liquid H_2O, D_2O, and T_2O: A Comparative Simulation Study. J. Phys. Chem. **98**, 728 (1994).

Svishchev I. M., P. G. Kusalik, J. Wang, and R. J. Boyd, Polarizable point-charge model for water: results under normal and extreme conditions. J. Chem. Phys. **105**, 4742 (1996).

Swiatla-Wojcik D., A. Pabis, and J. Szala, Density and temperature effect on hydrogen-bonded clusters in water - MD simulation study. Centr. Eur. J. Chem. **6**, 555 (2008).

Swope W. C., H. C. Andersen, P. H. Berens, and K. R. Wilson, A computer simulation method for the calculation of equilibrium constants for the formation of physical clusters of molecules: Application to small water clusters. J. Chem. Phys. **76**, 648 (1982).

Szalewicz K., C. Leforestier, Ad van der Avoird, Towards the complete understanding of water by a first-principles computational approach. Chem. Phys. Let. **482**, 1 (2009).

Szczęśniak M. M, G. Chałasiński, S. M. Cybulski, and P. Cieplak, *Ab initio* study of the potential energy surface of CH_4-H_2O. J. Chem. Phys. **98**, 3078 (1993).

Teixeira J, M. -C. Bellissent-Funel, S. H. Chen, and A. J. Dianoux, Experimental determination of the nature of diffusive motions of water molecules at low temperature. Phys. Rev. A. **31**, 1913 (1985).

Teleman O, B. Jönsson, and S. Engström, A molecular dynamics simulation of water model with intramolecular degrees of freedom. Mol. Phys. **60**, 193 (1987).

A. Tkatchenko and M. Scheffler, Accurate Molecular Van Der Waals Interactions from Ground-State Electron Density and Free-Atom Reference Data. Phys. Rev. Lett. **102**, 073005 (2009).

Tromp R. H., P. Postrino, G. W. Neilson, M. A. Ricci, and A. K. Soper, Neutron diffraction studies of H_2O/D_2O at supercritical temperatures. A direct determination of $g_{HH}(r)$, $g_{OH}(r)$, and $g_{OO}(r)$. J. Chem. Phys. **101**, 6210 (1994).

Tuckerman M. E., Ab initio molecular dynamics: basic concepts, current trends and novel applications. J. Physics: Cond. Matt. **14**, R1297 (2002).

Tyrrell H. J. V. and K. R. Harris, *Diffusion in liquids: A theoretical and experimental study.* (Butterworths, 1984).

Uematsu M. and E. Franck, Static dielectric constants of water and steam. J. Phys. Chem. Ref. Data. **9**, 1291 (1980).

Van Beek K. H., in *Dielectric behavior of heterogeneous systems* (C.R.C Press, 1967).

Vanneste M., M. De Batist, A. Golmshtok, A. Kremlev, and W. Versteeg, Multi-frequency seismic study of gas hydrate-bearing sediments in Lake Baikal, Siberia. Marine Geology. **172**, 1 (2001).

Varanasi S. R., P. Kumar, and S. Yashonath, Dependence of diffusivity on density and solute diameter in liquid phase: A molecular dynamics study of Lennard-Jones system. J. Chem. Phys. **136**, 144505 (2012).

Vega C., J. L. F. Abascal, and I. Nezbeda, Vapor-liquid equilibria from the triple point up to the critical point for the new generation of TIP4P-like models: TIP4P/Ew, TIP4P/2005, and TIP4P/ice. J. Chem. Phys. **125** 034503 (2006).

Vega C. and J. L. F. Abascal, Simulating water with rigid non-polarizable models: a general perspective. Phys. Chem. Chem. Phys. **13**, 19663 (2011).

Vega C., J. L. F. Abascal, M. M. Conde, and J. L. Aragones, What ice can teach us about water interactions: a critical comparison of the performance of different water models, Farad. Discuss. **141**, 251 (2009).

Vega C., E. Sanz, J. L. F. Abascal, and E. G. Noya, Determination of phase diagrams via computer simulation: methodology and applications to water, electrolytes and proteins. J. Phys: Cond. Matt. **20**, 153101 (2008).

Vega C. and J. L. F. Abascal, Relation between the melting temperature and the temperature of maximum density for the most common models of water. J. Chem. Phys. **123**, 144504 (2005).

Vega C., J. L. F. Abascal, and I. Nezbeda, Vapor-liquid equilibria from the triple point up to the critical point for the new generation of TIP4P-like models: TIP4P/Ew, TIP4P/2005, and TIP4P/ice. J. Chem. Phys. **125**, 034503 (2006).

Vega C., M. M. Conde, C. McBride, J. L. F. Abascal, E. G. Noya, R. Ramirez, and L. M. Sesé, Heat capacity of water: A signature of nuclear quantum effects. J. Chem. Phys. **132**, 046101 (2010).

Vega C. and E. de Miguel, Surface tension of the most popular models of water by using the test-area simulation method, J. Chem. Phys. **126**, 154707 (2007).

Verlet L., Computer "Experiments" on Classical Fluids. I. Thermodynamical Properties of Lennard-Jones Molecules. Phys. Rev. **159**, 98 (1967).

Vrentas J. S. and C. M. Vrentas, Evaluation of the Free-Volume Theory of Diffusion. J. Polymer Science Part B: Polymer Physics. **41**, 501 (2002).

Verwoerd W. and D. Kulasiri, Theory of diffusions applied to stochastic flow in porous media. Math. Comp. Modelling. **38**, 1453 (2003).

Wagner W., The IAPWS-95 software used to obtain reference data for water. URL http://www.thermo.rub.de/en/prof-w-wagner/software/iapws-95.html.

Wagner W. and A. Pruß, The IAPWS Formulation 1995 for the Thermodynamic Properties of Ordinary Water Substance for General and Scientific Use. J. Phys. Chem. Ref. Data. **31**, 387 (2002).

Wallace D. C. and G. K. Staub, Ensemble correction for the molecular dynamics ensemble. Phys. Rev. A. **27**, 2201 (1983).

Wang L. and R. J. Sadus, Effect of three-body interactions on the vapour-liquid phase equilibria of binary fluid mixtures. J. Chem. Phys. **125**, 074503 (2006).

Wang L. and R. J. Sadus, Three-body interactions and solid-liquid phase equilibria: application of a molecular dynamics algorithm. Phys. Rev. E. **74**, 031203 (2006).

Weck G., J. Eggert, P. Loubeyre, N. Desbiens, E. Bourasseau, J.-B. Maillet, M. Mezouar, and M. Hanfland, Phase diagrams and isotopic effects of normal and deuterated water studied via x-ray diffraction up to 4.5 GPa and 500 K. Phys. Rev. B **80**, 180202(R) (2009).

Wheeler D. and J. Newman, Molecular Dynamics Simulations of Multicomponent Diffusion. 1. Equilibrium Method. J. Phys. Chem. B **108**, 18353 (2004.)

Wojcik M. and E. Clementi, Molecular dynamics simulation of liquid water with three-body forces included. J. Chem. Phys. **84**, 5970 (1985).

Wu Y., H. Tepper, and G. Voth, Flexible simple point-charge water model with improved liquid-state properties. J. Chem. Phys. **124**, 024503 (2006).

Wu G., M. Heilig, H. Lentz, and E. U. Franck, High pressure phase equilibria of the water-argon system. Ber. Bunsenges. Phys. Chem. **94**, 24 (1990).

Yang L. M., Kinetic Theory of Diffusion in Gases and Liquids. II. General Kinetic Theory of Liquids Mixtures. Proc. R. Soc. Lond. A. **198**, 471 (1949).

Yigzawe T. M. and R. J. Sadus, Thermodynamic properties of liquid water from a polarisable intermolecular potential. J. Chem. Phys. **138**, 044503 (2013).

Yigzawe T. M., Molecular Dynamics Simulation of the Thermodynamic Properties of Water and Atomistic Fluids. PhD thesis. Swinburne University of Technology (2012).

Yoshida K., C. Wakai, N. Matubayasi, and M. Nakahara, A new high-temperature multinuclear-magnetic-resonance probe and the self-diffusion of light and heavy water in sub- and supercritical conditions. J. Chem. Phys. **123**, 164506 (2005).

Yoshii N., H. Yoshie, S. Miura, and S. Okazaki, A molecular-dynamics study of sub- and supercritical water using polarisable potential model. J. Chem. Phys. **109**, 4873 (1998).

Yu H. and W. F. van Gunsteren, Accounting for polarization in molecular simulation. Comp. Phys. Commun. **172**, 69 (2005).

Zaitsev A. A., V. N. Afanasiev, and A. N. Ustinov, Adiabatic and isothermal compressibility of aqueous solutions of sodium cloride. J. Struct. Chem. **51**, 881 (2010).

Zheng H., T. Duan, and Q. Sun, In situ observation of CH_4-H_2O binary system at high temperature and high pressure by diamond anvil cell and Raman spectroscopy. Exp. Therm. Fluid Sci. **38**, 262 (2012).

Zwanzig R., Time-Correlation Functions and Transport Coefficients in Statistical Mechanics. Annu. Rev. Phys. Chem. **16** 67 (1965).